Ponce de Leon Inlet, FL: An Integrated Hydrodynamic and Morphologic Assessment of Design Alternatives using the U.S. Army Corps of Engineers' Coastal Modeling System

by

Pamela Joan Christian

Bachelor of Science
Biology
Florida State University
1991

Master of Education
In Secondary Science
Winthrop University
1997

A dissertation
submitted to Florida Institute of Technology
in partial fulfillment of the requirements
for the degree of

Doctor of Philosophy
in
Oceanography

Melbourne, Florida
July, 2009

We the undersigned committee hereby recommend
that the attached document be accepted as fulfilling
in part of the requirements for the degree of
Doctor of Philosophy in Oceanography.

Ponce de Leon Inlet, FL: An Integrated Hydrodynamic and Morphologic Assessment of Design Alternatives using the U.S. Army Corps of Engineers' Coastal Modeling System

a dissertation by
Pamela Joan Christian

Gary A. Zarillo, Ph.D.
Professor
Marine and Environmental Systems
Committee Chair

Charles R. Bostater, Ph.D.
Associate Professor
Marine and Environmental Systems
Committee Member

Robert van Woesik, Ph.D.
Professor
Biological Sciences
Committee Member

George Maul, Ph.D.
Professor and Head
Marine and Environmental Systems
Committee Member

ABSTRACT

Ponce de Leon Inlet, FL: An Integrated Hydrodynamic and Morphologic Assessment of Design Alternatives using the U.S. Army Corps of Engineers' Coastal Modeling System

by

Pamela Joan Christian

Major Advisor: Gary A. Zarillo, PhD.

Ponce de Leon Inlet, FL is one of 154 federally-maintained inlets by the U.S. Army Corps of Engineers (USACE). Shoaling and channel migration have caused persistently hazardous navigation conditions since stabilization of the inlet in 1972 by a dual-jetty weir system, and eventual closure of the weir in 1984. In 1993, the Coastal and Hydraulics Laboratory (CHL) of the U.S. Army Engineer Research and Development Center (ERDC) initiated the Coastal Inlets Research Program (CIRP) to study the complex morphological and hydrodynamic changes of coastal inlets, which occur on a variety of temporal and spatial scales, and to develop technology specific for addressing operation and maintenance concerns. Ponce de Leon Inlet was chosen for the initial field investigation using long-term comprehensive monitoring from 1995 to 1997 (Howell, 1996; King et al., 1999) to generate a baseline analysis of physical conditions and to establish an available archive of data.

The present study utilized the Coastal Modeling System (CMS) developed by the USACE to produce high-resolution 2D, depth-integrated, fully coupled hydrodynamic, wave, sediment transport, and morphology change simulations of proposed alterations in the configuration of Ponce de Leon's dual-jettied inlet system. The primary objective is an assessment of predicted geophysical changes within the inlet system to determine the appropriate redesign that improves navigation and reduces structural stress on the north jetty and shoaling of the south spit.

After performing a 3-month calibration and 7-month validation of the model setup, 15 alternate designs were developed based on an extension of the south jetty and included reopening the weir, an artificial hard bottom in the deep water channel, realignment of the navigation channel, and south jetty spurs both emerged and submerged. Comparison of net morphologic changes, normalized volume changes within 15 sub-domains, and of hydrodynamic changes during both spring and neap tides allowed the best 6 options to be modeled for long-term changes, to include fall and winter storm events. Taken in total with the three areas of concern in mind, the South Jetty Extension with Submergent Spur, Hard Bottom, and Channel was considered the optimal candidate modeled in this study.

Table of Contents

List of Figures

List of Tables

List of Abbreviations

ADCIRC	Advective Circulation
ADCP	Acoustic Doppler Current Profilers
C	Channel
CEA	Channel Equilibrium Area
CHL	Coastal and Hydraulics Laboratory
CIRP	Coastal Inlets Research Program
CMS	Coastal Modeling System
CO-OPS	Center for Operational Oceanographic Products and Services
DOQQ	Digital Orthophoto Quarter Quadrangles (rectified digital images)
DWG	Directional Wave Gauges
ERDC	U.S. Army Engineer Research and Development Center
ES	Emergent Spur
FDEP	Florida Department of Environmental Protection
HB	Hard Bottom
ICWW	Intercoastal Waterway
IMS	Inlet Modeling System
LIDAR	Light Detecting and Ranging
M2D	Militello 2D (hydrodynamic model now called CMS-Flow)
MLW	Mean Low Water
NAD83	North American Datum of 1983
NAVD88	North American Vertical Datum 1988
NGDC	National Geophysical Data Center
NOAA	National Oceanic and Atmospheric Administration
NOS	National Ocean Service
nRMSD	Normalized Root Mean Square Deviation
PMAB	Prototype Measurement and Analysis Branch
RGB	Red, Green, Blue
RMSD	Root Mean Square Deviation
SHOALS	Scanning Hydrographic Operational Airborne Lidar Surveys
SJ	South Jetty Extension
SJRWMD	St. John's River Water Management District
SMS	Surface-water Modeling System

SS	Submergent Spur
STWAVE	Steady-State Spectral Wave
TRANQUAL	Transport Water Quality
USACE	U.S. Army Corps of Engineers
USGS	U.S. Geological Survey
W	Weir
WABED	Wave-Action Balance Equation with Diffraction
WES	Waterways Experiment Station
WIS	Wave Information Studies

Acknowledgement

I would like to express my deepest appreciation to my advisor, Dr. Gary A. Zarillo, for his guidance and support in every aspect of this study. His dedication to understanding coastal processes represents a lifetime achievement, which he generously shares. As a mentor, he is both accommodating and wise, providing his students the opportunity to follow their own path to excellence. I would also like to thank the members of our Coastal Processes Research Group: Florian Brehin, Jo-Ann Rosario Llantín, and John Bishop for sharing their expertise and joy during our projects. Many thanks are extended to committee members Dr. George A. Maul, Dr Charles R. Bostater, and Dr. Lee E. Harris (in absentia) for contributing significantly to my academic preparation and to Dr. Robert van Woesik for providing patient counsel on a number of topics.

My deepest thanks and appreciation are extended to my family: my sisters, Debbie and Sandy, who are always being available to listen and show support; my niece and nephews, Allison, Alexander, and Christian, who remind me to enjoy life (Thanks, CE, for proofing!); and Kenna, Barbara, Gustavo, Lucas, and Wolfie, who enrich my life in so many ways. I am most thankful for my mom, Charlotte, to whom this dissertation is dedicated, for always being there to edit my work.

Thanks are extended to the U.S. Army Corps of Engineers, Vicksburg, for support using CMS and access to the archived data used in this study. Other agencies providing access to data used in this study were the Florida Department of Environmental Protection, St. John's River Water Management District, National Oceanic and Atmospheric Administration, and Taylor Engineering.

Funding in support of my doctoral research was provided by the National Science Foundation under the GK-12 program, the Department of Defense under the Science and Mathematics for Research Transformation (SMART) program, Florida Tech under the Snowden and Skelly fellowships, and Dr. Gary A. Zarillo under the U.S. Army Corps of Engineers and Sebastian Inlet Tax District.

Dedication

This dissertation, which represents an achievement I had longed dreamed about, is dedicated to my Mother and Fathers…

To my mother, Charlotte:

What words can I say to convey my love for you, Mom, in my life? You are always there for me, guiding and suggesting, acting as a sound board for my beliefs, providing for my needs when I have been unable to do so for myself. You are the one constant force in my life and I pray you are always with me! You encouraged your girls to be more than you had the opportunity to be, and fought for justice within an entire government… on more than one occasion! And, although we may differ in opinion on several topics, you continue to be just an amazing role model for the power of a woman, and I admire you beyond words! I wish you peace of mind and peace of heart, as your girls are now, finally, at the top of their game. ☺

To my childhood father, Michael:

Although I knew you for only a short time in my youth, your physical absence has never hindered my sense of your presence in my life. Whenever I find things to be just too tough to handle, I think on your life experiences, and gain my perspective again. My aptitude for logic and reasoning came straight from your loins, whereas my spiritual twist is linked to always believing in those things we cannot see… like your face since I was a child. Your memory lives on in so many lives that you will never fade from my thoughts…though what I would give to talk to you as an adult?!

To my second father, Jim (the Col):

You filled a hole in the lives of us girls that was not easy to do. You came into this family of Strong women and offered a strong male rudder to help steer our futures. You gave my mommy the partner she so needed and for that I will always be grateful. Your time in the Army gave you the regimen to help regiment us, and when you passed, my heart was deeply torn! But life has come full circle again, since my dissertation work would not have been possible without the combined effort of men and women, like you, who dedicate their lives to the Corps of Engineers. I will think of you often in my new life as a physical oceanographer studying the forces of nature~!

To my academic father, Gary:

Your belief in my abilities is the reason I succeeded! Your generosity of spirit and patience, coupled with the kindness in your heart, is why I, and so many others, seek out your guidance. Your willingness to share your breadth of knowledge, whenever asked, without an ounce of condescension, is the greatest gift I could have been given! No, I will not just disappear now that I achieved my degree. Our group is a precious treasure in my life and my future, and I look forward to many years of learning from you… sorry, but you're stuck with me now! ☺

1 Introduction

Understanding the hydrodynamics and sediment transport along any coastline is a necessary first step in predicting future morphologic trends. As coastal populations continue to increase exponentially, a desire for stable shorelines and safely navigable waterways remains a priority in these communities. For the state of Florida, which depends on tourism to maintain a strong economy, the preservation of activities such as boating, fishing, diving, surfing, and sunbathing remain areas of special interest. While specific changes to the shoreline caused by interruption of the longshore transport in the vicinity of coastal inlets differs among inlets, general trends can be predicted based on even a superficial knowledge of the driving physical forces. Engineering activities in and around inlets are improved through the use of detailed numerical and physical models specific to the site of interest. The coupling of waves, currents, sediment transport, and morphologic change in the modeling effort allows for more informed management decisions, which can reduce cost, time, and negative public opinion regarding engineering projects. The production of fully integrated, numerical models using the U.S. Army Corps of Engineers' Coastal Modeling System, for the prediction and evaluation of geophysical changes to a redesigned dual-jettied system, is intended to remove the engineering stalemate for Ponce de Leon Inlet, FL (Figure 1) and is the subject of this dissertation.

1.1 Background and Motivation

In a broad sense, a coastal inlet is a waterway connecting a large body of water to a smaller body of water through a narrow landmass. The physical forces that drive the exchange of fluid between these two water bodies include tides, wind, waves, and river flow. Tidal inlets are distinguished from other inlets in that these passages, or channels, between the open ocean and the connected back bay, lagoon, or river entrance are maintained by tidal forcing (Bruun and Gerritsen, 1960; USACE, 2002); specifically, the balance between the pressure gradient, caused by the difference in water levels between the bay and the ocean, and the frictional forces, caused by bottom topography and configuration of the inlet. In its simplest analysis, if tidal flow, defined as $u(t)A_c$ (velocity times channel cross-section), is insufficient for the specific geomorphology, then the inlet will close due to shoaling. Understanding how adjustments to the minimum cross-sectional area of an entrance channel relates to the basic hydraulic and sedimentation characteristics of that inlet is of great importance for successful management of engineered inlets.

The volume of water flowing through the inlet channel from the ocean into the bay during rising tide is temporarily stored in the bay/lagoon area during the tidal cycle. This volume of stored water, known as the tidal prism (P), is estimated as the horizontal area of the bay (A_b) times the amplitude of the spring, flood tide in the bay (a_b) by the relation $P = 2\ a_b\ A_b$. Since LeConte (1905) first equated the tidal prism (P) to the channel area (A_c) available for the volume of water to move through, much empirical analysis has been done to advance this equilibrium area concept as a means to understand the morphodynamic changes within an inlet and to assess the stability of an

inlet to remain open (Brown, 1928; O'Brien, 1931; Keulegan, 1967; Nayak, 1971; Johnson, 1971; Jarrett, 1976; Escoffier, 1977).

As inlets are a part of the littoral drift system along the coast, they are affected by the wave-current interactions that drive the sand transport in these areas. Some of the sediment passes around the inlet and continues downdrift on the adjacent shorefaces. This bypassing can occur continuously or intermittently, as when the sediment is stored on ebb shoals and bypass bars. Some of the sediment, however, enters the inlet during flood tide and its fate is subject to the hydraulic processes within the inlet. Therefore, the natural ebb and flow of the tidal currents, as well as the presence of wind waves, contributes to the sedimentary processes within and around an inlet creating a variety of responses by the inlet. Some inlets migrate and/or realign in response to fluctuations in tidal currents and sediment transport. Some inlets are observed to adjust the hydraulic regime (i.e. hydrodynamics) to accommodate imposed changes and, thus, maintain stability. Other inlets are unable to address the changes causing the inlet to either close or to open too wide. In either case, these inlets are classified as unstable and in need of engineering support if they are to remain functional for navigation and fluid exchange between the ocean and bay (or estuary).

Stabilization of inlets by single, dual, or weir jetties may resolve navigation and water exchange issues but increases the sand management concerns. The dynamics associated with the interruption of littoral drift by the jetties, impoundment of sand on ebb- and flood-tidal shoals and bypass bars, and changes to the adjacent shorelines directly impact the sediment budget (Fitzgerald, 1984; Zarillo et al., 1985; Dean and Work, 1993). This interruption of sand transport requires further engineering support

through such activities as mechanical bypassing, dredging of the channel, and periodic optimal placement of beach-quality sand on downdrift beaches. Performance of inlet designs and proper management of maintenance projects are enhanced with the use of baseline and predictive numerical models of waves, current, sediment transport, and morphologic change within the given topography and expected geometry.

Ponce de Leon Inlet is one of 154 federally-maintained inlets for which the U.S. Army Corps of Engineers (USACE) is responsible at an annual operating cost of more than $1 billion dollars (Hughes and Kraus, 2006). The initiation in 1993 of the Coastal Inlets Research Program (CIRP) by the U.S. Army Engineer Waterways Experiment Station (WES) to study inlet behavior began with the comprehensive monitoring of Ponce de Leon Inlet from September 1995 to October 1997 (Howell, 1996; King et al., 1999; Zarillo and Militello, 1999). The goal of the field study was to generate a baseline analysis of physical conditions at the inlet and to establish an archive of the data obtained that could be used by the Corps and other interested parties for years to come. Ponce Inlet was chosen as the study site for numerous reasons, chief of which was the engineering concerns that persisted since stabilization of the inlet in 1972 by a weir-jetty system and subsequent closure of the weir in 1984 (Sargent, 1988; Harkins et al., 1997; King et al., 1999).

The closing of the weir was originally intended to be a temporary event leading to a realignment of the shorelines and migrating channel to both improve navigation conditions (Harkins et al., 1997) and alleviate mechanical and physical stress on the north jetty. Prior to reopening the weir, a feasibility study using numerical (Taylor et al., 1996a, 1996b) and physical modeling (Harkins et al., 1997) was undertaken to assess

design modification alternatives. Taylor et al. (1996a, b) produced a two-dimensional (2D) depth-integrated numerical model using only tidal forcing and no wave influence for the various proposed modifications. The physical model performed at WES by Harkins et al. (1997) included wave-current interaction in a steady state three-dimensional (3D) application of the proposed modifications. Subsequent numerical modeling by Taylor Engineering (Srinivas and Taylor, 1999) used the 2D depth-integrated circulation model TRANQUAL combined with a bed load transport formula (Nielsen, 1992). In the absence of a fully-coupled, circulation-sediment transport model, the steady flow conditions were used in reiterative calculations to simulate representative sediment transport fields for proposed design modifications.

The monitoring initiative by CIRP performed at Ponce de Leon Inlet from 1995 to 1997 (King et al., 1999) supported the collection and archiving of numerous types of data (e.g. bathymetric from Scanning Hydrographic Operational Airborne Lidar (Light Detecting and Ranging) Surveys (SHOALS), hydrographic, visual, tidal, wave, meteorologic, current profiles, etc). The project also supported the effort of the Coastal and Hydraulics Lab (CHL) to develop and validate the Inlet Modeling System's (IMS) circulation and wave models (King et al. 1999; Militello and Zarillo, 2000; Militello and Zundel, 2002; Militello and Zundel, 2003; Militello et al., 2004, Smith et al., 1998; Smith and Smith, 2001). At the time of the initial field study, the IMS hydrodynamic model used to simulate circulation at Ponce Inlet (Militello and Zarillo, 2000) was the 2D, depth-integrated, finite-element, ADvective CIRCulation model, ADCIRC (Luettich et al., 1992). Output calculations from this 2D numerical model agreed with the field measurements of tidal flow, thus, validating the ADCIRC model. However,

forcing at the ocean boundaries was by tidal constituents only and the resolution of the wind fields was only applicable for large-scale forcing in the simulations and not for the meso-scale motion of sea breezes (Militello and Zarillo, 2000). Depth-integrated currents obtained from the ADCIRC model were input into the Steady-State Spectral Wave (STWAVE) model to test and improve its ability to include wave-current interaction and shallow-water, steepness-induced breaking (Smith et al, 1998, Smith, 2001). However, the two models were not fully coupled.

Over the last decade, upgrades to the Inlet Modeling System by the U.S. Army Engineer Research and Development Center (ERDC) Coastal and Hydraulics Laboratory (CHL) have produced the robust and computationally efficient Coastal Modeling System (CMS). CMS is a coupled group of numerical models that work within the Surface-water Modeling System® (SMS) interface to simulate and calculate waves, circulation, sediment transport, constituent transport, and morphology change in either 2- or 3-dimensions. The CMS-Flow model is based on the two-dimensional, depth-integrated hydrodynamic model, M2D, first developed in the mid-90's at Florida Institute of Technology by Adele Militello-Buttolph (Militello, 1998) to examine nonlinear terms in the equations of motion for wind-dominated flows. CMS-Flow is a time dependent, 2D finite volume circulation and morphology model that calculates water surface elevations, two components of the current, and sediment transport on a rectilinear grid of variable cell sizes (Militello et al., 2004). Within CMS-Flow, three sediment-transport formulations are available for calculating sediment transport rates and resultant bottom elevation changes (Buttolph et al., 2006). Previous studies (Zarillo and Brehin, 2007; Zarillo et al., 2007) have highlighted the capabilities of CMS-Flow

for simulating long-term morphologic changes under the Lund Formula. CMS-Flow includes a hard bottom routine for representation of non-erodible substrates. This attribute is of great value to numerical modelers since it places a constraint on the sediment transport (Militello et al., 2004).

CMS-Flow can be fully-coupled with the CMS-Wave model through the SMS® steering option at user specified intervals (Buttolph et al., 2006). CMS-Wave is based on the Wave-Action Balance Equation with Diffraction (WABED) model and was chosen by CHL as the preferred wave model (over the previous use of STWAVE) for its benefit of approximating both diffraction and reflection (processes which are highly relevant at inlets). CMS-Wave is a steady-state, spectral, finite-differencing model capable of simulating shoaling, refraction, breaking, and growth of waves due to wind. It has been further supported by CHL/CIRP through the improvement of calculating radiation stresses applicable to wave-current interactions (Demirbilek et al., 2007) and continued upgrades to include bed friction, runup, variable cell size, and topographic modification due to rubble mounds, breakwaters, and walls.

Research resulting from previous numerical and physical models applied at Ponce de Leon Inlet suggested that a 305 m (1,000 ft) dogleg extension of the south jetty and a 244 m (800 ft) landward extension of the north jetty should alleviate the hazardous navigation conditions, shoreline erosion, and channel instability (Taylor et al., 1996b; Srinivas and Taylor, 1999). However, as stated by these design feasibility studies, a more detailed modeling effort from a fully-coupled hydrodynamic/sediment transport model is still necessary to obtain the complete description and prediction of topographic and morphologic changes within the inlet.

1.2 Problem and Hypothesis Statement

Upon announcement of the intended changes to the inlet design slated for 2004, the surfing community expressed concern that alterations by a jetty extension would affect the surfing break at New Smyrna Beach (south of the inlet). The County of Volusia-Inlet and Port Authority district asked the USACE Jacksonville District to redesign for a parallel south jetty (http://volusia.org/portauthority, 2007). However, details of the impacts from this design were not included in the 1996 feasibility study. Additionally, the local community expressed concern for negative impacts on circulation within the estuary west of the inlet and the probability of increased downdrift erosion caused by the south jetty extension.

These apprehensions prompted the extension project to be halted until the USACE could provide more substantiated results than those presented in the feasibility study. According to the Volusia County Waterways Assistance Projects website (2007), the redesign project was cancelled following construction of the 2004 landward extension of the north jetty to revet the north spit. Shoaling is still a major concern for navigation within the inlet, as is the channel's location, which also causes mechanical stress for the north jetty.

In light of the advances in numerical modeling techniques in the last decade and the large body of archived data specific to Ponce de Leon Inlet (King et al., 1999; Zarillo and Militello, 1999), it is asserted that a more detailed, predictive modeling effort integrating wind, waves, currents, sediment transport, and morphologic change is required to remove the stalemate over re-engineering Ponce de Leon Inlet, FL.

1.3 Study Objectives

The objective of this study is to utilize the Coastal Modeling System (CMS) developed by the USACE to produce and evaluate high-resolution, 2D, fully coupled hydrodynamic, wave, sediment transport, and morphology change simulations of proposed alterations to the configuration of Ponce de Leon's dual-jettied inlet system. Specific objectives of this study and the steps taken to meet the objectives are:

1. To perform an Escoffier stability analysis using the Channel Equilibrium Area (CEA) analysis software;
2. To analyze and apply the extensive field measurements obtained from the 1995-1997 site investigation by CIRP;
3. To develop fully integrated hydrodynamic and morphologic CMS models for several design alternatives under fair–weather and storm conditions;
4. To compare, qualitatively and quantitatively, the geophysical changes predicted by each alternative design;
5. To determine an appropriate redesign for Ponce de Leon Inlet, FL that improves navigation and reduces both structural stress on the north jetty and shoaling of the south spit;
6. To develop a representative methodology for utilizing the emerging CIRP technology designed for diagnosing and predicting tidal inlet behavior.

2 Study Site: Ponce de Leon Inlet, Florida

This section provides a description of the geographic setting, physical forcing, and available data. The information presented represents a compilation of several sources including observations, measurements, and numerical as well as physical simulation analysis.

2.1 Physical Setting

Ponce de Leon Inlet is located in the middle of Volusia County along the east coast of Florida at latitude 29°05'N, longitude 80°55'W (State Plane Florida East coordinates of 208112.7 easting, 526268.6 northing, NAD83, metric). It is approximately 20 km south of Daytona Beach, 75 km northeast of Orlando, and 80 km north-northwest of Cape Canaveral. The inlet connects the Atlantic Ocean to the Intercoastal Waterway (ICWW) via the dredged tidal channel known as Rockhouse Creek (Figure 1). This creek passes through the well-developed flood shoal that occupies most of the bay and is exposed during all phases of the tide. Ponce de Leon Inlet is hydraulically linked to the Halifax River from the north and to the Mosquito Lagoon from the south via the Indian River North. Within this system, the ICWW is the main channel for navigation as it spans the entire domain to the west of the inlet. The dimensions of the ICWW are 90 m wide and 3.7 m deep. The ICWW converges with the Halifax River 3.5 km north of the inlet and it converges with the Indian River North 2 km south of the inlet.

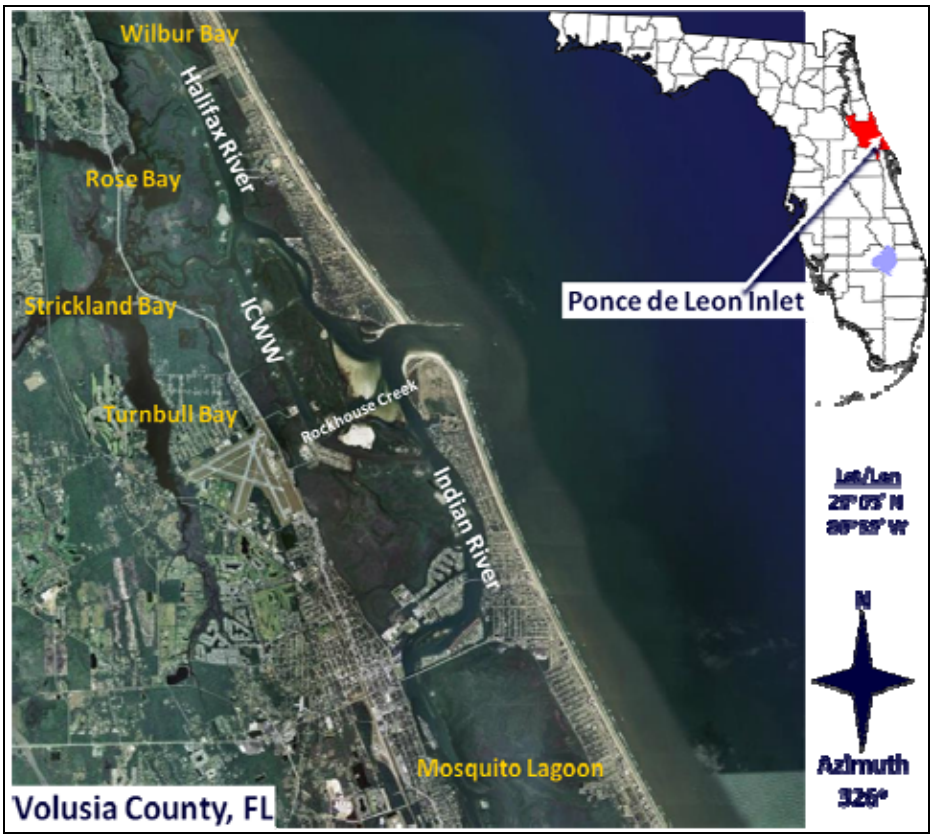

Figure 1. Ponce de Leon Inlet, FL study site. (2004 DOQQ, original scale 1:12,000, FDEP)

Ponce de Leon Inlet is the only inlet serving the Halifax River Lagoon and the main inlet for the North Indian River Lagoon. There are numerous salt marshes and mangrove habitats within the area, as well as Rose Bay and Turnbull Bay. These bays and numerous small channels allow interchange of water among the wetlands and act as storage for the water that passes though the inlet system.

The inlet sits upon the Pleistocene Anastasia formation with a shoreline azimuth of 326^{o} and land elevation of approximately 3 m above mean sea level. Water depths (Figure 2 and Figure 21) over the ebb shoal of 3.5 to 5.6 m increase to 10 m within 1 km of the shore. The contour diagram of Ponce de Leon Inlet (Figure 2) highlights the location of the long-term gauge deployment by King et al. (1999).

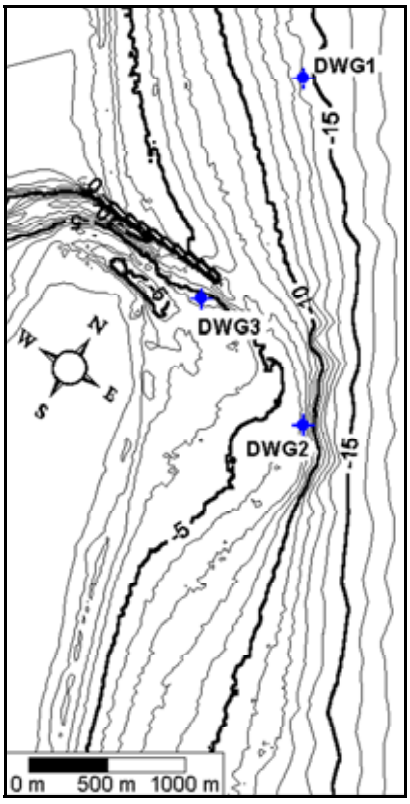

Figure 2. Ponce Inlet depth contours (m) with wave gauges. (From Smith and Smith, 2001)

The inlet in its present location was first described in the 1513 logbook of Spanish explorer Ponce de Leon but was deemed non-navigable and, subsequently, dredged by the U.S. Army Engineer District, Jacksonville in 1943 and 1944 for war effort purposes. Two offset jetties were constructed in 1967-1972 to stabilize the inlet and maintain a navigable, dredged channel of 4.6 m deep and 61 m wide (Figure 3). The north jetty design included a 152 m long concrete sheet pile, followed by a 549 m long weir section, and another 549 m long rubble mound section (total 1250 m). The weir concept was included to promote the continued natural bypassing of littoral transport. The south jetty was designed as a curved, rubble mound structure 1243 m long. The weir section of the north jetty did not perform as expected with scour occurring in the northern inlet throat and migration of the south spit into the inlet (Figure 4). In 1972,

the north jetty weir was supplemented with a rubble mound structure, but the weir was eventually closed with armor stones in 1984. Since its closing, however, the north jetty still experiences scour with the interior north jetty spit (west of north jetty) completely eroded today (Figure 5) and the south jetty is almost completely buried under sand. The present length of the south jetty is 120 m. The present length of the north jetty, including the landward revetment of the north spit, is 1868 m.

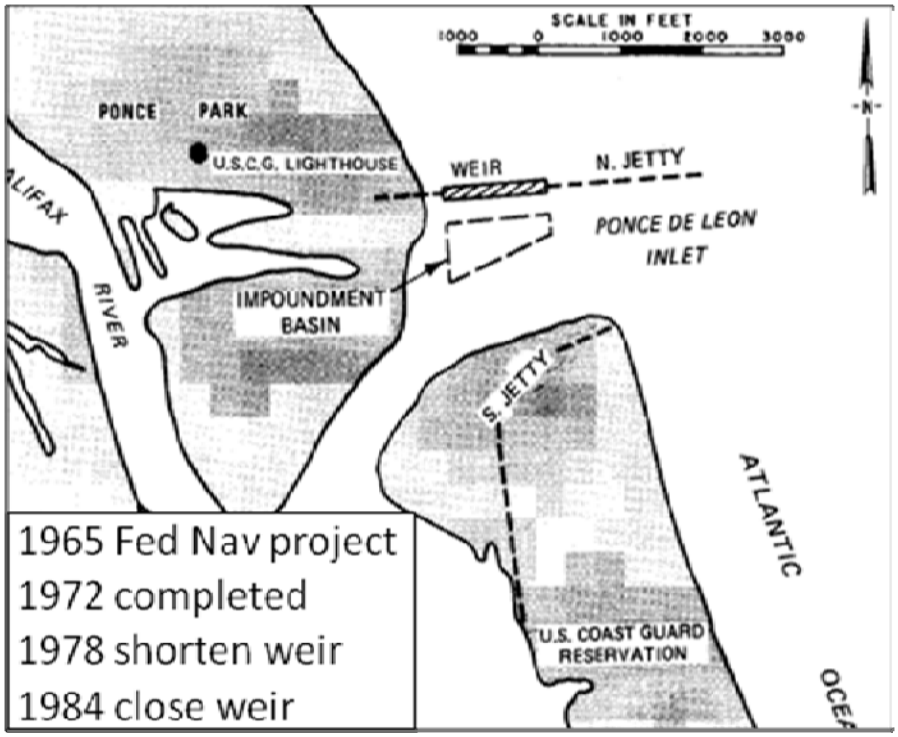

Figure 3. Map of original jetty design and locations. (From Sargent, 1988)

Figure 4. Aerial (1976) highlighting shoaling of south spit and original dimensions of the north spit. (From USACE, ERDC Federal Database of Inlets, scale 1:5,000)

The width of the main entrance to the inlet is 426 m and the cross-sectional area (A_c) at the throat is 1069 m^2 (Figure 5). Although the channel depth between jetties was designed and maintained for a depth of 4.57 m and a width of 61 m, present shoaling has resulted in estimates of minimum depth at mean lower low water (MLLW) of <1 m in places along the designed channel (U.S. Army Corps of Engineers, 2006). The present location of the navigation channel is aligned with and adjacent to the north jetty and is oriented approximately 90^o from north. Analysis of recent SHOALS surveys indicates depths approach 11.5 m (Figure 21) in places along the channel. The tidal prism is 1.7 $x10^7$ m^3 with a bay surface area of $1.3x10^8$ m^2. Ponce de Leon Inlet is considered a stable inlet by Escoffier analysis, performed using the CIRP Channel Equilibrium Area (CEA) tool and discussed in further detail in Section 5.1.

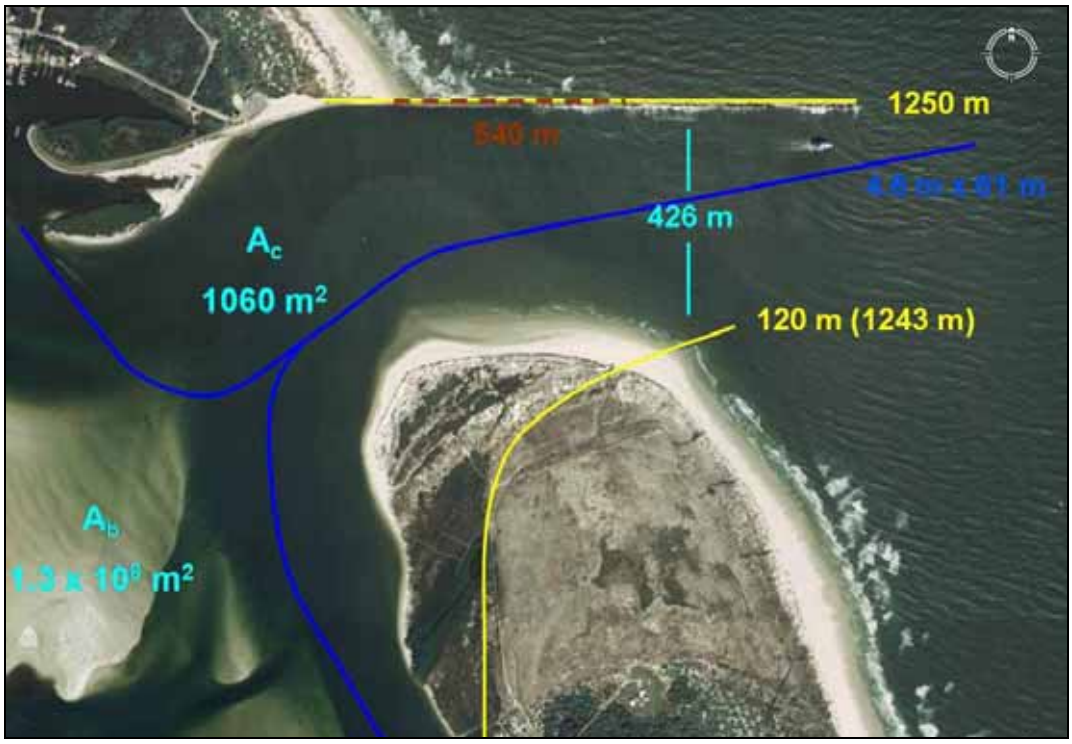

Figure 5. Aerial image with design parameters. (From Google Earth, 2006, original scale 1:12,000)

2.2 Hydrodynamics and Meteorology Overview

Offshore of the inlet, the tide has a mean range of 1.0 m and a spring range reaching 1.3 m. At the U.S. Coast Guard station inside the inlet, the mean tidal range is 0.8 m. Tidal harmonics indicate that the M2 tide dominates the signal with an amplitude of 0.45 m near the inlet. During a typical tidal cycle, peak inlet currents within the inlet throat are approximately 1.0 m/s, but can reach as high as 1.3 m/s during spring tides. Militello and Zarillo (2000) identified a low-energy area during the turning of the tide located to the south within the inlet throat associated with the same sediment accumulation that covered the south jetty. It was observed in numerical model results in which flood tide current begins to enter the inlet from the south over this fillet, the ebb

currents are still exiting in the north of the throat. The fully developed, bifurcated flood shoal suggests a flood-dominant system, although analysis of the maximum current velocities and duration during ebb and flood indicates Ponce Inlet varies spatially and temporally in its peak ebb and flood currents.

King et al. (1999) showed that the offshore wave heights were reduced by 20 to 30% upon reaching the ebb shoal gauges. This is the result of shoaling and refraction as the depths go from 15 m to 7 m on the outer ebb shoal. By the time waves reach the inlet throat, the wave heights reduce another 10 to 20% as a result of wave focusing on the ebb shoal. Modulation of wave heights within the throat can be up to 1 m from tidal influence. Zarillo and Militello (1999) observed significant wave heights averaging 0.9 m over the ebb shoal that were reduced to an average of 0.6 m within the inlet. The average wave period observed was between 8 to 9 s having maximum periods of 14 s. A comparison of all available research and year-long trends from offshore buoys indicates the dominant wave direction is from the northeast.

Based on analysis of meteorological data from King et al. (1999) and the NOAA/NOS and NDBC gauges (Appendix C), the average wind speeds range from 4 to 6 m/s with dominant wind directions from NNE and SSE. Analysis of hourly wind direction data obtained for March and July 1997 (King et al., 1999) captured the sea breeze/land breeze phenomenon typical of the eastern coast. This strong 24 hr cycle was represented by maximum winds from 1200-1600 (EST) blowing onshore and minimum wind speeds occurring between 0000-0500 (EST) blowing offshore.

Average air temperature ranges from 27 to 32^{o}C in summer and 10 to 16^{o}C in winter which represents a subtropical climate. Temperature variations between day and

night in summer are very limited but can reach as much as 10°C; winter differences average 15°C. Average water temperature in summer is 27°C and winter is 16°C. Average annual rainfall at the inlet is 125 cm evenly distributed throughout the year. September is typically the wettest month with average rainfall of 17 cm. The area is subject to tropical storms in summer and fall and nor'easters in winter months.

2.3 Available Data for Calibration and Validation of Models

The following sections provide an overview of the archived data available for calibrating and validating the present CMS models. Calibration covers July to October 1996 and validation from October 1996 to April 1997 providing a 10 month complete dataset. The additional 1997 short-term field measurements by Zarillo and Militello (1999) occurred from August 21 to November 1 and by King et al. (1999) from August 25-29 and September 15-19, and, thus, were not used for model verification.

2.3.1 Water Surface Elevation (WSE)

The 1995-1997 field investigation collected water level data from Paros pressure sensors deployed individually (on pilings) at three locations inside the bay (e, f, g) and as part of wave gauge packages at three locations within the inlet proper (a, b, c). Bay water level was also measured using a Vitel Model WLS2 stilling well tide gauge located at the Coast Guard station just inside the inlet (d). Water levels from the six pressure gauges were corrected for atmospheric pressure by the barometer readings from the trailer (i) at the Coast Guard station. Details of the data analysis procedure can be found in King et al. (1999) and gauge locations are shown in Figure 6. Access to

quality controlled data was retrieved electronically at the ERDC CHL Dataport (http://sandbar.cerc.wes.army.mil/). Only the gauges on the outer ebb shoal, inlet throat, and offshore are available (Table 1) and not all months have complete records. WSE data from the tide gauge at the Coast Guard Station inside Ponce de Leon Inlet (8721147) was retrieved from the NOAA Center for Operational Oceanographic Products and Services (CO-OPS) website.

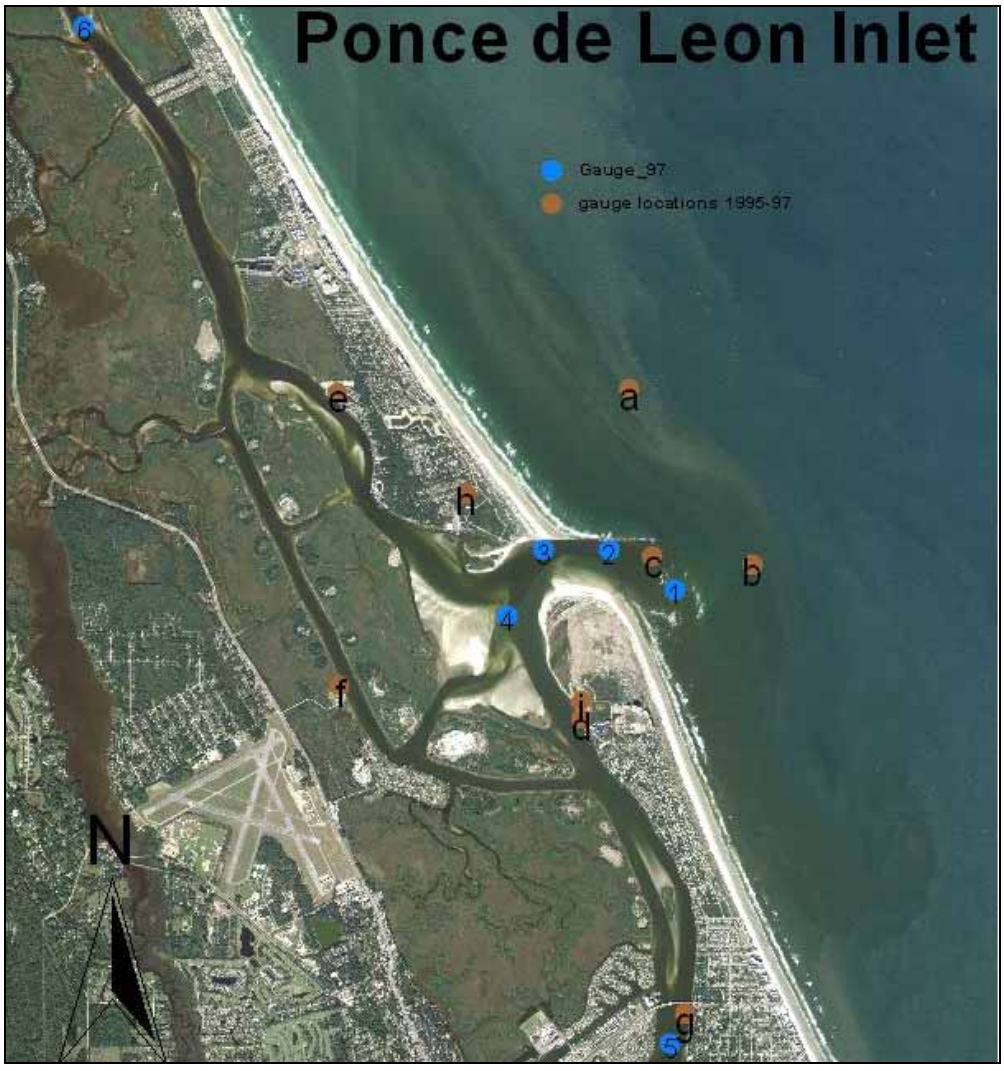

Figure 6. Gauge locations for long-term (1995-97) and short-term (1997) deployment; gauges a-d are referenced in this study for calibration and validation. (2004 DOQQ, original scale 1:12,000, FDEP)

Table 1. Available water surface elevation and wave data from the CIRP field investigation.

		Jan	Feb	Mar	Apr	May	Jun	Jul	Aug	Sep	Oct	Nov	Dec
1995	a (offshore)										X	X	X
	b (ebb shoal)										X	X	X
	c (throat)										X	X	X
1996	a (offshore)	X	X	X	X	X	X	X	X	X	X	X	X
	b (ebb shoal)	X	X	X	X	X	X	X	X	X	X	X	X
	c (throat)	X	X	X	X	X	X	X	X	X	X	X	X
1997	a (offshore)	X	X	X	X								
	b (ebb shoal)	X	X	X	X		X	X	X	X	X		

2.3.2 Waves

The 1995-1997 field investigation collected wave data from the directional wave gauges (DWGs) developed by the Prototype Measurement and Analysis Branch (PMAB) of CHL and discussed in general above, within the water level section. Each wave gauge was mounted on a trawler-resistant seafloor pod. The three gauges were located at stations a-c (Figure 6.). Hourly raw data was collected at 5 Hz and post-processed using analytical routines to derive the two-dimensional (2D) power density spectrum used to determine the zero moment wave height (H_{m0}), peak wave period (T_p) and peak wave direction (D_p). Details of the data analysis procedure can be found in King et al. (1999) and the data (Table 1) was retrieved from the ERDC CHL Dataport, although not all months have complete records.

2.3.3 Currents

The 1995-1997 field investigation used 1200 kHz broadband Acoustic Doppler Current Profilers (ADCPs), developed by RD Instruments, mounted horizontally, looking upward, on the wave gauge platforms at stations b and c (Figure 6.) only. The sampling rate was 1 Hz and the data was averaged in 6-min intervals. Unfortunately, the data suffered from a time stamp error and was not available for use. To supplement the, then, in development Inlet Modeling System, two 1-week intensive boat-mounted ADCP surveys were conducted in 1997 during August 25-29 (neap tide) and September 15-19 (spring tide). These surveys were performed to measure the current distributions across channels and throughout the vertical, along numerous transects, as well as discharges in the inlet system. Details of the sampling procedure and results obtained can be found in King et al. (1999). The graphic results of these surveys, as presented in that report, were used as spot-checks in the calibration of the present model since the months are the same, although the year is not. In general, these surveys measured neap tide maximum discharges through the inlet of 1,700 m^3/s on flood and 1,300 m^3/s on ebb, whereas the spring tide measurements were 2,200 m^3/s and 1,600 m^3/s, respectively. Depth-averaged velocity vector data measured average current speeds north and south of the inlet within the bay of 0.6 m/s and peak currents within the inlet of 1.00 m/s.

3 Methodology

This section discusses the datasets and methods used for the coupled CMS-Flow/CMS-Wave model setup, including the grid generation process, the assignment of morphological constraints (i.e. hard bottom cells), tagging of observation cells, boundary inputs, and overall model specifications.

3.1 Aerial photography

The Florida Department of Environmental Protection (FDEP) maintains a database of 1 meter resolution Digital Orthophoto Quarter Quadrangles (DOQQs) for download from the World Wide Web at http://data.labins.org. The scale of these images is 1:12,000. This website was accessed for Red, Green, Blue (RGB) color images for 1999 (Figure 8 and Figure 9) and true color images from 2004 (Figure 1 and Figure 6). These digitally, geo-referenced MrSID™ images were brought into SMS® and used to generate shoreline arcs within the map module. Defining the shoreline arc for land vs. water allows for the automation of ocean and land cells during grid development. The digital images (.sid) were also used in ArcView 3.2® to verify coverage and accurate positioning of the topographic data, as well as to generate geo-referenced polygon masks. Masks were used to clip the topographic data as needed and to facilitate comparison of net volume changes by sub-domain. The FDEP State Plane DOQQs were referenced in feet requiring conversion of the world files (.sdw) to metric using the CORPSCON 6 software, developed by the USACE.

3.2 Bathymetry

The comprehensive field investigation of Ponce de Leon Inlet performed by CIRP included four SHOALS surveys in July 1994, September 1995, September-October 1996, and December 1997. Details of the SHOALS Airborne Lidar Hydrographic Survey System can be found in Lillycrop, Parsons, and Irish (1996), whereas details of the July 1994 Ponce survey are in Irish, Parsons, and Lillycrop (1995) as well as Stauble (1998). For the present study, the 1994 and 1997 LIDAR surveys were the most comprehensive and representative of the study site for developing the high resolution contours within the vicinity of the inlet. The 1994 LIDAR survey was used for the nearshore region. The 1997 survey, which contained less along shore coverage, was cropped to cover the inlet proper. Data for offshore contours was obtained from the Coastal Relief Model developed by NOAA's National Geophysical Data Center (NGDC) database of bathymetric and topographic surveys. Data for the lagoon, bays, and Intercoastal Waterway were obtained from the St. John River Water Management District (SJRWMD). Beach profile surveys were obtained for Volusia County from FDEP for 1993 and 1997. The horizontal datum used is State Plane Florida East, NAD83, metric and the vertical datum is NAVD88, metric. Numerical models require depth (z values) to be positive downwards for purposes of calculating the equations of motion and continuity. Depth conversion for the data was performed using Ultra Edit v13. Horizontal datum conversions were calculated using CORPSCON 6 software. The ArcView 3.2® layout (Figure 7) shows the complete coverage of the scatter (xyz) data used to generate the Cartesian grids.

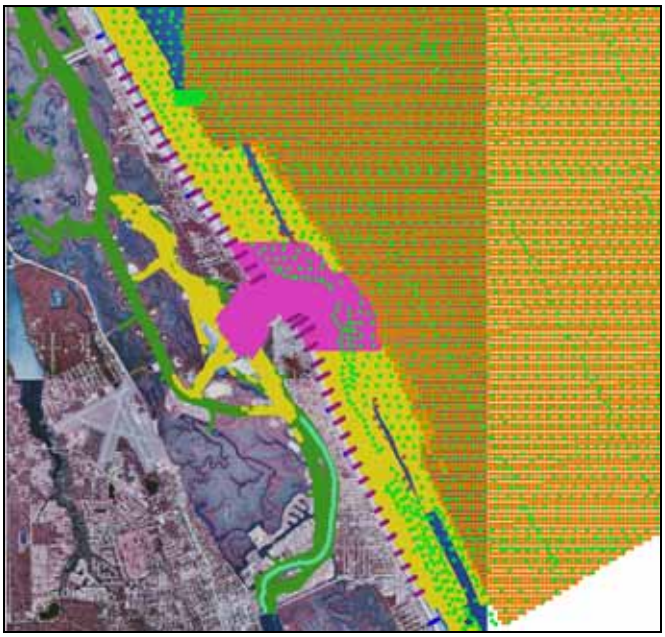

Figure 7. ArcView 3.2® layout of the topographic data coverage. (1999 DOQQ, original scale 1:12,000, FDEP)

3.3 Grid Development

Each model within CMS has its own Cartesian grid, with the wave model oriented so that the + x direction is onshore. The newest version of SMS® (10.1) allows for duplication of the CMS-Flow grid and transformation of that grid 180° so the CMS-Wave model computation assigns properly; thus, generating identical grids except in cell id numbering. This saves time when developing the models for two reasons. First, CMS grids can have variable cell size, which can be time-consuming to generate when they are refined by hand (as in this study). Refining by hand requires zooming in to split rows and columns and there is, as yet, no undo option in the software. Second, visual inspection of the generated grid must be performed to ensure that, during interpolation of the xyz data along the shoreline arcs, the z values returned appropriately assigned cells as ocean or land. This becomes especially important for assigning cells along the

upper shoreface as ocean, so that they remain in the calculations, despite having a negative cell depth (i.e. above water). For the present models, the ocean cell "depths" were limited to -0.3 m NAVD88 to capture processes on the upper shoreface without causing the model to become unstable.

The assignment of a CMS-Flow cell as land, ocean, or observation requires designation of the cell attribute. Land cells are omitted from calculations, ocean cells can wet or dry up to a specified depth, and observation cells act as ocean cells with specified output to a text file. Ocean cells can be further modified by specification as erodible hard bottom, under a variety of constraints, or non-erodible hard bottom. In this study, only the non-erodible hard bottom specification was used in alternative grid designs, as needed, and is described in that section (4.2.1). All CMS-Flow cells representing the location of inlet jetties were designated land having a depth of -2.24 m NAVD88 (recall z is positive down for depth) and effectively removed from calculations. However, flow velocity is accurately approximated along these jettied/land cells provided the wall friction option is turned on and the Manning's coefficient is set (here, 0.025). Manually changing a land cell depth within a CMS-Flow grid is only relevant when the grid is to be duplicated (and re-oriented by 180^{o}) to represent a CMS-Wave grid. In this case, assignment of a land cell depth as a negative z value (i.e. elevation) becomes very germane since CMS-Wave assigns structures differently than does CMS-Flow. To identify a jetty cell within the CMS-Wave grid, the cell is assigned the attribute of a structure to accurately model wave transmission and overtopping, as well as runup processes, associated with such features. Additional modifications are made by either changing the cell depth in the grid to be negative (emergent) with no

elevation modification made within the structural attribute dialogue box or, within the dialogue box, the cell elevation is modified (not the gridded depth) to the intended height of the rubble mound off the seafloor (submergent). The latter method is used for a variety of structural assignments besides a submerged rubble mound and its use in this study is described further in the section on alternate design grid development (4.2.1). Here, the initial model design identified jetties as rubble mound structures with a cell depth of -2.4 m NAVD88 (emergent) with no further modifications.

Each model has 61,182 cells (45,293 are ocean) ranging from 50 m x 50 m offshore to approximately 25 m x 25 m within the inlet (Figure 8). Although the grid orientations are the same, CMS-Flow lies at 31.03°, whereas CMS-Wave is 211.03°. Each domain covers an alongshore distance of 12.3 km, with the inlet just south of the midpoint, and an across shore distance of 7.5 km, extending 4.5 km into the Atlantic Ocean to a depth of approximately 22 m (Figure 9).

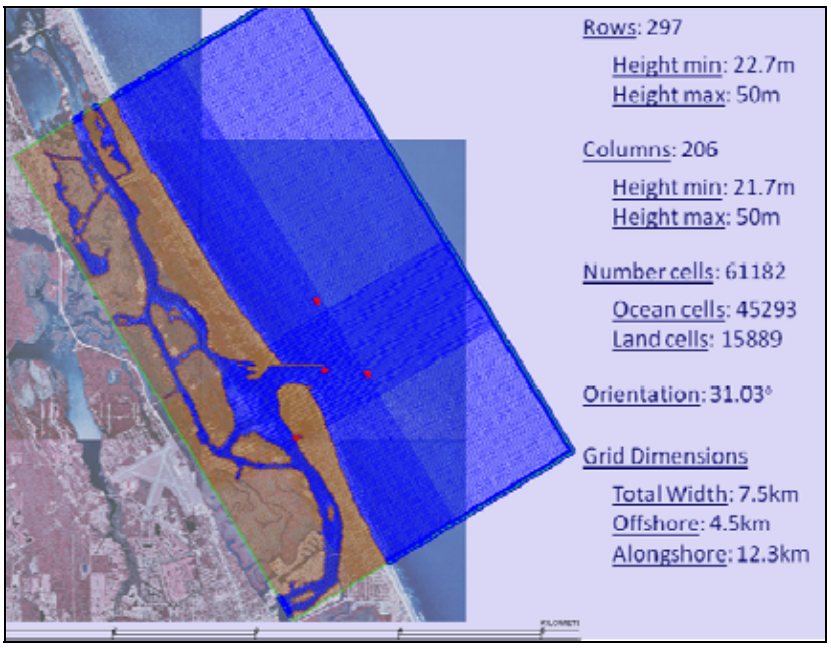

Figure 8. Design parameters for the CMS model grids. (1999 DOQQ, original scale 1:12,000, FDEP)

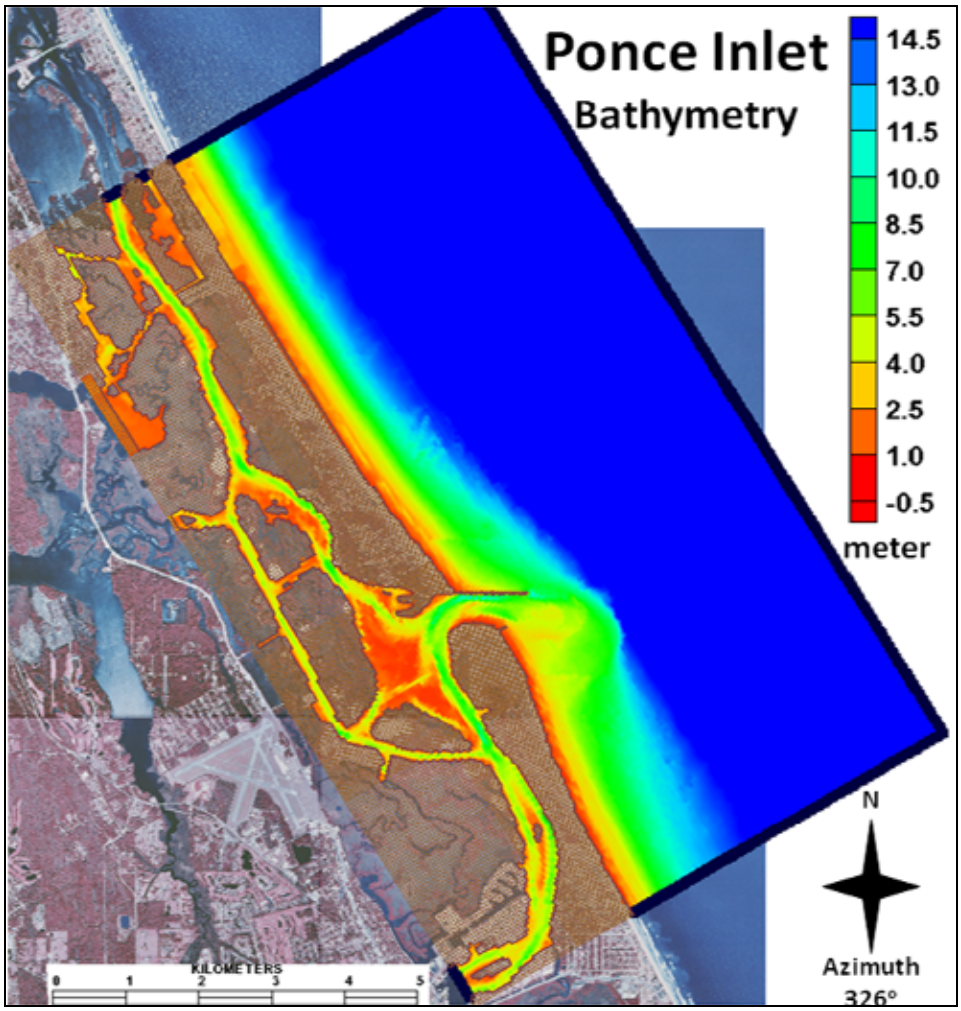

Figure 9. CMS model domain with depth contours. (1999 DOQQ, original scale 1:12,000, FDEP)

3.4 Boundary Conditions

The following section describes the physical forcing of the individual models. The circulation model is driven by time series of water surface elevations inserted along the domain boundary and winds are added to the model control. The wave model is forced using time series of wave height, period, and direction, as well as spreading parameters, to generate a spectral energy grid with the addition of winds appropriate for each time step.

3.4.1 Water Surface Elevation (WSE)

CMS-Flow was forced using WSE time series along three boundaries: offshore, north lagoon, and south lagoon. For the offshore boundary, data from the Trident Pier tide gauge (8721604, Appendix B) was adjusted from MLW to vertical datum NAVD88 by subtracting 0.81 m. For the south boundary, the archived time series for the now removed New Smyrna Beach/Mosquito Lagoon gauge (8721164, Appendix B) came from SJRWMD. These time series were already in NAVD88, metric. For the north boundary, the time series had to be generated since no tide gauges exist in this area of the lagoon. The St. Augustine gauge (8720587, Appendix B) was chosen to extract the tidal signal using a 31 hr low-pass filter (Rosario-Llantín, 2000) that separates the "tides only" signal from that which occurs at frequencies greater than 31 hr. The time series, which was available in NAVD88 from the NOAA CO-OPS website, was shifted by a 2 hr lag to compensate for the phase lag between the open ocean and the back lagoon. Further, to compensate for St. Augustine's gauge location on the ocean pier, the extracted tidal amplitudes were reduced by half for the north boundary. This adjusted "tidal only" signal was combined with the 31 hr, low-pass filtered signal from the Mosquito Lagoon gauge (Figure 10, blue), wherein the signal above the 31 hr frequency was retained to ensure local topographic effects would be modeled accurately within the lagoon. This combined time series was compared with the measured time series from the northern gauge used in the 1997 short-term field study by Zarillo and Militello (1999) and showed a 1 cm difference in average eta (η). After comparison to the other CMS-Flow boundary conditions, it was deemed an appropriate fit according to phasing and elevation (Figure 11 and Figure 12).

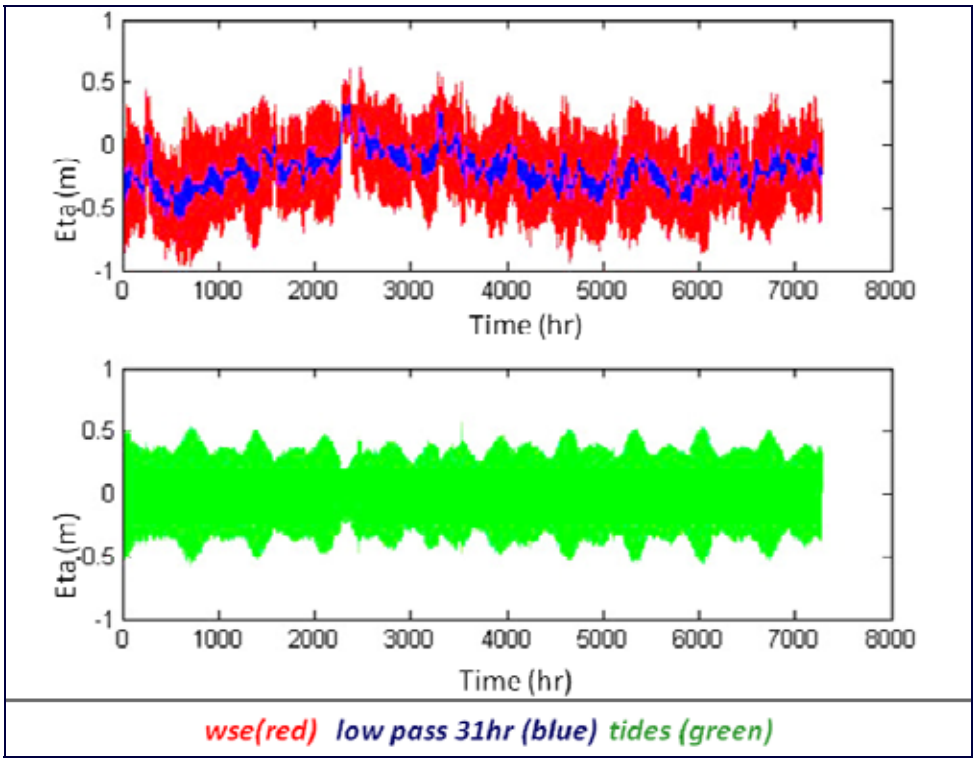

Figure 10. Low-pass filter analysis of the Mosquito Lagoon water surface elevations.

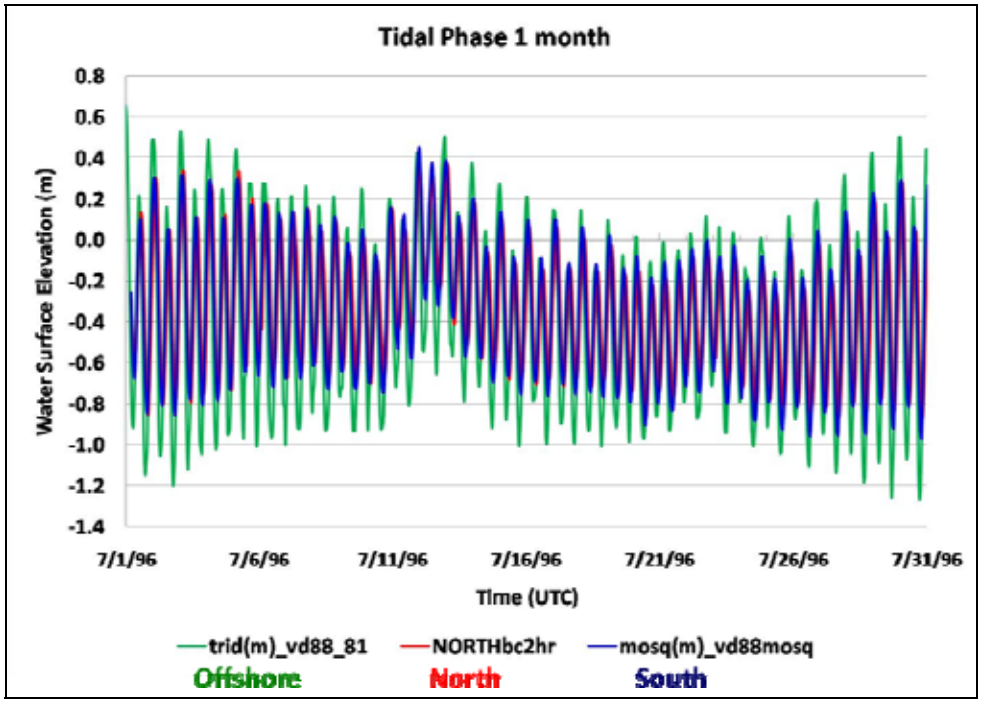

Figure 11. Comparison of CMS-Flow boundary conditions for the month of July 1996.

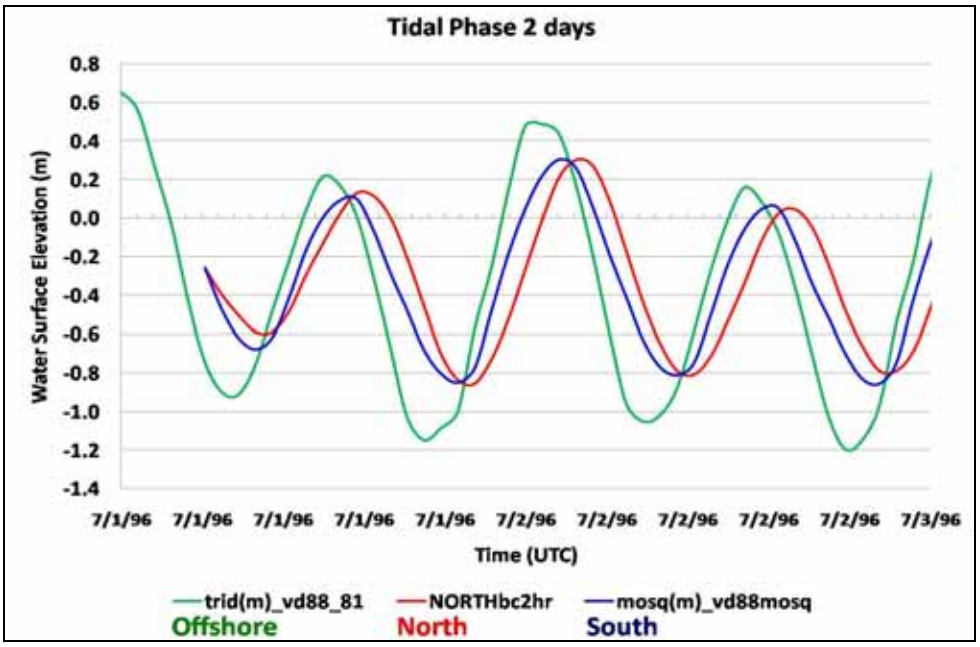

Figure 12. Boundary Conditions for CMS-Flow for two days, July 1-3, 1996.

It is an avoidable issue with instrumentation that there will be intermittent hardware failure causing gaps in the data that must be addressed. This was handled using MATLAB® and performing harmonic analyses (Pawlowicz et al., 2002) on the largest complete records. In all cases, a minimum of 45 days was available. All analyzed harmonic constituents were then used to predict the missing tides and a 31 hr low-pass signal from the closest tidal station was also added to complete the record.

3.4.2 Winds

Wind forcing data (speed and direction) for the CMS-FLOW model came from the NDBC offshore buoy 41009. Gaps in the data were supplemented by the closest buoy, typically 41010 (Appendix C). Although the CIRP field study measured winds and other meteorological parameters at the Batelle site (Figure 6., gauge h) these data were unavailable from the archives. The wind parameters were included in each model

through the model control dialogue. For CMS-Flow, the direction is based on meteorological convention (degrees from true N) while CMS-Wave requires conversion to local coordinates for forward-marching calculations. This conversion was handled by subtracting the meteorological direction of the wind from 59^{o}, which is the CMS-Wave grid's onshore orientation as observed from true North.

3.4.3 Waves

The hydrodynamic model CMS-FLOW included wave forcing by two-way coupling with the CMS-WAVE model. CMS-Wave is forced at the open boundaries by a TMA (shallow-water) spectral energy distribution generated from incident wave height, period and direction, as well as spreading parameters. Although the Canaveral buoys offshore of Ponce de Leon Inlet at 120 NM (41010) and 20 NM (41009) contain spectral wave density files available as input into the CMS-WAVE model (Appendix C), preference was given to using wave hindcasts from the CHL Wave Information Studies (WIS). These WIS hindcasts contain directional, spectrally-derived wave parameters for the water depth of 19 m at station 429 (517,102.7 northing, 240922.1 easting). This gauge is located 20 km offshore of the study site so the wave parameters were modeled in a larger domain (100 m x 100 m cell size), allowed to propagate towards the shore, and the results extracted at a center cell along the boundary of the high resolution grid (Figure 13). The hindcast time series was truncated to every 3rd hour of wave parameters to correspond with the chosen steering interval. Wave direction was converted within the CMS model from true north to a local coordinate system to ensure the +x direction is onshore for the wave grid.

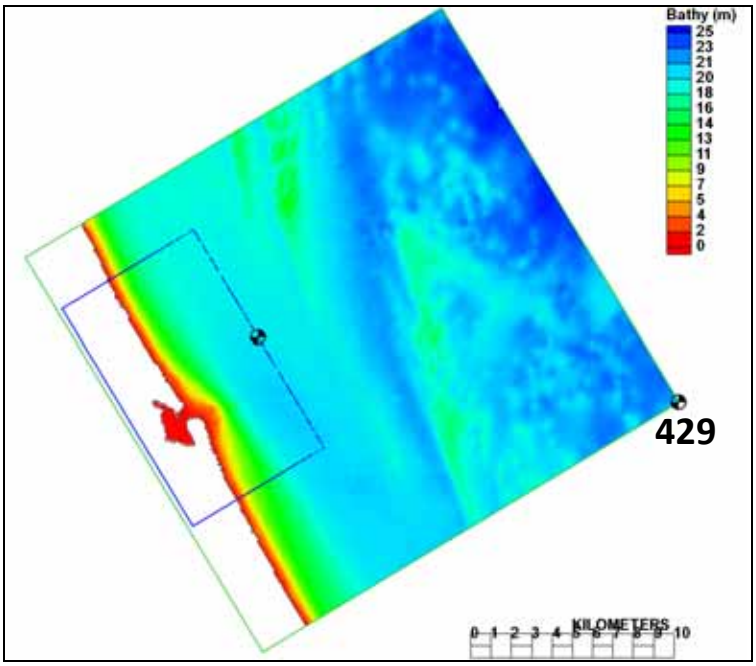

Figure 13. CMS-Wave domain for runs from WIS station 429 into high resolution domain.

3.5 Model Controls

The steering module command within the SMS® interface provided the two-way coupling with water levels, currents, and updated bed level input into CMS-WAVE every 3rd hour. The updated wave parameters were returned to CMS-FLOW at the end of each CMS-WAVE run. The computation scheme for steering between the CMS models (Figure 14) begins with CMS-Wave, which runs for two intervals, repeating the initial forcing twice to achieve stability. Radiation stresses and breaking are then transferred to CMS-Flow which runs for three, 1 hr intervals calculating sediment transport and bed level change at each hour, following explicit calculation of the vertically-integrated equations of motion and continuity. Sediment transport was calculated using the Lund-CIRP total load formula with inputs of water level, currents, waves, and orbital velocities returning hourly topographic updates.

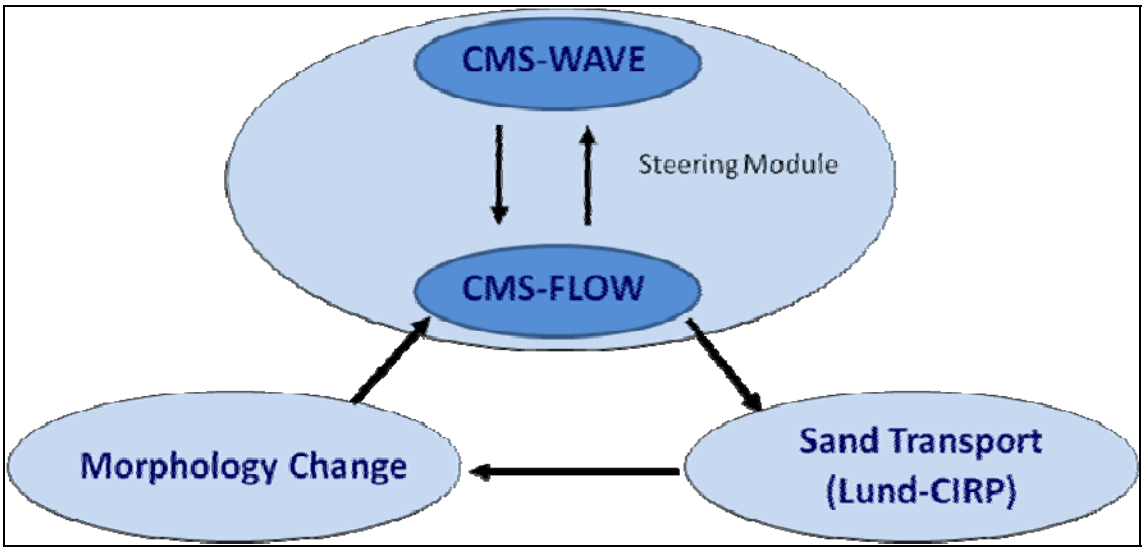

Figure 14. Illustration of the Coastal Modeling System computational scheme.

For the circulation portion of CMS-Flow, the momentum equations included advection and mixing terms as well as wall friction. The hydrodynamic time step was set at 1 s and only had to be lowered to 0.8 s on one of the longer runs so as not to violate the Courant number, which relates cell size to the amount of advection allowed in one time step. The default Manning's coefficient of 0.025 was kept constant over the domain, the depth to begin drying cells was 0.01m, and the latitude of 28.5^{o} N was averaged over the domain.

For the sediment transport portion of CMS-Flow, the transport rate time step was set at 20.0 s with output of morphology each hour. The following default parameters were chosen: sediment and water density of 2650 and 1025 kg/m^{3}, respectively; water temperature of 15^{o} C; bed load, suspended load, bed slope and morphologic acceleration coefficients of 1; sediment porosity of 0.4 and a D_{50} particle size of 0.2 mm, which is representative of the sandy coastlines in Volusia County (King et al. 1999).

For the CMS-Wave model, wetting and drying was allowed, the bed friction was spatially constant at a Manning coefficient of 0.005, the diffraction intensity was set to the recommended value of 4.0, and the forward reflection was spatially constant at 0.5. The output files included radiation stresses and depth-limited spectral energy dissipation, based on the Extended Goda formula (Lin et al., 2008), which accounts for waves on opposing currents and is pertinent for jettied inlets.

Details of the CMS parameters can be found in the CMS Technical Reports (Buttolph et al., 2006; Lin et al., 2008). An overview of the basic governing equations for the CMS models is provided in Appendix A.

.

4 Model Application

4.1 Model Calibration and Validation

The model setup was calibrated and validated by comparison to the water level data obtained from King et al. (1999) and the Ponce de Leon Inlet Coast Guard Station tide gauge (8721147, Appendix B). The year 1996 provided the most complete record for water level for the three available gauges from the long-term monitoring by King et al (1999) and the Coast Guard station had no limitations on available data. The 3-month time of July to October 1996 was used for calibrating the model. For validation of the model, the ebb shoal, offshore, and Coast Guard station had time series available through April 1997. However, not all records were complete, so the validation results were limited to 6 months (October 1996 to March 1997).

Given that the integrated approach of CMS under the steering module produces outputs that have been calculated using a combination of the hydrodynamic/sediment transport model, as well as the wave model, calibration was performed using the combined results evident in the water surface elevation (WSE) time series. Statistical analysis performed on the WSE time series between the measured and the modeled data included average difference (AVG-eta), normalized root mean square deviation (nRMSD) and linear regression (LR). Harmonic analysis was also performed on each series to compare tidal constituents for amplitude and phasing.

The modeled water level time series (eta) are in phase with the measured water level time series (eta) at all stations during calibration (Figure 15) and validation (Figure 16). Differences between the measured and modeled WSE occur in the amplitude with the 0 to 24 hr window reflecting the ramping up period of the model and the ebb shoal having the largest offset. The average difference in water surface elevation, eta, (Table 2), for the ebb shoal is 11.6 cm, whereas the other three gauges show minimal average offsets: 0.02 cm for the entrance to the inlet, 1.0 cm at the coast guard station inside the inlet, and 5.0 cm at the offshore gauge (refer to Figure 6 for gauge locations). The root mean square deviation after the 24 hr ramp-up (RMSD_24) shows that the modeled eta differs from the measured eta by 4 to 15 cm depending on the gauge location. When these values are normalized to the range of eta differences, the variation lowers to 3 to 11 cm. Normalizing a quantity produces a dimensionless value ranging from 0 to 1, but is typically described in terms of percentages. Since the tidal range at Ponce de Leon Inlet is 1 m, nRMSD is described using centimeters.

Table 2. Statistics for Calibration (all) and Validation (Coast Guard and Ebb Shoal)

GAUGE	AVG eta (meas-model) (m)	RMSD_24 (m)	Normalized RMSD_24 (m)	ABS Diff (m)
ebb	0.116	0.15	0.11	0.13
ent	0.002	0.08	0.06	0.07
off	0.050	0.10	0.08	0.09
coast	0.010	0.04	0.03	0.04
coastVal	0.015	0.04	0.08	0.04
ebbVal	0.381	0.41	0.35	0.38

GAUGE	Tidal amp M2 (m)		Tidal phase M2 (°)	
	Measured	Model	Measured	Model
ebb	0.58	0.52	307	311
ent	0.57	0.52	308	311
off	0.58	0.53	307	311
coast	0.47	0.44	326	324

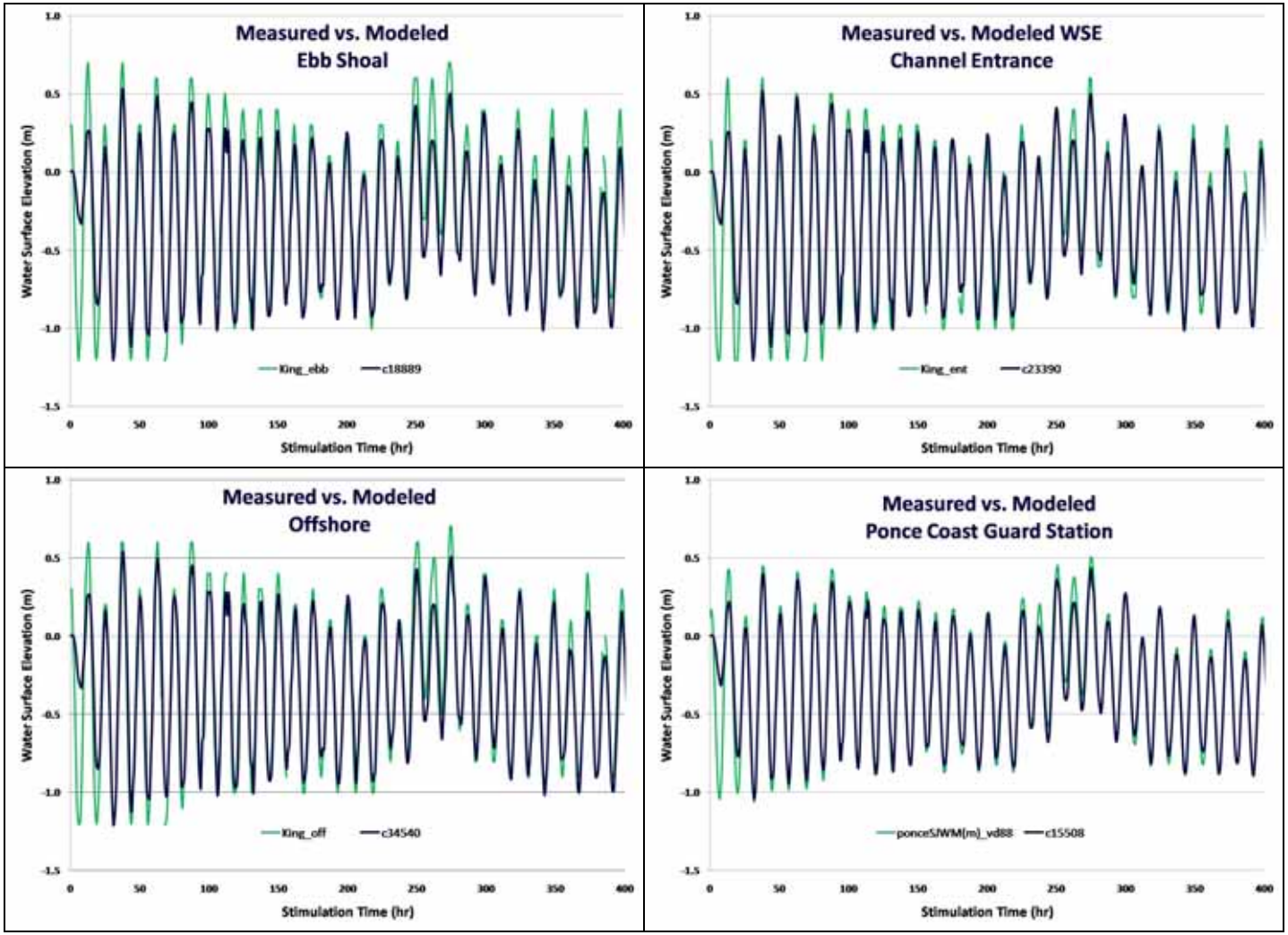

Figure 15. Measured vs. Modeled Water Surface Elevations (WSE) for July 1 to July 17, 1996. (Green is measured; Blue is modeled).

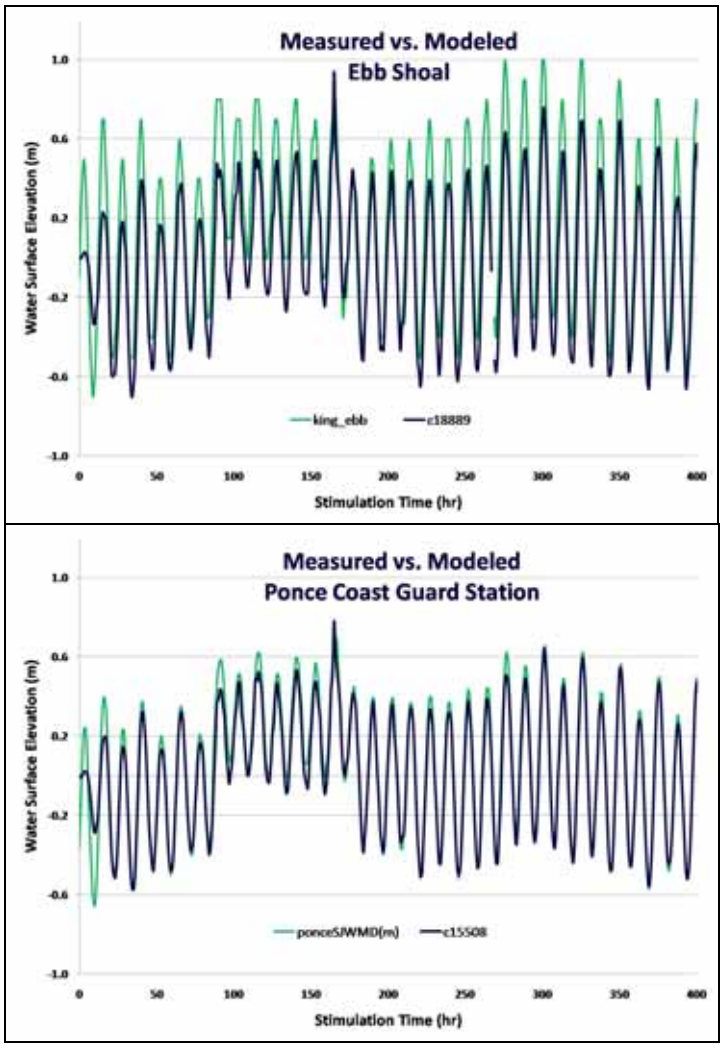

Figure 16. Measured vs. Modeled WSE of analysis extremes for Oct 1 to Oct 17, 1996. (Green is measured; Blue is modeled).

How well the modeled data correlates to the measured data is addressed by linear regression analysis (Figure 17). The R^2 values for the coast guard station of 0.98 (calibration) and 0.99 (validation) and for the ebb shoal of 0.96 (calibration) and 0.90 (validation) are good indicators that the model is well calibrated and validated. The harmonic analysis (Table 2) also supports the model being well calibrated in that the dominant tidal constituent, M2, matches in both amplitude (within 3 to 5 cm) and phase (within 2 to 4 degrees).

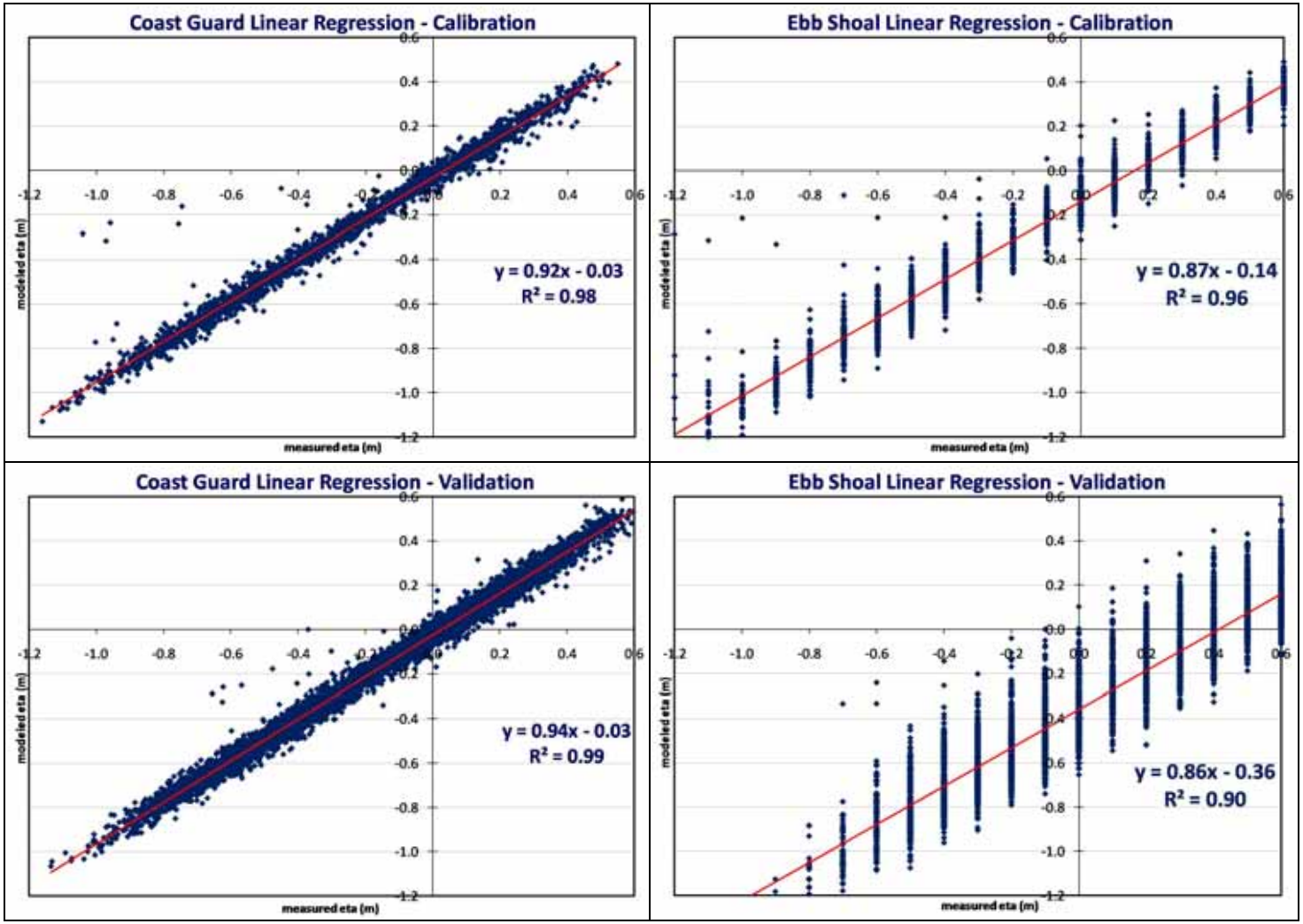

Figure 17. Linear Regression analysis of measured (x) vs. modeled (y) WSE for Coast Guard Station (left) and Ebb Shoal (right) for calibration period (top) and validation period (bottom). Note: Ebb shoal data was truncated to 0.1 m from source.

An overall look at the resulting analyses of all stations for the calibration period indicates that the ebb shoal was the least calibrated whereas the Coast Guard was the most. This was not surprising, given that the ebb shoal gauge was located on a platform attached to the most dynamic body of sand among the CIRP gauge locations, whereas the Coast Guard gauge was attached to a land-based piling. Additionally, modeled data was significant to 0.0000001 m, whereas CIRP data was only significant to 0.1 m. Therefore, differences between these data will generate more variability during statistical analysis, which becomes especially relevant when the range of variation is on the order of 0.01 m. The effect of truncating the data to 0.1 m is quite evident in the linear regression plots generating the clustering of data points (Figure 17, right). Despite the effect of this anomaly, statistical analyses supports the model's calibration.

Analysis of the Coast Guard water levels during the validation period are essentially identical to the calibration period, except for the nRMSD_24, which was a bit higher (8 cm up from 3 cm), but easily explained given that the data range covers a longer time series (7 months). Despite this longer period, the average eta difference was only 1.5 cm (Table 2) and the correlation coefficient was 0.99 for the Coast Guard gauge. The ebb shoal gauge presented the largest deviation of all gauges, with a nRMSD_24 of 35 cm. This gauge's anomaly was attributed to the shifting morphology of the ebb shoal and the extended time period for validation. Water levels from the CIRP gauges were determined by subtracting the nominal depth of the gauge from the barometrically-adjusted pressure readings, with gauges calibrated only on deployment. Despite the ebb shoal deviation, the R^2 coefficient was 0.90, and the total statistical analysis supports validation as well as calibration.

4.2 Model Design Alternatives

Design alternatives for Ponce Inlet covered a variety of options involving extending the south jetty: with and without spurs, reopening the north weir with and without adding a deposition basin adjacent to the north jetty, that did or did not have an artificial rubble mound hard bottom, and re-dredging the navigation channel to its design location with depths of 4.6 m (to address the shoaling that has occurred over the three decades since the inlet was stabilized). Table 3 shows the full array of alternate designs that were run for 3 months to determine their feasibility. The color scheme of the table highlights the modifications into groups around a main configuration. This table also presents the abbreviations used to describe the modifications made. Only the most viable options were chosen for the long-term runs of 10 months allowing for modeling of both fair weather and winter storm conditions. These options are indicated in Table 3.

4.2.1 Design Alternatives Grid Development

Once the statistical analysis revealed the model to be calibrated and validated, all remaining changes made to the model were based solely on changing individual cell attributes and cell depths. For the south jetty extensions where new rubble mound structures would be emergent (SJ, SJR, SJ/ES), CMS-Flow required changing the grid's cell attribute from ocean to land, which removed that cell from calculation. CMS-Wave required changing the cell depth to represent elevation above 0 m NAVD88 (-2.24 m) and identifying the cell attribute as a rubble mound structure with no other elevation modification. For the submerged rubble mound spur structure (SJ/SS), CMS-Flow's cell

attribute remained as ocean for calculations but the cell depth was changed to +0.5 m so that the structure was just below 0 m NAVD88. CMS-Wave required changing the cell attribute to rubble mound structure, but with modification of the cell's elevation to a depth of 0.5 m less than the assigned cell depth. For example, a cell with z = 3.7 m depth was identified as +3.2 m elevation for the structure. In this way, CMS-Wave categorizes the cell as a structure that is elevated 3.2 m off the seafloor, but in a water depth of 3.7 m.

For the weir reopening (W) in both CMS-Flow and CMS-Wave, the cell attribute was changed from land to ocean and the cell depth was adjusted to be the same as the adjacent cell to the north within the grid. For the weir option, a deposition basin became a consideration as well. One choice for the weir option included no other cell changes to the grid beyond the weir itself and it allowed the existing depths of the shifted navigation channel (as much as 11.5 m in places) to serve as the deposition basin that would be used for mechanical bypassing as needed. Another option was to redesign the navigation channel to its original design location and depths (C) and to put the removed sediment as filler in portions of the deep, shifted navigation channel in order to return to the original configuration of the deposition basin (B). This was accomplished by changing the cells depths located along the original navigation channel to a minimum of 4.6 m (C) and by changing the cell depths within the "basin" area of the present channel to a maximum of 7.6 m (B).

Another option for the basin (the deepened, shifted channel) was to fill in the "basin pit" with the 8-12 ton rubble mound rocks that would be removed from the jetty while reopening the weir (HB). This was accomplished within the grids by changing the

appropriate cell depth to 7.6 m, as was done for the other basin option. Additionally, for CMS-Flow, the cell attribute was further specified as being non-erodible to cell depth (HB), whereas CMS-Wave required no further changes, given that this model does not perform the topographic change calculations.

This artificial hard bottom option (HB) was also continued beyond its use as a deposition basin with the weir option. Once the grids were assigned for the hard bottom (HB) and channel re-dredging (i.e. relocation, C) option, this combination proved useful as a design alternative for keeping the main channel from migrating back into the north jetty once re-dredged. The preliminary 3-month runs using the hard bottom (HB) and channel re-dredged (C) option suggested their use with the South Jetty Extension options might be beneficial and was, therefore, added to the long-term runs.

Table 3. Design alternatives for model runs utilizing the abbreviations associated with each modification. Colors indicate category of modification: South Jetty only, Weir open, South Jetty extension with Channel and artificial Hard Bottom basin, South Jetty spurs: Emergent and Submergent.

Alternative Number	South Jetty Extension	South Jetty Rebuild	South Spur Emergent	South Spur Submergent	North Weir	Channel Dredge	Deposition Basin	Hard Bottom Basin	Long-Term Run (10mo)
1	SJ								LT
2		SJR							
3					W				
4					W	C	B		
5	SJ				W	C	B		
6		SJR			W	C	B		
7	SJ				W	C		HB	
8		SJR			W	C		HB	
9	SJ					C		HB	LT
10		SJR				C		HB	
11	SJ		ES						
12	SJ		ES			C			LT*
13	SJ		ES			C		HB	LT
14	SJ			SS		C			LT
15	SJ			SS		C		HB	LT

* 4.5 months only due to software error

5 Results and Discussion

This section presents the results of the analyses performed during this study. Please note that in the parts of section 5.1 that describe how to interpret the Channel Equilibrium Area (CEA) output plots (Figure 18) metric units are replaced by English customary units due to engineering convention. However, the analysis performed and presented for Ponce de Leon Inlet was done in metric units.

5.1 Inlet stability using Escoffier analysis

The maximum calculated versus equilibrium velocities through an inlet channel can be determined using a 1-D analytical model called the Channel Equilibrium Area (CEA) developed by CIRP using the solutions of DiLorenzo (1986). These velocities are plotted against the cross-sectional area of the channel to determine if an inlet will reverse deviations from equilibrium (stabilize) or perpetuate deviations (unstable inlet). An example of how to interpret the results obtained from the analysis follows. As shown in Figure 18, a decrease in channel area to 4000 ft^2 will be accompanied by a decrease in flow velocity below the required equilibrium to maintain the opening, and the inlet will close. This is an unstable condition. On the other hand, an increase to 10,000 ft^2 will result in an increase in velocity above the equilibrium velocity required to maintain the inlet. This is considered to be a stable configuration. If the channel area continues to increase to 30,000 ft^2, the velocity will again fall below the equilibrium and

accretion will ensue. In this case, though, the channel area will begin to reduce as the accretion continues and the inlet can move back toward equilibrium, and is considered a stable inlet.

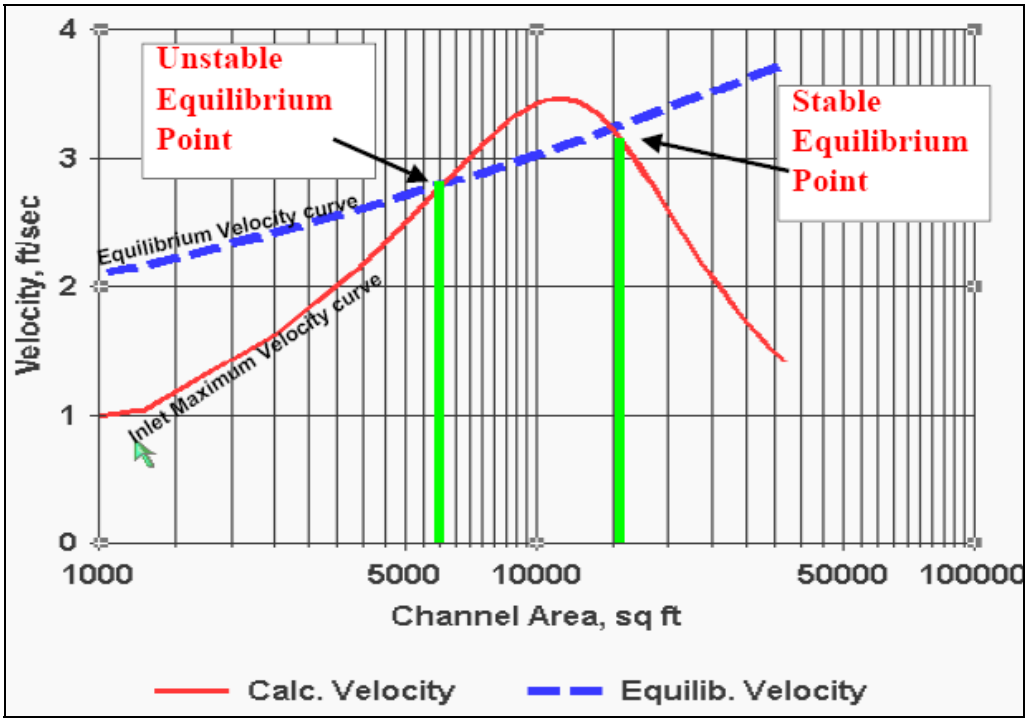

Figure 18. Diagram for interpreting stability from Channel Equilibrium Area analysis. (After Zarillo, 2003).

According to the results obtained for the present design of Ponce de Leon Inlet, the cross-sectional area of the originally designed navigation channel (1069 m^2) lies between the intersection equilibrium values (minimum of 700 m^2 and maximum of 14110 m^2) and thus classifies Ponce as a stable inlet (Figure 19). However, this channel area for Ponce de Leon Inlet exists very close to its lower equilibrium values and the room for flexibility in maintaining this equilibrium will be reduced unless cross-sectional area increases to shift the balance toward the right (more stable). Further

surveys need to be performed to acquire the up-to-date dimensions of the channel as it has migrated and deepened since the original design, which were the values used in this analysis. The present location of the navigation channel is, however, both a stress on the north jetty structure and a hazard to small craft navigating its length. This study aims to model a return of the navigation channel to its original design location through the centerline of the inlet with original design dimensions.

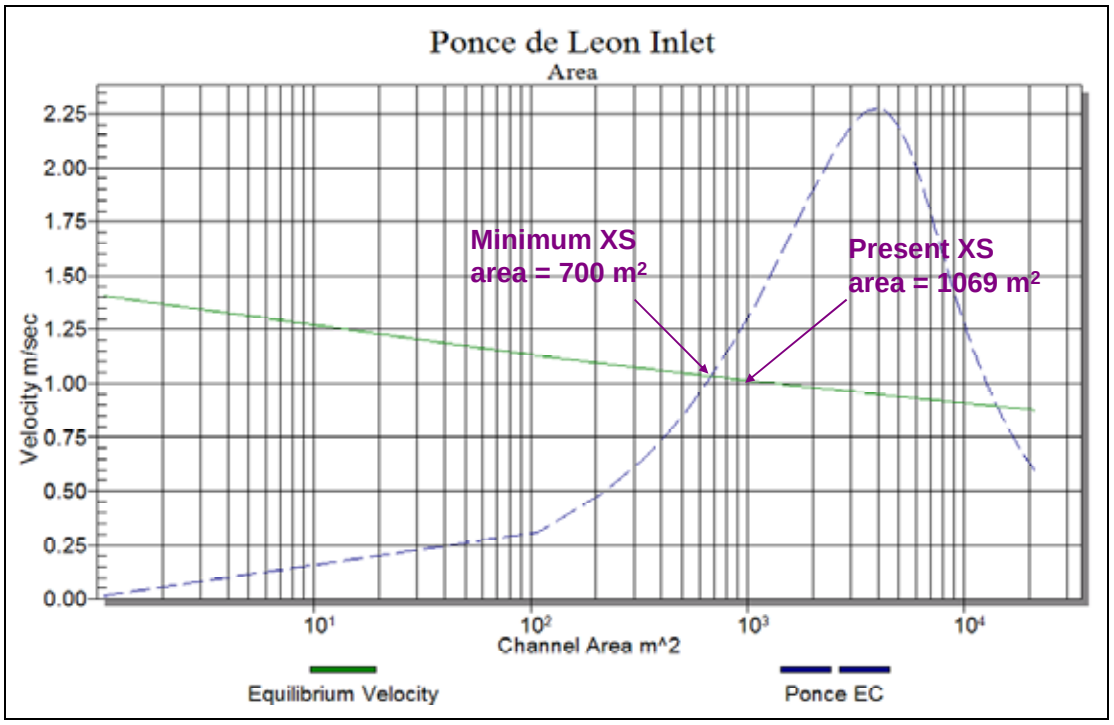

Figure 19. Stability diagram for Channel Equilibrium Area analysis of Ponce de Leon Inlet.

5.2 Short-term / Preliminary Runs

The results of the preliminary, three month runs (July 1 to September 30, 1996) are presented individually, with reference to other designs as appropriate, followed with a summative comparison of alternate designs to each other and to the present configuration. Analysis of each design's feasibility is addressed qualitatively by visual examination of several categories of contoured and vector plots: before and after morphology, net change of the start minus the end morphology, and flow velocity (with and without morphology) during a spring and a neap tide. The feasibility of the design is addressed quantitatively by volume change analysis within an area of interest using polygon masks to represent both key areas of concern and key components of the inlet system (Figure 20). The volume change within the polygon's area (Δvol) between the start and end of a run was normalized by the starting volume in that mask for that design. Volumes were determined by the cell depth times the planform area of the polygon mask. The area of a particular mask, or sub-domain, did not change among the designs. However, the starting depth of a cell may have been altered or that cell removed from the calculation. In either case, the starting volume would be unique for that design in that sub-domain. Normalized net volumes were converted to percentages to facilitate comparison for the total volume changes occurring among the design options.

The polygon masks, or sub-domains, were chosen based on areas of concern or where design changes would require a closer examination. Most areas and their names are self-explanatory, but a few need clarification for this study. Considering the general

morphologic features of an inlet system, the entire ebb shoal was grouped with the seaward part of the downdrift bypass bar and is referred to as the Ebb Complex. The nearshore portion of the bypass bar was combined with the nearshore and adjacent beaches immediately south of the extended south jetty, to include the attachment bar, and is referred to as the South Jetty mask. The remainder of offshore activity downdrift of the inlet forms the Outer Bypass, which is adjacent to the South Beach (~ 2 km).

The present channel is deep and lies extremely close to the north jetty and much work was done in the designs to address this concern. Therefore, the channel was broken into three masks for the volume analysis with two masks actually overlapping each other. The Basin Channel mask covers the majority of the present channel, including some of the deepest parts of the channel, and is the section that was "filled in" by sediment for the deposition basin option to a depth of 7.6 m. The Hard Bottom mask is a subset of the Basin Channel and represents the cells where the rubble mound rocks would be placed to limit the depth of erosion for those cells for those design options. The Hard Bottom mask is needed only during comparison for the designs that included this routine; otherwise, the basin channel is the main area to be used. Adjacent to the east of the Basin Channel is the Channel>7m mask representing the remaining length of channel out of the inlet and was not changed in depth during any runs. The centerline of the inlet is referred to as Channel~4.6m representing the option where the starting depth, along the original navigation channel, was lowered to a minimum of 4.6 m as needed.

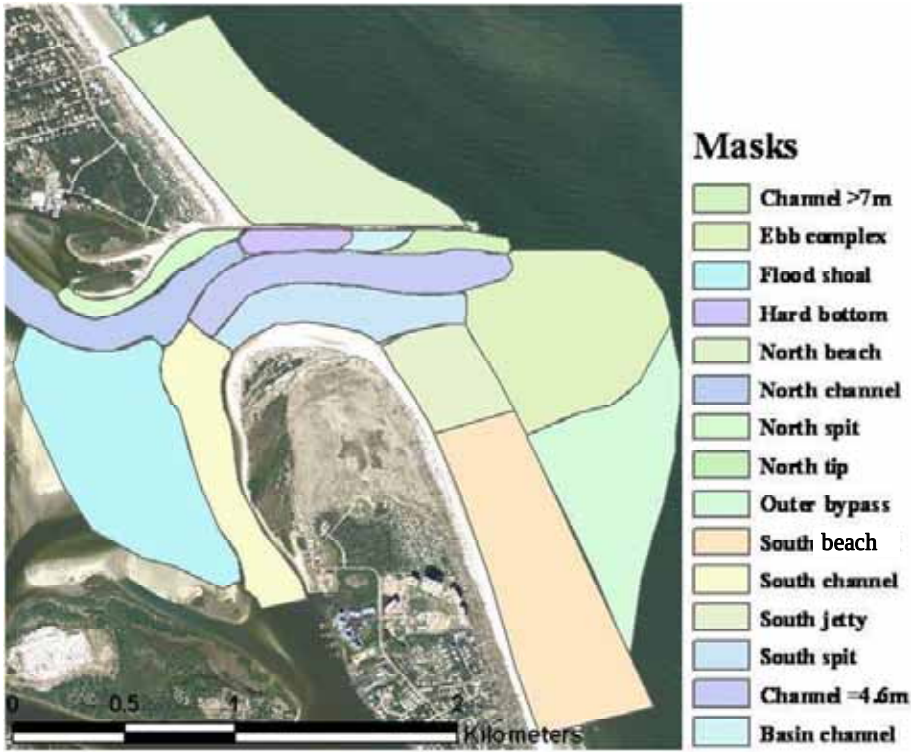

Figure 20. Schematic representing polygon masks used for volume analysis.

5.2.1 Present Conditions

Starting morphology for the Present Design (Figure 21) shows an azimuth of about 90° for the navigation channel running parallel to, and along the southern side of, the north jetty with depths as much as 11.5 m. Whereas the original design parameters (Figure 4) placed the channel in the centerline of the inlet throat, oriented about 75° with depths of 4.6 m, the present morphology shows little remnants of this design with depth as shallow as 2.3 m where the original channel once existed. The dredged channel through the flood shoal, Rockhouse Creek, has been reduced to z ~ 3 m since the original design restricting its navigation. The 3-month morphology (Figure 22) shows a reworking along the inlet's centerline with depths now ~ 4 m. The present navigation channel is also reduced in depth to ~ 9.5 m for most of its length.

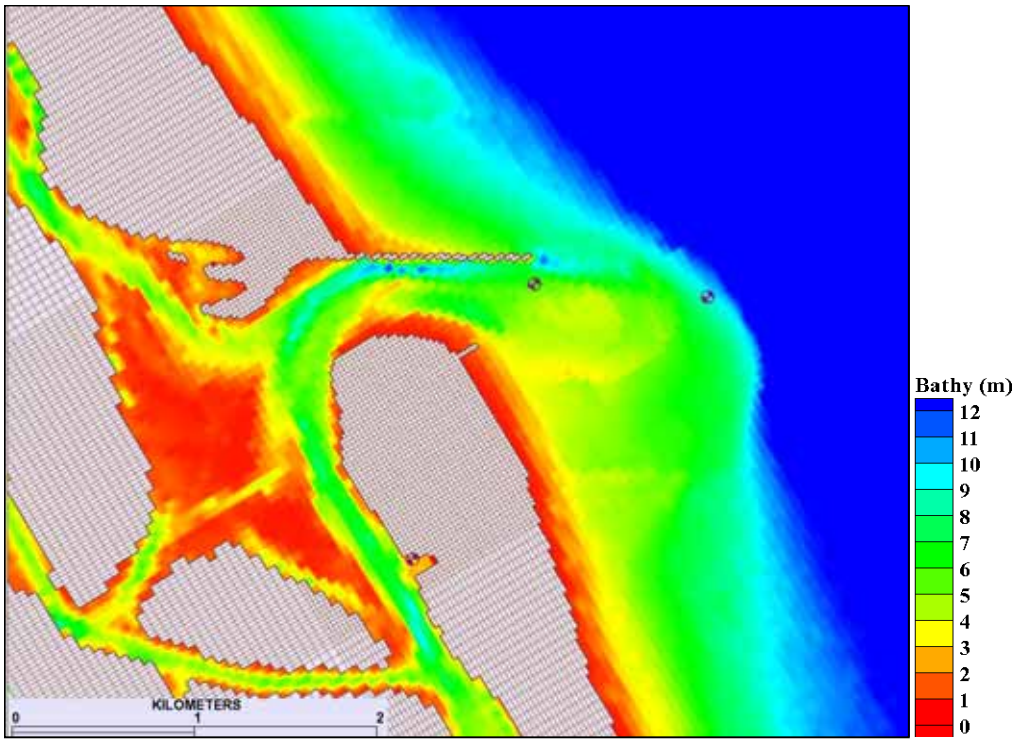

Figure 21. Morphology at 0 hr for Present Design.

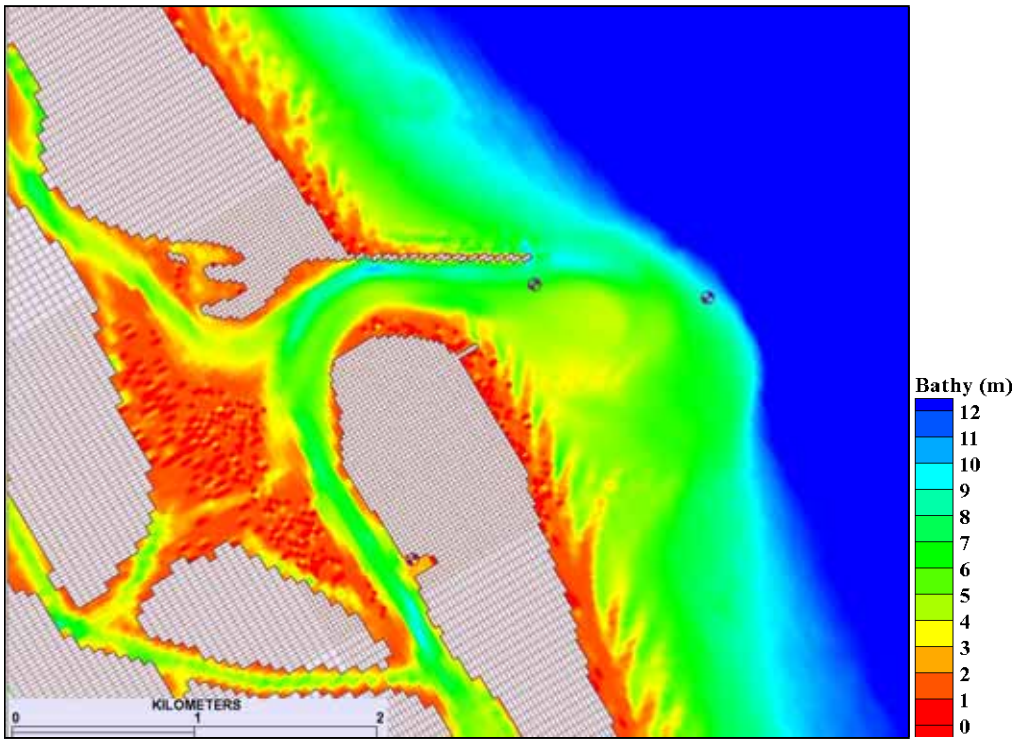

Figure 22. Morphology at 2197 hr (3 months) for Present Design.

The most obvious net change in morphology (Δz) for the Present Design (Figure 23) is deposition (deep red) of more than 3 m in places south of the inlet's centerline, referred to as the South Spit. Despite some erosion (-0.5 m, blue) along the south spit beaches, there was a net deposition of +65,304 m³ within the South Spit mask reflecting a +13% growth over the initial volume (Table 4), the largest percent of accretion for all masks. The equally large deposition (red) within the present channel (in the Basin Channel mask) represents a growth of +26,205 m³, or +4.6%. Scouring (blue) between -0.5 to -2 m occurred within the centerline of the inlet (referred to as Channel ~4.6 for its location as the original navigation channel), with a loss of -77,841 m³ of sediment, or -6.6% erosion. Scouring of the centerline of the inlet, even at small quantities, agrees with the Escoffier analysis that Ponce Inlet is stable, as far as remaining open is concerned. The goal will be to shift the channel back to the centerline, by taking full advantage of this self-scouring process, thereby, alleviating the present navigation hazard of vessels having to hug the north jetty.

The Flood Shoal lost -1.9% of its volume as indicated by the shift in color between the morphology images (Figure 21 and Figure 22) from deep red (z = 0 to 1 m) to a patchwork of golden yellow (z = 2 to 3m), as well as the light blue (Δz = -1 m) in the net change plot (Figure 23). The largest gain for the Flood Shoal occurred within the Rockhouse Creek channel (Δz ~ +2.5 m), which is a concern for navigation from the open ocean and Intercoastal Waterway. Intense scouring at the tips of jetties is a common process and expected process. In the present configuration of the dual-jetty system at Ponce de Leon Inlet, the largest loss of volume (-34%) occurs at the North Tip. The North Beach lost only -1.3% of its volume. Since the sub-domains covering

the typical pathways for sand transport around an inlet (Ebb Shoal and Outer Bypass) showed little to no change and the South Jetty mask showed -3.3% volume loss, it is a fair assertion that the shoaling within the inlet is due to northward transport around the south jetty. Despite the alternating color scheme for the net changes along the South Beach, there was essentially no volume change.

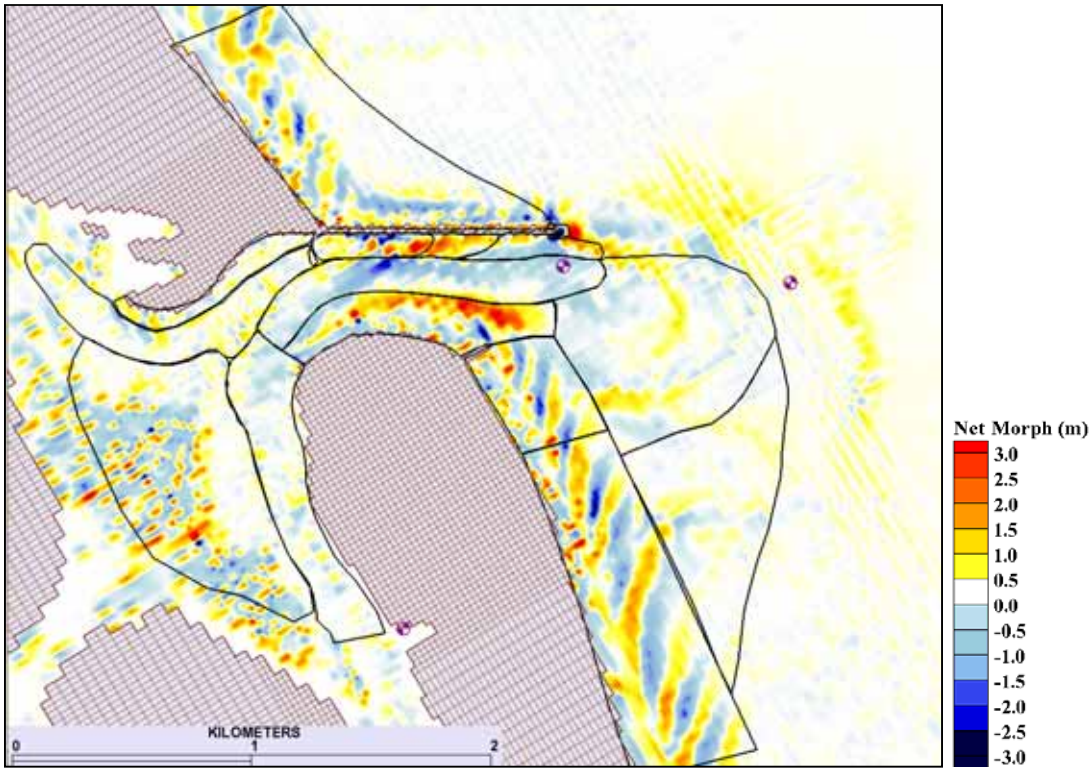

Figure 23. Net 3-month change in morphology for Present Design.

Table 4. Volume Change (3 months) for Present Design: Normalized (%) and Net (Δvol).

Polygon Mask	%	Δvol (m^3)
Ebb complex	-0.19	-4550
South spit	12.98	65304
Channel ~4.6m	-6.62	-77841
Channel >7m	-1.77	-5065
Basin channel	4.58	26205
North channel	0.58	5572
South Jetty	-3.31	-12876
South channel	-0.88	-11813
South beach	0.00	3.3
Outer bypass	0.46	10595
North tip	-33.76	-7366
North spit	3.68	4792
North beach	-1.32	-27385
Hard bottom	1.08	3857
Flood shoal	-1.88	-16317

Maximum flow velocities (Figure 24 and Figure 25) during the last neap tide of the 3-month run (September 20, 1996) are larger on ebb than flood (0.95 vs. 0.62 m/s, respectively), both of which occur in the mid to north section of the inlet throat, but are evenly distributed in the conveyance channel to the west. During ebb cycle (Figure 25a and b), the flow is directed east out of the inlet toward the ebb shoal, but the southern portion of the flow turns southeast just past the tip of the south jetty as it crosses the inner ebb shoal. As this southeasterly flow meets the northward flowing offshore waters to the south during the last hour of ebb (slack water), positive and negative vortices (eddies) begin to form in the nearshore, which helps to explain the sweeping morphology along the south beaches. Peak ebb velocities reach 0.7 m/s across the ebb shoal (Figure 24a) and a positive vortex (counter-clockwise, or cyclonic, eddy) spins off the northern edge of this ebb flow. At maximum flood (Figure 25c), there is separation in the flow to the west and east over the outer ebb shoal (z = 5.5 m) aligned with the tip

of the south jetty. During the last hour of flood (Figure 25d), the flow over the ebb shoal sweeps to the south following the downdrift bypass pathway before separating along the outer bypass bar, with easterly directed flows. Although the offshore flow is northward south of the ebb shoal, the nearshore region flows to the south. In all cases, there is limited circulation along the eastern part of the south spit.

The increased flow velocities for the last spring tide of the 3-month run (September 27, 1996) for the Present Design (Figure 26 and Figure 27) are, again, larger on ebb than flood (1.38 vs. 0.85 m/s, respectively). During maximum ebb (Figure 26a), flow velocities of more than 1.0 m/s reach beyond the outer ebb shoal and numerous eddies are formed, both north and south of the inlet entrance, which carryover throughout all parts of the tidal cycle. During this spring tide, the offshore flow is directed to the south, but the negative vorticity (clockwise rotation) of the nearshore eddies produces localized reversals and contributes to the north flowing longshore currents, evident within the nearshore waters both north and south of the inlet. The consequence of this process, in combination with the short south jetty, is that during the last hour of ebb (Figure 26b and Figure 27b) the inlet has bi-directional flow well north of the inlet's centerline, so that while the northern third of the inlet is still flowing east, the inlet to the south is already in flood. This inertial effect is often observed in nature. The vectors clearly show that flow is directed northward across the centerline toward the ebb-directed flow. As during the neap tide, the strong ebb flow produced a cyclonic eddy offshore from the north edge of the ebb jet. During maximum flood, flow separation over the ebb shoal is gone, as all flow is southerly except for that which passes over the ebb shoal proper, turning northwest to enter the inlet from the south.

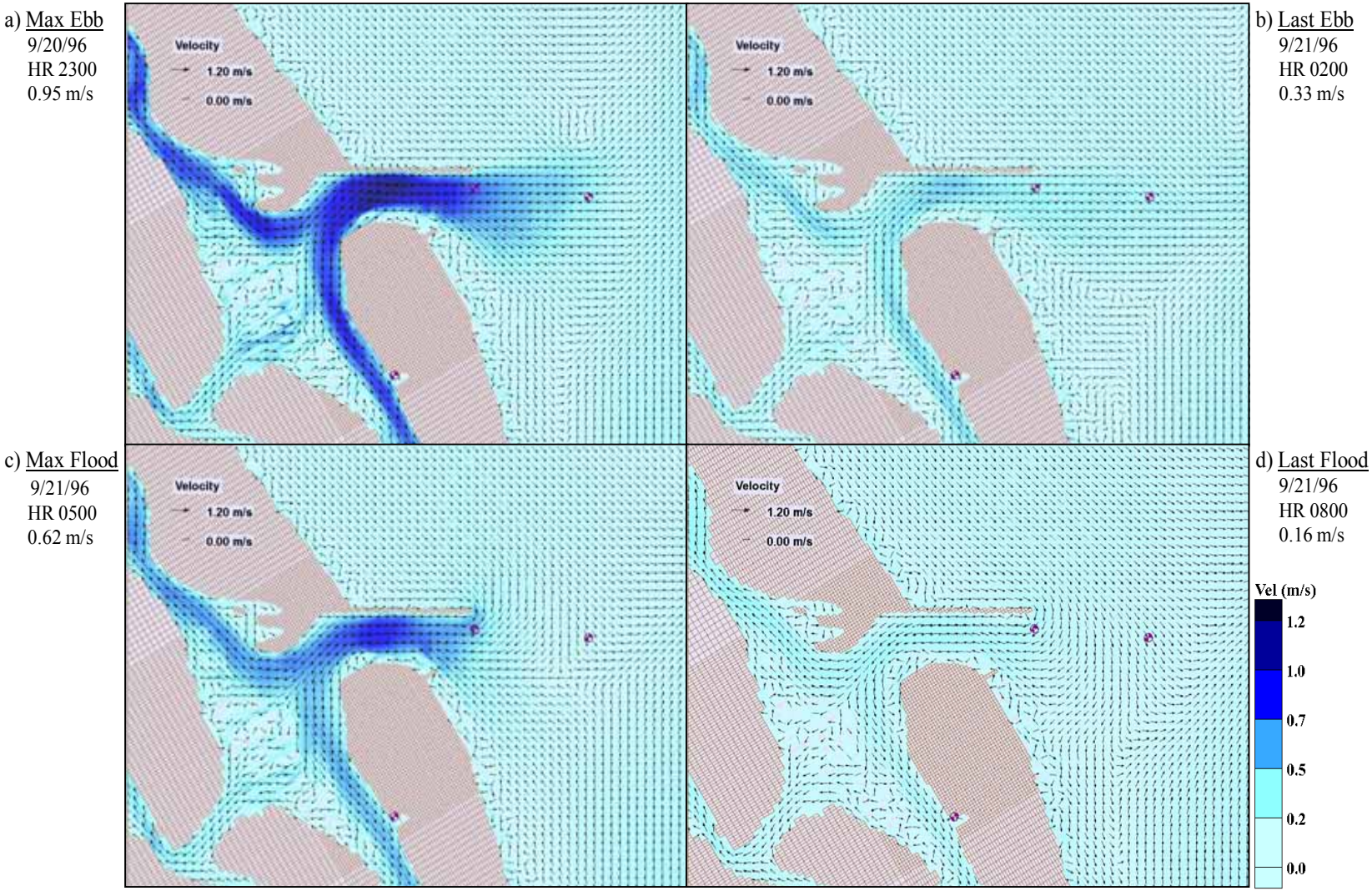

Figure 24. Flow velocities for Present Design during neap tide of 9/20/96. Maximum value from cell 25844 in channel.

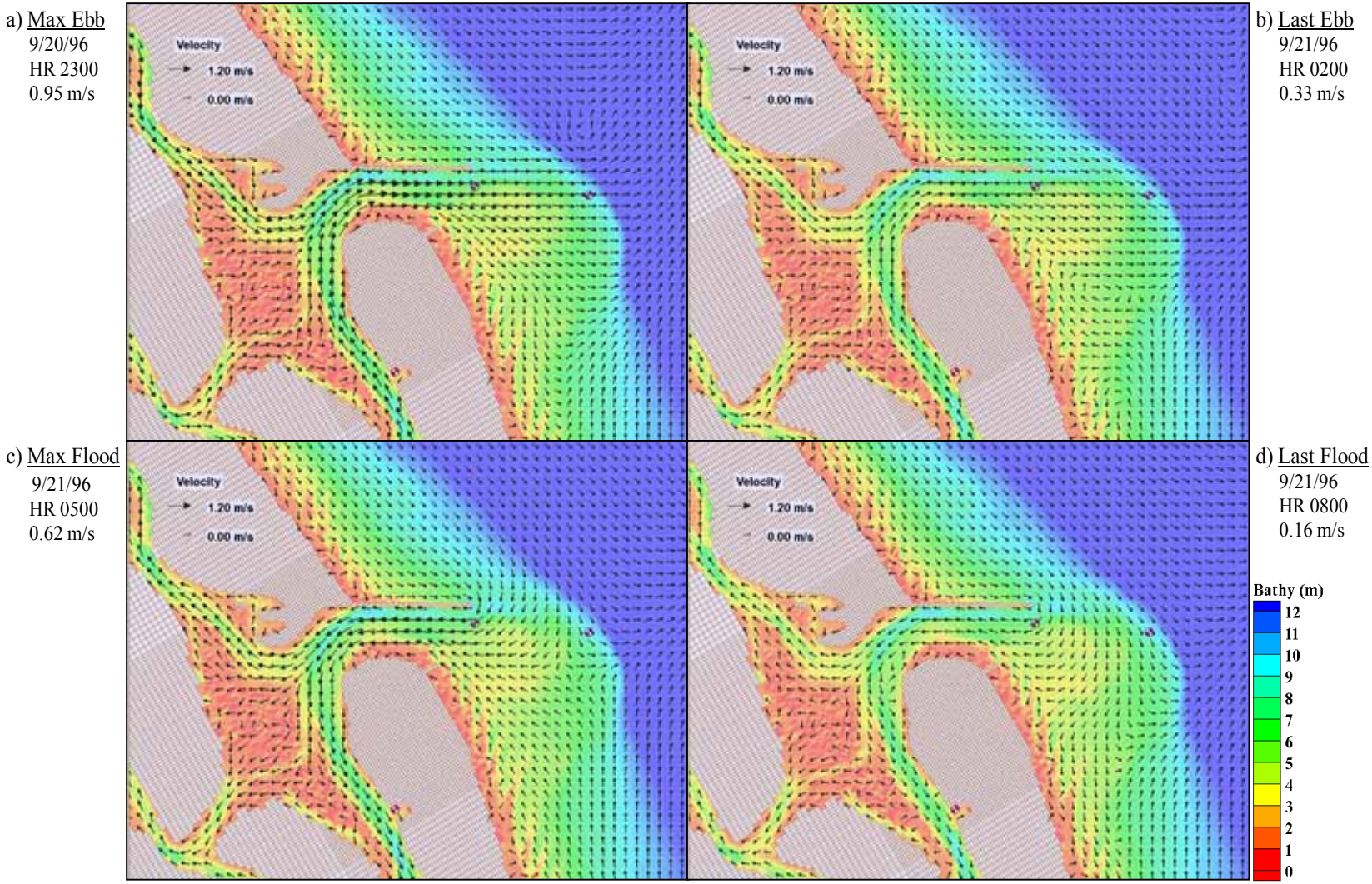

Figure 25. Morphology and flow velocities for Present Design during neap tide of 9/20/96. Maximum value from cell 25844 in channel.

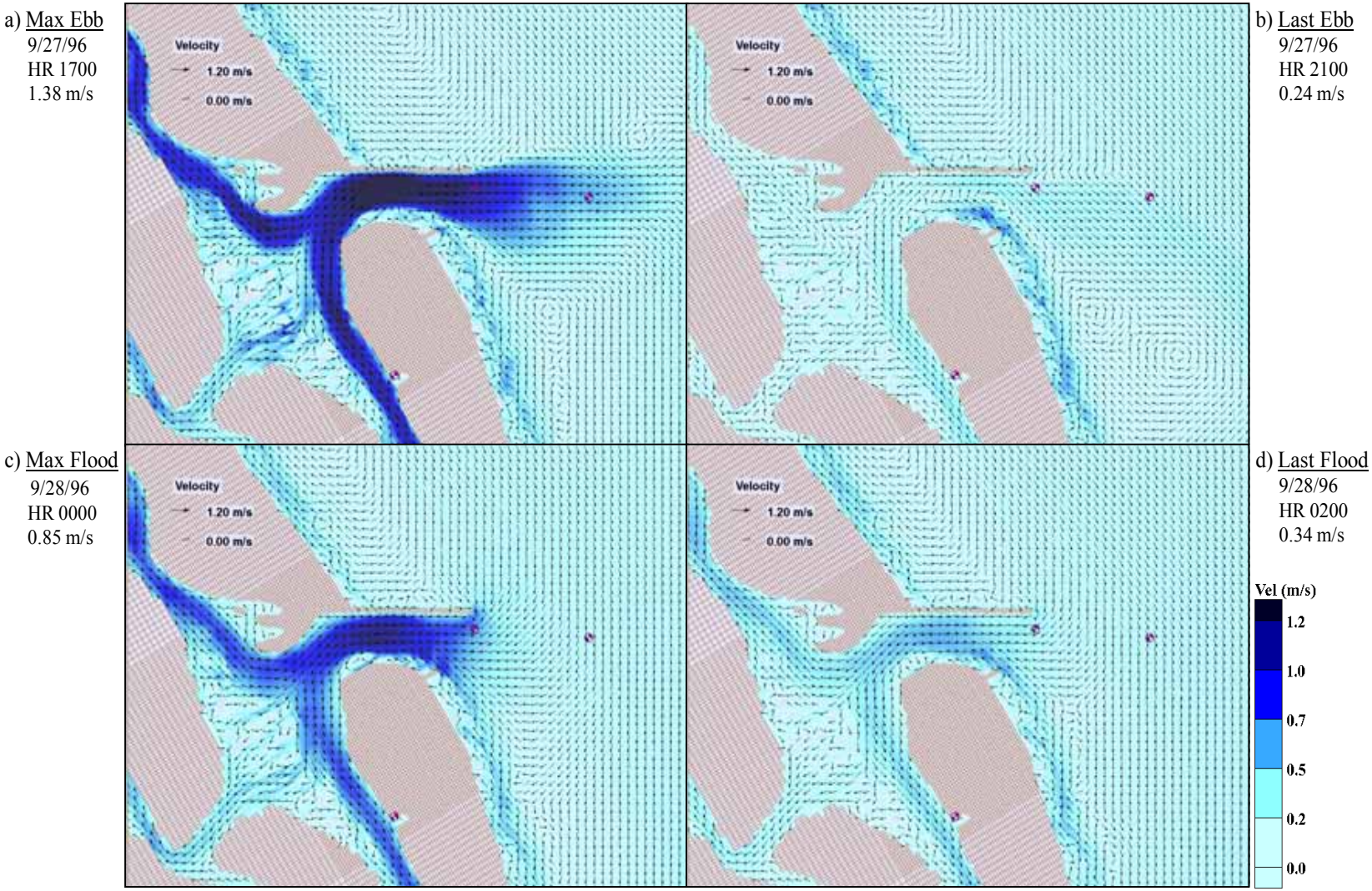

Figure 26. Flow velocities for Present Design during spring tide of 9/27/96. Maximum value from cell 25844 in channel.

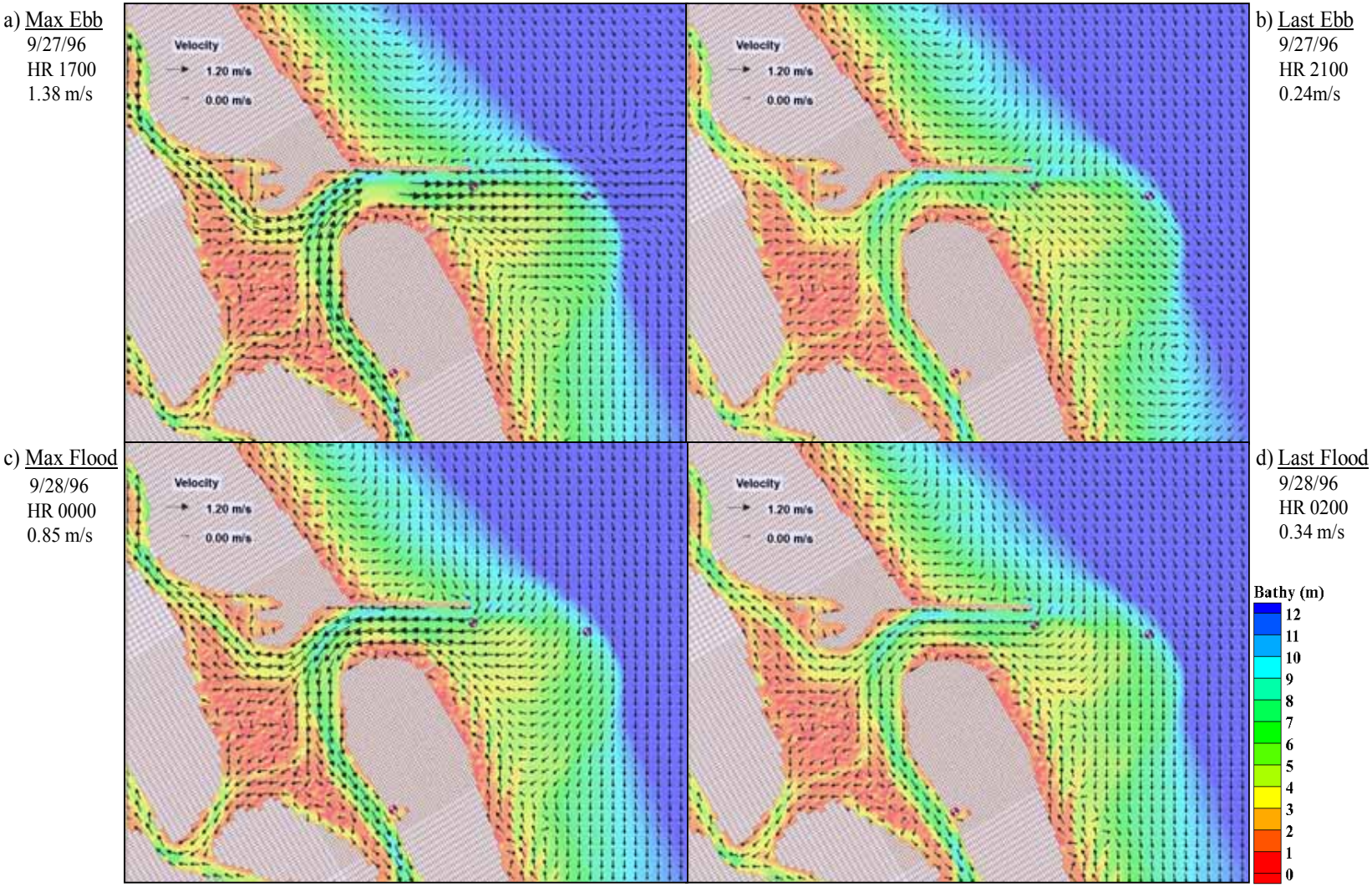

Figure 27. Morphology and flow velocities for Present Design during spring tide of 9/27/96. Maximum value from cell 25844 in channel.

5.2.2 South Jetty Extensions without Bathymetric Change

This section on extending the south jetty includes no other design changes to the inlet, but covers the possibility of actually rebuilding the south jetty to be more parallel and more inside the southern entrance. Due to the extreme shoaling since stabilization of this inlet by the dual jetty (and weir) system, the growth of the southern spit has not only buried all but the remaining 130 m seaward stretch of the curved jetty, it actually produced a configuration whereby the south jetty is farther south of the actual entrance than was originally designed. Both designs for extension of the south jetty produce a configuration parallel to, and longitudinally aligned with, the north jetty, but the rebuilt structure essentially cuts off the inner south spit producing a slightly narrower inlet width. The results of the preliminary runs are presented below.

5.2.2A South Jetty Extension

The addition of ~300 m of rubble mound seaward of the present tip of the south jetty creates no significant change in the starting morphology (Figure 28) as compared to that of the Present Design (Figure 21). The final morphology (Figure 29) shows an increase in yellows (becoming more shallow) at the tip of the south jetty (i.e. the downdrift bypass bar) coupled with a reduction in reds (less shoaling) for the inner south spit. This indicates the south jetty extension is facilitating the natural bypassing of the sediment from the north to the south beaches and is disrupting the sands return around the south jetty tip back into the inlet, as in the present design scenario.

The net morphologic change plot (Figure 30) supports the bypassing scenario in that the South Spit shows little deposition (red) gaining only +6448 m^3, or 1.3% sand (Table 5) as compared to the +13% for the Present Design. Although volume losses occurred for the North Beach (-1.8%) and Ebb Complex (-0.7%), the gains in volume for the South Jetty (+2.9%), the South Beaches (+0.6%) and the Outer Bypass (+0.7%) suggest the natural bypassing to the downdrift beach is functioning properly. Volume change for the Ebb Complex sub-domain is now susceptible to localized intense scour at the tip of the new south jetty ($\Delta z > -3.0$ m). The significant streak of red seaward of the north tip ($\Delta z \sim +3$ m) further supports the notion of the enhancement to natural bypassing with the South Jetty Extension. The expected scouring at the North Tip produces a volume loss of -39%. As in the Present Design, there is deposition in the Basin Channel (+31,686 m^3, 5.5%) and erosion in the Channel~4.6m (-51,927 m^3, -4.4%), though both are of greater magnitude in this design. With the South Jetty Extension, the Channel>7m is now in deposition (+3297 m^3, 1.2%) and the Flood Shoal loses less volume (-0.9%). All other masks show little difference to the Present Design.

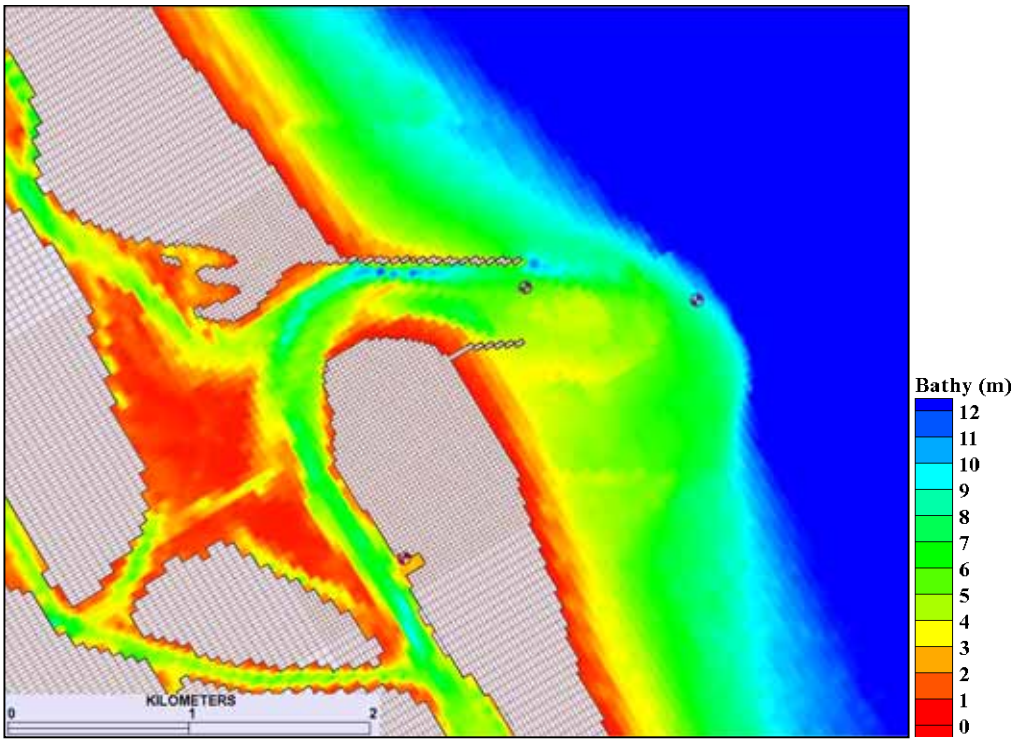

Figure 28. Morphology at 0 hr for South Jetty Extension.

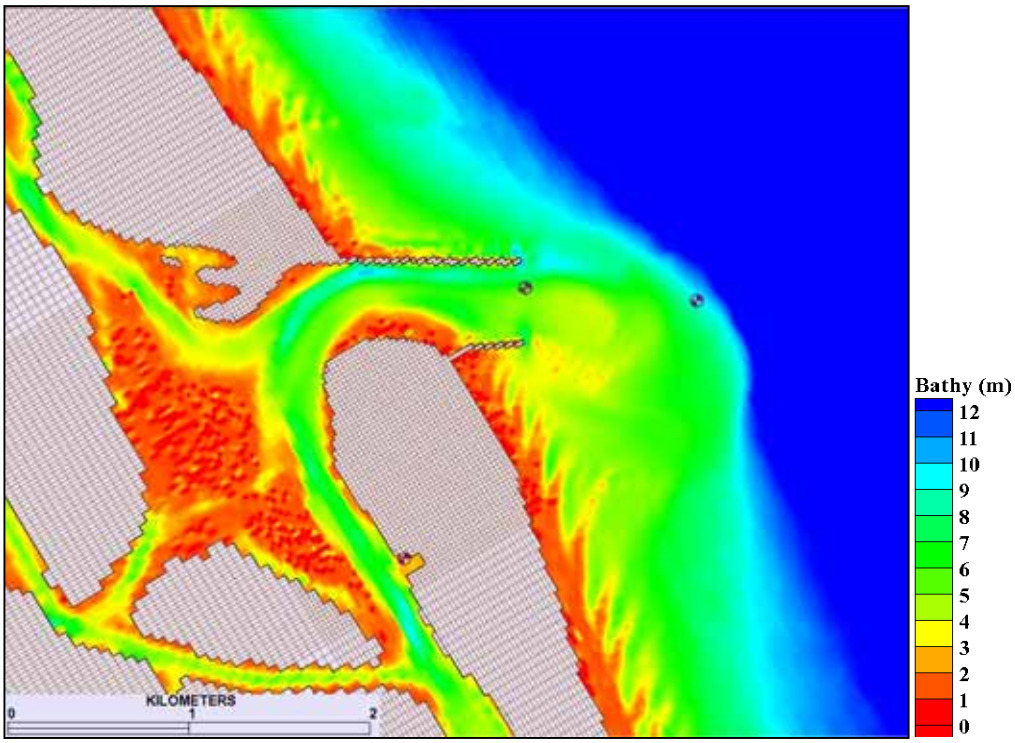

Figure 29. Morphology at 2197 hr (3 months) for South Jetty Extension.

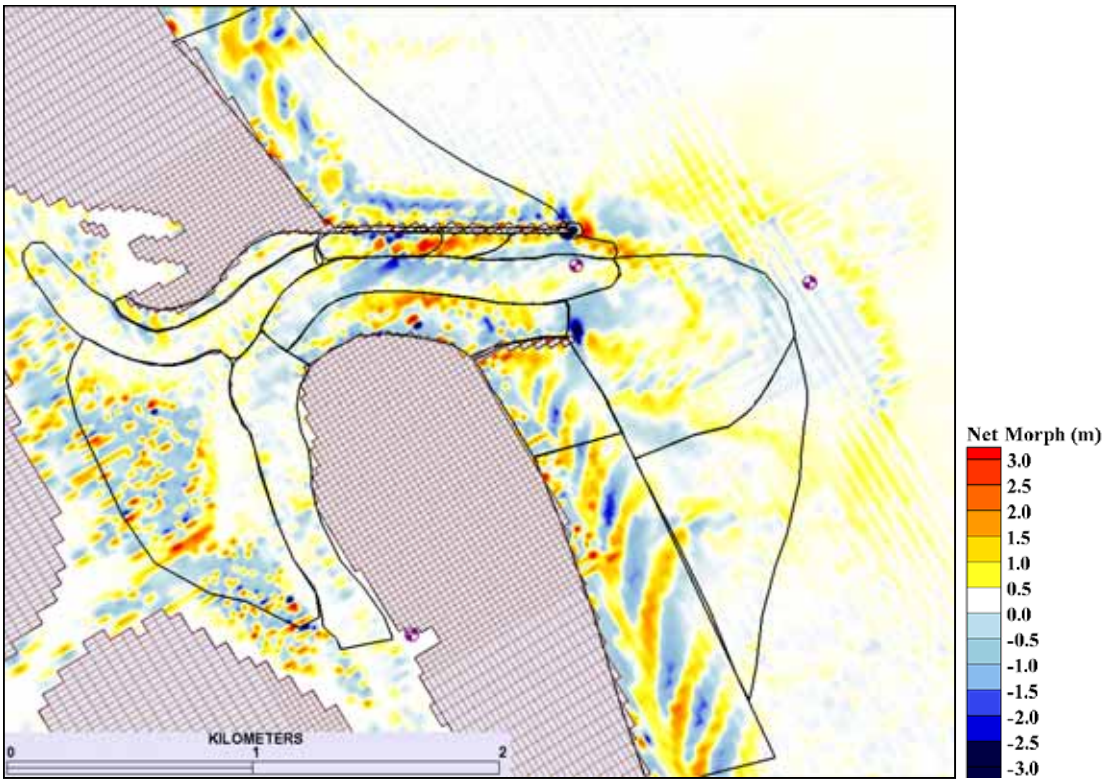

Figure 30. Net 3-month change in morphology for South Jetty Extension.

Table 5. Volume Change (3 months) for South Jetty Extension: Normalized (%) and Net (Δvol).

Polygon Mask	%	Δvol (m^3)
Ebb complex	-0.67	-15670
South spit	1.28	6448
Channel ~4.6m	-4.42	-51927
Channel >7m	1.15	3297
Basin channel	5.54	31686
North channel	0.41	3969
South Jetty	2.94	10873
South channel	-0.68	-9078
South beach	0.59	10272
Outer bypass	0.68	15703
North tip	-38.77	-8461
North spit	3.69	4804
North beach	-1.75	-36225
Hard bottom	2.46	8770
Flood shoal	-0.90	-7800

Maximum predicted flow velocities (Figure 31 and Figure 32) during the last neap tide of the 3-month run (September 20, 1996) are of greater magnitude than the Present Design, although they follow the same pattern, with ebb (1.04 m/s) greater than flood (0.73 m/s). During ebb (a and b in the figures), the South Jetty Extension allows for a wider ebb jet and a greater majority of the cross-sectional flow moving east over the ebb shoal with only a slight southeast component well outside the inlet entrance. Although at maximum ebb, the cyclonic eddy is, again, generated off the north edge of the ebb flow, no well-defined eddies are present in the slack water phase of the ebb. During flood (c and d in the figures), the South Jetty Extension also provides for a more westward directed flow through the entrance of the inlet, with slower velocities for the flow approaching northward from the south beaches during maximum flood (Figure 31c) as the current moves offshore before joining the main flow into the southern portion of the inlet. The separation of flow seaward of the outer ebb shoal now has a northeasterly component to it. During the last hour of flood, the combination of extended jetty and adjusted morphology presents a distinct downdrift bypassing pathway (Figure 32d) so flow passing into the southern half of the inlet keeps velocities sufficient to actually move across the south spit beaches and perhaps contribute to the reduction in shoaling in this area.

The increased flow velocities predicted during the final spring tide (September 27, 1996) for the South Jetty Extension design (Figure 33 and Figure 34) reach 1.48 m/s for maximum ebb and 1.01 m/s for maximum flood. The bi-directional flow during the last hour of ebb is evident, although it appears to be a product of rotation of exiting flow trapped by water moving northward in longshore currents coming around the south

jetty, and is of lower magnitude. The flood flow that previously directly entered into the inlet from the south is now directed eastward along the south jetty contributing to the development of the downdrift bypass bar instead of the south spit (Figure 34d) and, upon joining the flow into the inlet, creates a more even distribution of the flood flow across the entrance that no longer has a northwest component.

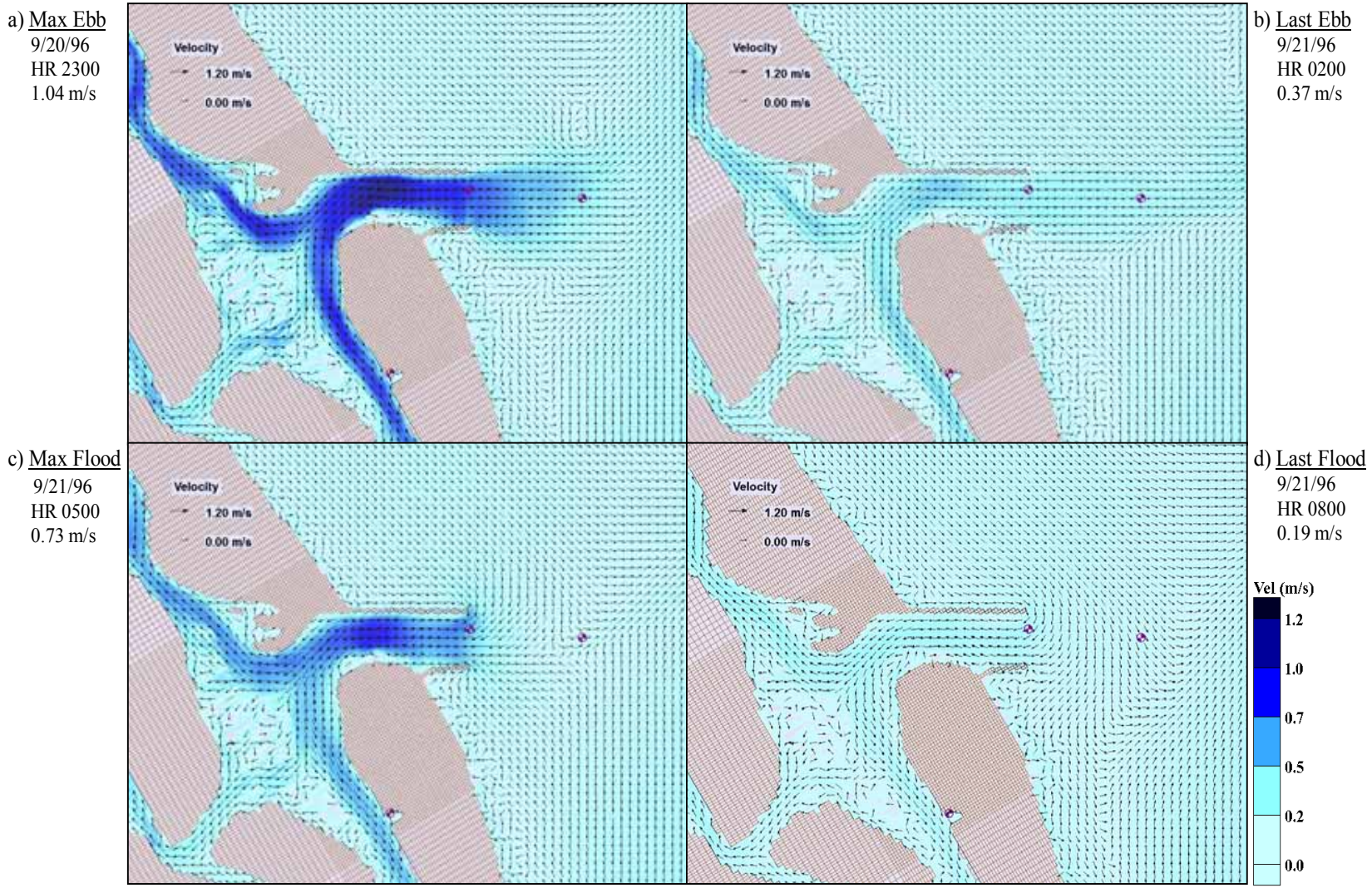

Figure 31. Flow velocities for South Jetty Extension during neap tide of 9/20/96. Maximum value from cell 26660 in channel.

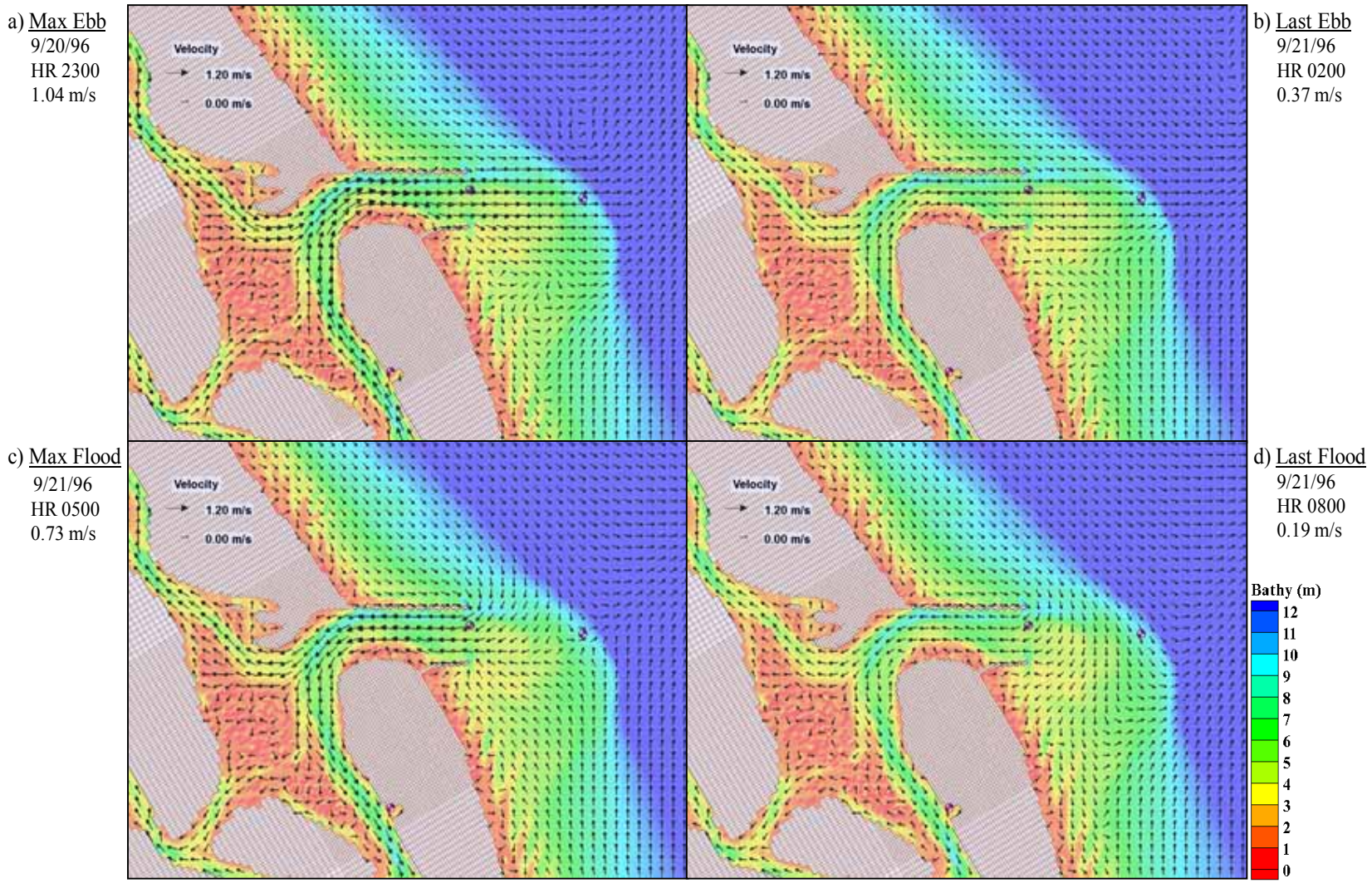

Figure 32. Morphology and flow velocities for South Jetty Extension during neap tide of 9/20/96. Maximum value from cell 26660 in channel.

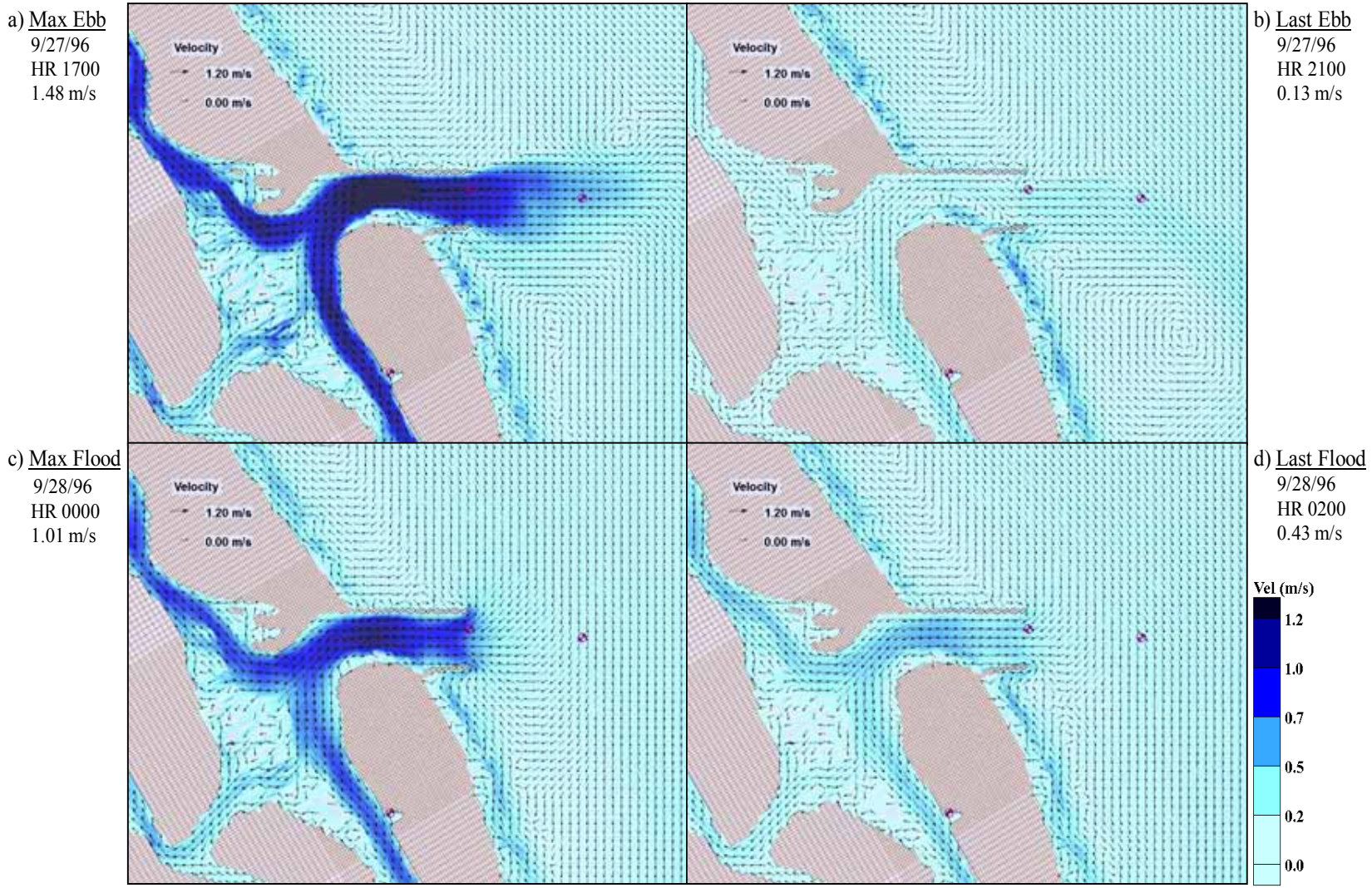

Figure 33. Flow velocities for South Jetty Extension during spring tide of 9/27/96. Maximum value from cell 26660 in channel.

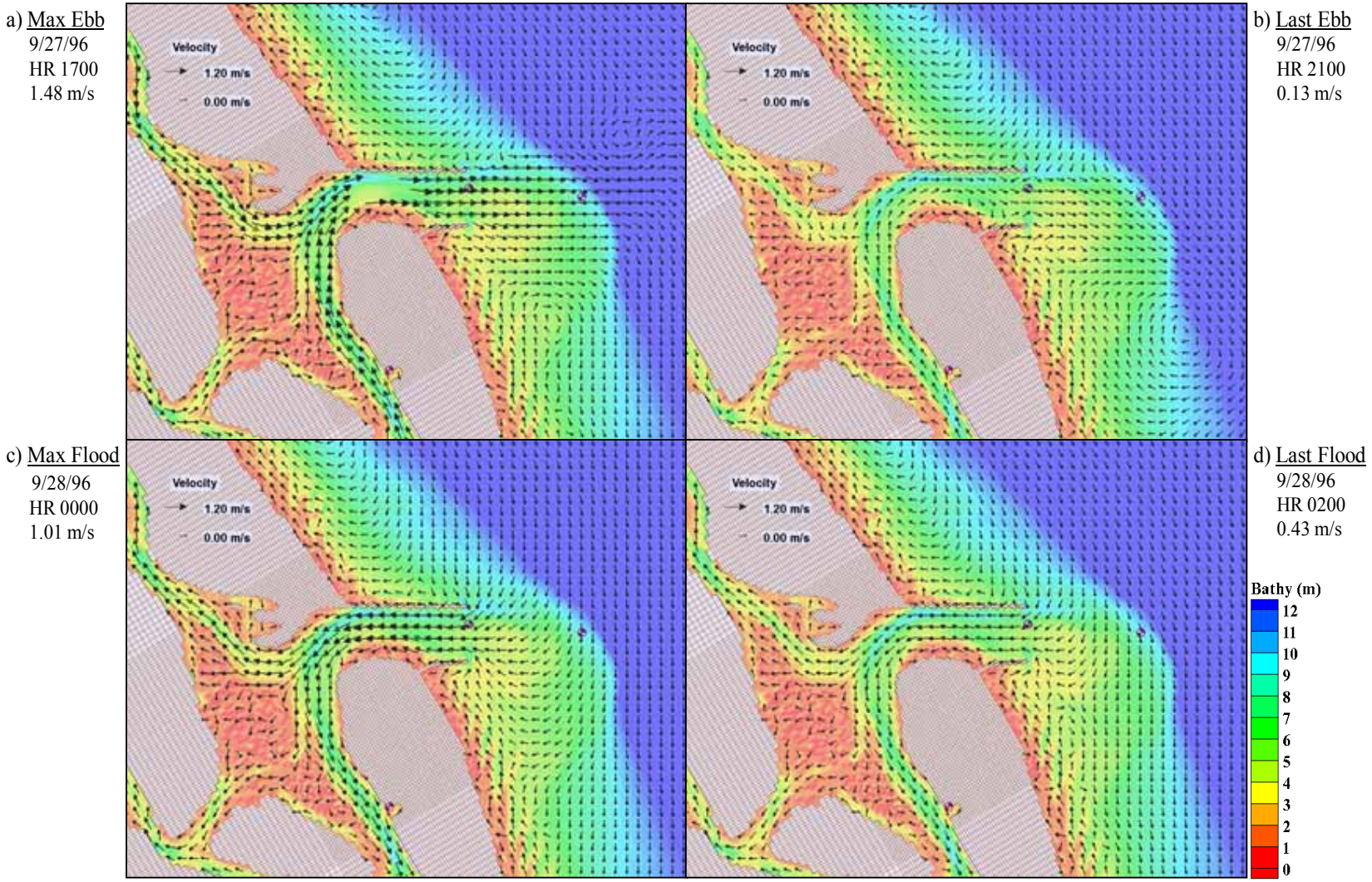

Figure 34. Morphology and flow velocities for South Jetty Extension during spring tide of 9/27/96. Maximum value from cell 26660 in channel.

5.2.2B South Jetty Rebuild Extension

The rebuilding of the south jetty is a very hypothetical design since the cost to create the structure in its new location is much more than simply adding on to the present length. Thus, this cost-prohibitive design will only be briefly discussed and all subsequent designs indicated in Table 3 utilizing this method for extending the south jetty are not included in the analysis. As evidenced in the final morphology (Figure 35), the design did consider reducing the cost of rebuilding by modeling the new configuration without removing the 130 m jetty remnant allowing it to be kept tucked in the shadow of the newly extended and more parallel rubble mound design.

The 3-month morphology for the South Jetty Rebuild is not completely unlike the South Jetty Extension except for the unique shape of the south spit, that has moved into the centerline of the inlet (+2.3% volume gain), and the reduced depths ($z \sim 6$ m) of the scour hole at tip of the north jetty (only -11% volume loss). With the sub-domains having roughly the same percent volume change (Table 6) as the basic extension, the key difference beyond those mentioned is the minimal accretion in the South Jetty mask of +0.6%. Although this volume change is an improvement over the Present Design, which shows losses in this domain (-3.3%), it is not as large a gain as for the South Jetty Extension (+2.9%).

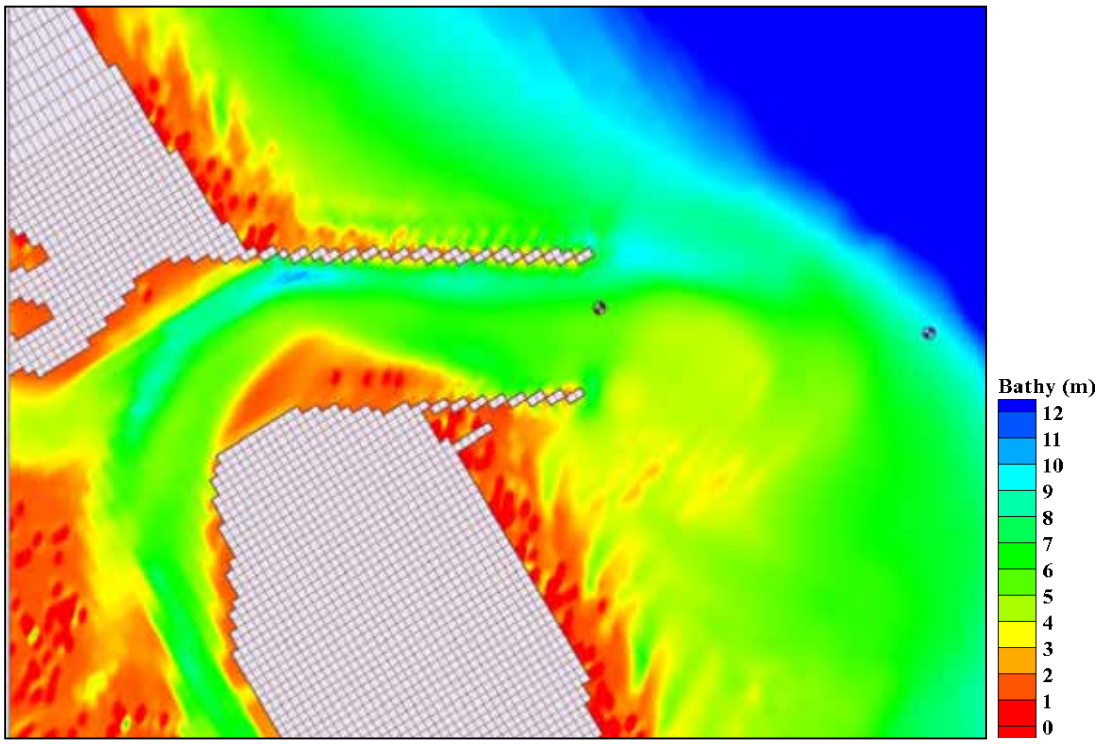

Figure 35. Morphology at 2197 hr (3 months) for South Jetty Rebuild.

Table 6. Volume Change (3 months) for South Jetty Rebuild: Normalized (%) and Net (Δvol).

Polygon Mask	%	Δvol (m^3)
Ebb complex	0.04	938
South spit	2.34	11028
Channel ~4.6m	-5.11	-60063
Channel >7m	2.52	7218
Basin channel	6.16	35202
North channel	0.36	3436
South Jetty	0.62	2408
South channel	-0.33	-4370
South beach	1.31	22953
Outer bypass	0.37	8603
North tip	-11.09	-2421
North spit	3.20	4177
North beach	-2.54	-52670
Hard bottom	2.90	10319
Flood shoal	-0.13	-1100

5.2.3 South Jetty Extension with Weir, HB, and Channel

The design of the weir model was discussed in Section 4.2.1. Although several versions of the weir being reopened were modeled (Table 3), only the best candidate is presented. This design includes not only the addition of 300 m of rubble-mound to extend the south jetty to be equal and parallel to the north jetty (SJ), but also includes removing 475 m of rubble-mound from the landward end of the north jetty for the weir (W) and placing it as hard bottom in the deep channel to the south of this jetty (HB). Additionally, the remaining areas of the deep, shifted channel to the east, along the north jetty, was reduced, as needed, to a depth of 7.6 m by the sediment obtained from re-dredging the original navigation channel through the centerline of the inlet (C).

A different starting morphology is now presented (Figure 36) with the yellow-green line ($z \sim 5$ m) indicating the "new" location of the channel, replacing the previously shallow depth that had extended into the centerline from the south spit. The hard bottom is indicated by the gold triangles just south of the weir opening, and the weir follows the very shallow depth of the adjacent seafloor to the north ($z = 0$ to 3 m). After the 3-month run (Figure 37), the weir has allowed a deeper passage from the north beach, the south spit has become deeper along most of the northern extent, and the downdrift bypass bar near the end of the south jetty tip is impounding sediment as it bridges the distance from the ebb shoal to the attachment bar behind the south jetty. The scour hole at the tip of the north jetty has deepened ($z > 12$ m) during the 3-month run. The Rockhouse Creek passage through the flood shoal will prove to be more hazardous given that depths are now only 1 to 2 m along most of that channel.

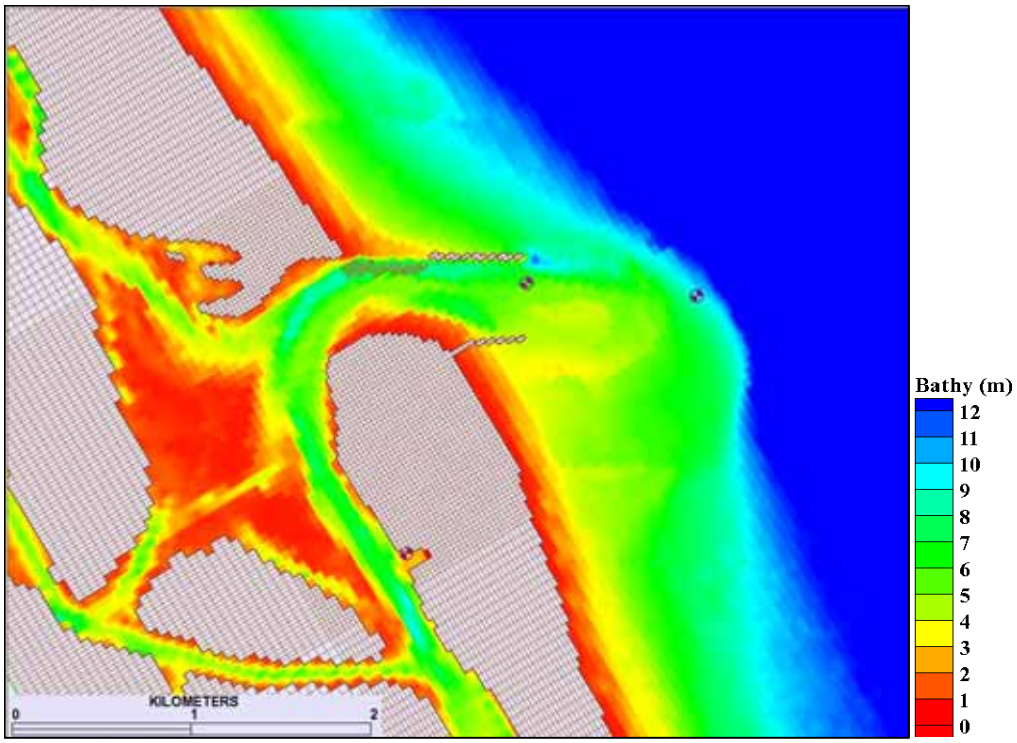

Figure 36. Morphology at 0 hr for South Jetty Extension with W, HB, and C.

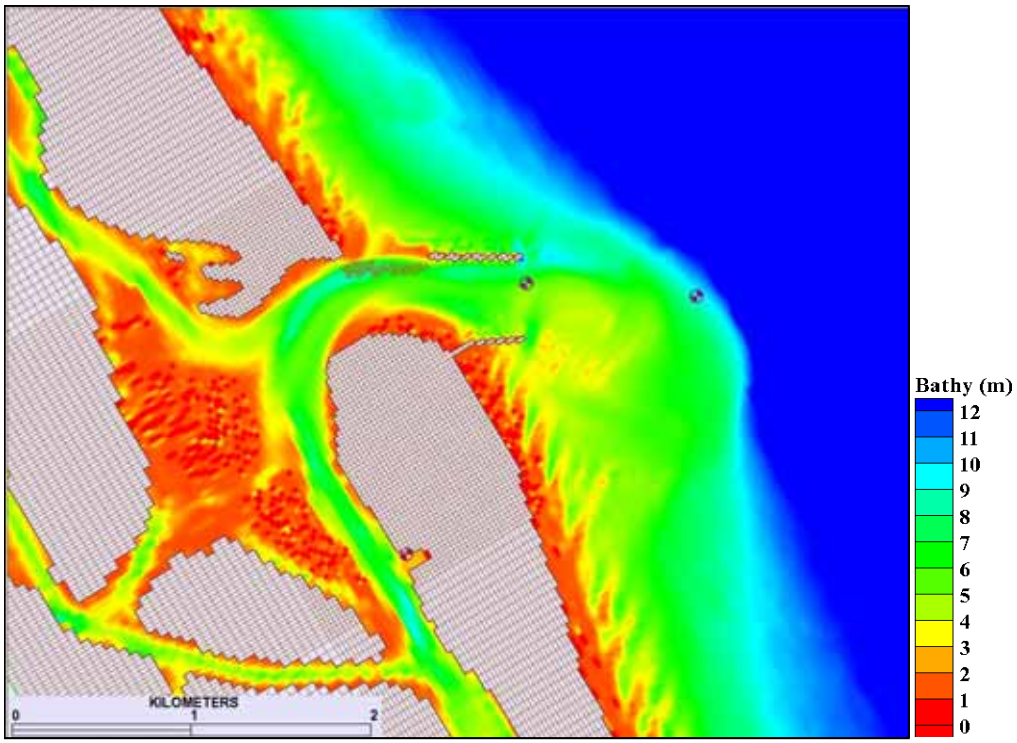

Figure 37. Morphology at 2197 hr (3 months) for South Jetty Extension with W, HB, and C.

The net change in morphology (Figure 38) shows less deposition (red) than the previous designs for the Basin Channel and Channel >7m (Δz = 2 to 2.5 m), although the volume change (Table 7) indicates these areas had significant increases (+9.9% and +1.9%, respectively). Examination of the Hard Bottom subset, which has only a small section of notable net change, shows it, specifically, has impounded +8.3% sand, indicating the basin is working as expected. The discrepancy between net morphology (Δz) and volume change (Δvol or %), is due to the cumulative nature of the volume change calculation within a mask. Whereas the net change plots show discrete changes in depth, the net volume changes combine the losses and gains within a set area for a cumulative value. The net change plots for both the Present Design (Figure 23) and the South Jetty Extension (Figure 30) show intense scouring in the Basin Channel, specifically the Hard Bottom subset, which would be balanced by the intense deposition of these areas during volume change calculations. This is why it is necessary to perform both types of analyses and cross-reference their differences during comparisons. The net change plot shows scouring at the tip of the south jetty, but of less magnitude than for the South Jetty Extension. This erosional area has actually spread about 500 m northeast/southwest along the downdrift bypass pathway. The loss of sediment in this area does not interfere with the South Jetty accumulating +22,589 m^3, or 6.1% volume, but certainly does impact the Ebb Complex total (-0.6%), which is almost identical to the South Jetty Extension volume loss, but morphologically different. The Channel~4.6m does not scour as well as other designs (-2.7% volume loss and light blue, Δz = -0.5m) but the South Spit shoals less (Δz ~ +2 m) and actually shows a small volume loss (-0.02%). The South Beach gains volume (+0.94%).

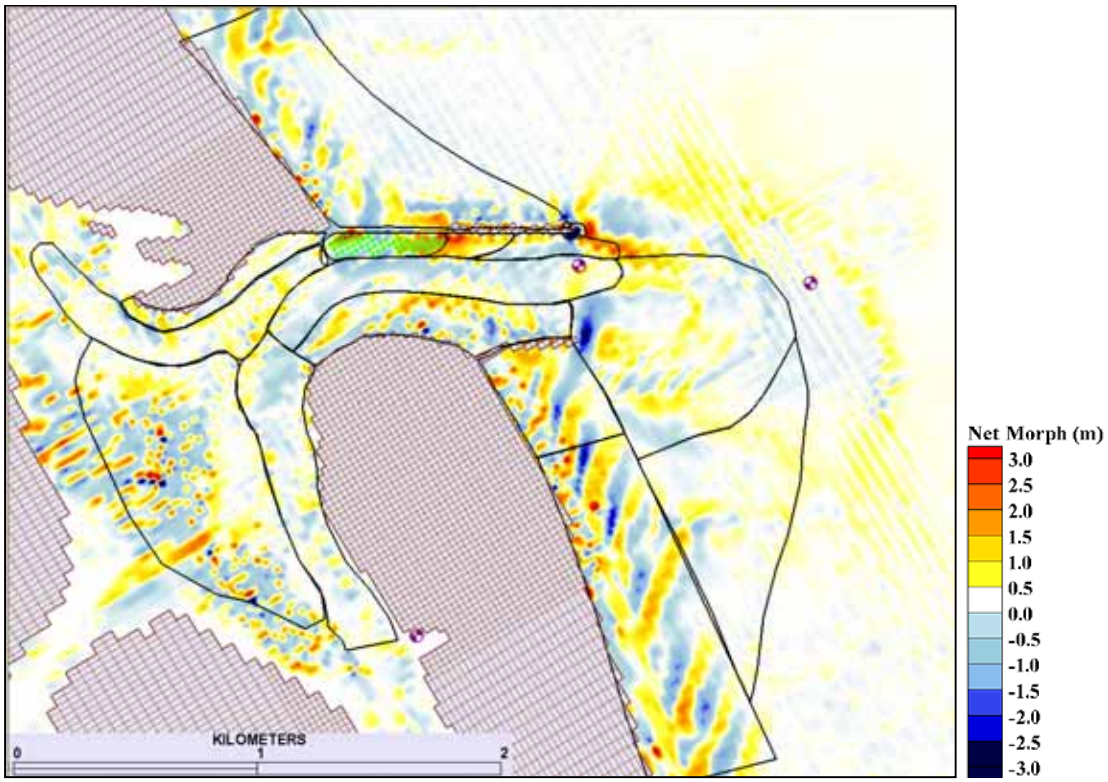

Figure 38. Net 3-month change in morphology for South Jetty Extension with W, HB and C.

Table 7. Volume Change (3 months) for South Jetty Extension with W, HB and C: Normalized (%) and Net (Δvol).

Polygon Mask	%	Δvol (m^3)
Ebb complex	-0.61	-14350
South spit	-0.02	-116
Channel ~4.6m	-2.66	-32512
Channel >7m	1.92	5488
Basin channel	9.85	51741
North channel	0.84	8102
South Jetty	6.10	22589
South channel	-0.98	-13145
South beach	0.94	16377
Outer bypass	0.56	12981
North tip	-41.63	-9083
North spit	4.31	5620
North beach	-1.53	-31797
Hard bottom	8.33	27658
Flood shoal	-0.35	-2990

Flow velocities (Figure 39 and Figure 40) during maximum ebb of the last neap tide (September 20, 1996) have the lowest magnitude (0.88 m/s) of all the designs for any cells in the inlet. However, in the weir design, the ebb jet splits at the inlet throat with the strongest flow leaving the inlet through the weir opening. Here, cells in the region just north of the weir reach as high as 0.96 m/s at maximum ebb. Only a slight curvature exists north of the ebb shoal from the current shear off the eastern flowing ebb jet, where previous designs resulted in a cyclonic eddy forming. Instead, an eddy forms just north of the north jetty 1km offshore. Maximum ebb velocities over the ebb shoal barely reach 0.2 m/s. For maximum flood, the flow reaches 0.68 m/s in the main channel and 0.72 m/s outside the weir. Except for reduced magnitudes at the entrance of the inlet and flood flow concentrated through the weir, no other differences stand out during maximum flood. During last ebb and flood, the south jetty extension blocks the flow from entering the south spit area as observed in the South Jetty Extension design.

Flow velocities (Figure 41 and Figure 42) during maximum ebb for the last spring tide (September 27, 1996) also have the lowest magnitude (1.24 m/s) of all the designs for any cells within the inlet; however, the maximum ebb flow just north of the weir reaches 1.36 m/s. Current shear from the ebb jet passing over the weir produces both positive and negative vortices. The easterly arm of the ebb jet reaches the ebb shoal with velocities of 0.4 m/s. Despite southern currents offshore, morphology downdrift of the inlet forms a series of eddies during the last hour of ebb (Figure 42b). This process rotates the flow clockwise back to the north, where the current meets the ebb flow again and produces more of the same eddies. Maximum flood reaches 0.91 m/s in the channel and 0.96 m/s just north of the weir.

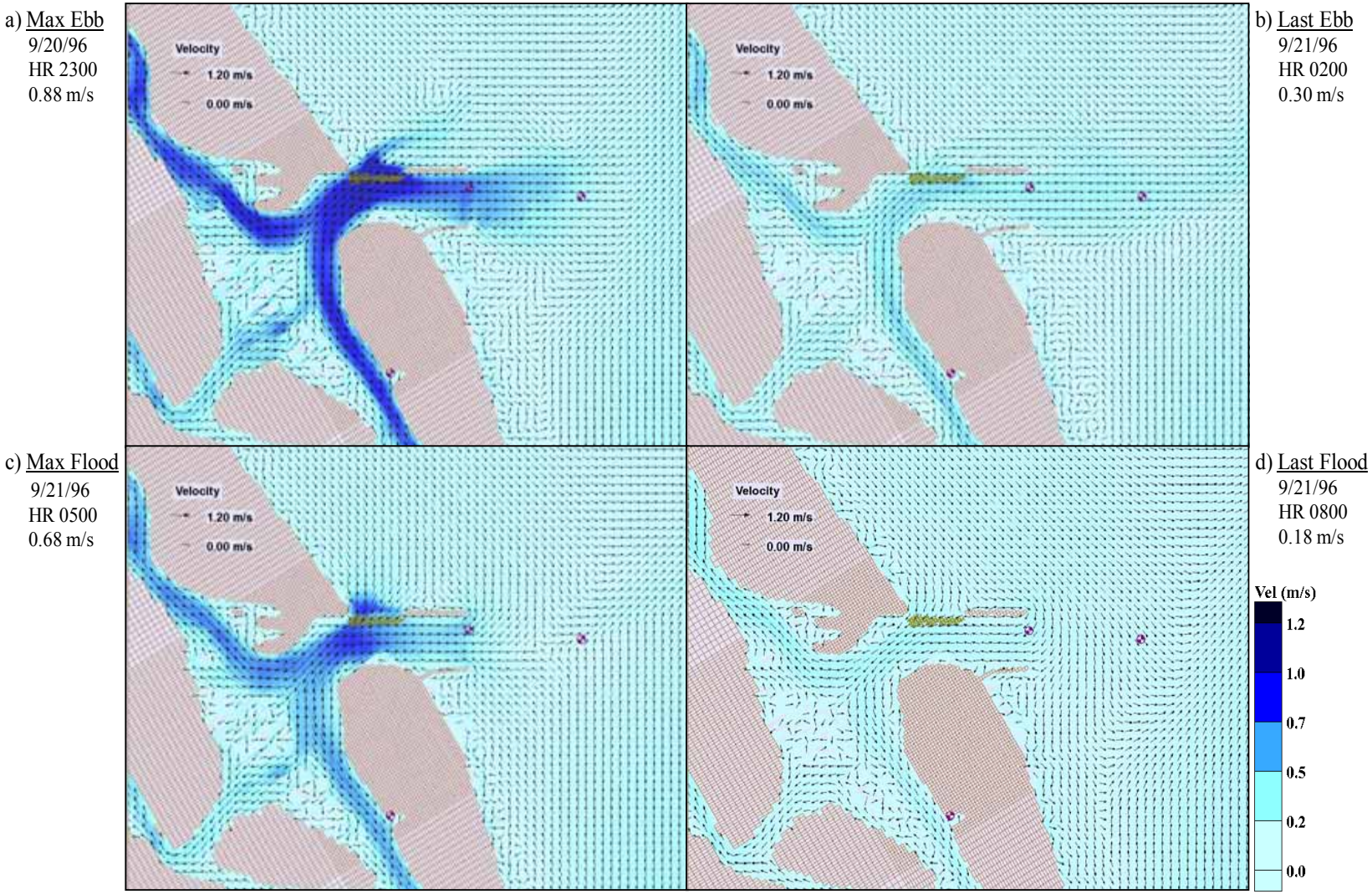

Figure 39. Flow velocities for South Jetty Extension with W, HB, and C during neap tide of 9/20/96. Maximum value from cell 26859 in channel.

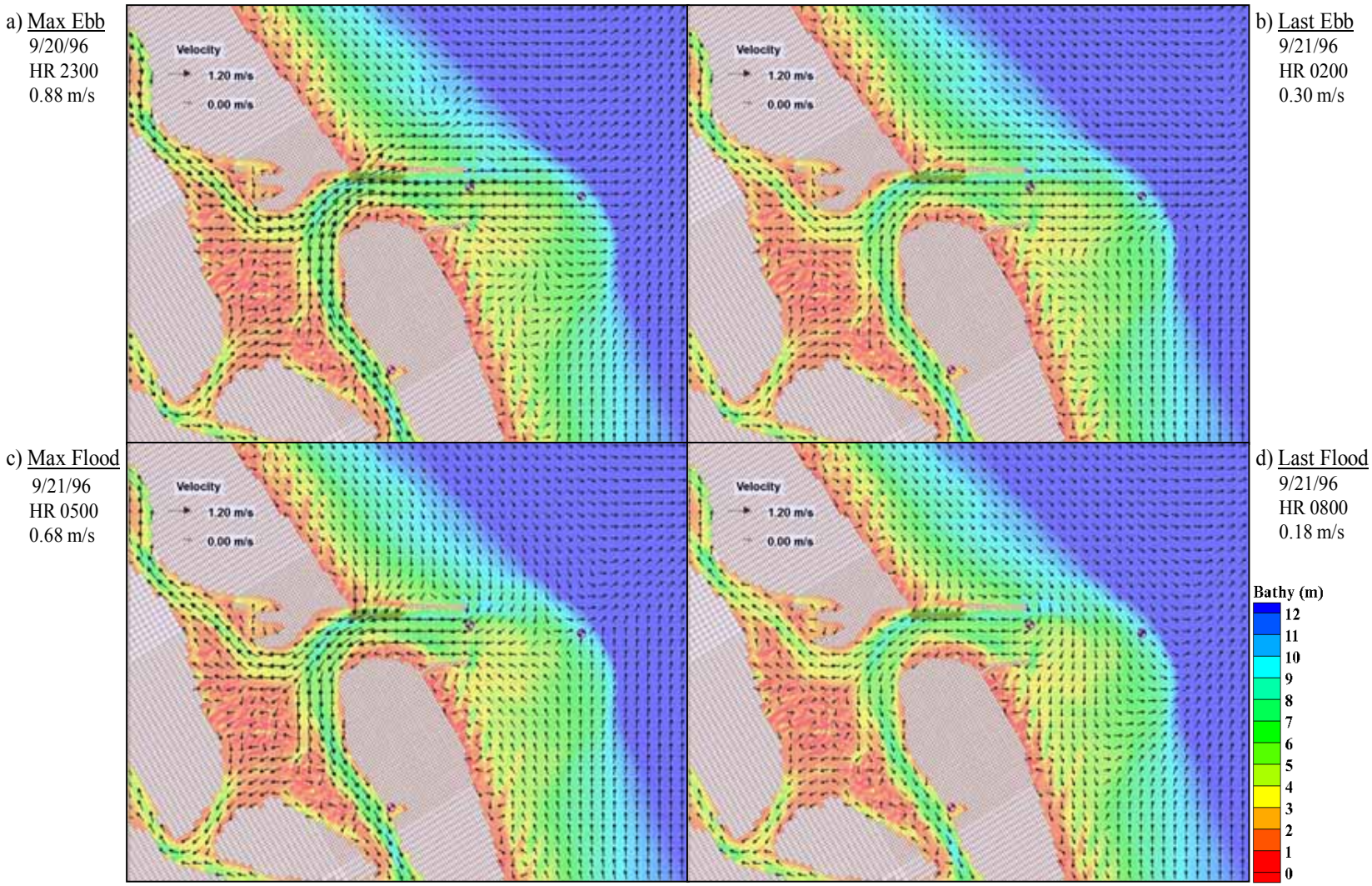

Figure 40. Morphology and flow velocities for South Jetty Extension with W, HB, and C during neap tide of 9/20/96. Maximum value from cell 26859 in channel.

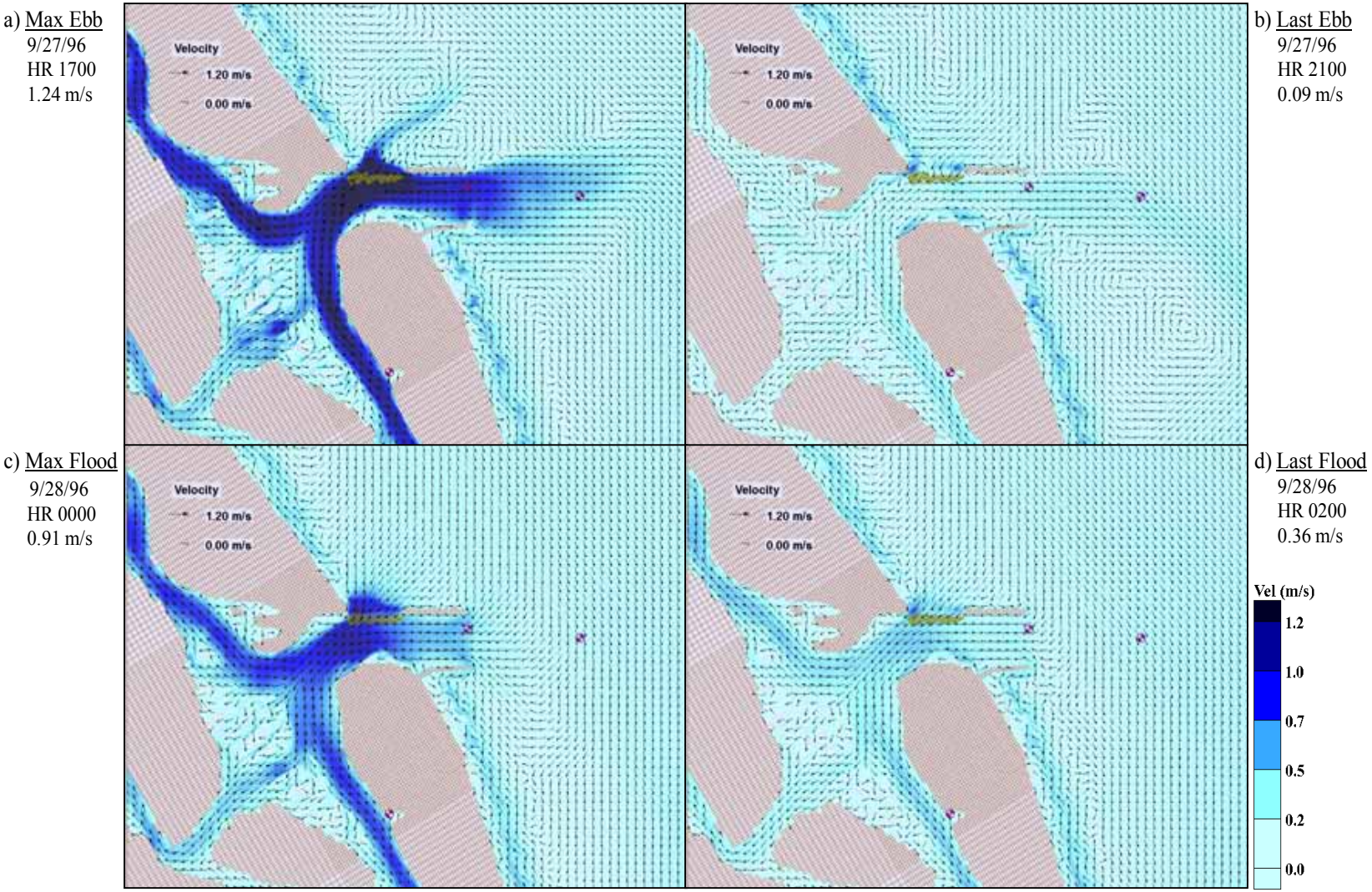

Figure 41. Flow velocities for South Jetty Extension with W, HB, and C during spring tide of 9/27/96. Maximum value from cell 26859 in channel.

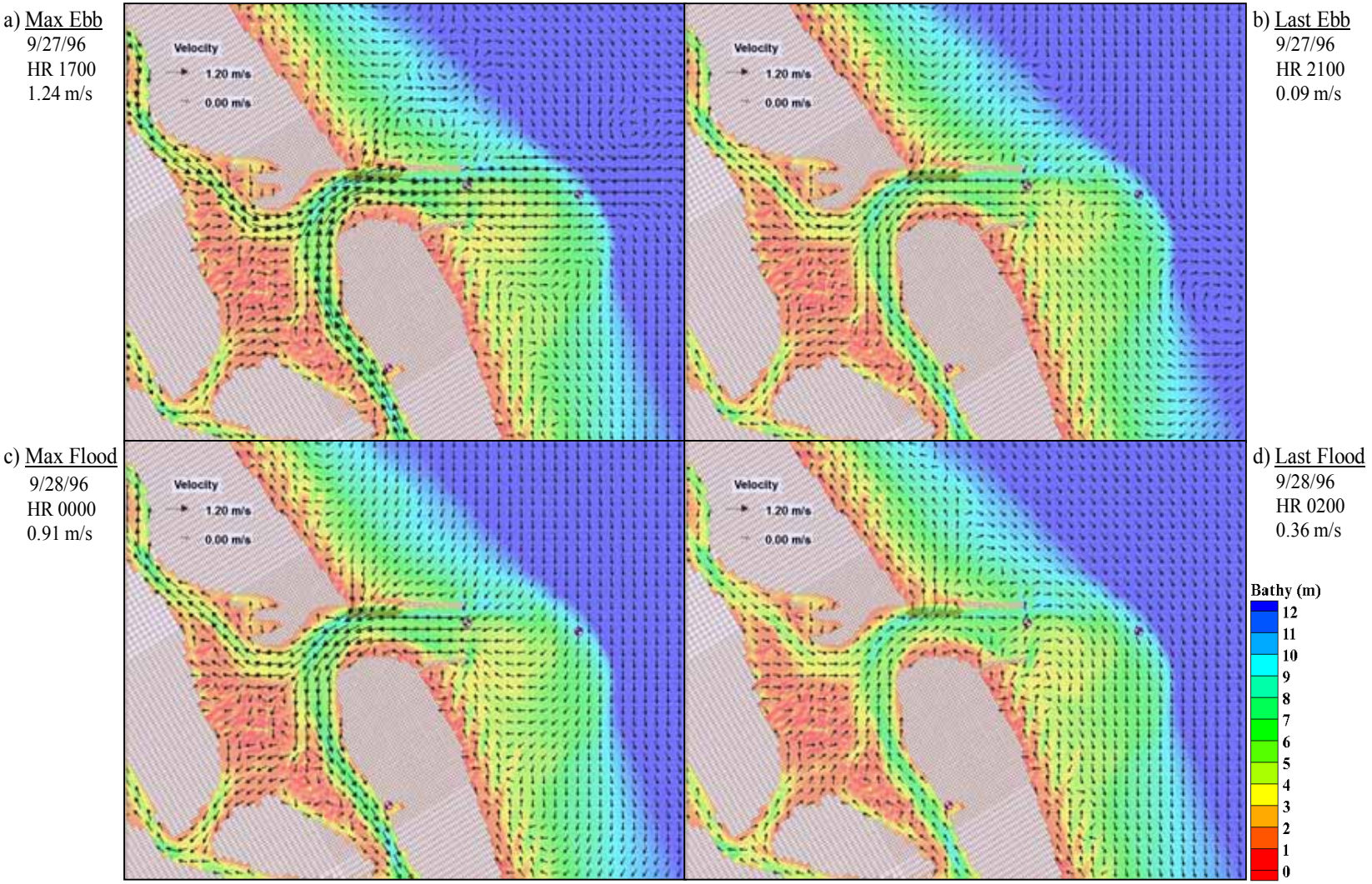

Figure 42. Morphology and flow velocities for South Jetty Extension with W, HB, and C during spring tide of 9/27/96. Maximum value from cell 26859 in channel.

5.2.4 South Jetty Extension with Hard Bottom and Channel

The South Jetty Extension (SJ) with Hard Bottom (HB) and Channel (C) is the same as the Weir Design (W) discussed above without the weir and has identical starting morphology (Figure 43). The final morphology after 3 months (Figure 44) is almost identical to that for the South Jetty Extension, except for three key areas. The south spit beaches reveal more shoaling along the shoreline (red patches) with depths less than 1 m and possibly above the water line. The deep water channel along the north jetty has remained shallow (z ~ 7 m) due to the hard bottom rubble-mound; and the dredged channel has gotten deeper (z ~ 5 to 6 m) than the starting design.

The net change plot (Figure 45) echoes the similarities between these South Jetty Extension designs and highlights how the starting bathymetric changes have influenced the final morphology. The Basin Channel (+4.48% volume change) and South Spit (+2.2% volume change) are now showing net topographic changes (Δz) of at most +1.5 m. The deposition in the South Jetty (+3.65%) is now occurring further down the shoreface than right behind the south jetty as it was for the South Jetty Extension. Although the self-scouring of the original navigation channel (Channel~4.6m) produced essentially the same volume loss (-4.3%) and net topographic change (Δz ~ -1.5 m) as in the previous design, consideration should be made for the fact that the starting depth was already deeper in this South Jetty Extension with HB and Channel. One might reasonably argue that this change is more productive for maintaining the new design depths. The Flood Shoal shows a very definite pattern of intense erosion (Δz > -3 m) and accretion (Δz > +3 m) on its lobes with the cumulative volume change in favor of erosive processes (-1.4%).

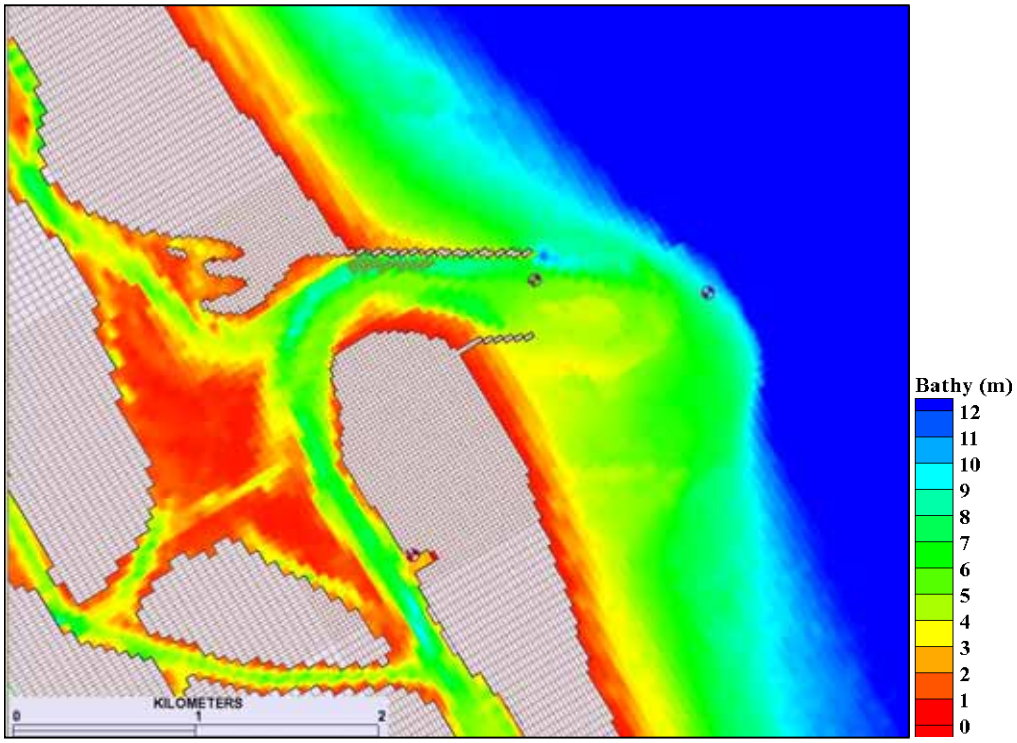

Figure 43. Morphology at 0 hr for South Jetty Extension with HB and C.

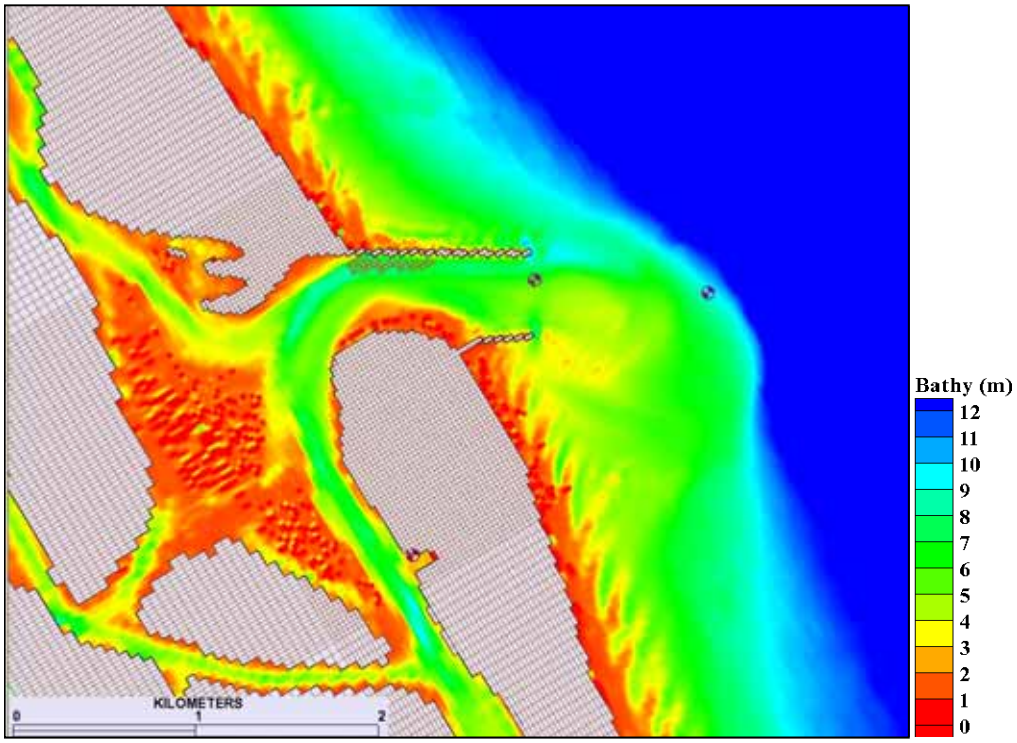

Figure 44. Morphology at 2197 hr (3 months) for South Jetty Extension with HB and C.

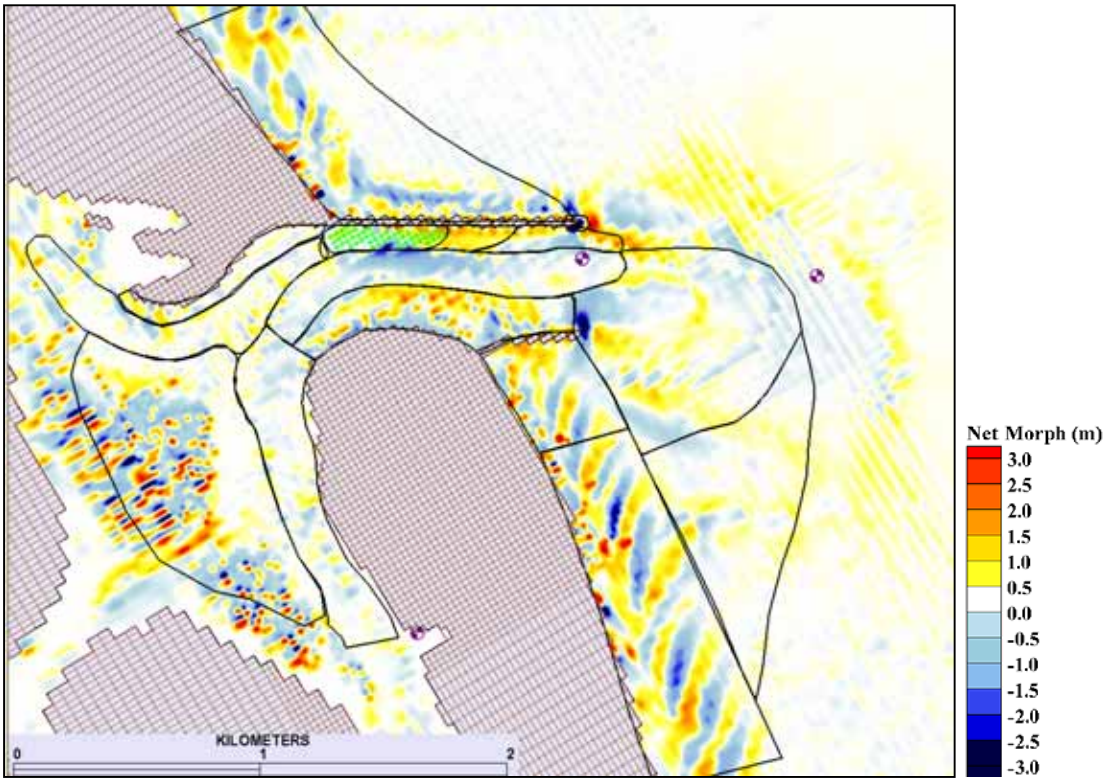

Figure 45. Net 3-month change in morphology for South Jetty Extension with HB and C.

Table 8. Volume Change (3 months) for South Jetty Extension with HB and C: Normalized (%) and Net (Δvol).

Polygon Mask	%	Δvol (m^3)
Ebb complex	-0.81	-19114
South spit	2.22	11162
Channel ~4.6m	-4.28	-52297
Channel >7m	2.12	6038
Basin channel	4.48	23562
North channel	0.49	4684
South Jetty	3.65	13518
South channel	-0.52	-6983
South beach	0.58	10204
Outer bypass	0.81	18575
North tip	-37.97	-8286
North spit	3.41	4440
North beach	-1.75	-36326
Hard bottom	1.89	6257
Flood shoal	-1.39	-12024

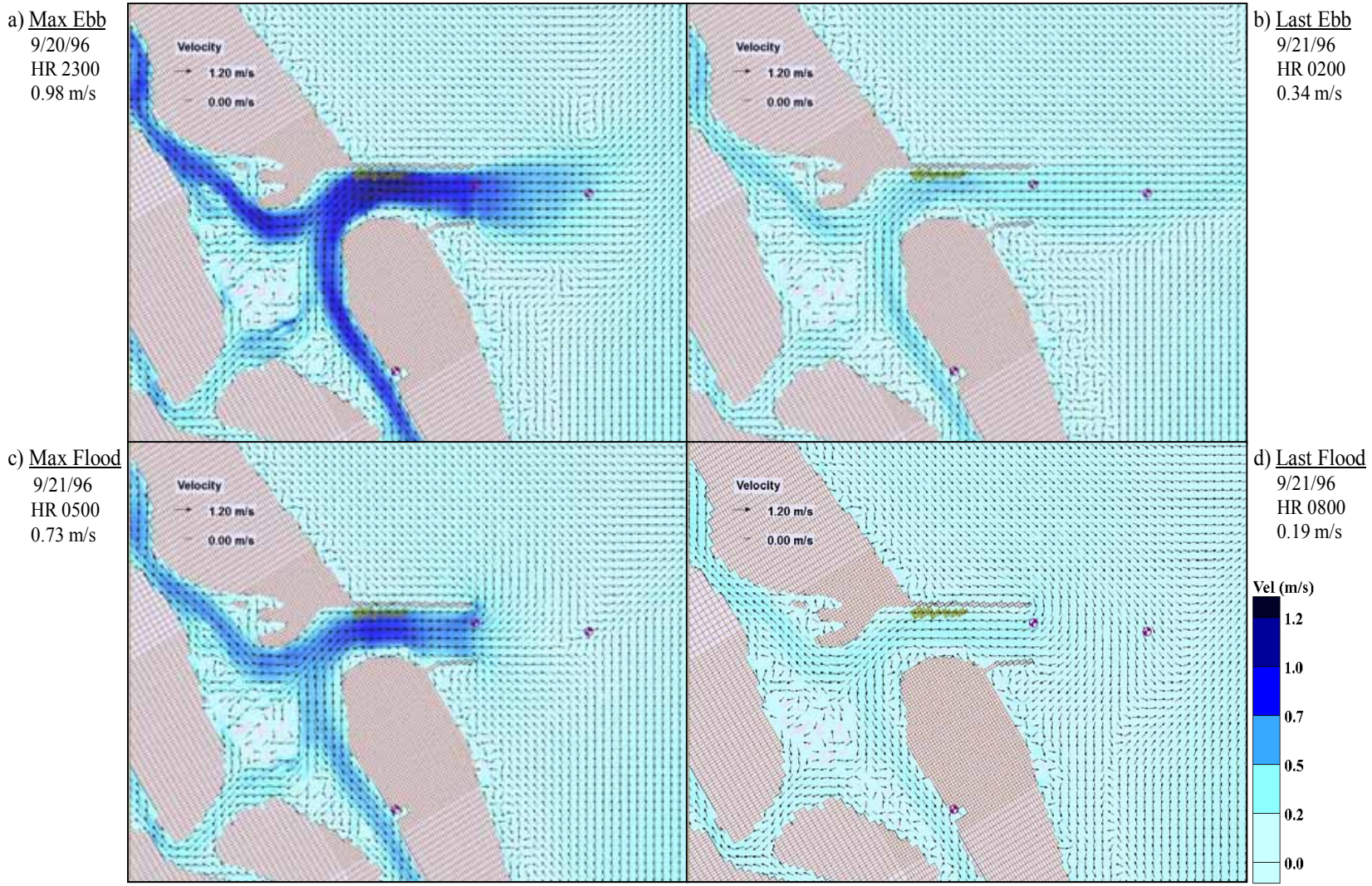

Figure 46. Flow velocities for South Jetty Extension with HB and C during neap tide of 9/20/96. Maximum value from cell 26450 in channel.

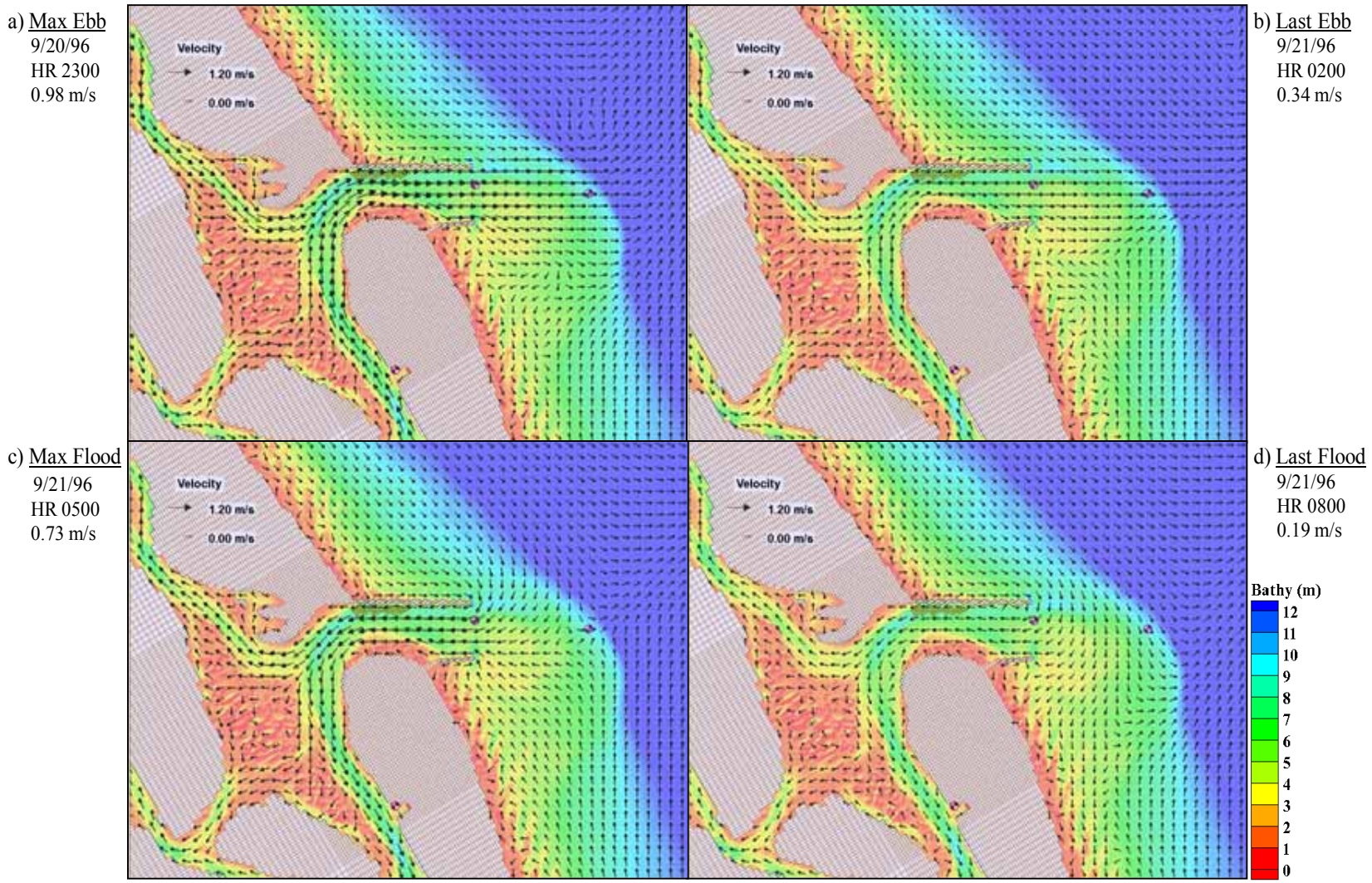

Figure 47. Morphology and flow velocities for South Jetty Extension with HB and C during neap tide of 9/20/96. Maximum value from cell 26450 in channel.

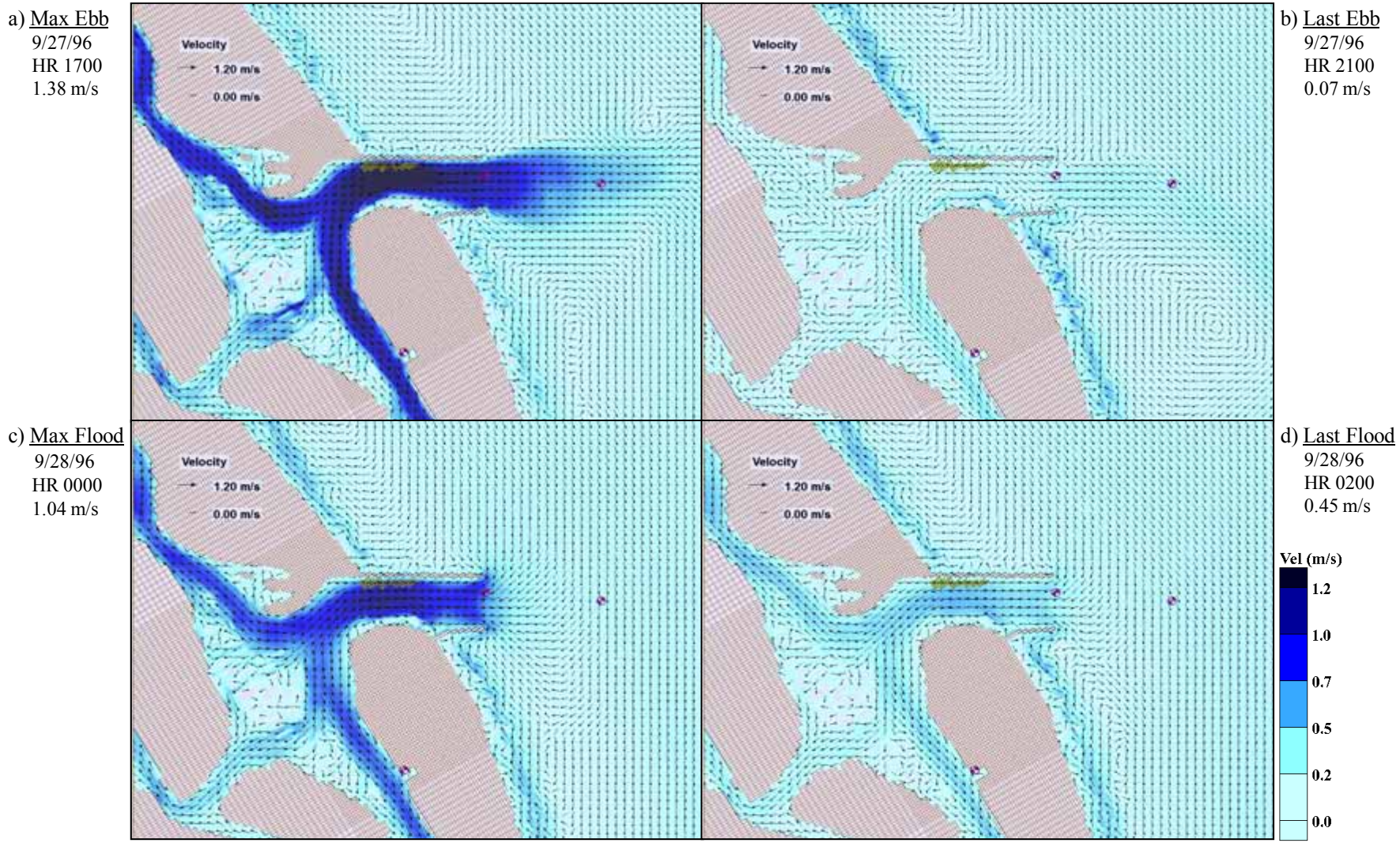

Figure 48. Flow velocities for South Jetty Extension with HB and C during spring tide of 9/27/96. Maximum value from cell 26450 in channel.

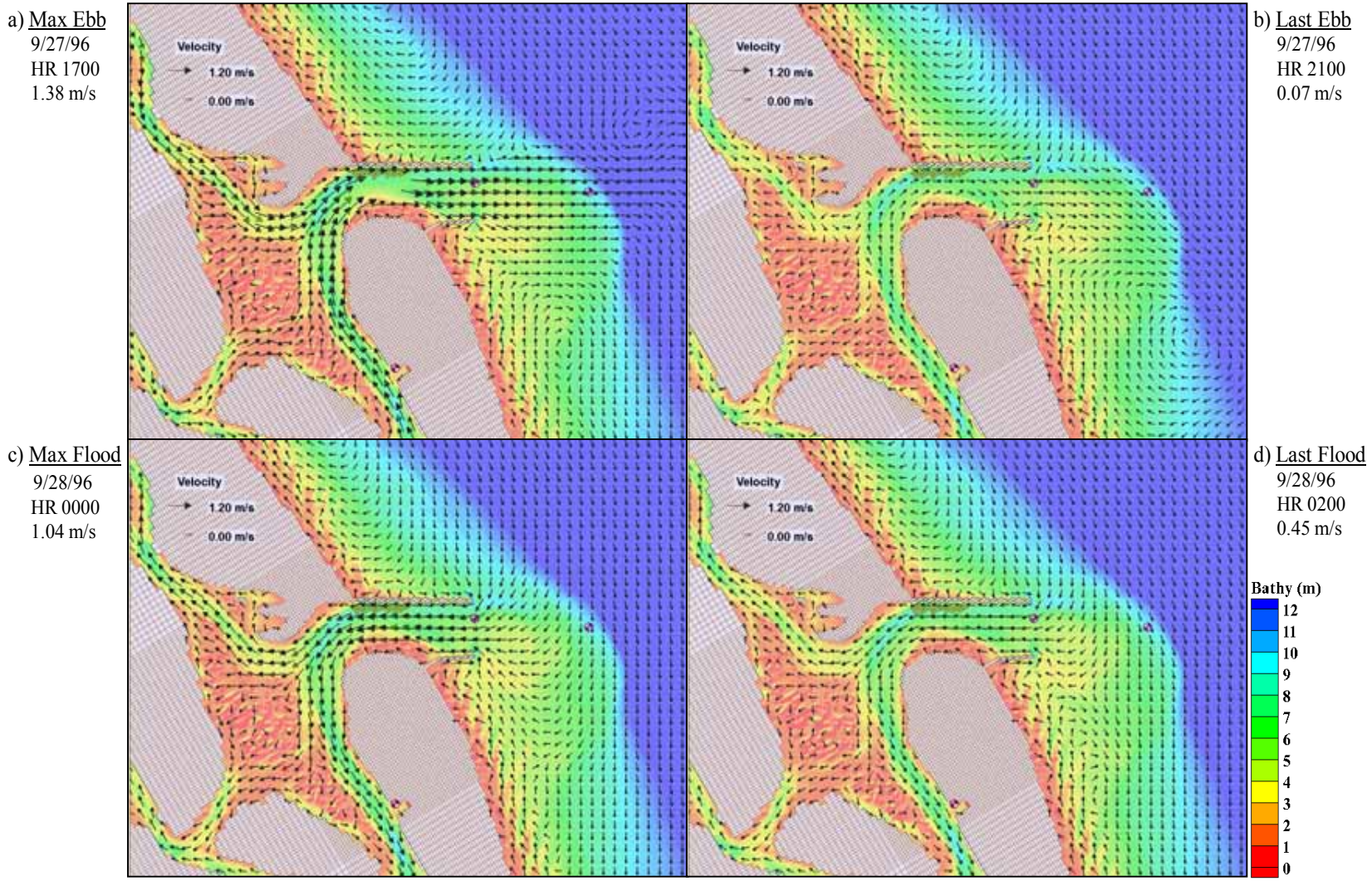

Figure 49. Morphology and flow velocities for South Jetty Extension with HB and C during spring tide of 9/27/96. Maximum value from cell 26450 in channel.

Maximum predicted flow velocities (Figure 46 and Figure 47) during the final neap tide (September 20, 1996) are 0.98 m/s for ebb and 0.73 m/s for flood. Not only are these magnitudes virtually identical to the South Jetty Extension design without the starting bathymetry changes, the flow pattern is essentially the same as well. Maximum flow velocities (Figure 48 and Figure 49) for the last spring tide (September 27, 1996) are 1.38 m/s on ebb and 1.04 m/s on flood. As with the neap tide, these magnitudes and flow patterns at all stages of the tidal cycle mirror the South Jetty Extension, although the maximum ebb is a bit lower (down from 1.48 m/s) and slows down more before reaching the outer ebb shoal. The only other difference observed is in the longshore currents, which run in the same direction, but at reduced magnitudes (~ 0.3 m/s, here, vs. ~ 0.5 m/s, without the HB and Channel).

5.2.5 South Jetty Extension with Emergent Spur

The use of jetty spurs has been studied with both physical and numerical models (Seabergh et. al, 2008). Its use as a deflector of sediment, away from the channel, was worth investigating at Ponce de Leon Inlet. The majority of uses for the spur jetty have been on the updrift side of the inlet to divert the sediment towards the ebb shoal and facilitate bypassing to the downdrift beach. Both emergent (surface-piercing) and submergent (below water line) types have been studied with little difference in results (Seabergh et al., 2008). Although using a submerged spur may be less costly, it creates a navigation hazard for small boats and, if favored, should be marked appropriately.

The jetty spur on the downdrift side of an inlet, as designed here, acts as a breakwater for waves approaching from the southeast. It was attached at a 45^{o} angle with the south jetty tip to allow direct sediment that would enter the inlet from around the south jetty towards the ebb shoal during northward transport and flood conditions. Whether the transport pathway returns the bulk of the sediment back into the channel during maximum flood for Ponce de Leon Inlet is addressed in this analysis. Several bathymetric versions of the emergent spur were modeled and are presented here.

5.2.5A South Jetty Extension with Emergent Spur

Starting morphology (Figure 50) for the South Jetty Extension (SJ) with Emergent Spur (ES) is the same as the South Jetty Extension since no bathymetric changes were made. Final morphology (Figure 51) shows impoundment of sediment on the seaward side of the spur ($z = +1$ m) and the downdrift bypass bar ($z < 3.5$ m).

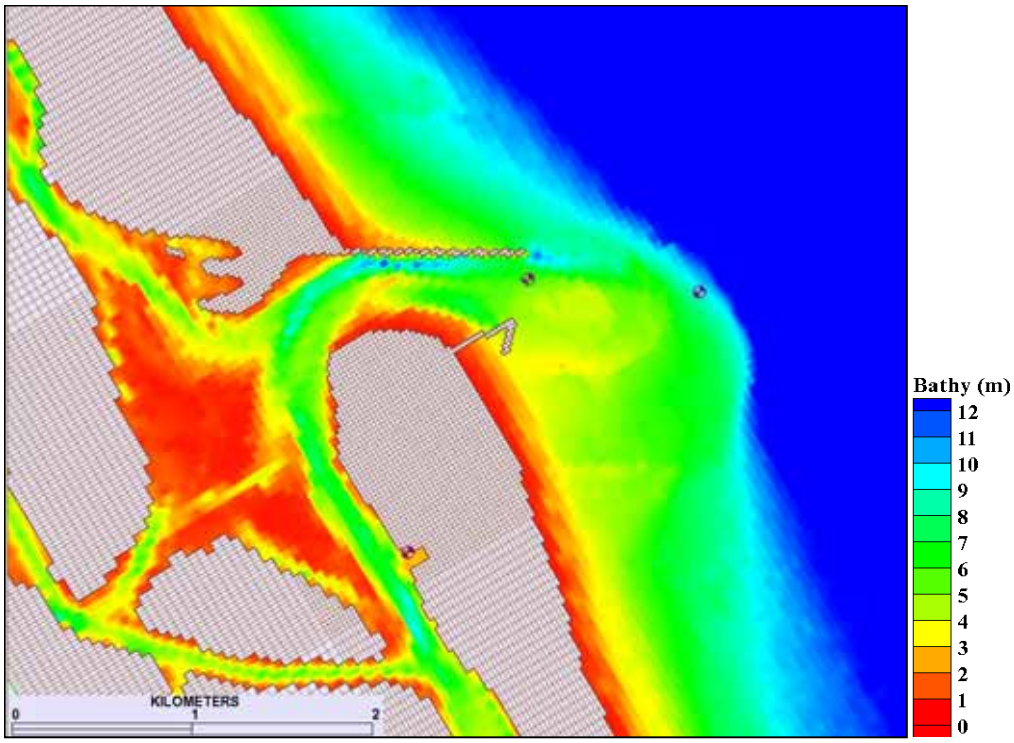

Figure 50. Morphology at 0 hr for South Jetty Extension with ES.

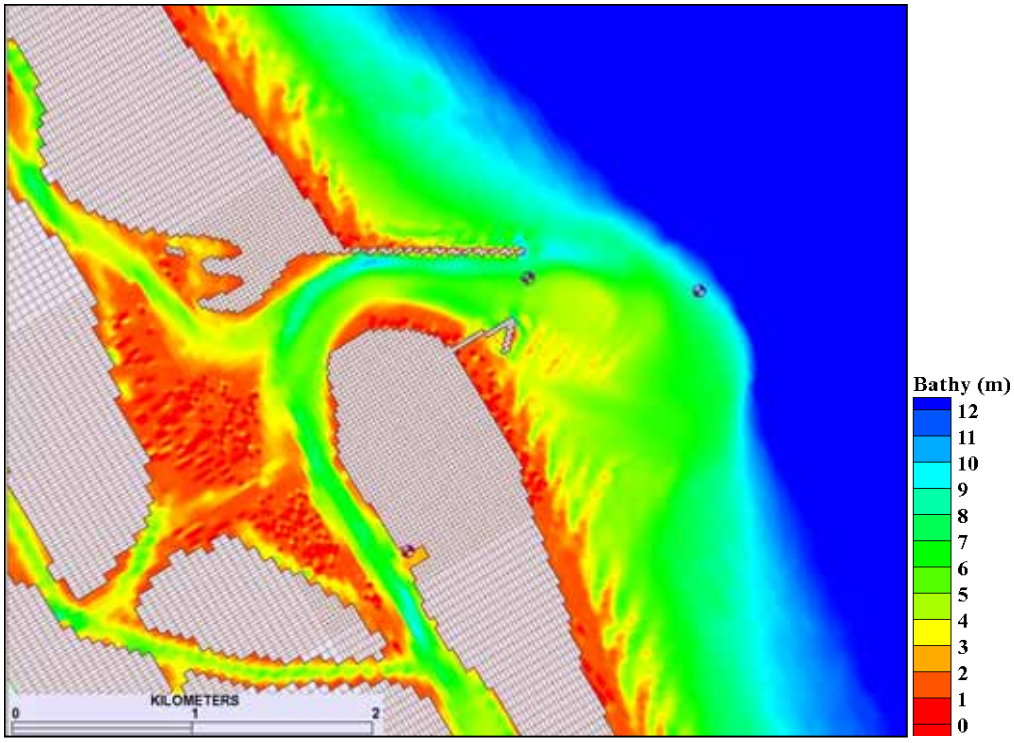

Figure 51. Morphology at 2197 hr (3 months) for South Jetty Extension with ES.

The net topographic change plot (Figure 52) for the 3-month run shows deposition in the South Spit of $\Delta z < 1$ m for most of the mask and slight erosion ($\Delta z = -1$ m) north of the original jetty length with a minimal total volume change (Table 9) of +0.6%. Although scouring at the tip of the south jetty (apex of spur and jetty connection) is not as great as for the non-spur options ($\Delta z \sim -2.5$ m), its orientation has moved more westerly, adding these losses to the South Spit where it was previously contributing to the Ebb Complex mask. In this design, the net depositional areas within the Ebb Complex are visually comparable to the South Jetty Extension Only design, although aligned parallel with the spur orientation rather than sweeping back toward the jetty tip and having slightly larger net gains ($\Delta z \sim 1.5$ m). The combination of this depositional pattern and shifting jetty tip scour moves the Ebb Complex into a volume increase status (+0.09%).

The South Beach has decreased in total volume (-0.23%) despite a few localized depositional areas (deep red, $\Delta z > +3$ m) and the South Jetty does not acquire as much of the bypassed sediment as in the South Jetty extension design. In the shadow of the extended south jetty, more yellow than red is present in the net change plots (less deposition), with a total increase of +1.6% as compared to +2.9% without the spur.

Scouring in the Channel~4.6m sub-domain (blue colors) produces a volume loss of -4.7% whereas the Basin Channel gains +4.7%. Since the deepest scour hole of Channel~4.6m is adjacent to the Basin Channel ($\Delta z = -2$ m), this change of equal magnitude, but opposite sign, suggests the scoured sediment is moving northward to fill in this deepened, shifted channel. The Flood Shoal loses its greatest quantity of sediment with this Emergent Spur design (-2.8%).

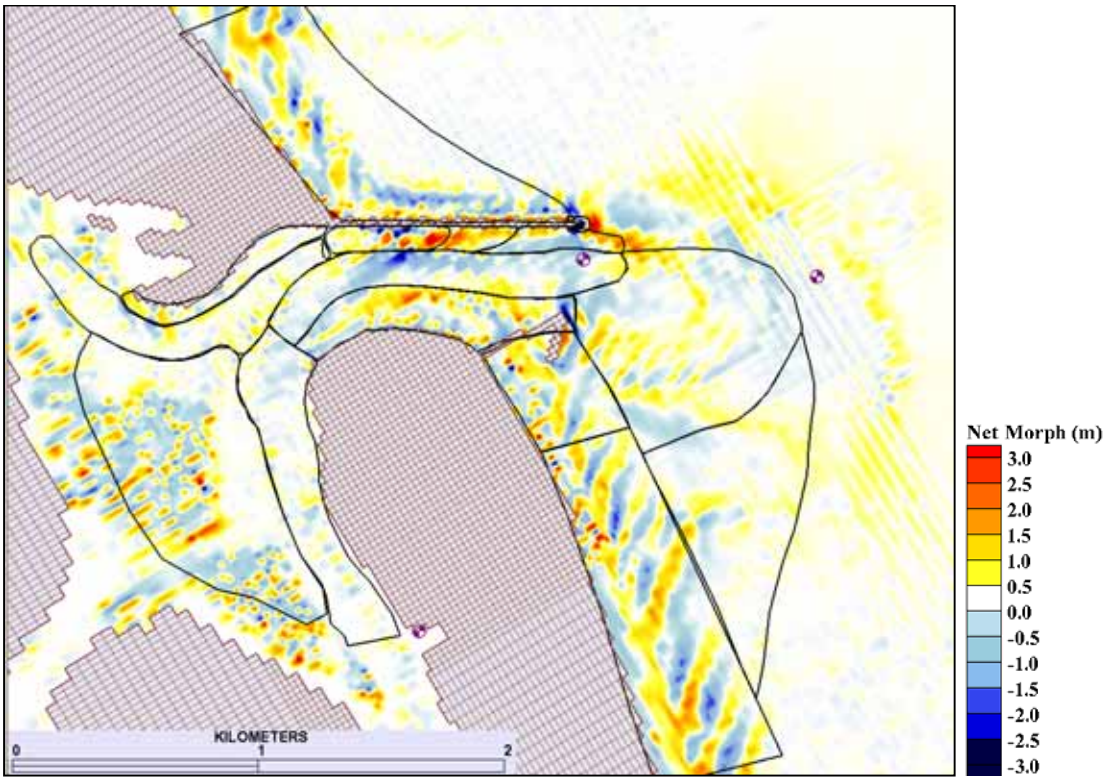

Figure 52. Net 3-month change in morphology for South Jetty Extension with ES.

Table 9. Volume Change (3 months) for South Jetty Extension with ES: Normalized (%) and Net (Δvol).

Polygon Mask	%	Δvol (m^3)
Ebb complex	0.09	2027
South spit	0.63	2975
Channel ~4.6m	-4.65	-54683
Channel >7m	-0.37	-1065
Basin channel	4.67	26701
North channel	0.55	5251
South Jetty	1.59	5962
South channel	-0.61	-8107
South beach	-0.23	-3956
Outer bypass	0.58	13348
North tip	-39.26	-8567
North spit	3.43	4469
North beach	-1.22	-25410
Hard bottom	1.90	6753
Flood shoal	-2.79	-24137

Maximum flow velocities are essentially identical to those of the South Jetty Extension design during the last neap (Figure 53 and Figure 54) and spring (Figure 55 and Figure 56) tides, with values of 1.04 m/s for neap and 1.49 m/s for spring. The most noticeable difference in the hydrodynamics represented in these images is that during maximum ebb (image a in all figures) the ebb jet is no longer as diffuse upon leaving the inlet entrance, allowing higher velocities to reach beyond the outer ebb shoal before turning northeast. No component of this flow is southeast, unlike in all previous designs. For the neap tide, since the offshore flow is directed northward, this produces a well-defined anti-cyclonic (clockwise) eddy southeast of the spur seaward of the bypass bar (in the Outer Bypass mask area) not observed previously. No flow along the downdrift bypass pathway is present during maximum ebb, as in other designs, which explains impounding within the Ebb Complex and loss of sediment to the South Beach.

During maximum neap flood, flow is directed along the spur toward the entrance, producing currents of greater magnitude coming around the south jetty tip than previously seen. This shearing effect contributes to the amount and orientation of the scour hole observed in the net change plots. Since the majority of the nearshore flow approaching the south spur travels along the spur, it is reasonable that the South Jetty mask (Figure 20) gains little volume. During maximum ebb of the spring tide, which has a southerly offshore flow, the larger ebb jet velocities reach even more seaward and produce eddies south and southeast of the inlet. The last hour of ebb has bidirectional flow in the inlet, with higher magnitude currents coming up the spur and around the jetty tip to join the ebb flow, pushing it north and generating a small positive vortex where the scour hole was observed (Figure 55b).

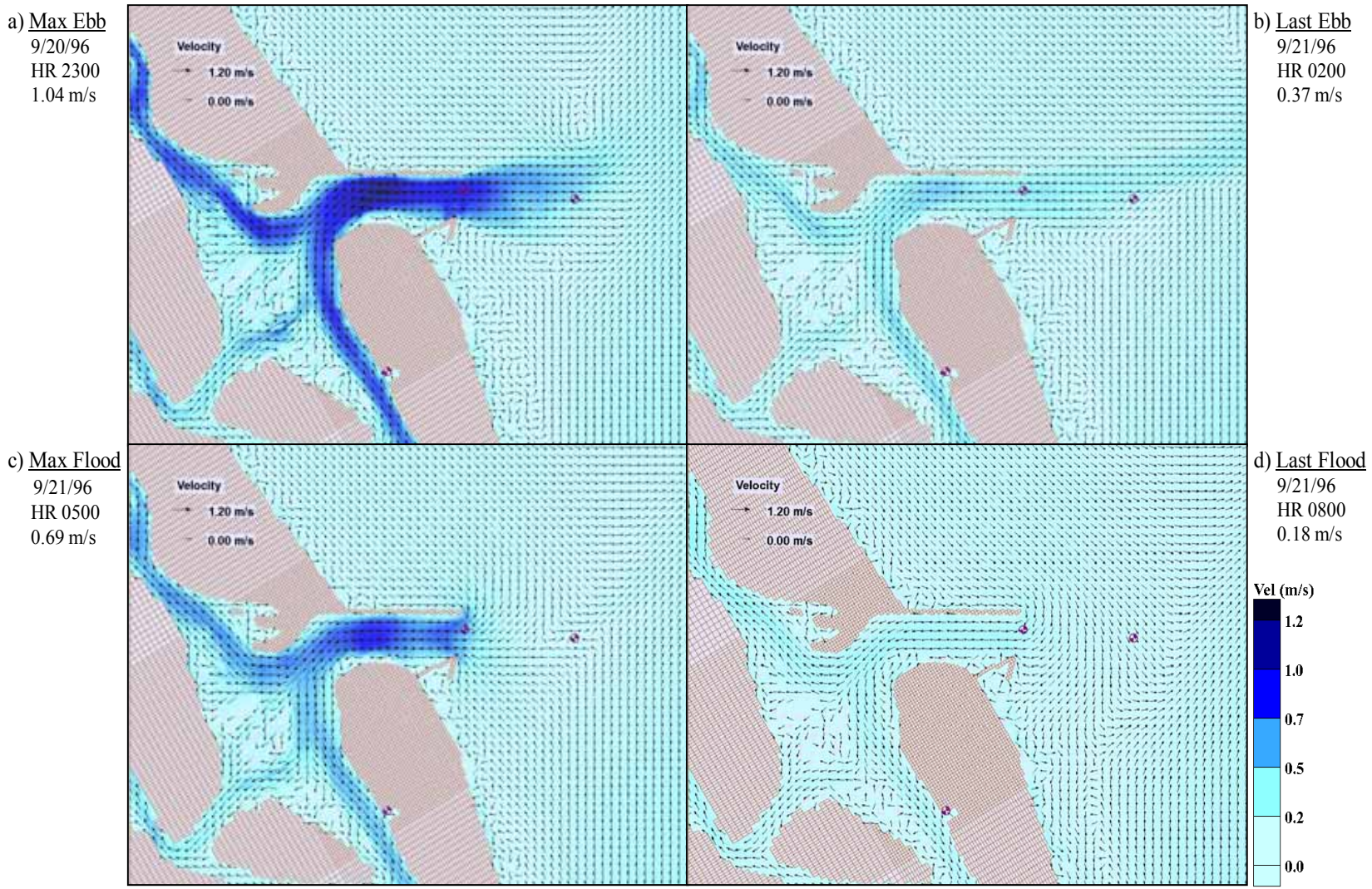

Figure 53. Flow velocities for South Jetty Extension with ES during neap tide of 9/20/96. Maximum value from cell 26657 in channel.

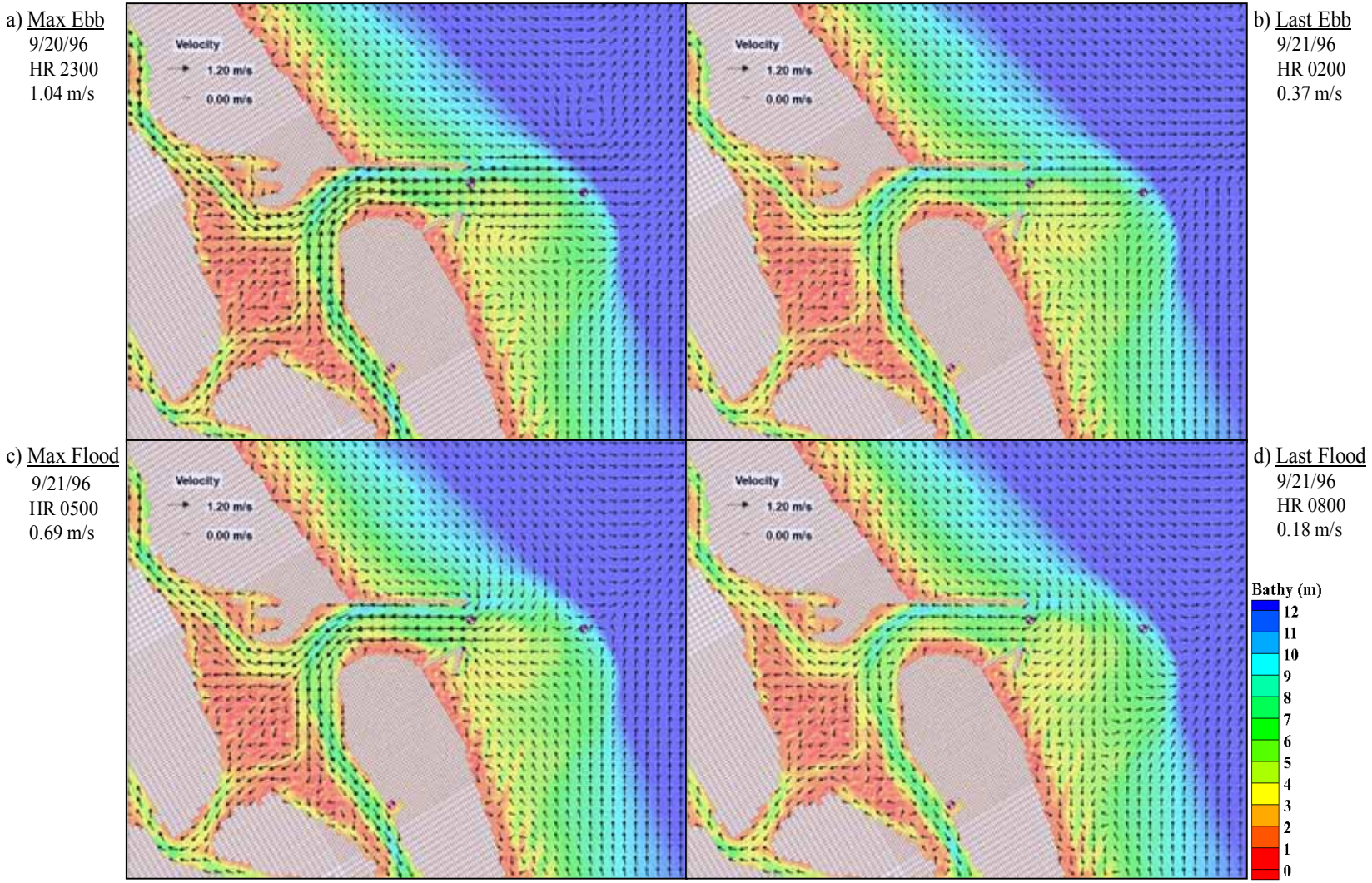

Figure 54. Morphology and flow velocities for South Jetty Extension with ES during neap tide of 9/20/96. Maximum value from cell 26657 in channel.

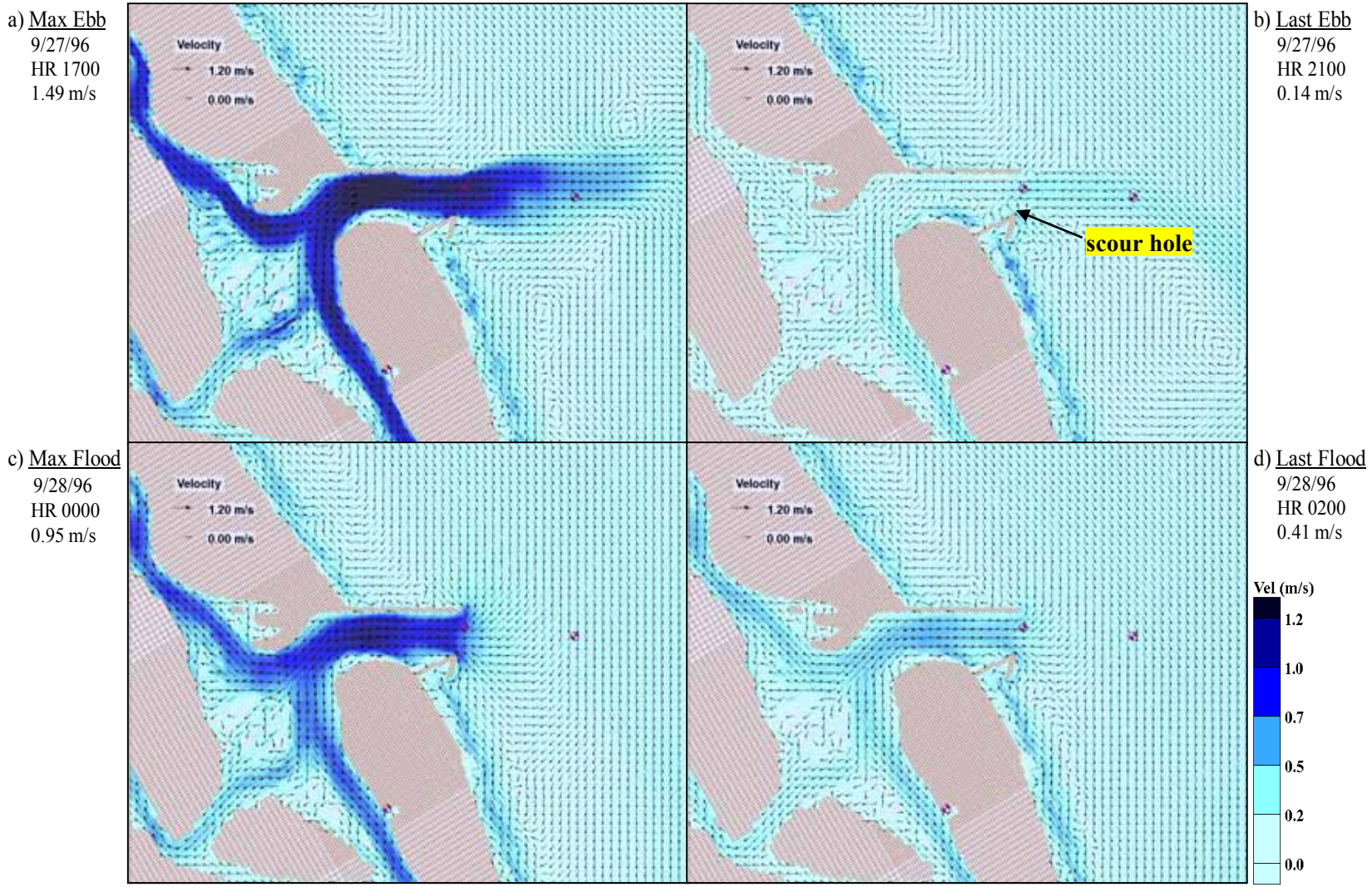

Figure 55. Flow velocities for South Jetty Extension with ES during spring tide of 9/27/96. Maximum value from cell 26657 in channel.

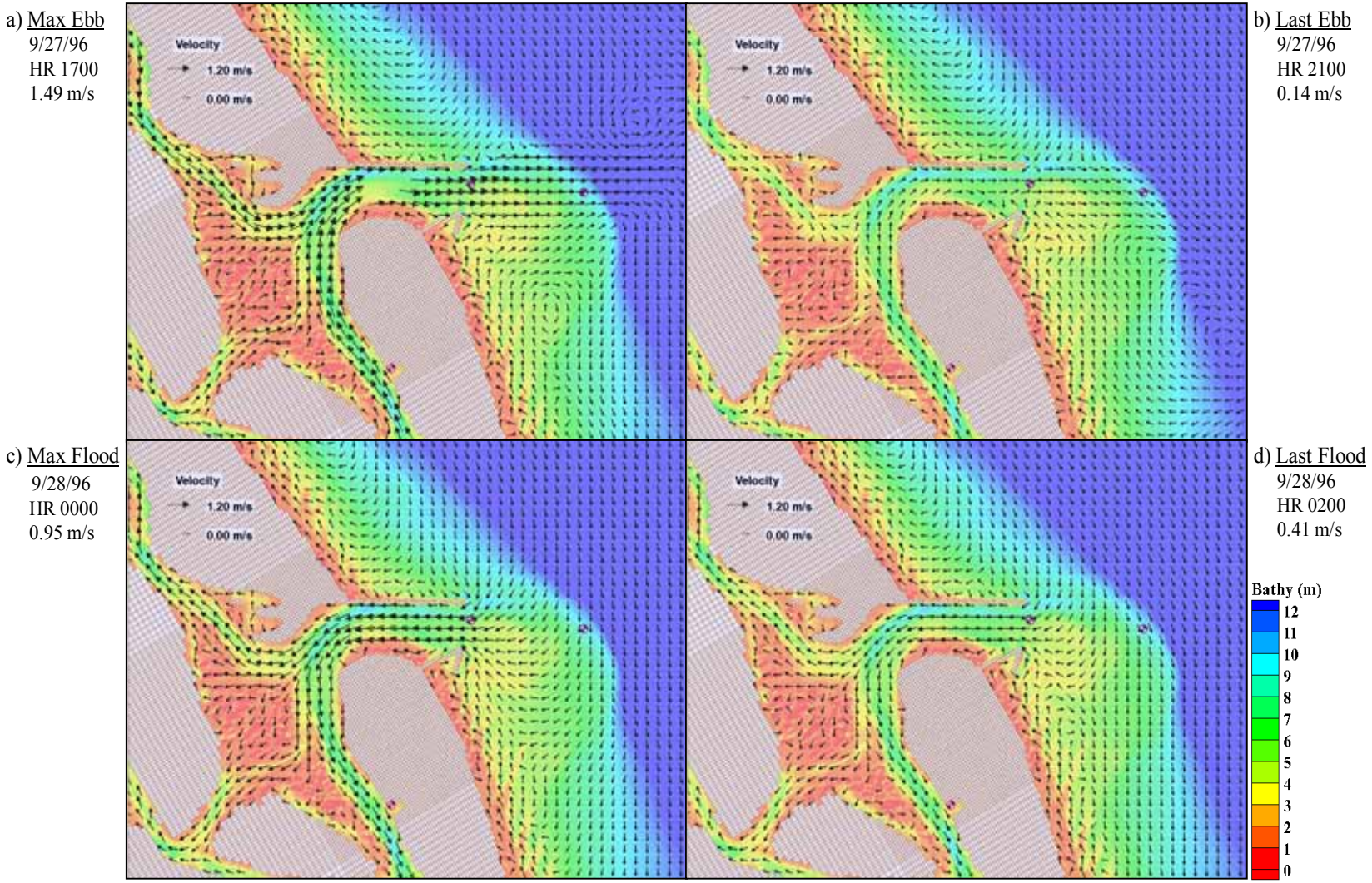

Figure 56. Morphology and flow velocities for South Jetty Extension with ES during spring tide of 9/27/96. Maximum value from cell 26657 in channel.

5.2.5B South Jetty Extension with Emergent Spur and Channel

This alternative adds changes in depth along the original navigation channel (C) to the Emergent Spur (ES) design. Starting morphology (Figure 57) is virtually identical to all Hard Bottom (HB) designs, except that the deepened, shifted channel along the north jetty is still present. Final morphology (Figure 58) lacks the intense deposition (z = 3 m) at the spur, as observed without the channel being re-dredged, and shows an increase in erosion (Figure 59) at the south jetty tip ($\Delta z < -3$m), which has shifted east and spread to the north. The South Spit has increased in shoaling (z = 0 m in places) with a volume change (Table 10) of +3.5%. Although the scouring of Channel~4.6m caused a -4.9% loss of volume, the Basin Channel only picked up +4.2% volume. The shallower bathymetry (z = 1 to 3 m) over the downdrift bypass bar off the spur, coupled with a gain in sediment for the Ebb Complex (+0.4%), South Beach (+0.7%), and South Jetty (+0.98%), supports the assertion that this design does enhance natural bypassing.

Maximum velocities and circulation follow the Emergent Spur for the last neap and spring tides, though the flow along the spur toward the inlet is not as well formed. During maximum ebb for the neap tide (Figure 62a and Figure 63a), this produces a less developed eddy that is slightly south of that produced without the Channel. During the last hour of ebb on the spring tide (Figure 62b and Figure 63b), turbulence generated along the spur impacts flow at the entrance, explaining the increase in scour there for this design. During flood (c in all figures), the flow between the south spit and re-dredged channel shows a slightly northwest component, as if leaning towards the deeper bathymetry.

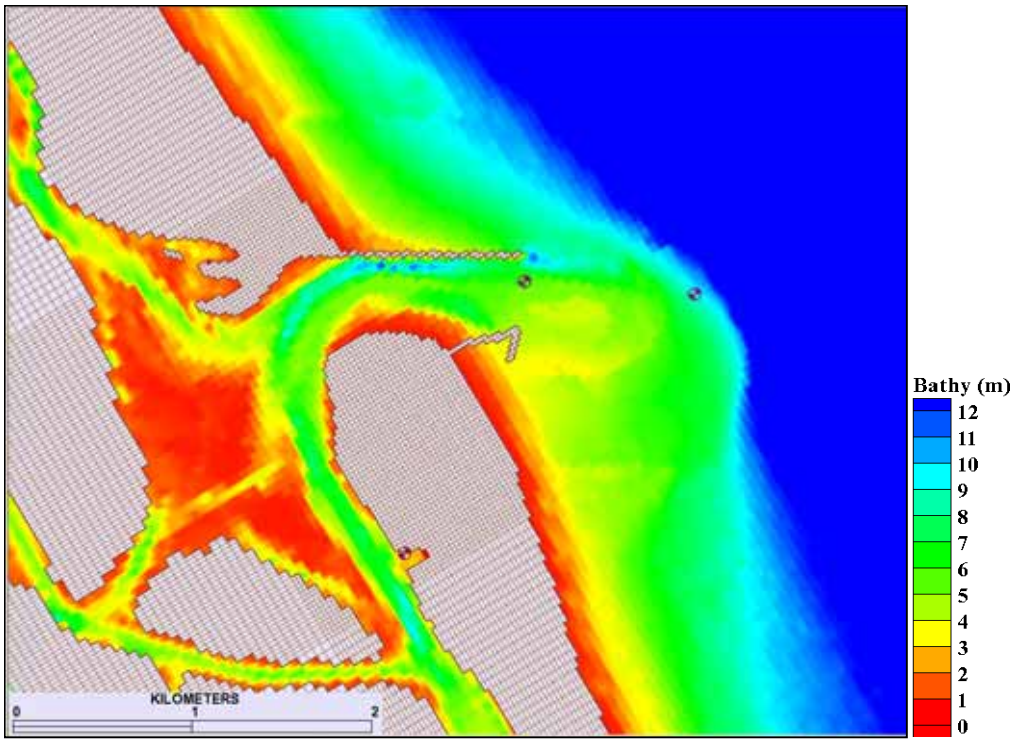

Figure 57. Morphology at 0 hr for South Jetty Extension with ES and C.

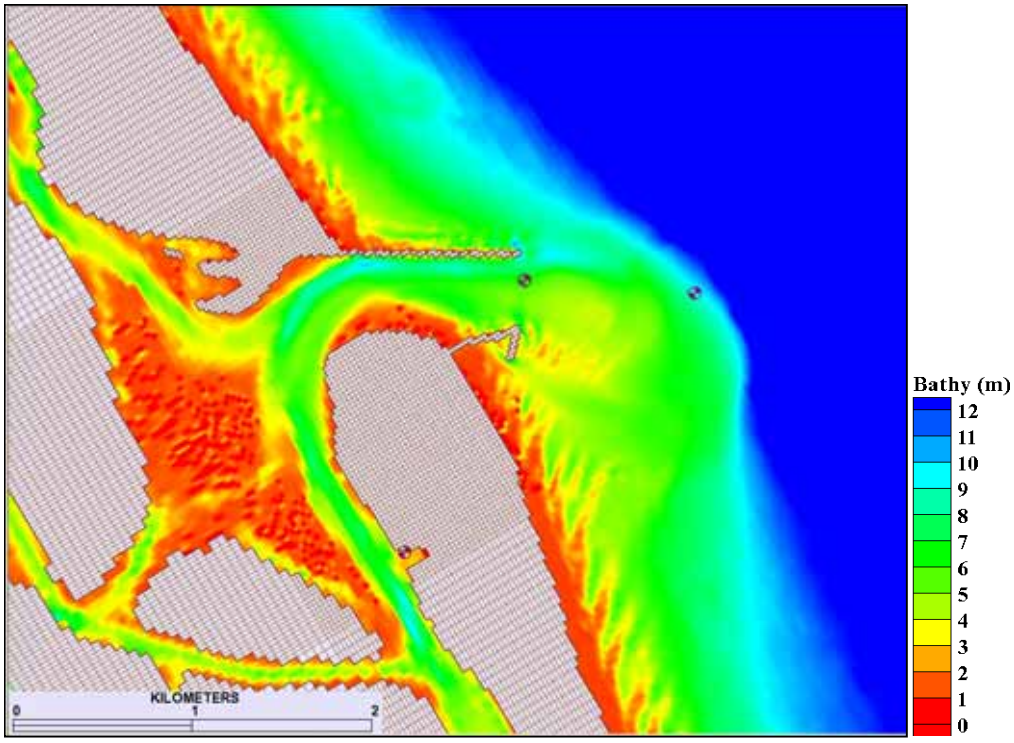

Figure 58. Morphology at 2197 hr (3 months) for South Jetty Extension with ES and C.

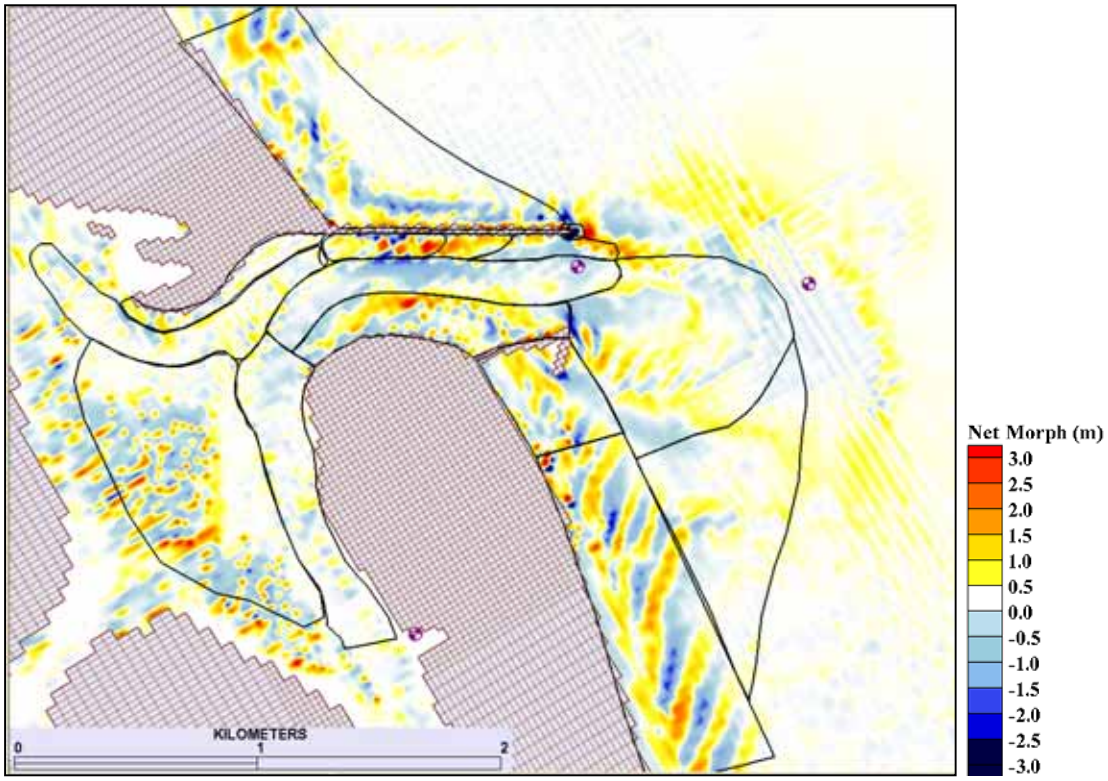

Figure 59. Net 3-month change in morphology for South Jetty Extension with ES and C.

Table 10. Volume Change (3 months) for South Jetty Extension with ES and C: Normalized (%) and Net (Δvol).

Polygon Mask	%	Δvol (m^3)
Ebb complex	0.39	9247
South spit	3.48	17106
Channel ~4.6m	-4.93	-60209
Channel >7m	-0.41	-1175
Basin channel	4.19	24023
North channel	0.40	3883
South Jetty	0.98	3453
South channel	0.72	9650
South beach	0.66	11460
Outer bypass	0.77	17845
North tip	-35.41	-7727
North spit	2.93	3817
North beach	-0.88	-18294
Hard bottom	1.98	7101
Flood shoal	-1.78	-15426

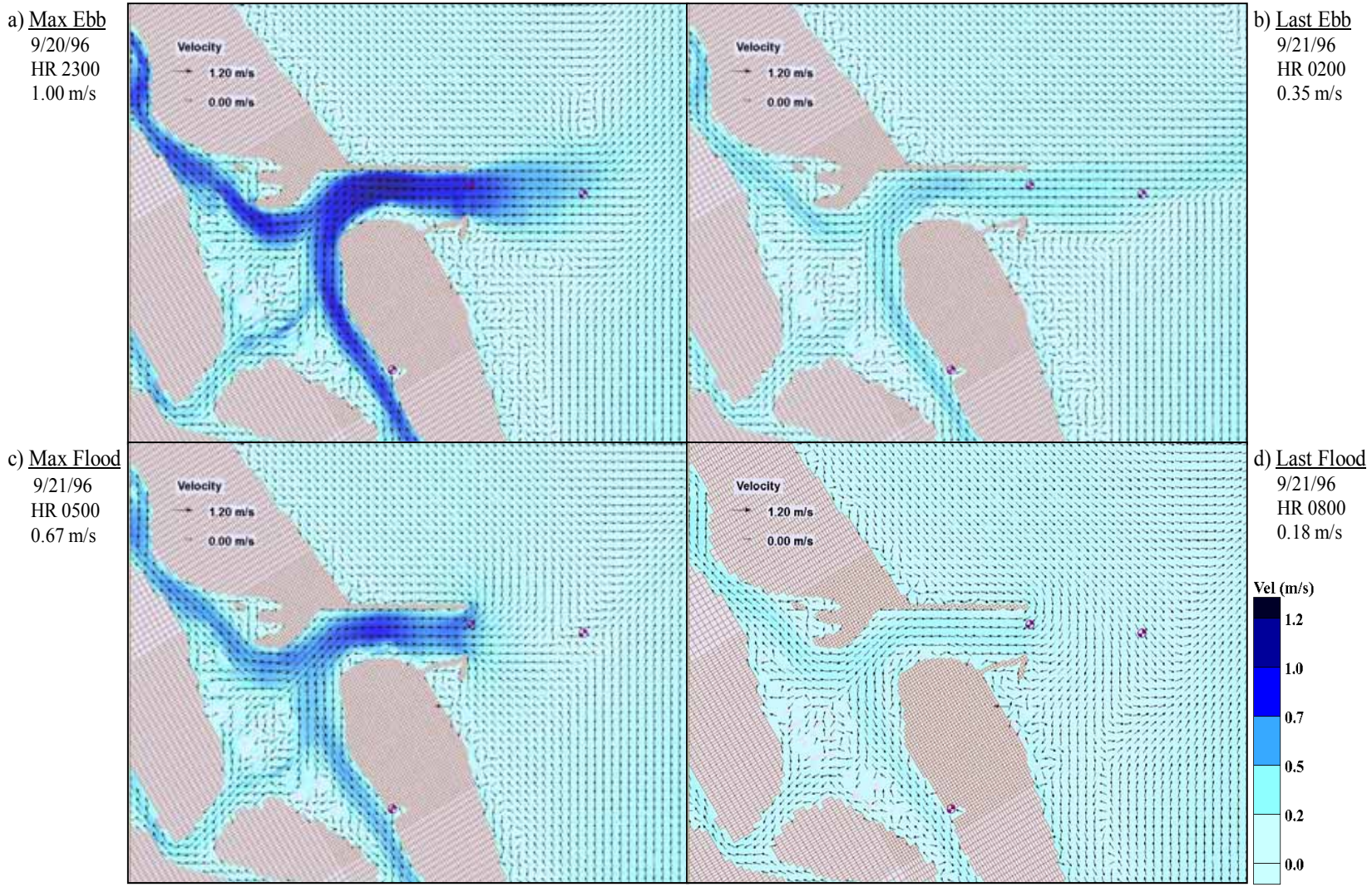

Figure 60. Flow velocities for South Jetty Extension with ES and C during neap tide of 9/20/96. Maximum value from cell 26456 in channel.

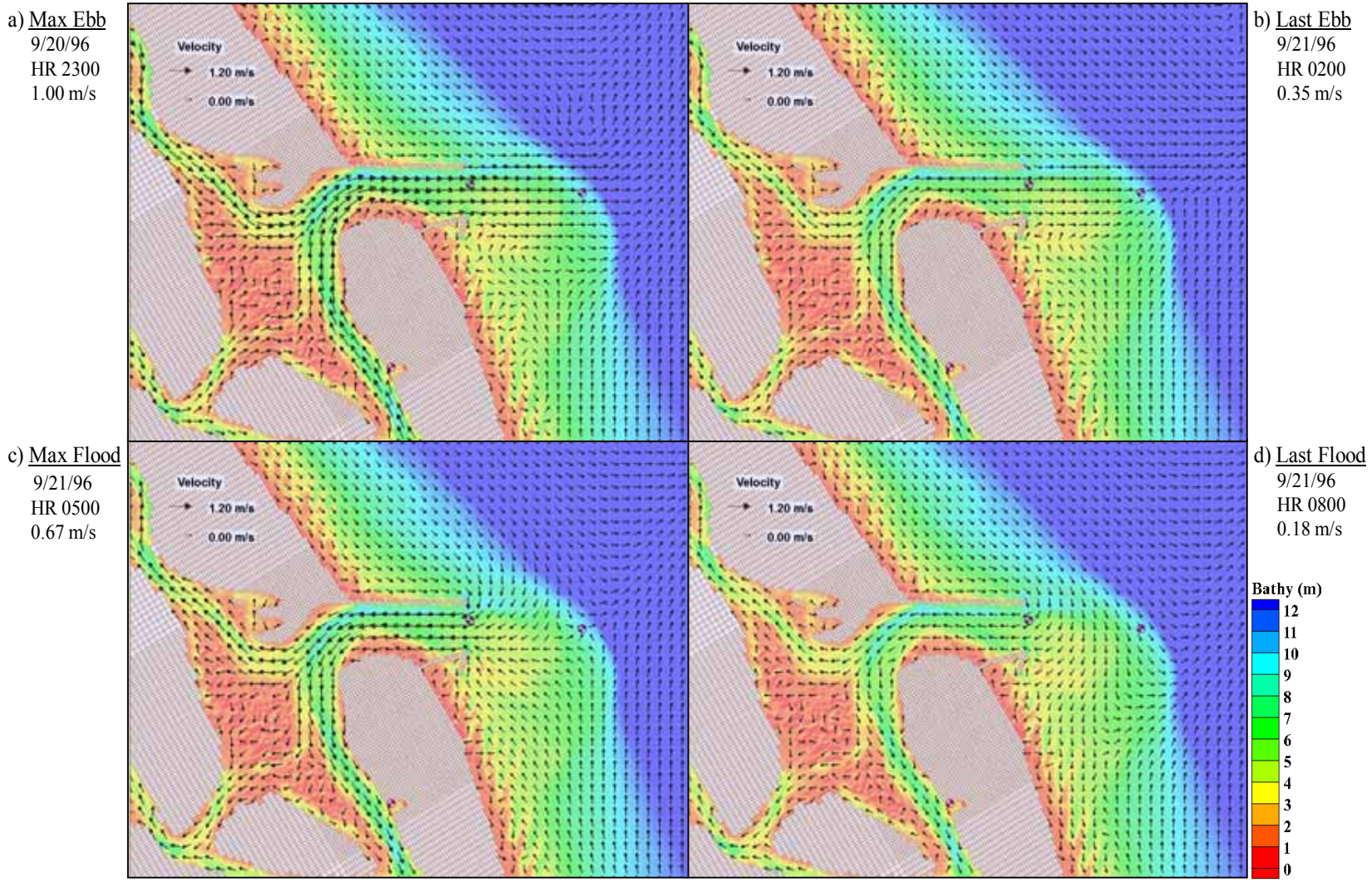

Figure 61. Morphology and flow velocities for South Jetty Extension with ES and C during neap tide of 9/20/96. Maximum value from cell 26456 in channel.

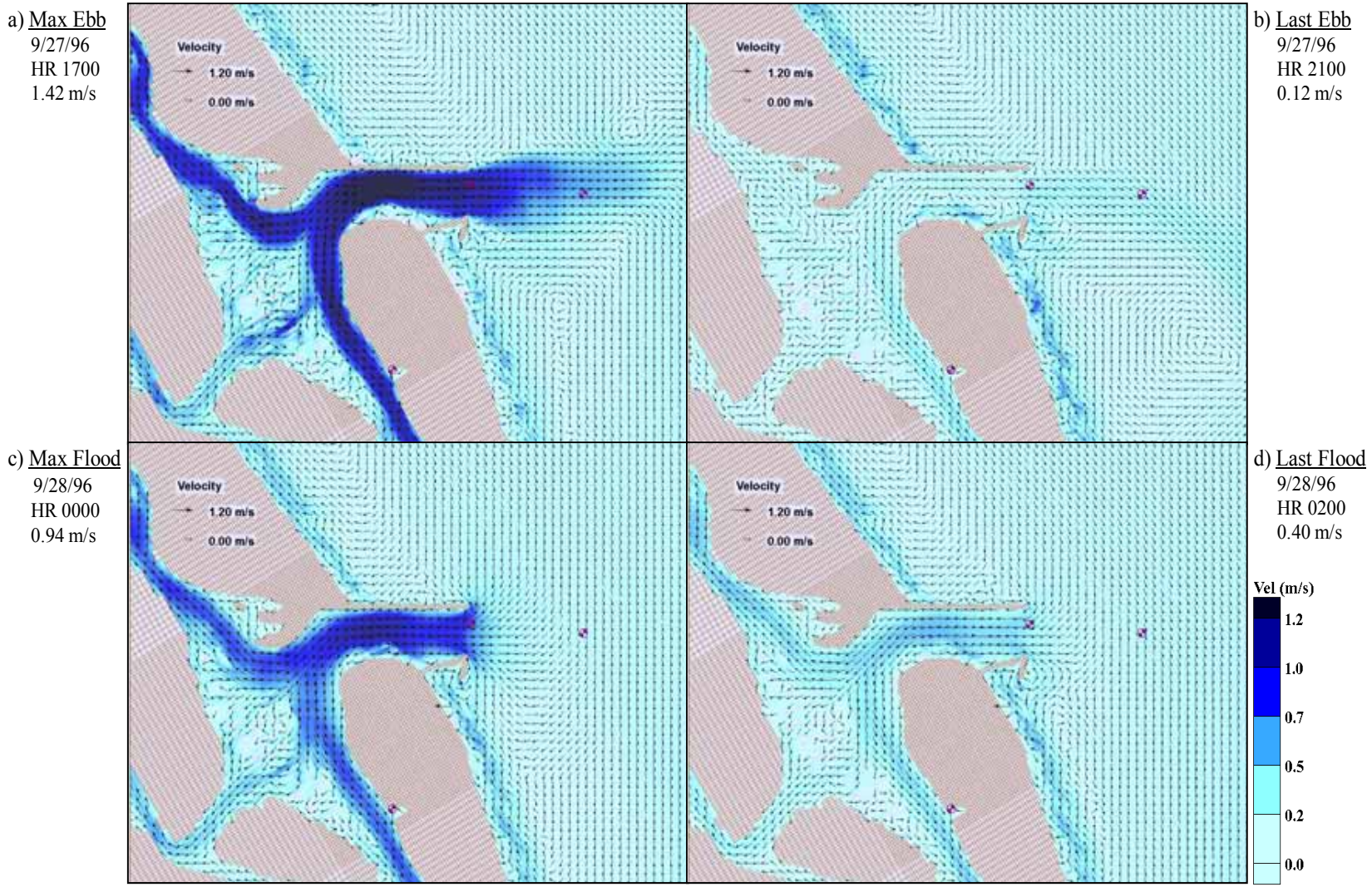

Figure 62. Flow velocities for South Jetty Extension with ES and C during spring tide of 9/27/96. Maximum value from cell 26456 in channel.

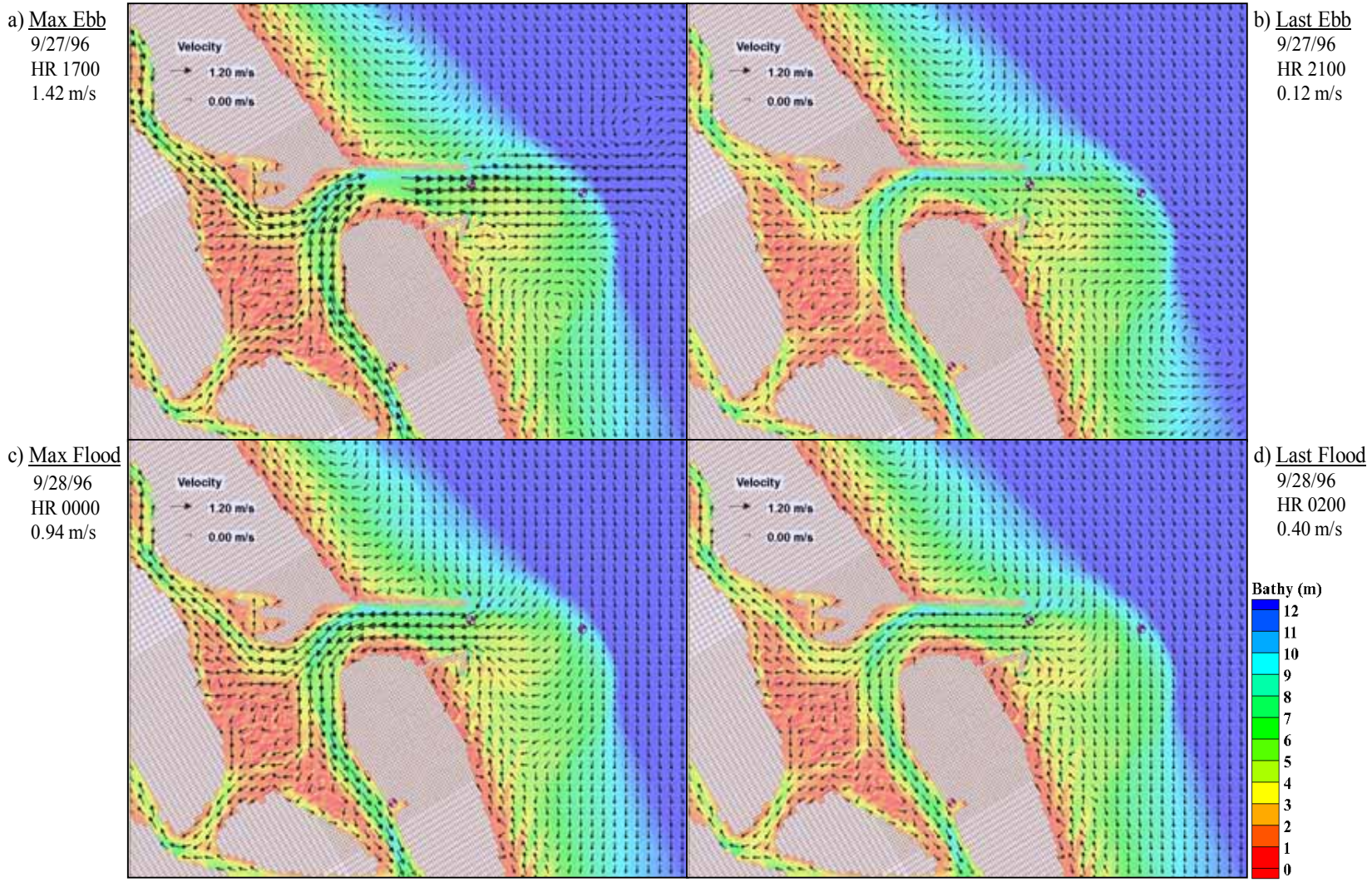

Figure 63. Morphology and flow velocities for South Jetty Extension with ES and C during spring tide of 9/27/96. Maximum value from cell 26456 in channel.

5.2.5C South Jetty Extension with Emergent Spur, HB, and Channel

The final version of South Jetty Extension (SJ) with Emergent Spur (ES) design adds the Hard Bottom (HB) basin option. Starting morphology (Figure 64) mirrors the South Jetty Extension with HB and Channel (Figure 43). Once again, the bypass bar is predicted to gain sediment (z = 1 to 3 m) by the end of the 3-month run (Figure 65). Although the morphology of the south spit indicates a deepening of the bathymetry by having cooler colors than at the 0 hr, this may just be a reworking of the sediment. The net change plot (Δz) shows few areas of intense deposition (Figure 66) and is visually comparable to the Emergent Spur Only design for the South Spit mask (Figure 52). The volume change (Table 11) indicates that this mask has the largest gains of the Emergent Spur designs (+4.2%). There appears to be a shift from blues (erosion) to white/yellow (slight deposition) throughout the South Spit. The intense scouring at the tip of the south jetty, which had been part of the South Spit domain for the Spur Only option, is now in the Ebb Complex mask again, contributing to the -0.6% decrease in volume. The Basin Channel has the smallest gain in volume gain for the Emergent Spur designs (+2.7%). The adjacent Channel~4.6m shows net morphology change of Δz = -1.5 m and a total volume loss of -5.8%.

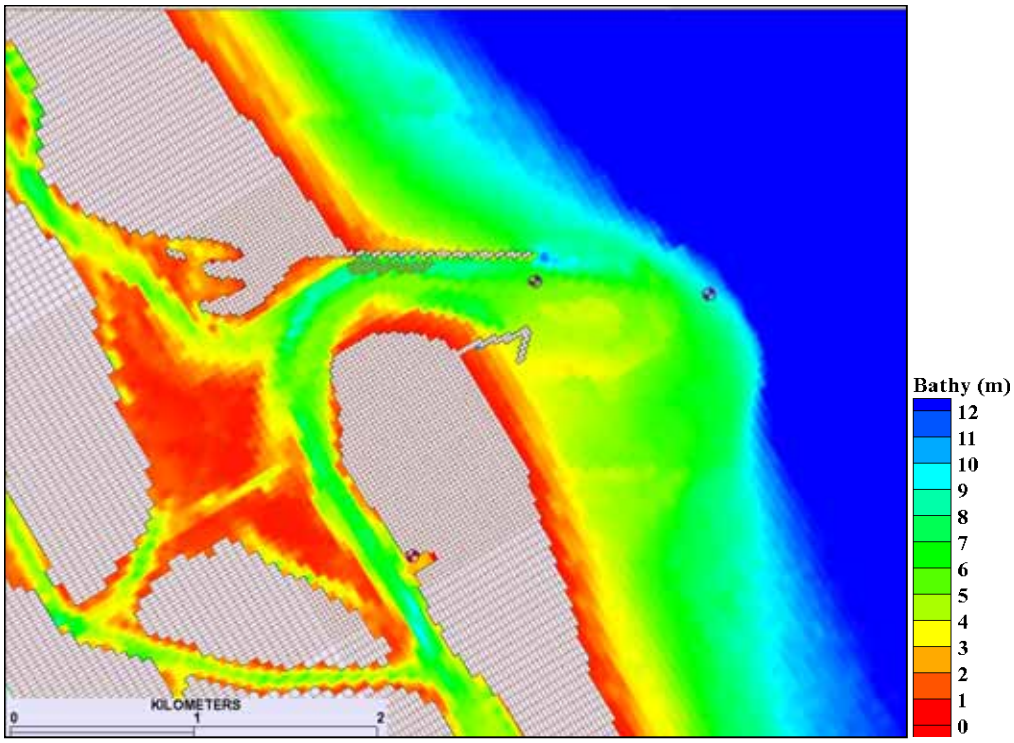

Figure 64. Morphology at 0 hr for South Jetty Extension with ES, HB, and C.

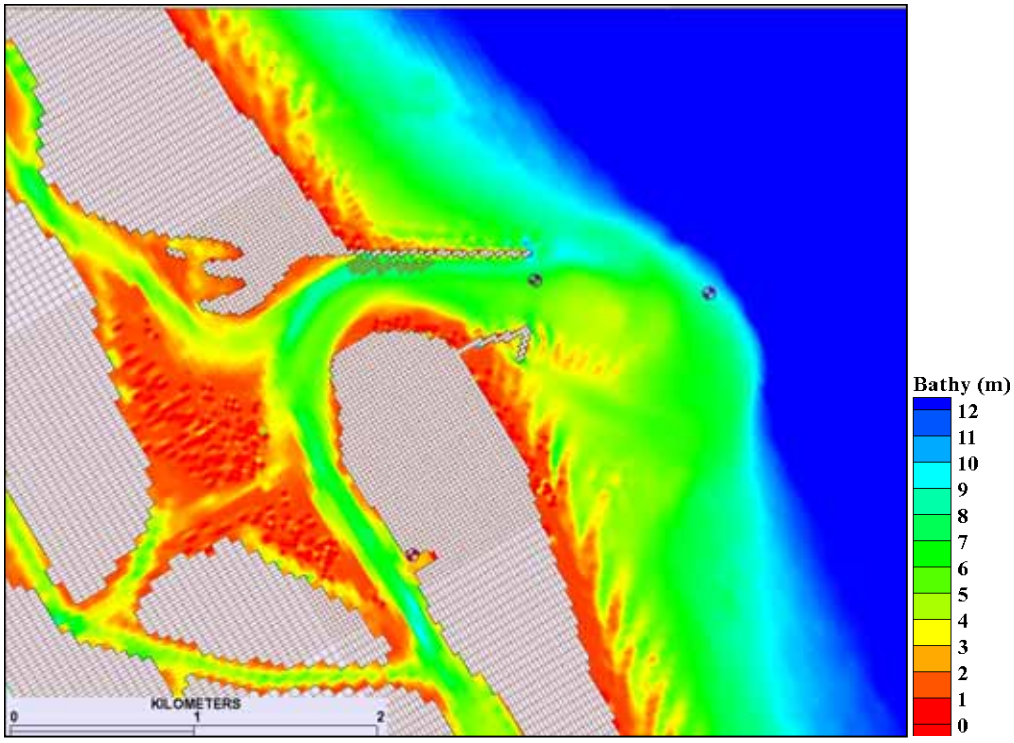

Figure 65. Morphology at 2197 hr (3 months) for South Jetty Extension with ES, HB, and C.

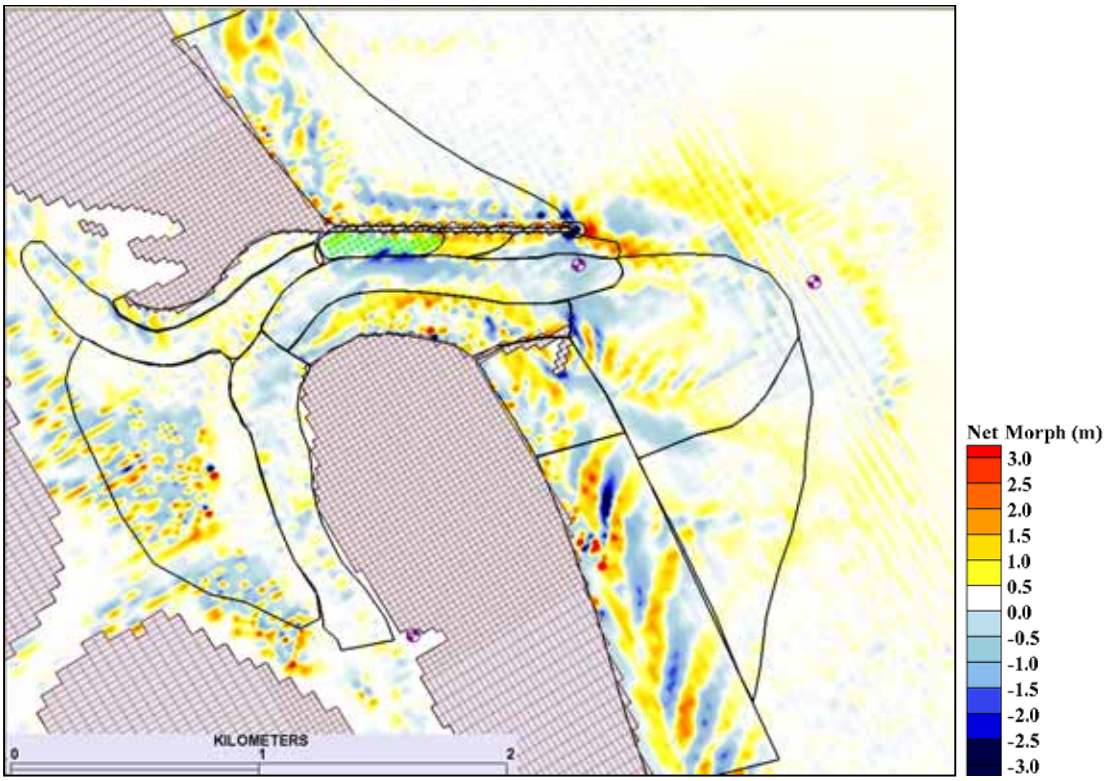

Figure 66. Net 3-month change in morphology for South Jetty Extension with ES, HB, and C.

Table 11. Volume Change (3 months) for South Jetty Extension with ES, HB, and C: Normalized (%) and Net (Δvol).

Polygon Mask	%	Δvol (m^3)
Ebb complex	-0.58	-13780
South spit	4.18	20571
Channel ~4.6m	-5.79	-70646
Channel >7m	0.19	535
Basin channel	2.68	14083
North channel	0.29	2751
South Jetty	0.83	2925
South channel	-1.03	-13757
South beach	-0.29	-4982
Outer bypass	0.80	18342
North tip	-41.38	-9029
North spit	3.29	4290
North beach	-0.98	-20447
Hard bottom	-0.38	-1273
Flood shoal	-2.25	-19485

Vector diagrams for the predicted flow velocities during the last neap and spring tides of the 3-month runs are presented in Figure 67 - 70 for the South Jetty Extension with Emergent Spur, Hard Bottom, and Channel. Only a few differences are evident among the Emergent Spur designs. During neap tide (Figure 67 and Figure 68), there is the presence of more actual flow over the flood shoal, where previously there were more dry cells. For the northerly flow approaching the inlet from the south during the last hour of ebb, the vector direction along the shear line following the southern tip of the spur goes from NW to ENE as the northerly current hits the ebb jet (Figure 67b and Figure 68b). This is a more dramatic rotation than for the other two Emergent Spur designs. During the last hour of ebb of the spring tide (Figure 69b and Figure 70b), the turbulence observed with the Channel option has increased in the nearshore along the entire south beach, but is reduced along the spur and inlet entrance.

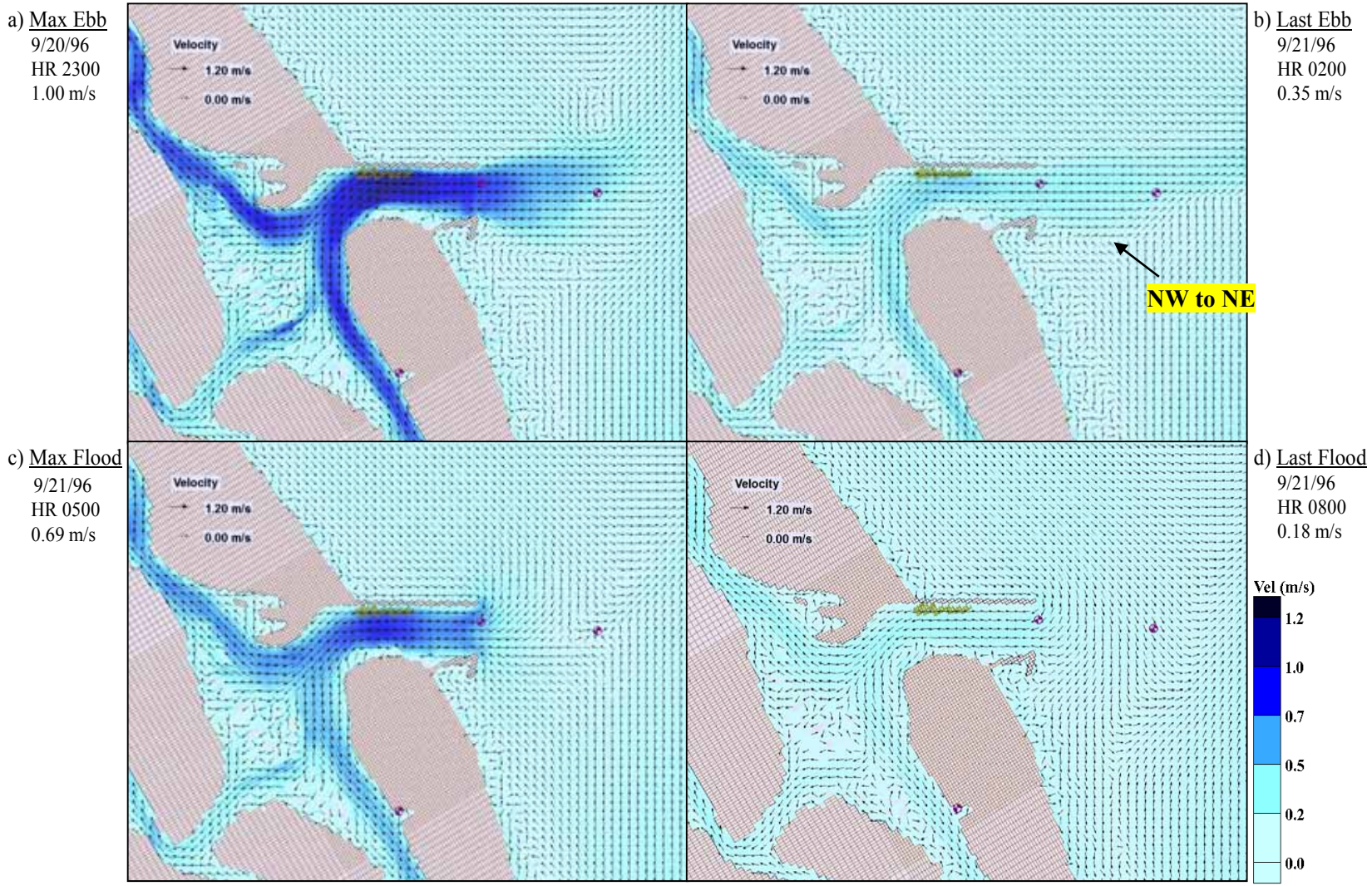

Figure 67. Flow velocities for South Jetty Extension with ES, HB, and C during neap tide of 9/20/96. Maximum value from cell 27069 near HB.

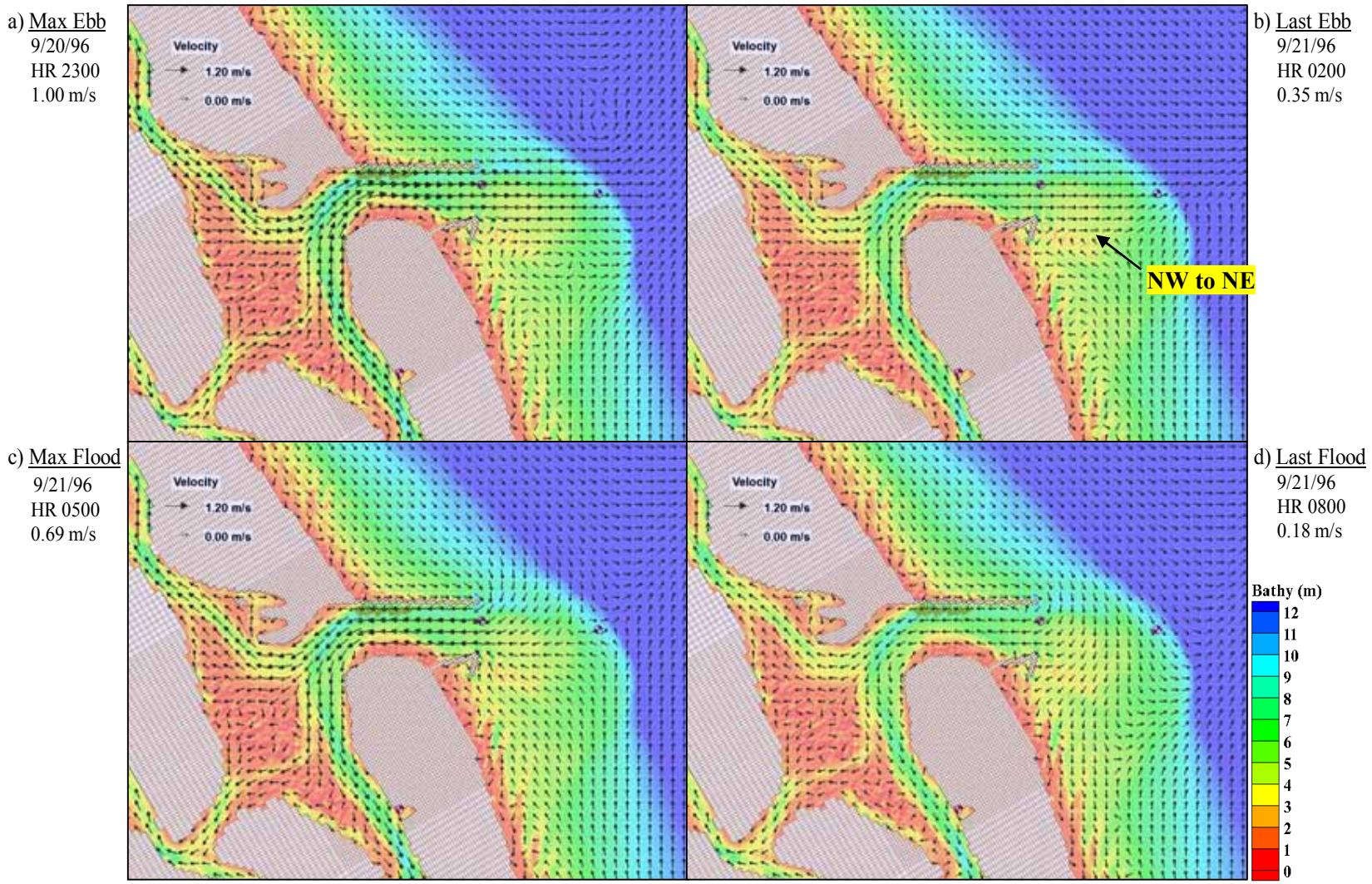

Figure 68. Morphology and flow velocities for South Jetty Extension with ES, HB, and C during neap tide of 9/20/96. Maximum value from cell 27069 near HB.

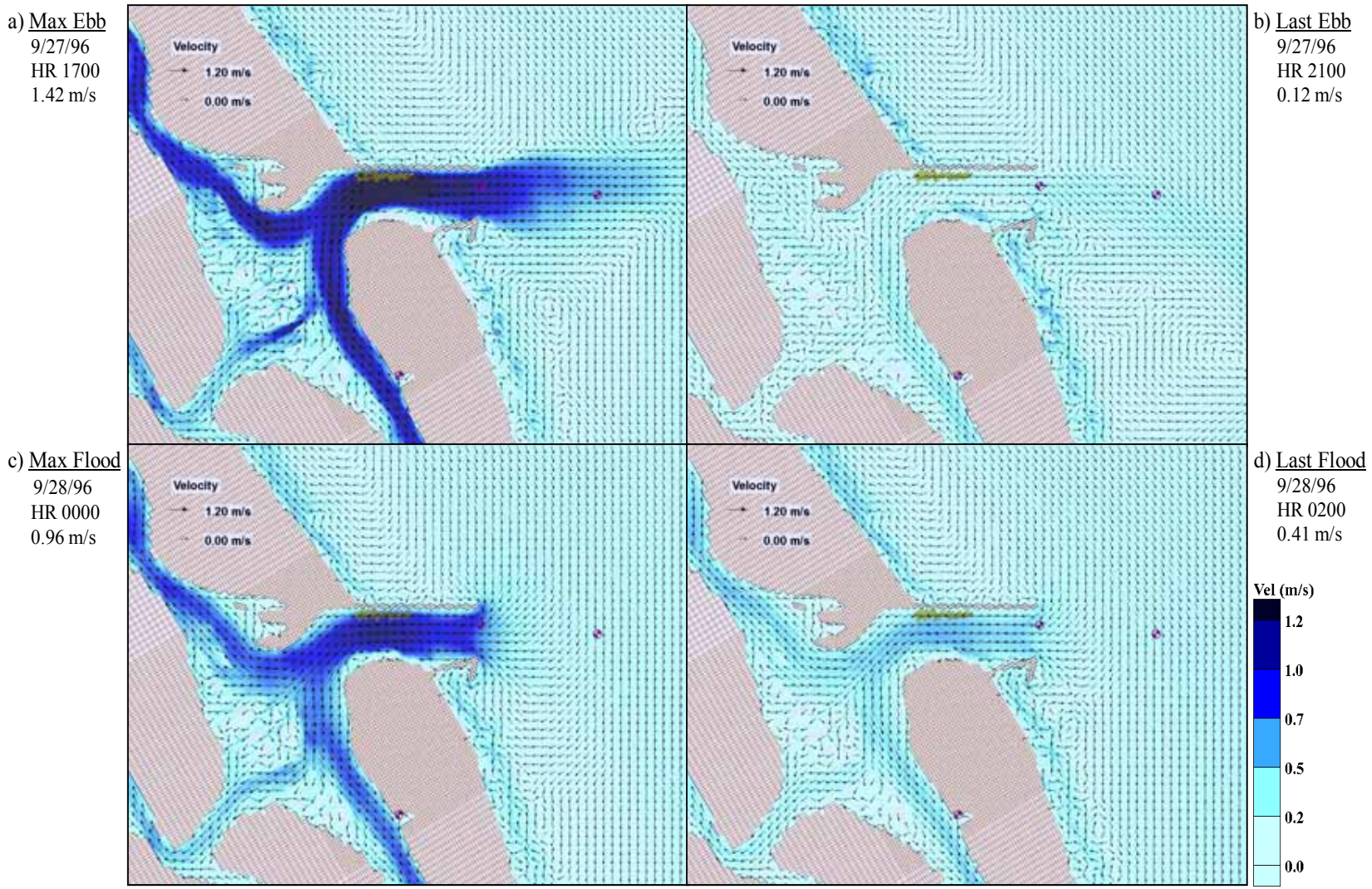

Figure 69. Flow velocities for South Jetty Extension with ES, HB, and C during spring tide of 9/27/96. Maximum value from cell 27069 near HB.

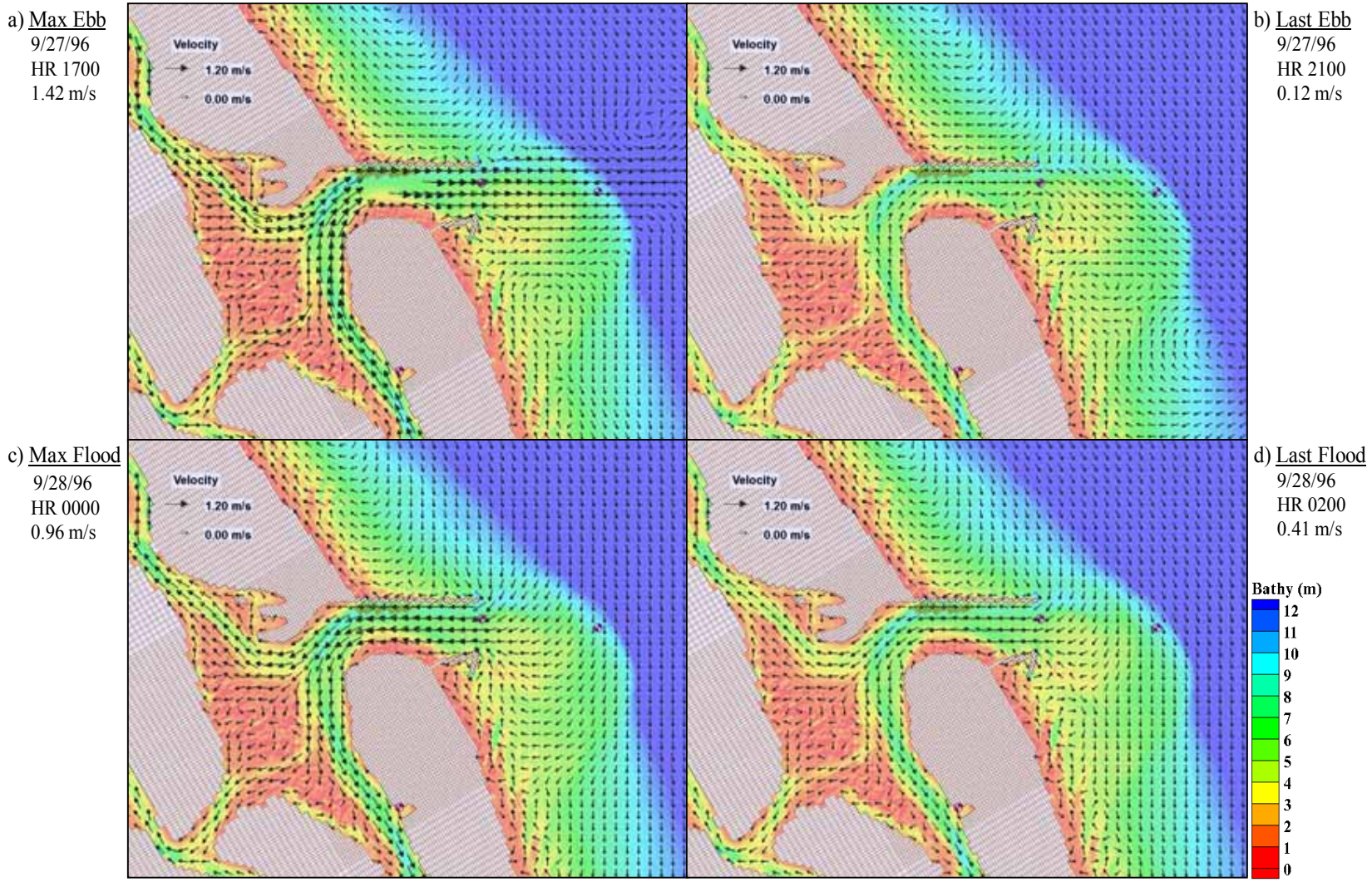

Figure 70. Morphology and flow velocities for South Jetty Extension with ES, HB, and C during spring tide of 9/27/96. Maximum value from cell 27069 near HB.

5.2.6 South Jetty Extension with Submergent Spur

For both of the South Jetty Extension (SJ) with Submergent Spur (SS) designs, bathymetry was changed. One option included only the re-dredge of the navigation channel back in its original design location (C). The other option added the artificial hard bottom (HB) to the deepened, shifted channel as well, reducing it to a shallow channel serving as a deposition basin. The impetus for submerging the spur just below the 0 m NAVD88 water level follows the design benefits for nearshore submergent breakwaters and their ability to reduce wave action without drastically impeding flow, as water can pass over the crest. The results of the enhanced wave-break may be beneficial to the local surfers. Additionally, as indicated by the physical and numerical models of Seabergh et. al (2008), submerged spurs provide similar benefits as their emerged counterparts, but are less costly.

5.2.6A. South Jetty Extension with Submergent Spur and Channel

Starting morphology (Figure 71) for the South Jetty Extension with Submergent Spur (SS) and Channel (C) indicates that the design includes the re-dredged navigation channel via the lime-green color through the centerline of the inlet. The deep, shifted navigation channel is also visible (z ~ 12 m) and the gold triangles coming off at an angle from the end of the south jetty represent the submerged spur. The final, 3-month morphology (Figure 72) shows an active downdrift bypass bar and reduced depths for the deepest sections of the shifted navigation channel (z ~ 9.5 m).

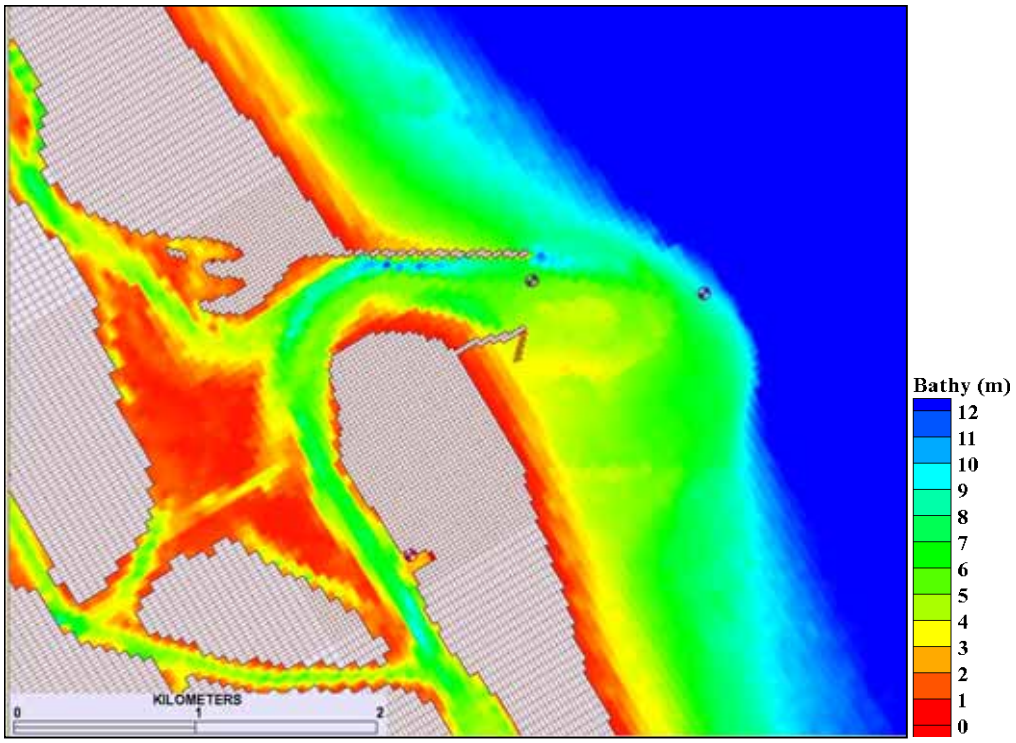

Figure 71. Morphology at 0 hr for South Jetty Extension with SS and C.

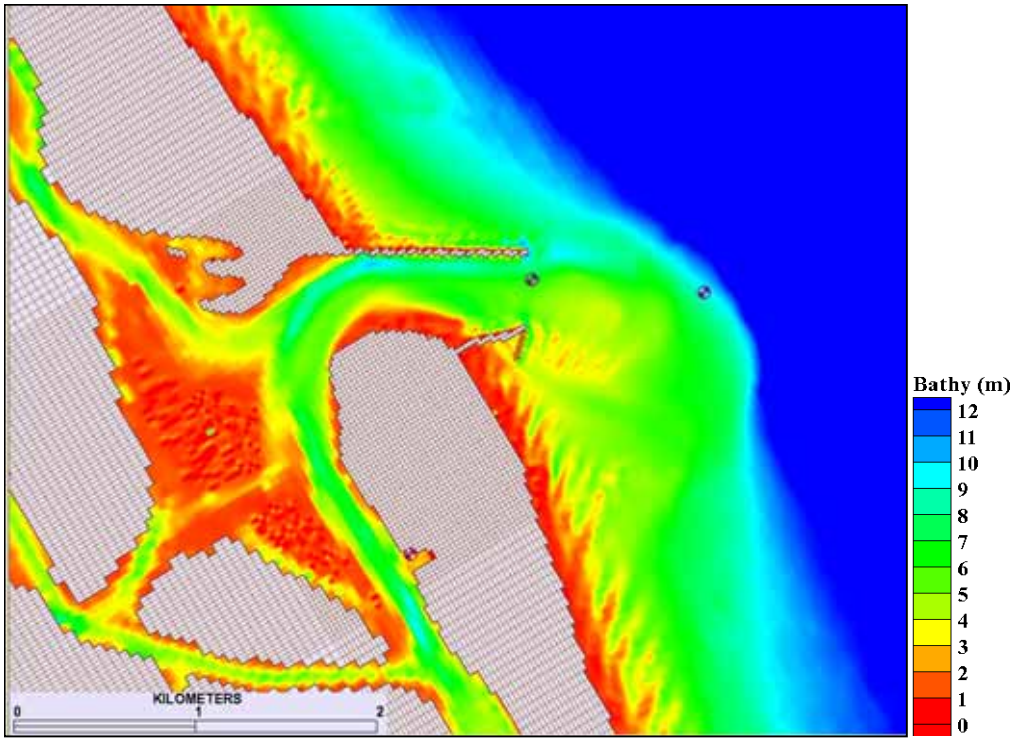

Figure 72. Morphology at 2197 hr (3 months) for South Jetty Extension with SS and C.

The net morphology (Figure 73) shows the change within the deep, navigation channel, with mostly gold and deep red (Δz of +1 to > +3m) in the Basin Channel and Channel>7m masks. There is deposition of +1 to +2 m in the South Spit with localized changes of + 3 m along the inlet side of the south jetty for a total volume increase of +3.8% (Table 12). Scouring of more than -3 m occurs at the tip of both jetties, with the North Tip sub-domain losing -42% volume. Net changes in the Ebb Complex show the outer area is slightly eroding (light blue), but since the Outer Bypass is mostly pale yellow (Δz ~ +1 m) with a volume gain of +0.9%, it is fair to say that southerly transport is occurring. At the inlet's entrance adjacent to the south jetty tip, further erosion is occurring (Δz ~ -1m) producing a cumulative loss in volume for the Ebb Complex (-0.4%) despite the downdrift bypass bar's sediment gain (Figure 72). The alternating deposition and erosion pattern is again present along the south beaches, with the anomaly of an intense depositional spot (red) adjacent to an equally intense erosional spot, all of which balances out for a total volume change of -0.04% for the South Beach. The Channel~4.6m mask is still scouring quite successfully, even with the deeper starting depth having lost -5.7% volume.

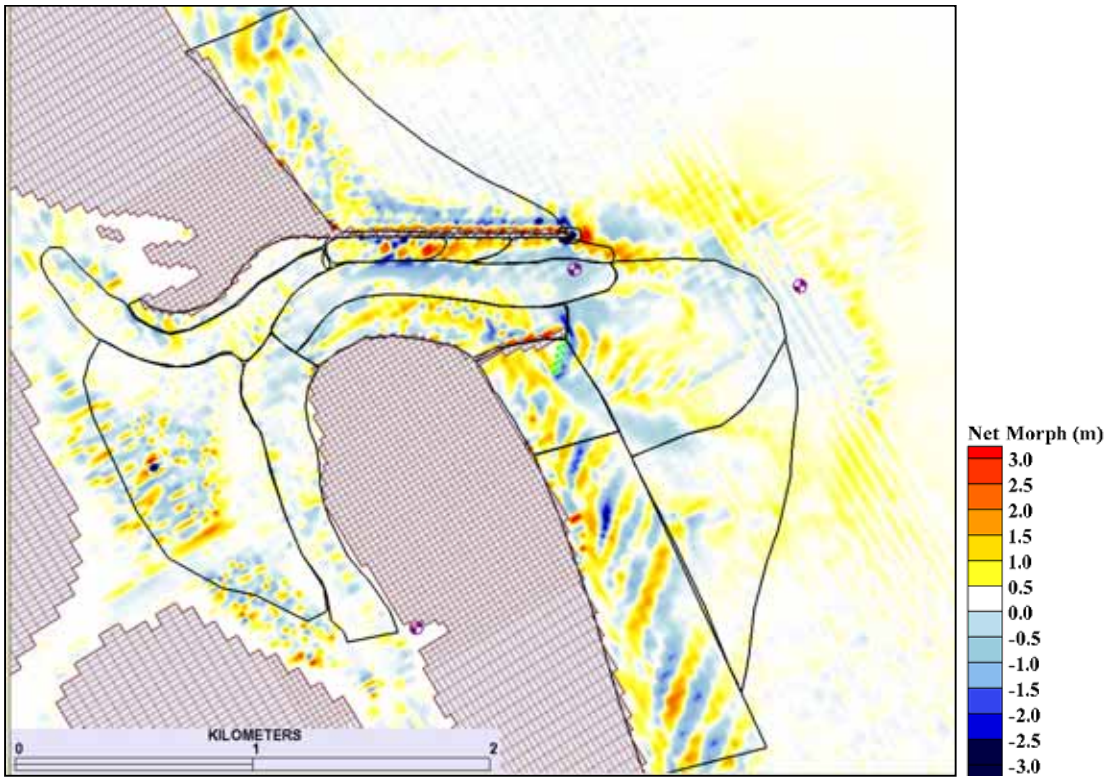

Figure 73. Net 3-month change in morphology for South Jetty Extension with SS and C.

Table 12. Volume Change (3 months) for South Jetty Extension with SS and C: Normalized (%) and Net (Δvol).

Polygon Mask	%	Δvol (m^3)
Ebb complex	-0.38	-8979
South spit	3.75	18445
Channel ~4.6m	-5.66	-69086
Channel >7m	-0.47	-1357
Basin channel	3.30	18968
North channel	0.24	2347
South Jetty	1.64	5838
South channel	-0.70	-9362
South beach	-0.04	-640
Outer bypass	0.85	19643
North tip	-41.67	-9092
North spit	2.34	3049
North beach	-0.55	-11372
Hard bottom	0.63	2250
Flood shoal	-1.24	-10733

Maximum predicted flow velocities for the neap and spring tides are lower now than for the Emergent Spur designs, with neap tide maximum ebb of 0.97 m/s (Figure 74 and Figure 75) and spring tide maximum ebb of 1.32 m/s (Figure 76 and Figure 77). Well-defined eddies form at the landward tip of the spur in all but the maximum flood phase for both types of tides. This was not observed for the Emergent Spur with Channel design. During the last hour of flood for the neap tide (Figure 74d), the eddy actually moves in behind the south jetty, working on the sediment in this mask, which had +1.6% volume change.

During maximum flood for the spring tide (Figure 77c), the southerly flow across the ebb shoal splits on the downdrift side of the outer bypass bar, with the northern portion turning clockwise to join the flood tide back toward the inlet (z = 4 m) and the southern part moving further down the south beach before splitting again in the nearshore (z = 3 m). This corresponds with the alternating deposition and erosion pattern observed on the net change plot and, specifically, to the intense patches of both types of change.

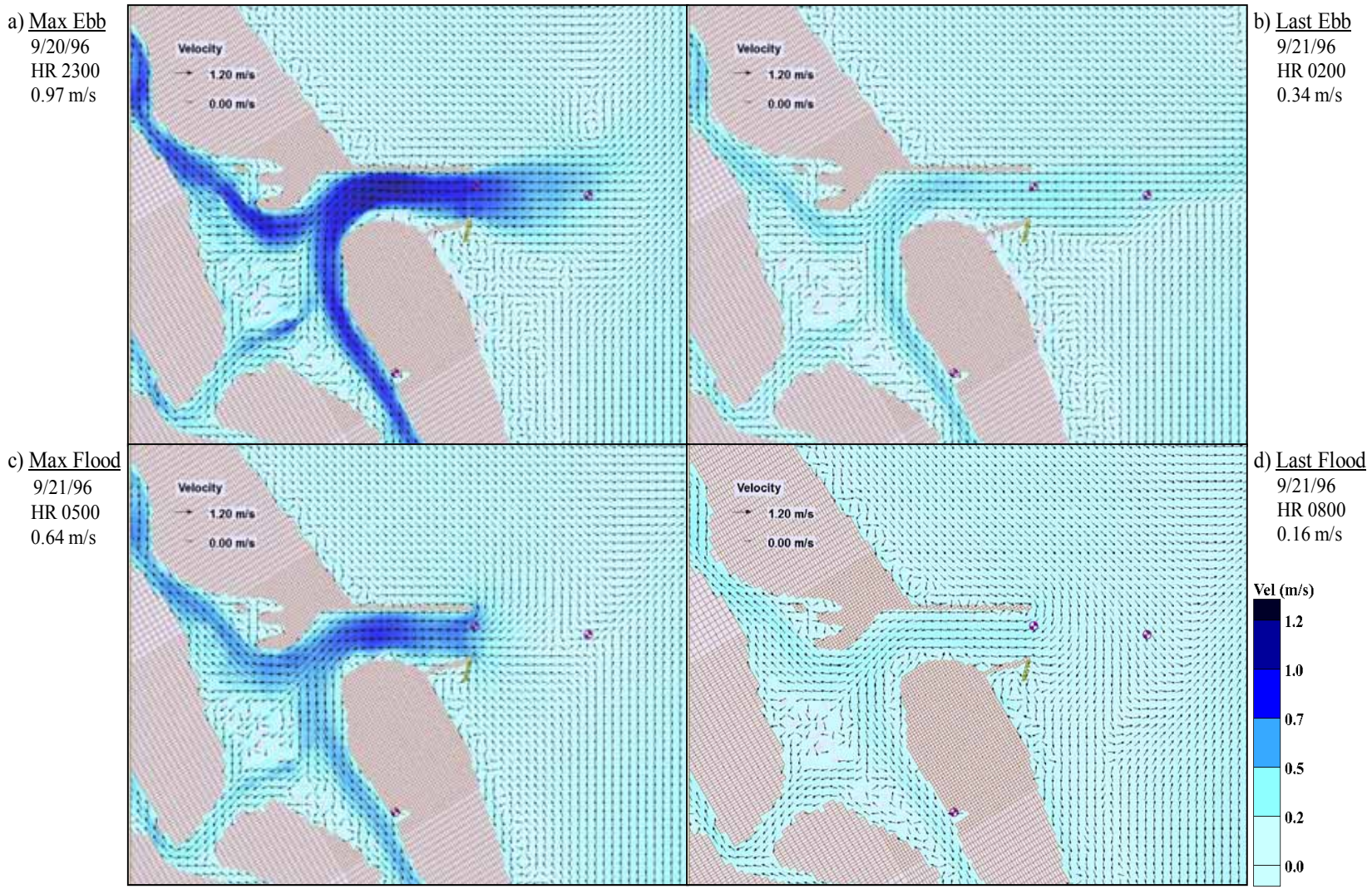

Figure 74. Flow velocities for South Jetty Extension with SS and C during neap tide of 9/20/96. Maximum value from cell 26447 near HB.

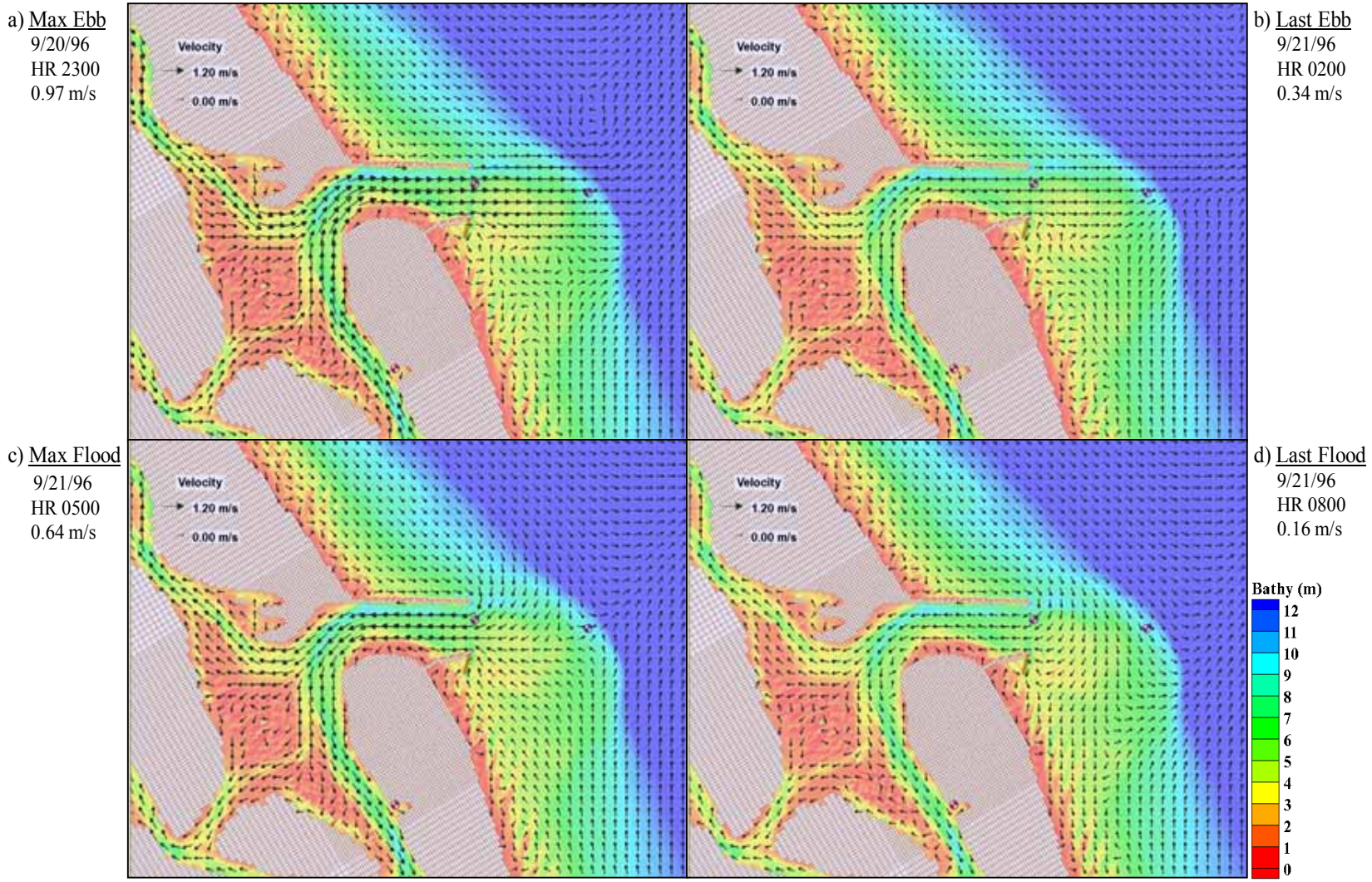

Figure 75. Morphology and flow velocities for South Jetty Extension with SS and C during neap tide of 9/20/96. Maximum value from cell 26447 near HB.

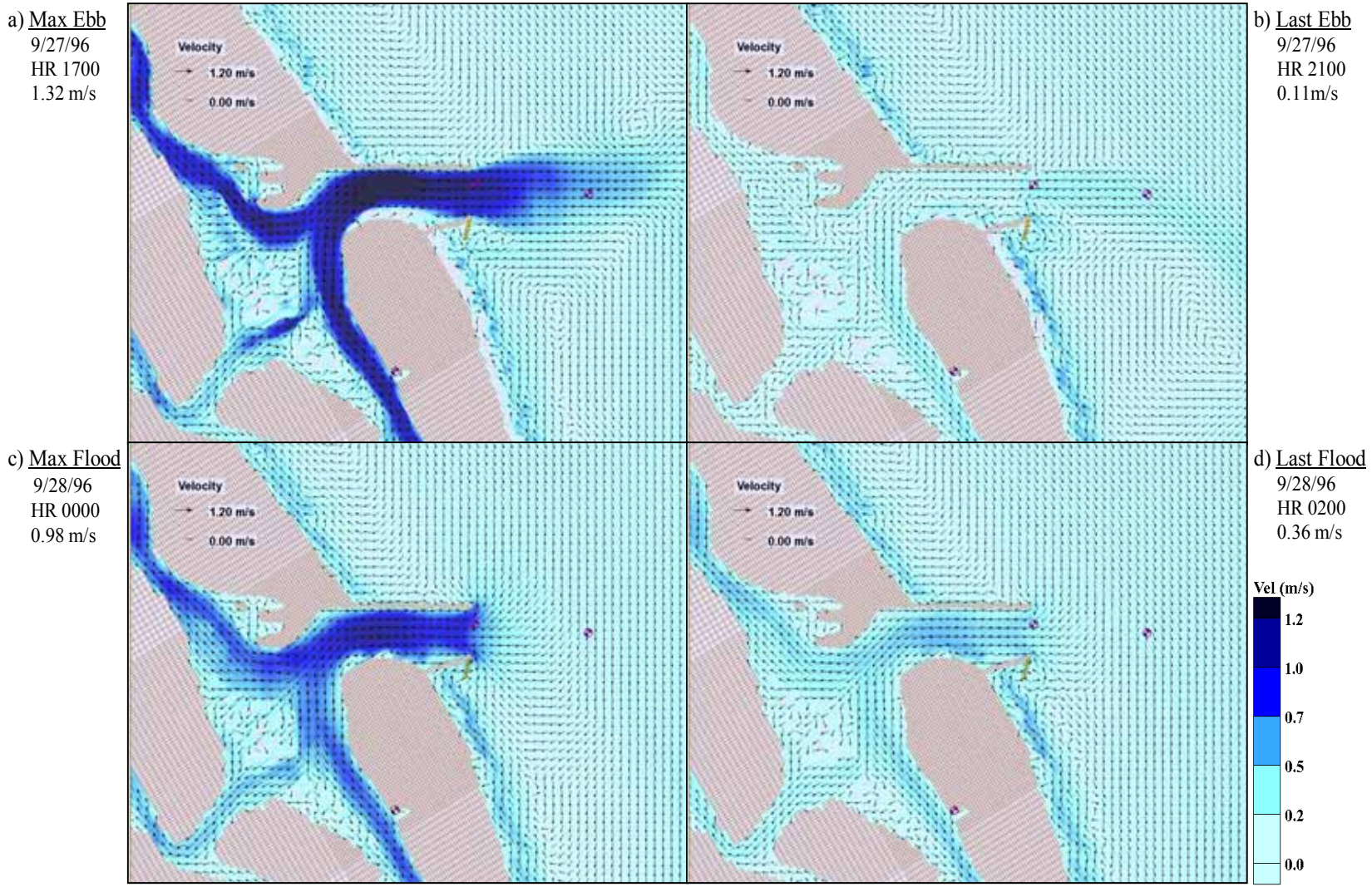

Figure 76. Flow velocities for South Jetty Extension with SS and C during spring tide of 9/27/96. Maximum value from cell 26447 near HB.

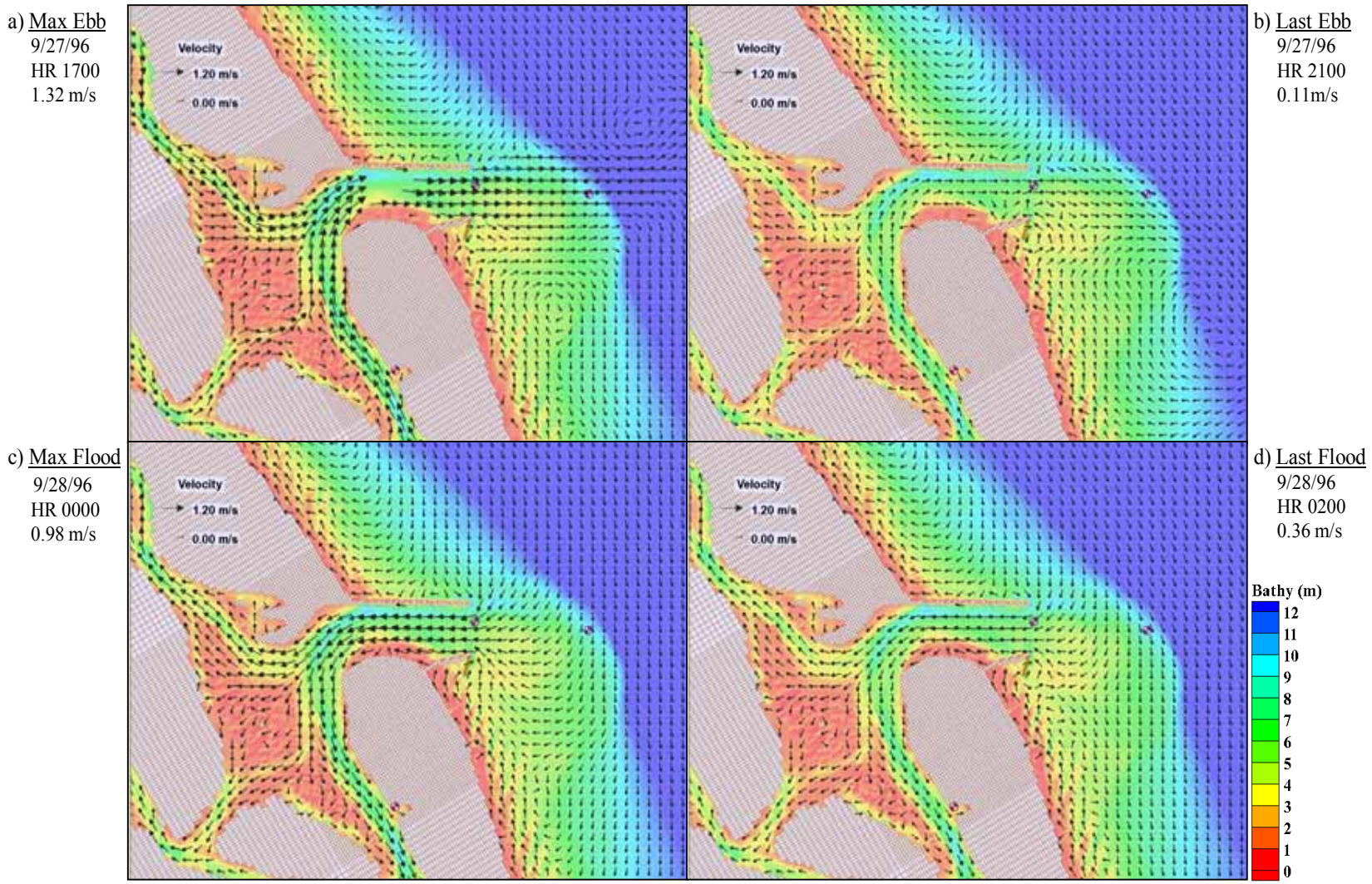

Figure 77. Morphology and flow velocities for South Jetty Extension with SS and C during spring tide of 9/27/96. Maximum value from cell 26447 near HB.

5.2.6B South Jetty Extension with Submergent Spur, HB, and Channel

The addition of the Hard Bottom basin (HB) is identified in the morphology contour plots (Figure 78 and Figure 79) by the gold triangles in the inlet. At the end of 3-months, the south beaches have been reworked to depths of about 0 m in parts of the nearshore. The downdrift bypass bar has impounded more sediment than in the Channel version (z ~ 1m).

The net topographic change plot (Figure 80) shows little deposition in the Basin Channel (Δz ~ 1 m). However, scour occurring on the southern edge of the Hard Bottom subset mask (Δz = -2 m) brings a total volume increase of +2.8% (Table 13) to the larger sub-domain. The Channel~4.6m sub-domain self-scours along the entire length producing a net change of approximately -1.5 m and a total volume loss of -5.8%. The South Spit shows more deposition than for the previous Submergent Spur design (Δz ~ +2 m), but with a similar pattern for the deposition adjacent to the jetty inside the inlet, for a total volume gain of +4.4% for the South Spit. Scouring along the spur/south jetty tip is again present, contributing to decrease in volume for the Ebb Complex of -0.5%. The area along the south beaches that previously saw intense deposition adjacent to the intense scour appears again, but over a larger area, for a total volume loss of -0.2% for the South Beach. The navigation channel, Rockhouse Creek, cutting though the flood shoal shows deposition of up to +2 m. However, the volume change for the Flood Shoal is -0.3%, indicating that the spots of intense scour (deep blue) on the flood shoal contribute to the total change.

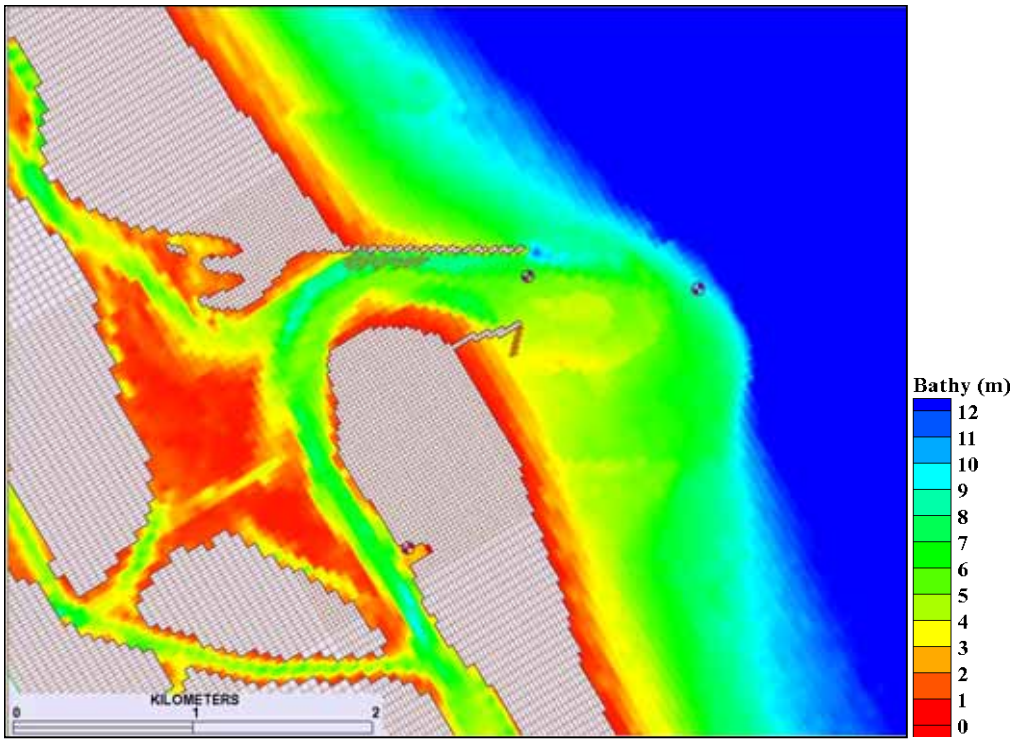

Figure 78. Morphology at 0 hr for South Jetty Extension with SS, HB and C.

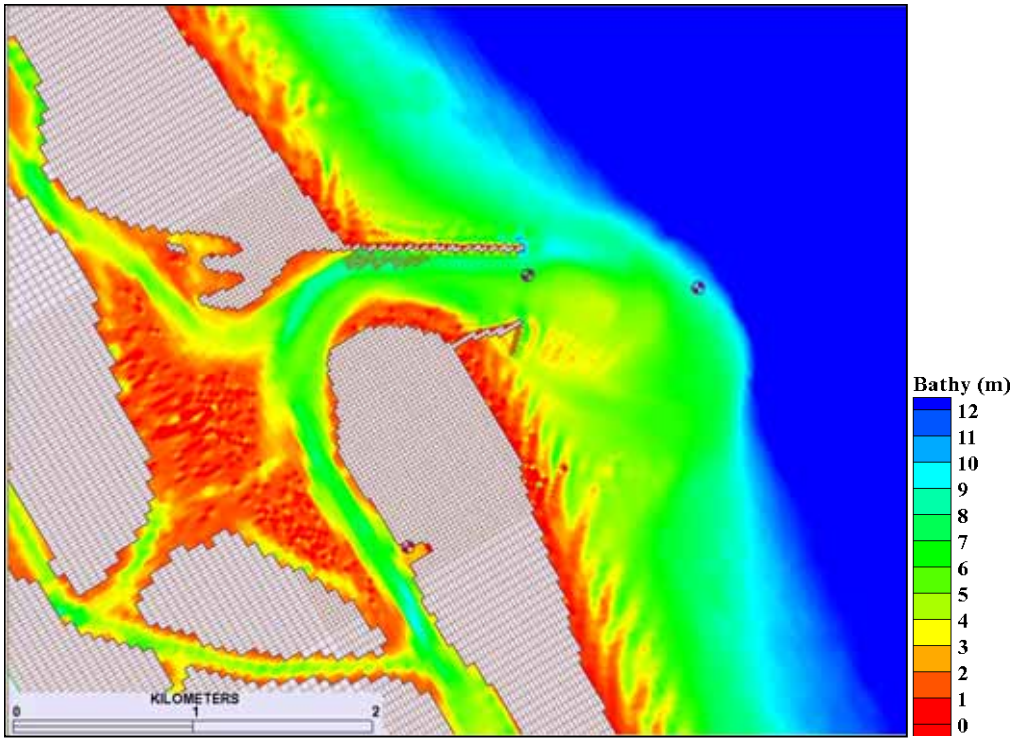

Figure 79. Morphology at 2197 hr (3 months) for South Jetty Extension with SS, HB and C.

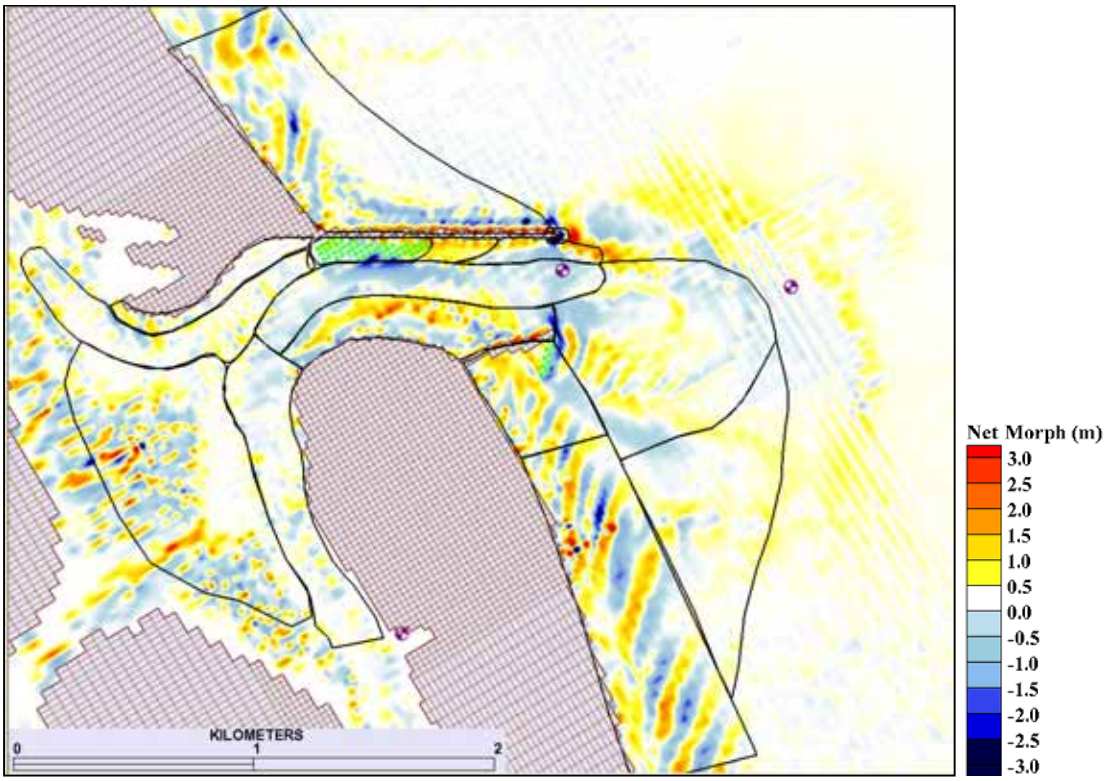

Figure 80. Net 3-month change in morphology for South Jetty Extension with SS, HB, and C.

Table 13. Volume Change (3 months) for South Jetty Extension with SS, HB, and C: Normalized (%) and Net (Δvol).

Polygon Mask	%	Δvol (m^3)
Ebb complex	-0.51	-11977
South spit	4.36	21449
Channel ~4.6m	-5.78	-70499
Channel >7m	0.65	1867
Basin channel	2.79	14667
North channel	0.40	3854
South Jetty	1.39	4934
South channel	-0.55	-7366
South beach	-0.23	-3988
Outer bypass	0.89	20530
North tip	-42.32	-9235
North spit	2.53	3299
North beach	-0.71	-14759
Hard bottom	-0.04	-125
Flood shoal	-0.27	-2341

For the circulation patterns during neap and spring tides (Figure 81-84), predicted velocity vectors show less flow over the flood shoal than for the design without the Hard Bottom as well as reduced magnitudes for the flow through Rockhouse Creek. The eddies that formed at the landward tip of the spur are still present. All maximum velocities are of equal magnitudes to the previous Submergent Spur design, with maximum ebb for neap tide of 0.99 m/s and maximum ebb for spring tide of 1.40 m/s. No other major differences in circulation appear.

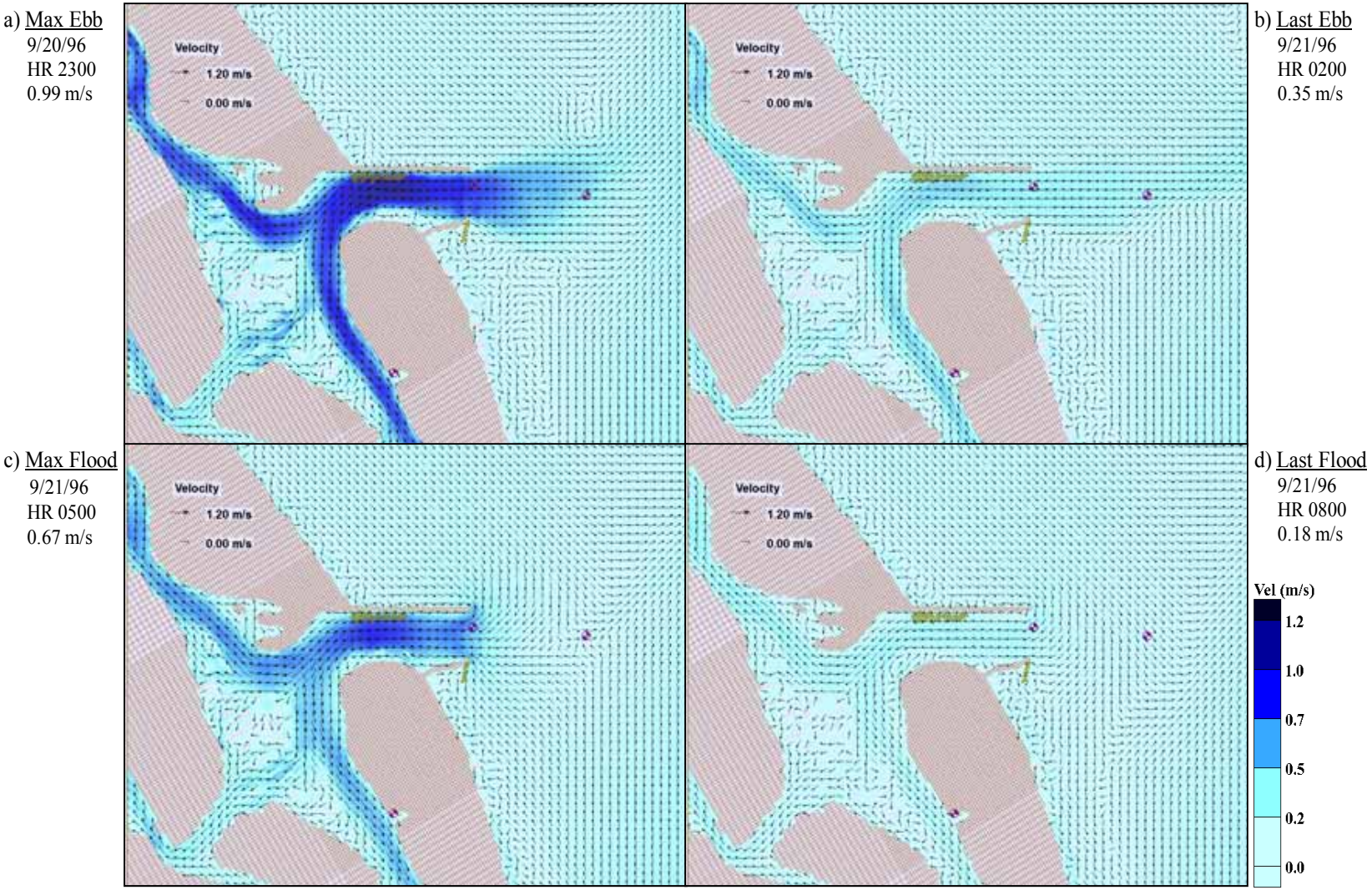

Figure 81. Flow velocities for South Jetty Extension with SS, HB and C during neap tide of 9/20/96. Maximum value from cell 26449 in channel.

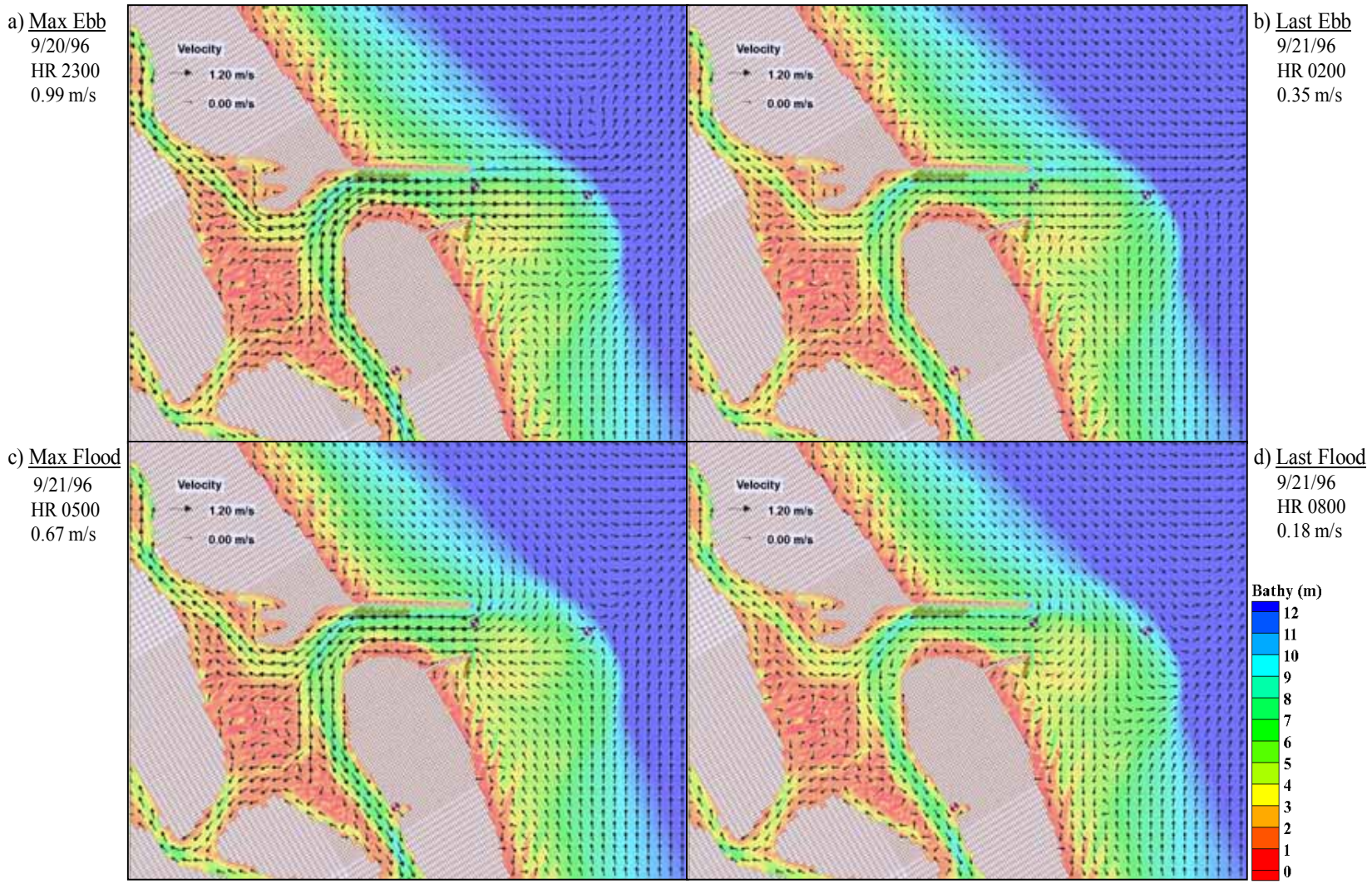

Figure 82. Morphology and flow velocities for South Jetty Extension with SS, HB and C during neap tide of 9/20/96. Maximum value from cell 26449 in channel.

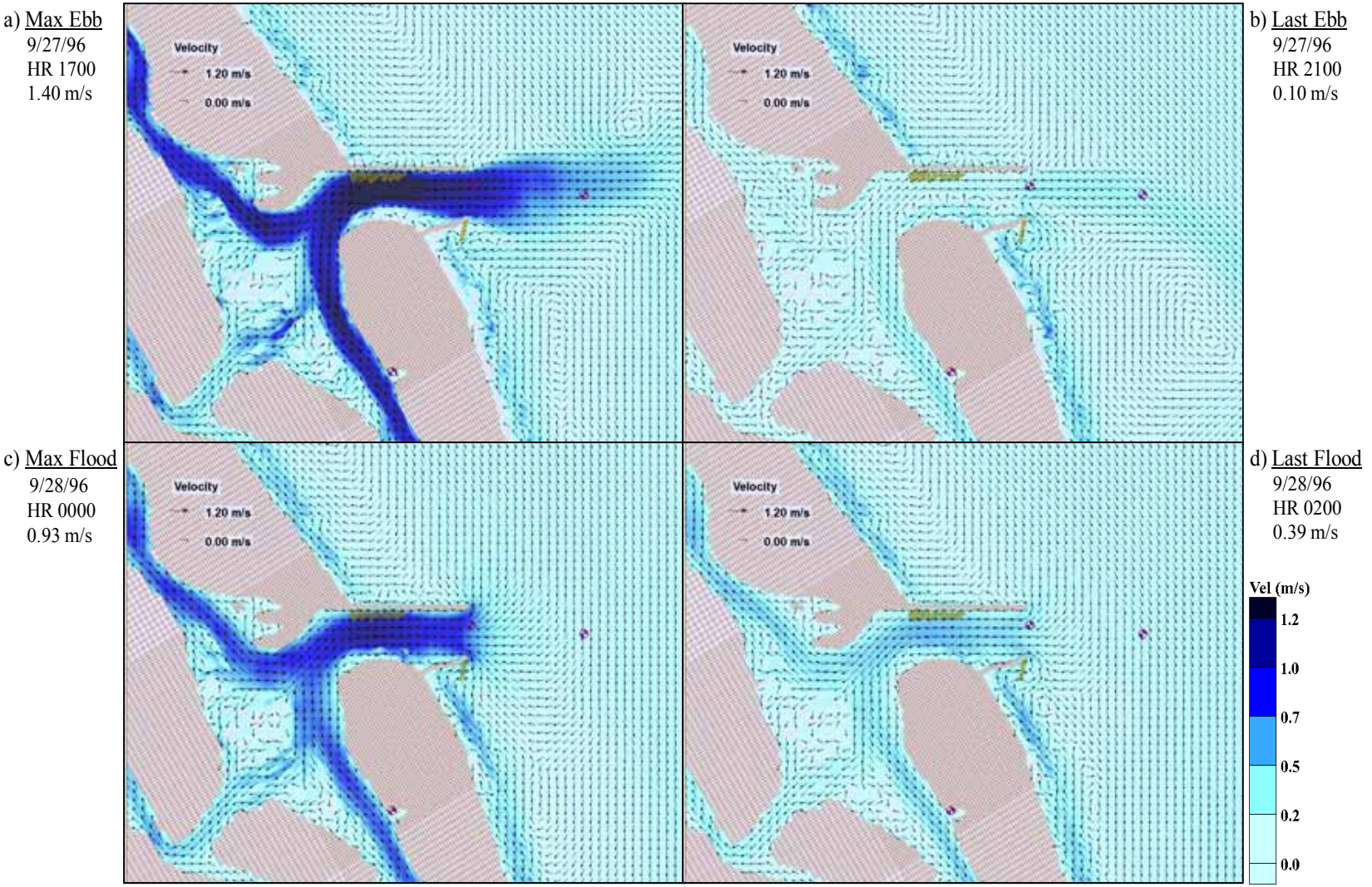

Figure 83. Flow velocity for South Jetty Extension with SS, HB and C during spring tide of 9/27/96. Maximum value from cell 26449 in channel.

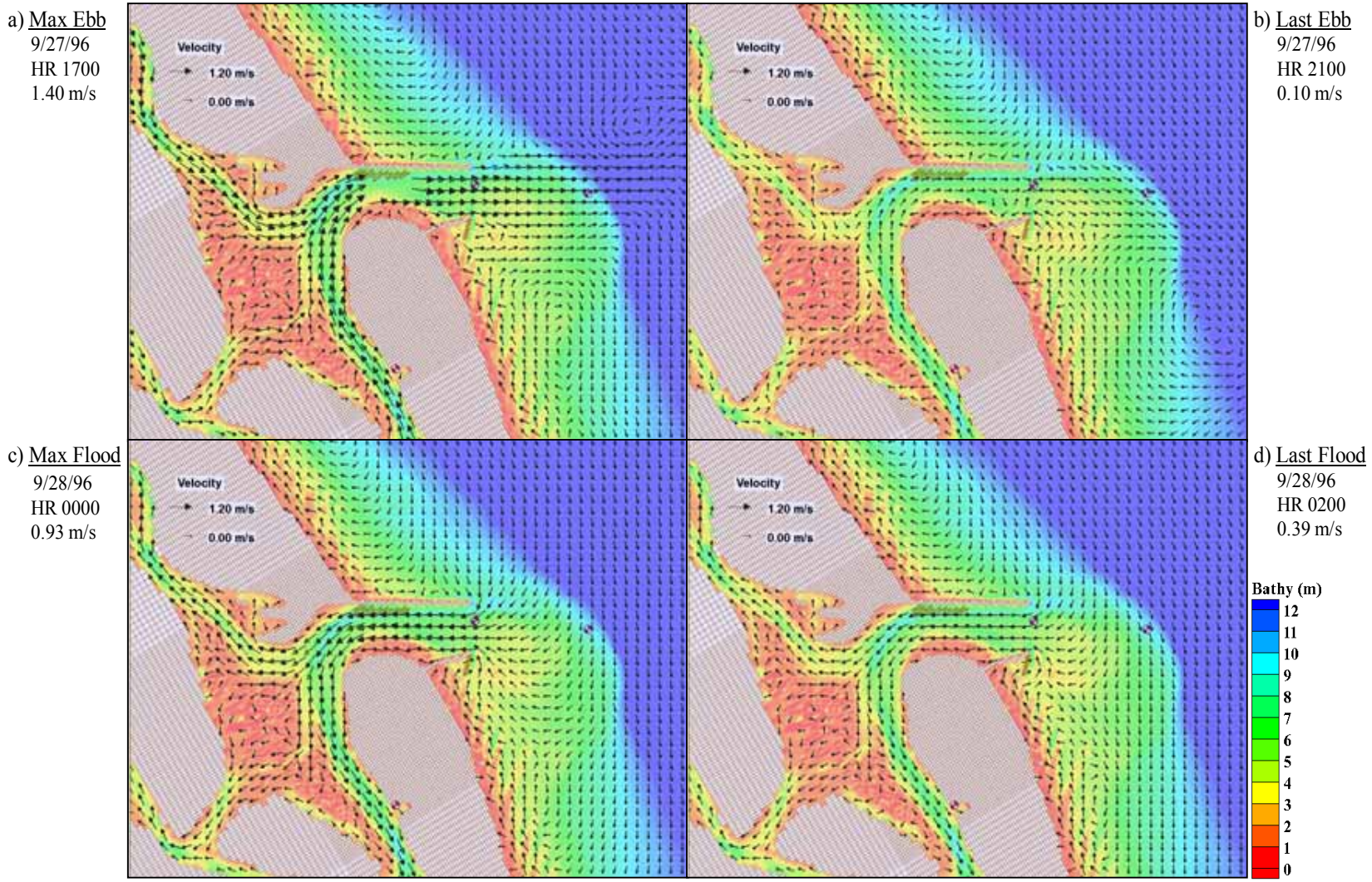

Figure 84. Morphology and flow velocities for South Jetty Extension with SS, HB and C during spring tide of 9/27/96. Maximum value from cell 26449 in channel.

5.2.7 Comparison of Short-Term/Preliminary Runs

This section provides a cumulative examination of the morphologic changes produced by each design option with consideration for how the hydrodynamics of relevant designs impacts the observed morphologies. Details for each design option are found in previous subheadings. Abbreviations for the design options, referenced in Table 3, will be employed in this section to facilitate their comparison.

As previously discussed, the relevance of the normalized volume changes within identified polygon masks needs to be understood with reference to the net morphology that occurs in that area. Although the inlet system has key sub-domains that behave in both general and site-specific fashion, the very nature of shifting sand bodies makes it difficult to set boundaries that are appropriate for all jetty stabilization designs, which complicates their comparison. The combination of this artifact of analysis with the sheer volume of data generated from numerical model outputs requires the assignment of analytical masks that may not be as specific and localized as one would prefer. Therefore, it is important to combine the quantitative net volume change analysis with qualitative net topographic change analysis to help decipher the true nature of the total gains, or losses. This was especially evident when intense erosion occurred along a boundary between masks and shifted in and out of a specific analysis mask from one design to another, changing the total volume from gain to loss in one fell swoop. With this caveat in mind, a major step in choosing the optimal design alternative for Ponce de Leon Inlet is to compare the volume changes (Table 14) in key areas of concern.

All the net morphology comparison contour plots presented in this section (Figure 85 - 87) include the Present Design net changes for ease of comparison. However, the masks are no longer highlighted on the plots to get a better sense of the scope of the design changes. If necessary, the reader should refer to Figure 20 to review the mask/sub-domain locations.

Table 14. Comparison of Normalized Volume Change (%) for Short-Term Runs (3 months).

Polygon Mask	present Present	a1 SJ	a2 SJR	a7 SJ/W/HB	a9 SJ/HB	a11 SJ/ES	a12 SJ/ES/C	a13 SJ/ES/HB	a14 SJ/SS/C	a15 SJ/SS/HB
Ebb complex	-0.19	-0.67	0.04	-0.61	-0.81	0.09	0.39	-0.58	-0.38	-0.51
South spit	12.98	1.28	2.34	-0.02	2.22	0.63	3.48	4.18	3.75	4.36
Channel~4.6m	-6.62	-4.42	-5.11	-2.66	-4.28	-4.65	-4.93	-5.79	-5.66	-5.78
Channel >7m	-1.77	1.15	2.52	1.92	2.12	-0.37	-0.41	0.19	-0.47	0.65
Basin channel	4.58	5.54	6.16	9.85	4.48	4.67	4.19	2.68	3.30	2.79
North channel	0.58	0.41	0.36	0.84	0.49	0.55	0.40	0.29	0.24	0.40
South Jetty	-3.31	2.94	0.62	6.10	3.65	1.59	0.98	0.83	1.64	1.39
South channel	-0.88	-0.68	-0.33	-0.98	-0.52	-0.61	0.72	-1.03	-0.70	-0.55
South beach	0.00	0.59	1.31	0.94	0.58	-0.23	0.66	-0.29	-0.04	-0.23
Outer bypass	0.46	0.68	0.37	0.56	0.81	0.58	0.77	0.80	0.85	0.89
North tip	-33.76	-38.77	-11.09	-41.63	-37.97	-39.26	-35.41	-41.38	-41.67	-42.32
North spit	3.68	3.69	3.20	4.31	3.41	3.43	2.93	3.29	2.34	2.53
North beach	-1.32	-1.75	-2.54	-1.53	-1.75	-1.22	-0.88	-0.98	-0.55	-0.71
Hard bottom	1.08	2.46	2.90	8.33	1.89	1.90	1.98	-0.38	0.63	-0.04
Flood shoal	-1.88	-0.90	-0.13	-0.35	-1.39	-2.79	-1.78	-2.25	-1.24	-0.27

Starting with the South Spit, all alternate designs provide relief from the extreme shoaling that the Present Design produces (+13% volume gain, and $\Delta z > +3$m along the entire length of the south spit). As far as the volume change is concerned, the SJR, SJ/W/HB and SJ/ES option reduce the shoaling the most for the South Spit; however, the net change plots indicate the SJ/HB may provide the greatest relief (Figure 85).

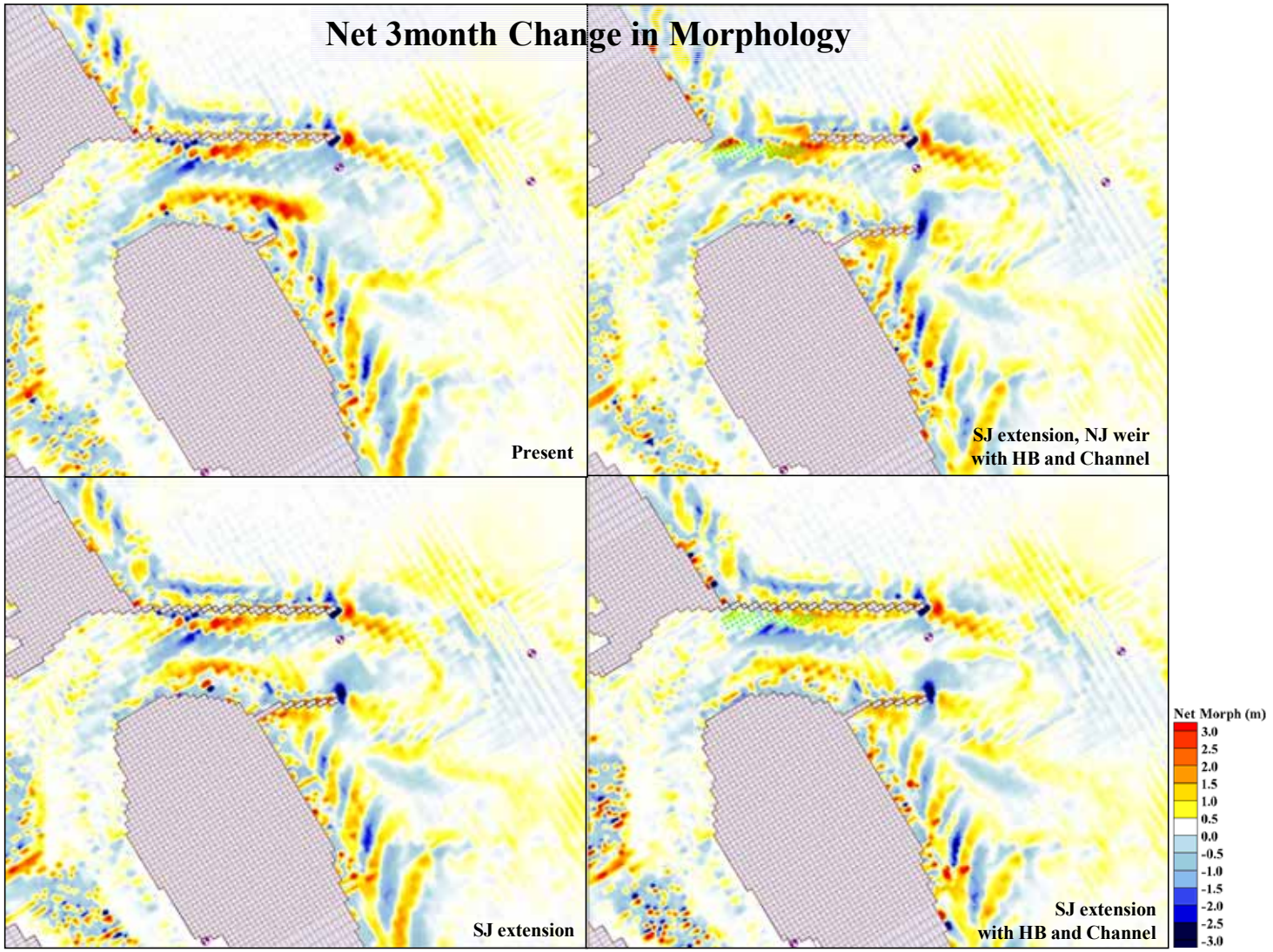

Figure 85. Comparison of net 3-month change in morphology for South Jetty Extensions with no Spur.

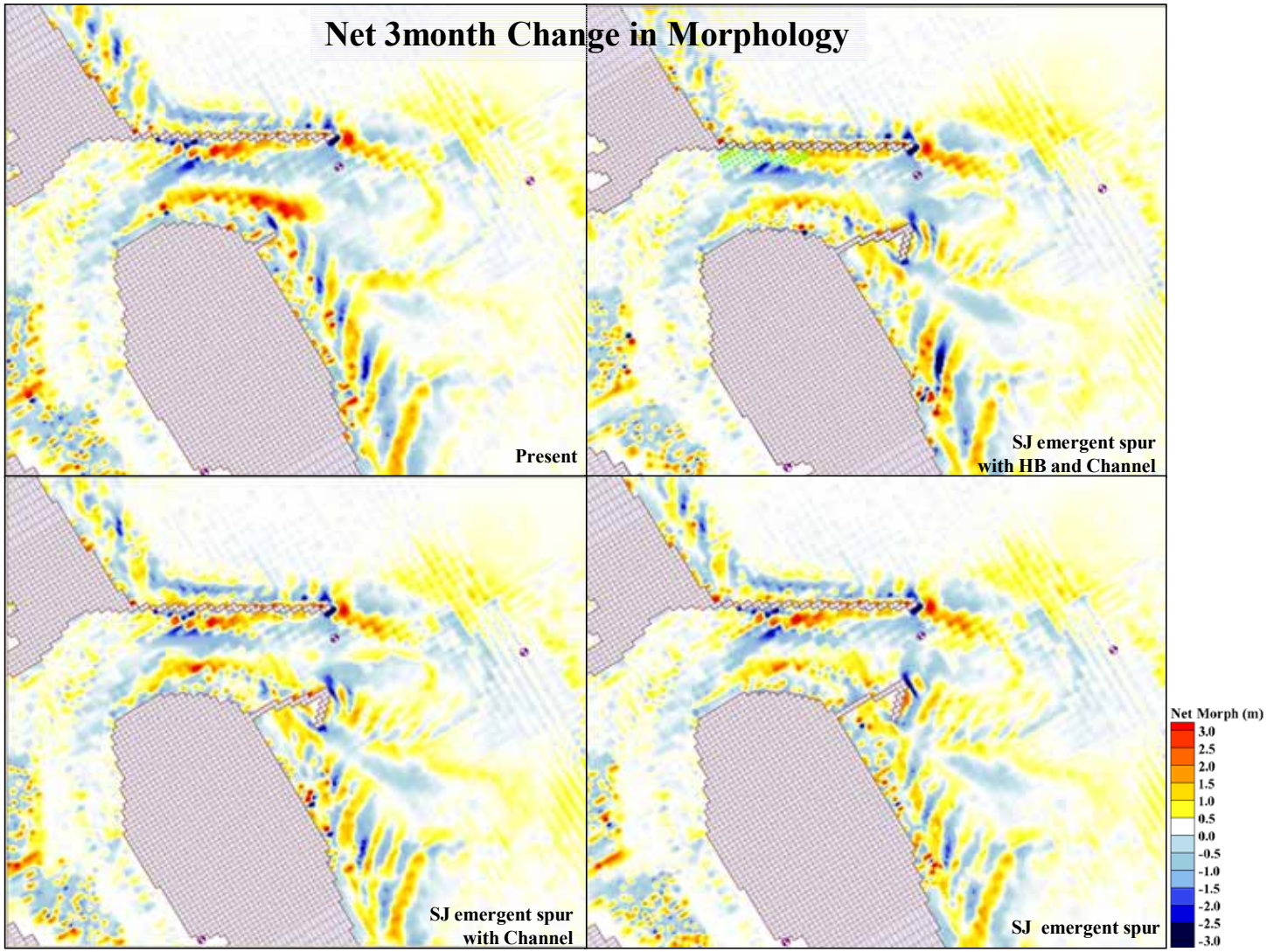

Figure 86. Comparison of net 3-month change in morphology for South Jetty Extensions with Emergent Spur.

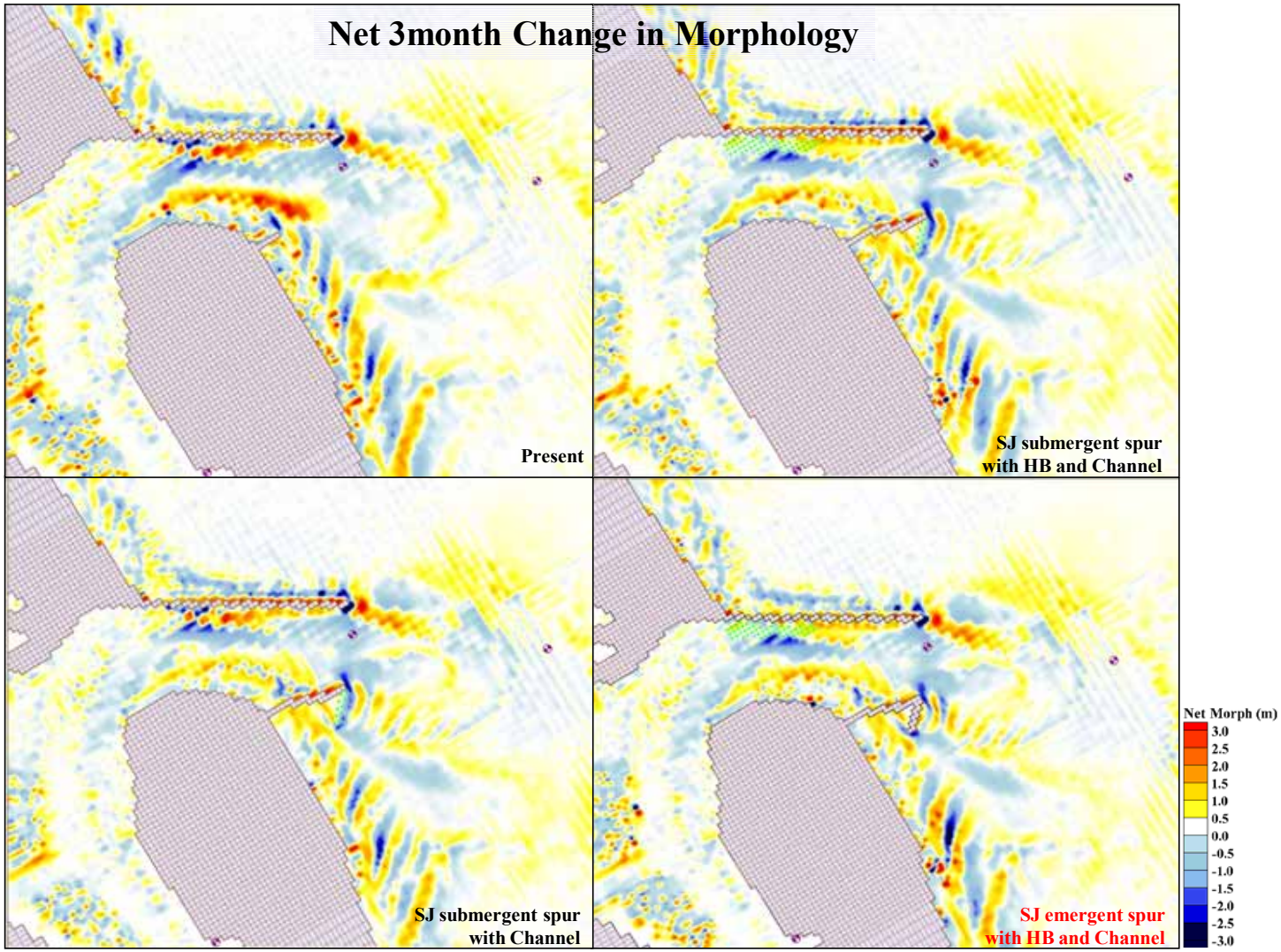

Figure 87. Comparison of net 3-month change in morphology for South Jetty Extensions with Submergent Spurs (and one Emergent Spur, HB and C).

For the adjacent Channel~4.6m, all designs continue the self-scouring ability of this navigation channel (-6.6%), except that the SJ/W/HB (Figure 85) is far less efficient than other designs (-2.7% volume loss, and $\Delta z \sim -1$ m). As expected, the SJ/W/HB is successful at filling in the Basin Channel (+9.9% volume gain), but other designs produce equivalent gains as the Present Design does (+4.6%) and consideration must be made for those designs that filled in the basin for the starting bathymetry.

With this factor in mind, those designs that showed deposition in the Channel>7m mask may actually contribute more to the repositioning of the navigation channel away from the north jetty since this sub-domain was not changed in starting bathymetry for any designs. Where the Present Design actually continues to show scouring in this area ($\Delta \sim -1$ m and -1.8% volume loss), all other designs improve on this situation to varying degrees of success, with the SJR (+2.5%), SJ/HB (+2.1%), SJ/W/HB (+1.9%), and SJ (+1.2%) having the largest volume gains.

The Hard Bottom subset of the Basin Channel mask was examined to see how the designs that used the HB option performed. All of these designs showed volume gains for the Basin Channel, but only those designs without the addition of a spur (SJ/W/HB and SJ/HB) also showed net accretion, specifically over the rubble mound artificial hard bottom. Given that the majority of tidal volume flows directly across this area through the weir opening, it is no surprise that the SJ/W/HB performed the best with a volume gain of +8.3%, which represents the majority of the Basin Channel sub-domain of +9.9%, of which it is a part. The SJ/HB design showed a +1.9% volume increase, out of the larger +4.5% Basin Channel mask. The Spur HB designs actually

predicted HB volume losses of -0.4% out of the +2.7% for the larger Basin Channel gains for the SJ/ES/HB design and -0.04% out of the +2.8% Basin Channel gains for the SJ/SS/HB design.

The South Jetty sub-domain accretes in all but the Present Design (-3.3%). This is actually an exaggeratedly large area for understanding the immediate morphologic changes downdrift of an inlet encompassing both the upper shoreface behind the south jetty, parts of the downdrift bypass bar, and the scouring areas at the south jetty tip depending on specific designs. Since all alternatives include extending the south jetty and show a range for volume changes of +0.6% for the SJR to 6.1% for the SJ/W/HB, performance here becomes more flexible variable. It is worth noting that the SJR option, which is deemed cost-prohibitive and not fully included in the final analysis for this study, may have the lowest gains in this mask, but consideration should be made for the choice to keep the present south jetty in the downdrift of the newly rebuilt and extended south jetty. Doing so would clearly have an impact on the South Jetty sub-domain volume changes for this design.

The South Beach showed no change in volume at all for the Present Design and any design that showed volume losses did so minimally, with the largest loss being for the SJ/ES/HB (-0.3%). The designs showing gains in volume are the SJR (+1.3%), SJ/W/HB (+0.9%), SJ/ES/C (+0.7%), SJ and SJ/HB (+0.6%). All designs, present and alternate, show the hydrodynamic effect of reversals in transport direction by virtue of the alternating deposition and erosion pattern observed on the net change contour plots, as well as in the ending morphology images previously presented.

For the Outer Bypass mask, all designs except the SJR produce volume gains of greater magnitude than those of the Present Design (+0.5%). The SJR design only accumulates +0.4% total sediment. All other designs contribute between +0.6 to +0.9% increases in volume. This sub-domain actually covers the farthest reaches of the bypass pathway and acts as a storage area for cross-shore transport, which is why all erosional net changes (light blue) occur on the landward side of the mask.

Predicted design performance in the Ebb Complex is perhaps the most difficult to compare. With the addition of the spur option and the dynamic nature of the downdrift bypass bar in response to changing hydrodynamic conditions, there was no real way to cover the planform area and account for detailed net volume changes. In hindsight, small subsets in the adjacent corners of the three masks close to the jetty (South Spit, South Jetty, and Ebb Complex) would have proved quantitatively useful for reference on the true nature of the volume change in these areas. Still, net topographic contours suffice for qualitatively ascertaining localized performance of the designs.

The largest gain in volume for the Ebb Complex occurs for the SJ/ES/C design, which showed a volume gain of +0.4% (Figure 59 and Figure 86). This occurs even though the intense scour at the south jetty tip is included in the total volume. The only other designs to show any gain in volume were the SJR (+0.04%) and the SJ/ES (+0.09%). In comparing performance across all sub-domains, it should be noted that the lower Ebb Complex volume gains for the SJ/ES design, as compared with those of the SJ/ES/C design, may be due to the orientation of the intense scour at the south jetty tip. For the SJ/ES option, these losses contribute to the noticeably reduced gain in volume of only +0.6% for the South Spit.

Scouring at the north jetty tip is an expected event and this small mask wrapped closely around the tip of the jetty to capture the intensity of the changes. The only design to truly cause a prominent reduction in the scouring of the North Tip sub-domain was the SJR. By rebuilding the jetty straighter, parallel, and closer to the north jetty, the width of the entrance was reduced and the flow more symmetrical. The net effect of which was a reduction in shoaling from -34% volume loss for the Present Design, to a mere -11% for the SJR. All other design options performed equally well, in that, they were all within the -35 to -42% volume loss.

The North Beach supplies the bulk of the sediment being captured within the inlet. The remaining sediment comprising the inlet morphology comes from the southern beaches during periods of longshore transport reversal or from the lagoon system. Although it is virtually impossible to account for the exact source of sediment entering the inlet, given the constant reworking that goes on at tidal inlets, the North Beach should show a cumulative volume loss; for the Present Design, that amounts to -1.3%. For the alternate designs, losses range from -0.6% for the SJ/SS/C to -2.5% for the SJR. Most designs show losses within ±0.5% of the Present Design conditions.

Based on the results of previous numerical modeling efforts aimed at redesigning Ponce de Leon Inlet (Taylor et al. 1996a, b; Srinivas and Taylor, 1999), the decision was made to revet the north spit with hardening by the addition of rubble mound from the landward edge of the north jetty fully around the western tip of the north spit (Figure 5). The ultimate goal was to bifurcate the lobes and re-dredge the north channel to remove the dogleg nature as it enters the main conveyance channel, although the original design called for such a dogleg design. Being deemed cost-

prohibitive, the full redesign of the north channel did not occur, but the revetment of the north spit was definitely considered worth adding to the budget. The North Spit mask covers the shoreline and shallow waters adjacent to the eastern part of the revetment and around the non-revetted southern lobe of the north spit. This area is subject to deposition for all designs ranging from 2.5 to 4.3% volume increases, with the Present Design showing +3.7%. All of the net change plots show very subtle net changes, mostly white to yellow in color (Δz = +0.5 m). The relatively large increases in total volume are a result of virtually no erosion observed in this mask.

The North Channel mask covers the dogleg hook of the north conveyance channel and shows virtually zero net change in bathymetry for any designs. The total volume increases range from approximately +0.2% for the SJ/SS/C and SJ/ES/HB designs to +0.8% for the SJ/W/HB designs. The Present Design increased by +0.6%. The South Channel, on the other hand, is able to scour ($\Delta z \sim$ -1 m) along the bend around the south spit and is observed to decrease in volume (~ -1%) for all but the SJ/ES/C design, which accumulates +0.7% sediment.

The Flood Shoal is difficult to fully observe in the net change plots due to the limits placed on the size of the images for comparative purposes. All the individual net change plots showed patchworks of blue and red/yellow indicating the dynamic nature of this sub-domain. The main concern here is for Rockhouse Creek to remain as direct passage from the ocean via the inlet to the Intercoastal Waterway (ICWW). For the comparison net morphology plots, the southwest corner indicates the location of this channel. In all the plots, there is a streak of intense deposition (red) just north of the

scour (light blue) in the center of the channel. Although losses by the SJ/ES/HB (-2.3%) and SJ/ES (-2.8%) are the most advantageous of the designs, only the HB version actually showed the lowest deposition ($\Delta z \sim +1.5$ m) in Rockhouse Creek (Figure 86). The Present Design lost -1.9% volume and the SJR lost the least volume (-0.1%).

Thoughts on which design should be supported are preliminary but helped to determine those runs worthy of the longer term analysis that includes the effects of tropical depressions in Fall and northeasterly events in Winter. For this 3-month analysis, the SJR is judged to be the best design option. However, due to engineering costs, it was decided to forego further modeling of this alternative. The SJ/W/HB option also performs quite well for all key areas of concern. Shoaling within the inlet was notably reduced for the South Spit (-0.02%), but the North Spit produced the largest volume gains among the designs (+4.31%). However, given that this spit is adjacent to the weir opening, it could be to be accessed, along with the rest of the designed deposition basin, for mechanical bypassing. Unfortunately, based on the present limits for weir design performance and recommendations made by Taylor et al (1996a, b), it was decided to forego long-term analysis of this design. The third best option is the South Jetty Extension, with no further modification. This design reduced accretion for the South Spit, increased scouring in the location of the original navigation channel and deposition in the present navigation channel, and allows sand to accumulate within the South Beach sub-domain. Although it loses more sand from the Ebb Complex as compared to the present configuration and a few other designs, the net topographic changes indicate this is likely an artifact of the intense scour at the south jetty tip.

5.3 Long-Term Models

This section presents the results of the best 3-month options that were run for ten months to show fall and winter storms as part of the longer term changes. The time period was from July, 1996 to April, 1997. Each design category is presented individually, with reference to other designs as appropriate, followed with a cumulative comparison of all designs. Starting morphology images for each design is the same as for the short-term runs and are presented here as a visual reference.

5.3.1 Present Conditions

Starting morphology for the Present Design (Figure 88) shows a general smoothing of the contours and that by the end of the 10-month run (Figure 89) the passage through Rockhouse Creek is < 2 m. The shoal in the North Channel (western tip of north spit) shifted northward into the cove. Shoaling on the south spit continued and, although it is not as shallow in the centerline of the inlet to the west, the depths at the inlet entrance (z = 2 to 3 m) are certainly a concern for navigation. Scouring at the north jetty tip has wrapped around and into the inlet and has connected with the rest of the deep, shifted navigation channel now reduced a bit (z ~9 m). There is evidence that this deepened channel has shifted toward the center of the entrance. Whereas navigation through this shifted channel is beneficial for keeping vessels away from the jetty structure, it now puts them close to the newly formed shoal from the south. Depths over the ebb shoal have increased (z ~ 4 to 5 m) and evidence of sand transport to the south is clear.

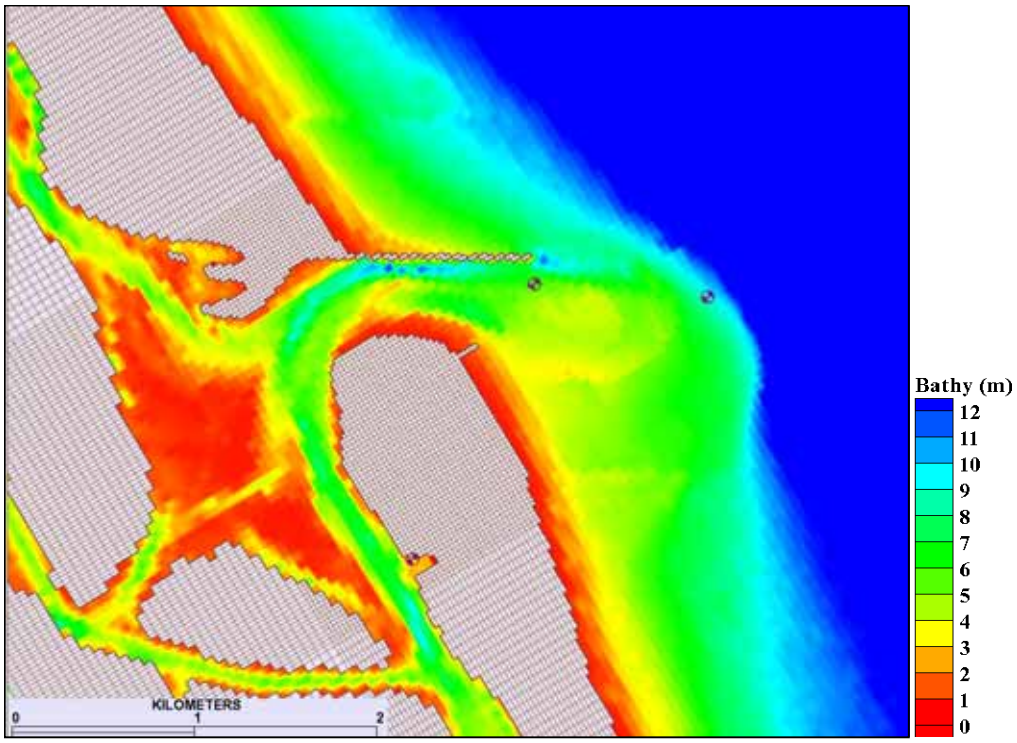

Figure 88. Morphology at 0 hr for Present Design.

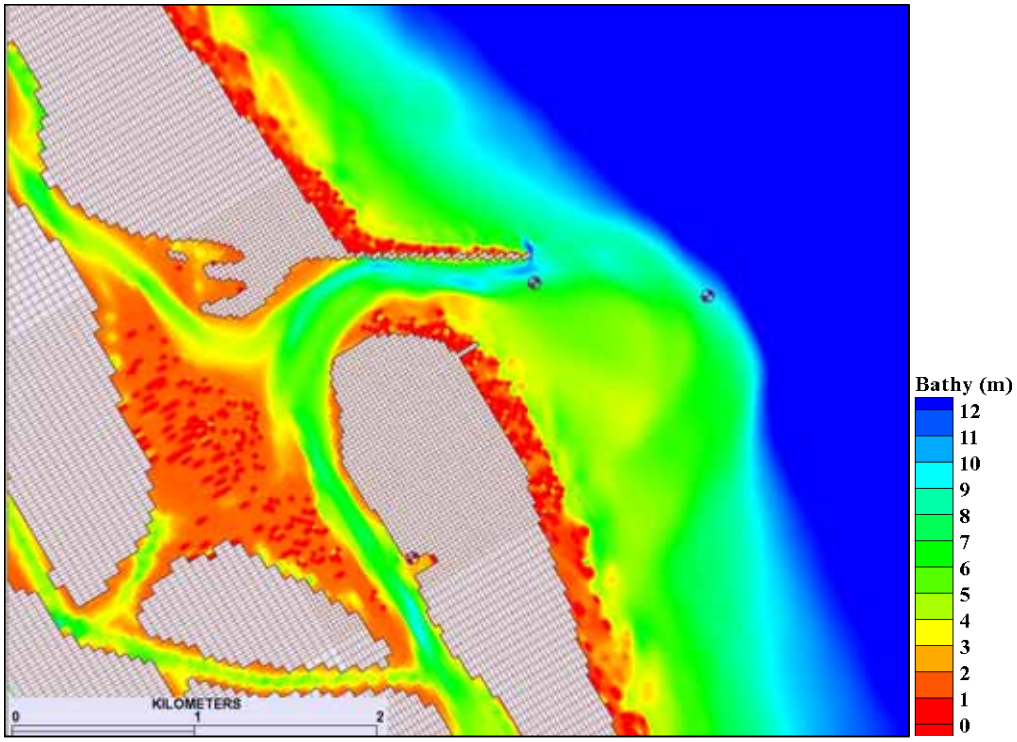

Figure 89. Morphology at 7284 hr (10 months) for Present Design.

The net change in morphology (Figure 90) highlights the migration of the deep navigation channel toward the centerline discussed above. Scouring of more than -3 m occurs here, whereas deposition just south of the channel is greater than +3 m. Since these two major areas of activity lie across mask boundaries, total volume changes (Table 15) are likely skewed and should be handled cautiously during comparisons. Channel>7m shows a volume loss of -21%, whereas Channel~4.6m shows only -13%. Shallowing of the present navigation channel along the north jetty observed in the final morphology image shows to be a change of more than +3 m in places. However, volume losses in the western half of this basin, in the Hard Bottom subset (-2.5%), also contribute making the total volume change for the Basin Channel +4.1%. This change for the Basin Channel is on par with the 3-month analysis, but for the Hard Bottom the predicted 10-month loss is greater than its 3-month gain had been.

Although scouring of shoal in the North Channel is present (light blue), it was not enough to compensate for the accretion of +0.5 to +1.5 m producing a +3.3% gain (up from +0.6%). The opposite trend occurred for the North Spit with the volume gain reducing from +3.7% (3-month) to only +0.3%. The erosional concern at this North Spit that prompted the revetment is indicated from this analysis in that the depth change of about -0.8 m is now deposition for the North Channel. The South Spit gained about double the volume it had after 3 months and is now at +22%. The long-term effect of storm activity on the open coast is evident in that the Ebb Complex and South Jetty have both eroded ($\Delta z \sim -1.5$ m) passing sand to the Outer Bypass bar, as expected (+7.8% increase). North Beach shows accretion (+4.9%), whereas South Beach upper shoreface accretion does not compensate for erosion in the lower for a loss of -5.1%.

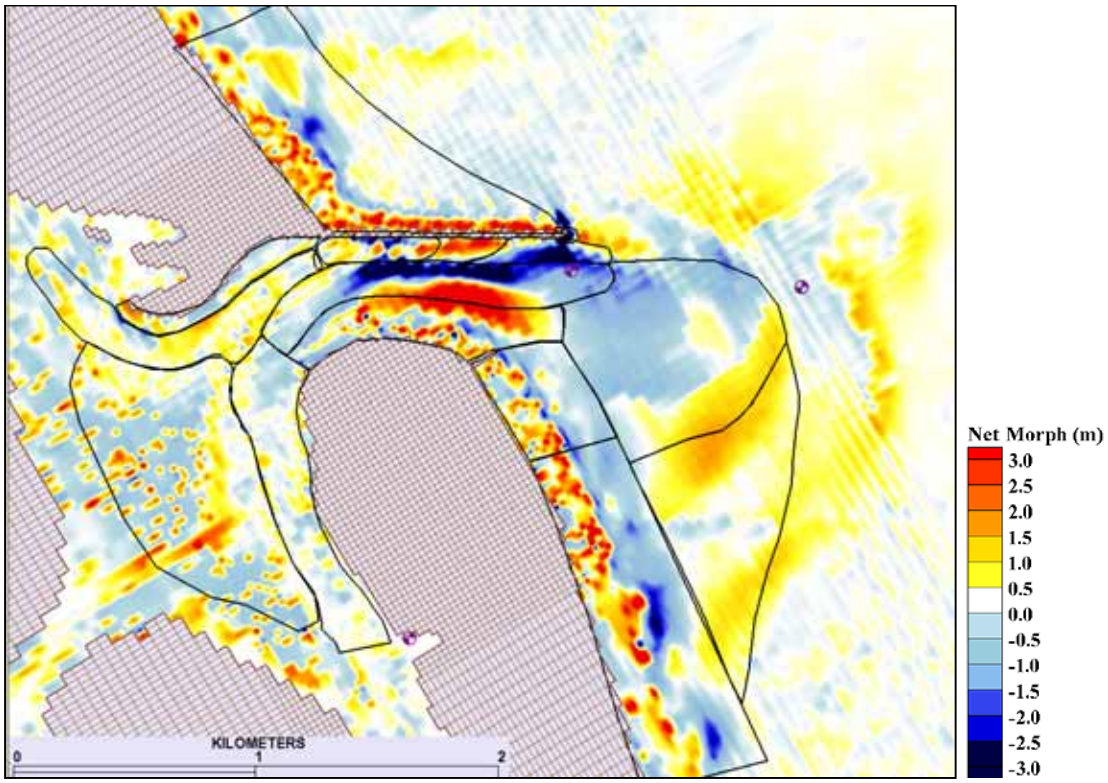

Figure 90. Net 10-month change in morphology for Present Design.

Table 15. Volume Change (10 months) Present Design: Normalized (%) and Net (Δvol).

Polygon Mask	%	Δvol (m^3)
Ebb complex	-8.62	-202505
South spit	21.54	108346
Channel ~4.6m	-13.29	-156190
Channel >7m	-20.58	-58833
Basin channel	4.12	23569
North channel	3.32	32004
South Jetty	-6.70	-26048
South channel	-1.25	-16647
South beach	-5.13	-89669
Outer bypass	7.76	178854
North tip	-51.35	-11204
North spit	0.26	338
North beach	4.85	100597
Hard bottom	-2.47	-8801
Flood shoal	-0.19	-1677

Maximum predicted velocities are reversed for the last spring tide (April 23, 1997) of the 10-month run (Figure 91 and Figure 92) with flood greater than ebb. A storm occurred during that tidal cycle having winds of 9.5 m/s out of the WNW (~280^{o}), reducing maximum ebb velocity to 1.28 m/s. By the time of maximum flood, the winds had increased to 13.1 m/s out of the SW contributing to an increased flood velocity of 1.33 m/s in the same eastern channel cell (25844, z = 8.3 m), with highest maximum flood velocity of 1.39 m/s found in the center of the inlet throat as the flow begins to round the south spit (cell 27065, z = 5.3 m). This storm also contributed to an ebb jet that was less diffuse coming out of the entrance and directed north of the ebb shoal. This shifted the eddy, typically forming here, farther north. The bidirectional flow found during last hour of ebb for the 3-month spring tide is limited to the southern shoal. Most of the northward current trying to creep around the short south jetty is re-directed offshore in the ebb flow. Velocities during this slack water are greater in magnitude than expected (0.42 m/s) and are of the same order as for the last hour of flood (0.41 m/s). The flood tide is also enhanced by the northern current offshore, which is 0.6 m/s just 1 km offshore and 0.3 m/s just 250 m from the shoreline. The shearing effect for the nearshore waters generates a number of eddies along the south beach.

During the last neap tide (April 30, 1997), circulation returns to normal as indicated by the southwest orientation of the ebb jet sweeping over the ebb shoal. Maximum ebb flow of 1.07 m/s (Figure 93 and Figure 94) joins the gentle southern currents (0.12 m/s) and forms an anticyclonic eddy just south of the jetty over the downdrift bypass bar. During the last hour of ebb, bidirectional flow within the inlet

reworks the sediment over the south spit well into the throat and centerline. Maximum flood velocities are higher than previously observed for neap tide in the Present Design (0.94 m/s), no doubt induced by the addition of the southern flow offshore. Unlike the last hour of the 3-month neap flood, anticyclonic eddies are formed along the south beaches with a large, well-defined one just offshore about 2 km south of the inlet (Figure 93d and Figure 94d).

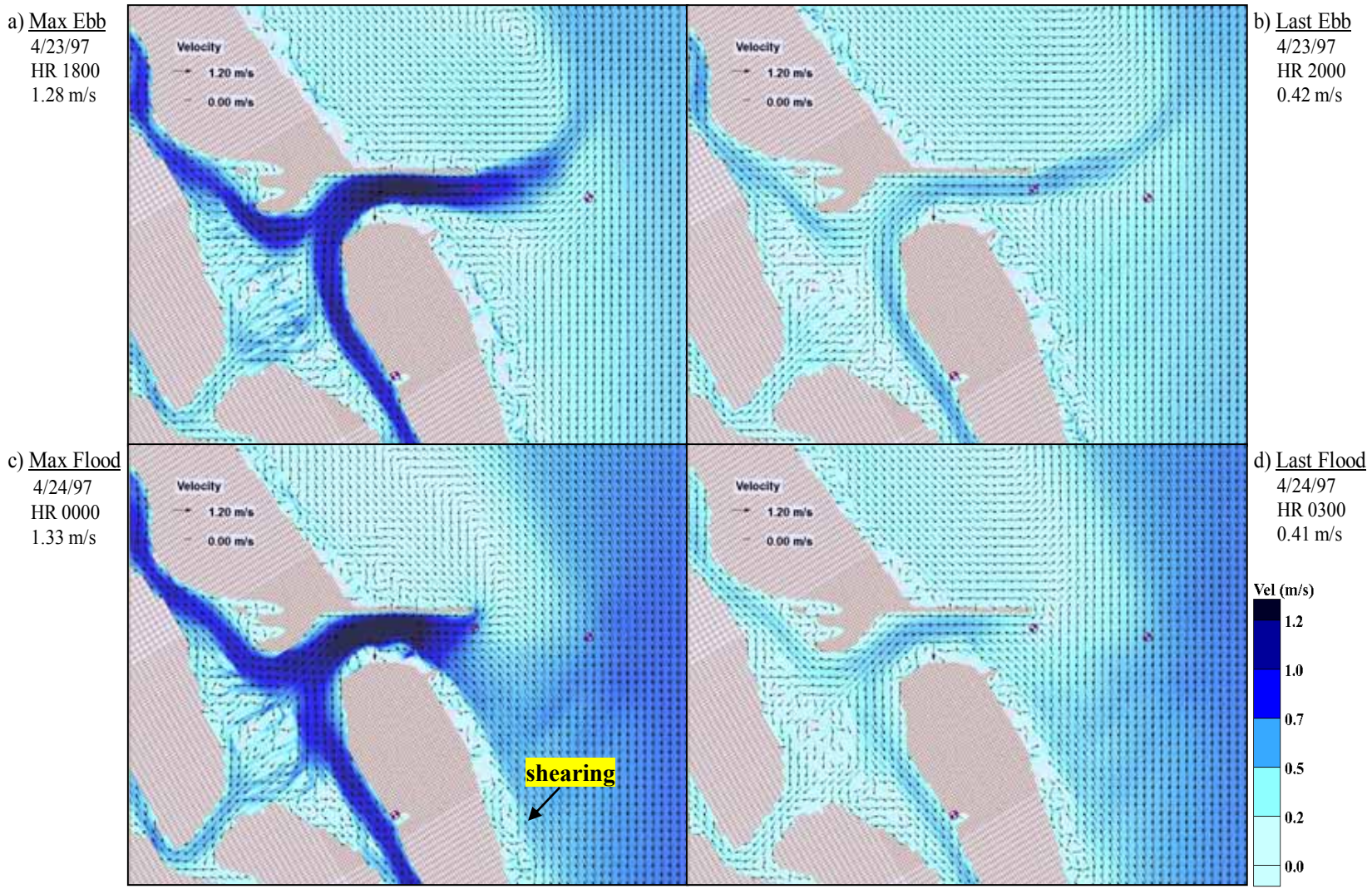

Figure 91. Flow velocities for Present Design during spring tide of 4/23/97. Maximum value from cell 25844 in channel.

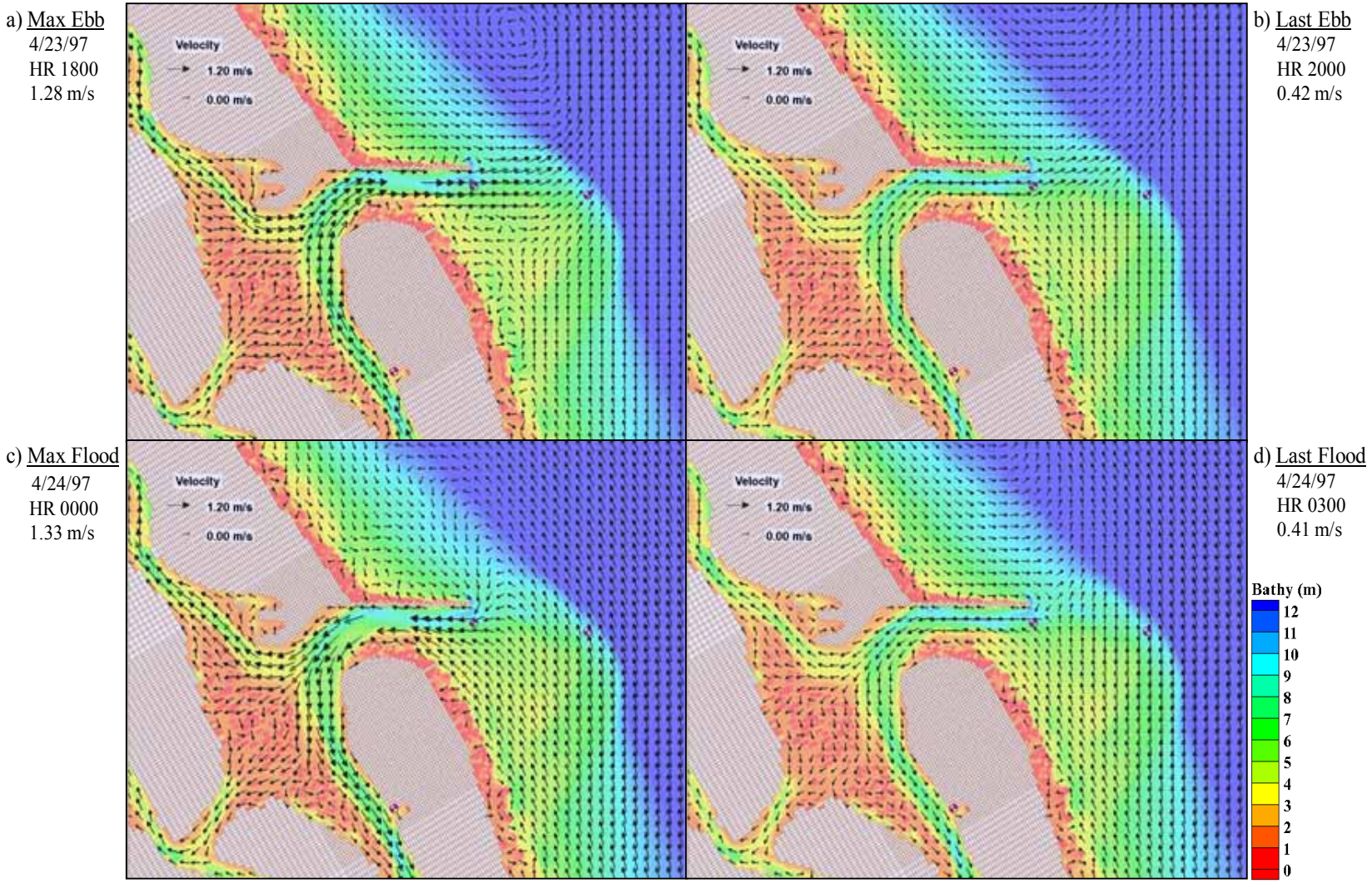

Figure 92. Morphology and flow velocities for Present Design during spring tide of 4/23/97. Maximum value from cell 25844 in channel.

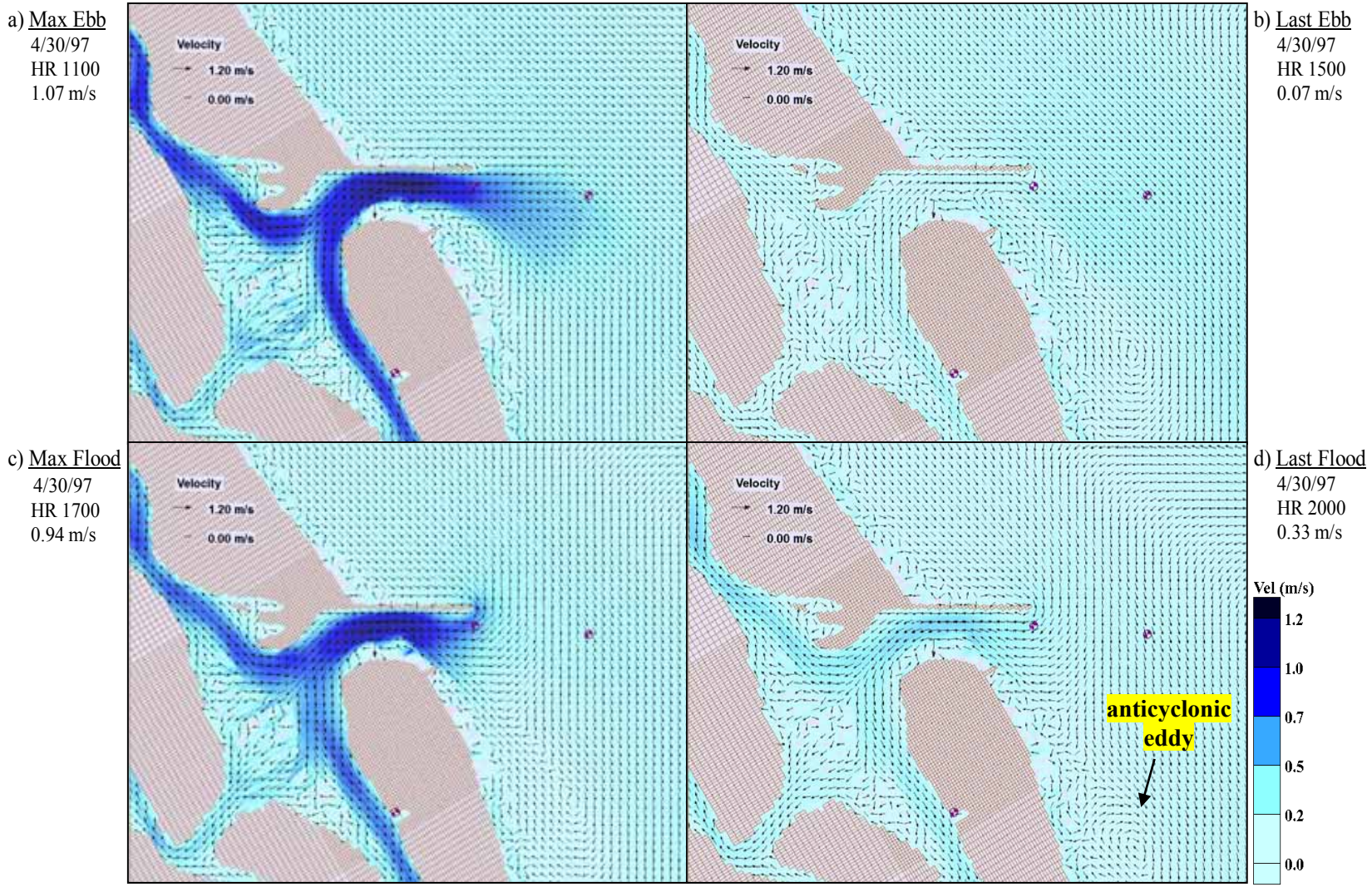

Figure 93. Flow velocities for Present Design during neap tide of 4/30/97. Maximum value from cell 25844 in channel.

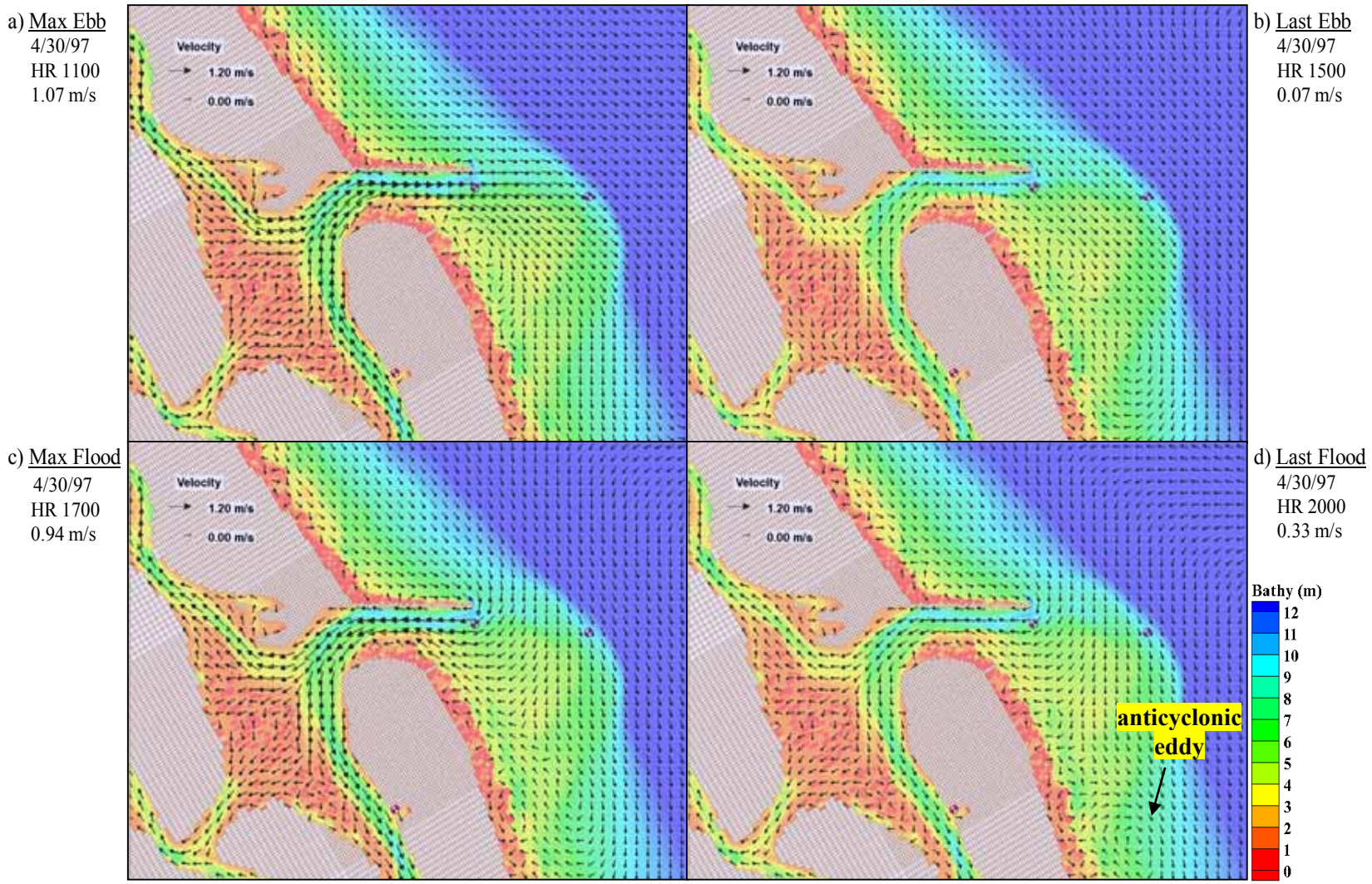

Figure 94. Morphology and flow velocities for Present Design during neap tide of 4/30/97. Maximum value from cell 25844 in channel.

5.3.2 South Jetty Extension

Starting morphology (Figure 95) is the same as for the Present Design. However, a 300 m jetty extension produces a strikingly different 10-month morphology (Figure 96). The ebb shoal has shifted in a unique downdrift pattern, with the bulk of the bypass bar oriented southeast (z = 3 m). Intense shoaling (z < 2 m) has continued on the south spit, encroaching on the southerly-shifted deep navigation channel. Rockhouse Creek is, again, made virtually impassable for access to the Intercoastal Waterway with depths < 2 m. Along the south beaches, a deep score hole (~ 11 m) has formed 1 km south of the jetty, which has itself accumulated sediment on its downdrift side.

Net morphologic changes (Figure 97) repeat the natural bypassing pattern of the Present Design, but with more deposition (Δz ~2 m). Despite scouring of -3 m at the tip of the south jetty, volume loss for the Ebb Complex (Table 16) is still less (-5.2%) than for the Present Design. Erosional areas in the nearshore south of the jetty produce South Beach volume losses of -3.3% and -11% for the South Jetty, despite deposition immediately south of the extension. Deposition for the South Spit (+13% volume) and adjacent Channel~4.6m (Δz = +3 m) had less coverage than for the Present Design and was shifted west due to scour at the newly extended jetty. This lower net deposition for Channel~4.6m, combined with the reduced scour of the channel, now confined to Hard Bottom and Channel>7m masks, produced a volume loss of only -14%, but one still larger than for the Present Design. Because of intense scour (Δz < -3 m) in the channel in the Hard Bottom, this design reduced Basin Channel volume gains of +1.3%.

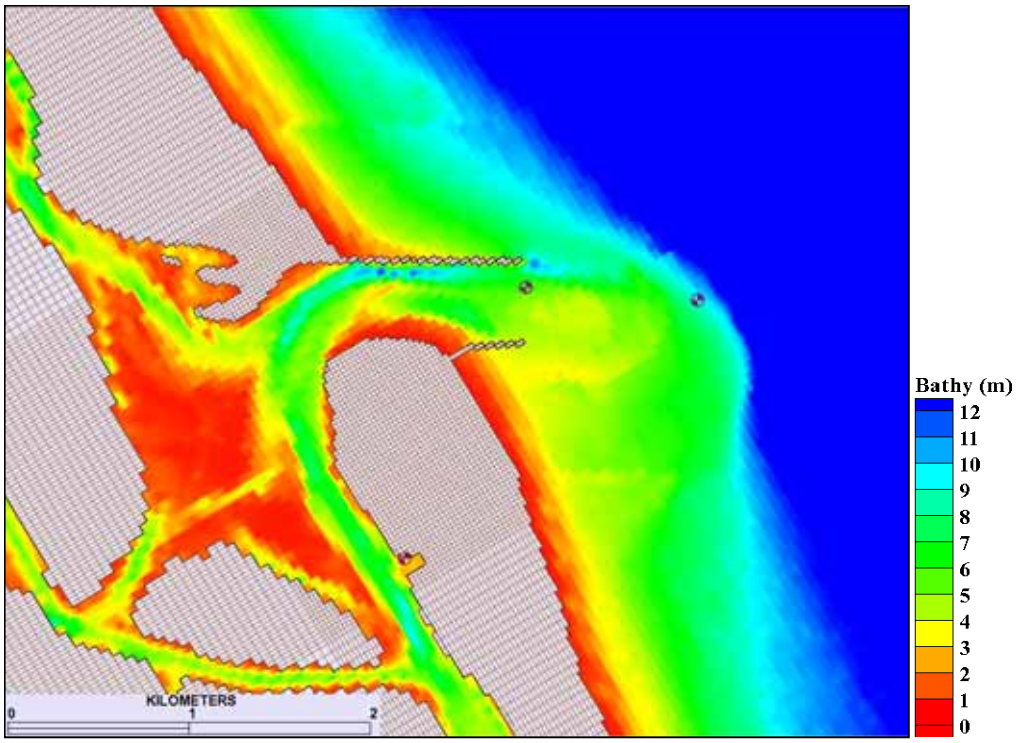

Figure 95. Morphology at 0 hr for South Jetty Extension.

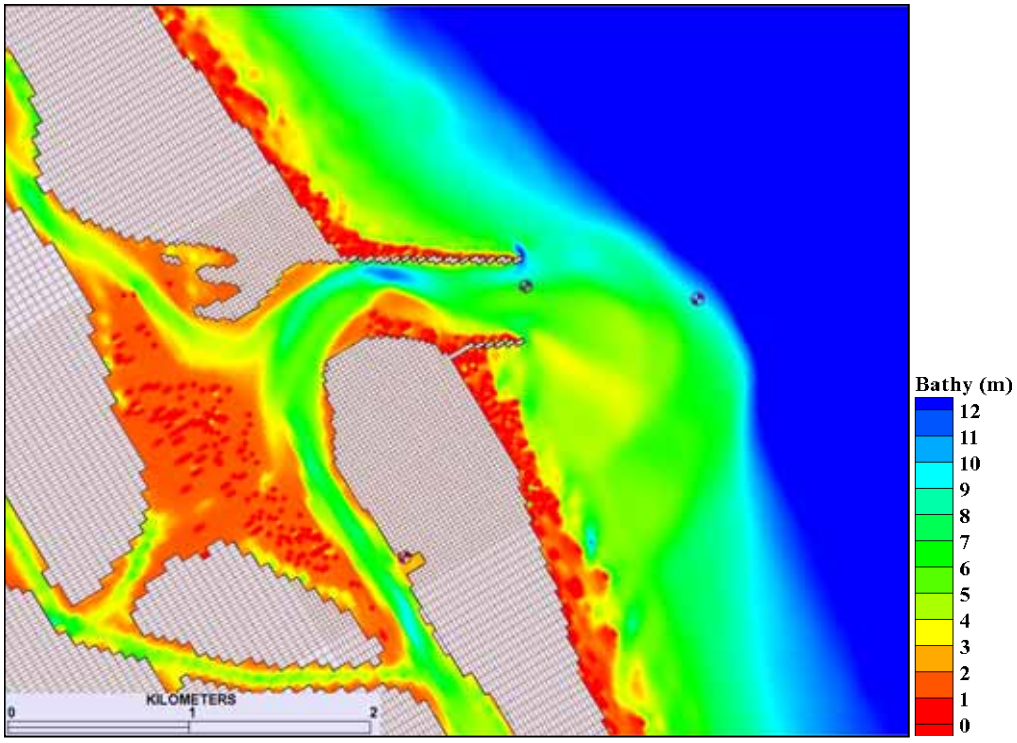

Figure 96. Morphology at 7284 hr (10 months) for South Jetty Extension.

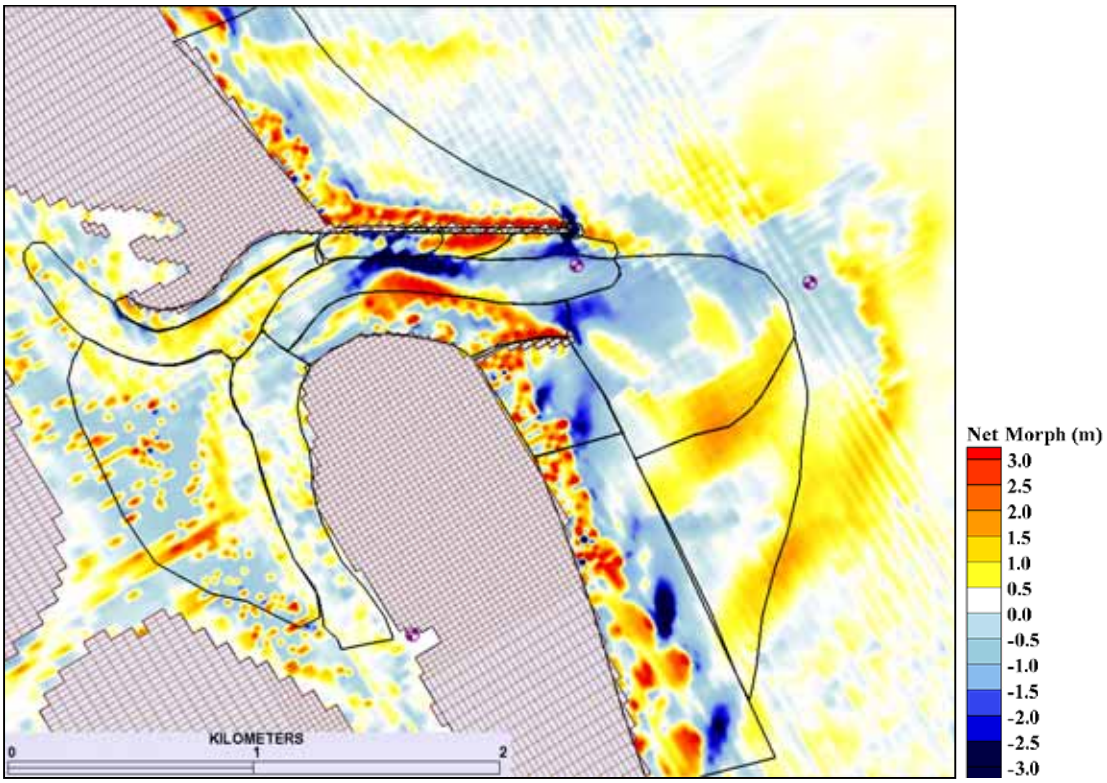

Figure 97. Net 10-month change in morphology for South Jetty Extension.

Table 16. Volume Change (10 months) South Jetty Extension: Normalized (%) and Net (Δvol).

Polygon Mask	%	Δvol (m^3)
Ebb complex	-5.19	-121857
South spit	12.57	63257
Channel ~4.6m	-14.14	-166207
Channel >7m	-10.51	-30062
Basin channel	1.28	7343
North channel	3.32	31957
South Jetty	-11.25	-41663
South channel	-1.09	-14558
South beach	-3.31	-57799
Outer bypass	5.77	132942
North tip	-62.38	-13613
North spit	-5.67	-7393
North beach	3.94	81647
Hard bottom	-9.65	-34368
Flood shoal	0.04	358

Maximum flow velocities for the last spring tide (April 23, 1997) are reversed for ebb (1.31 m/s) and flood (1.36 m/s) due to the storm previously discussed (Figure 98 and Figure 99). More dry cells are observed over the flood shoal. During maximum ebb, the ebb jet narrows through the throat, funneled over the deep, navigation channel by the encroaching southern shoal. At the inlet entrance, the ebb jet diverges. Although bidirectional flow is evident over the south spit for the last hour of ebb, it is more a product of turbulence from reduced water depth than for flow entering from the south around the extension. The benefit of designing parallel jetties is especially observed during maximum flood with symmetric distribution of flood flow though the entrance. Unfortunately, the southern shoal interrupts this flow as it bends around the south spit. During the last hour of flood, a well-defined cyclonic eddy develops in this area.

Maximum ebb (1.10 m/s) and flood (0.96 m/s) are slightly larger with the jetty extension (Figure 100 and Figure 101) for the last neap tide (April 30, 1997). The previous anticyclonic eddy that formed at the shorter jetty tip, limiting the southern extent of the ebb jet through the entrance, has moved SE reworking the south beaches. The jetty extension now performs the ebb jet funneling process. During last hour of ebb, since no flow is observed around the jetty, bidirectional flow in the inlet is generated from an anticyclonic eddy formed from shearing due to the encroachment of the south shoal on the centerline of the inlet, adjacent to the deep channel (Figure 100b and Figure 101b). This shoal redirects maximum flood flow at its western end (Figure 101c), creating a small series of eddies along this shallow path ($z = 1$ m), more readily observed in close-ups not presented in this paper. During the last hour of flood, more flow south of the ebb shoal, along the downdrift bypass bar, connects to the shoreface.

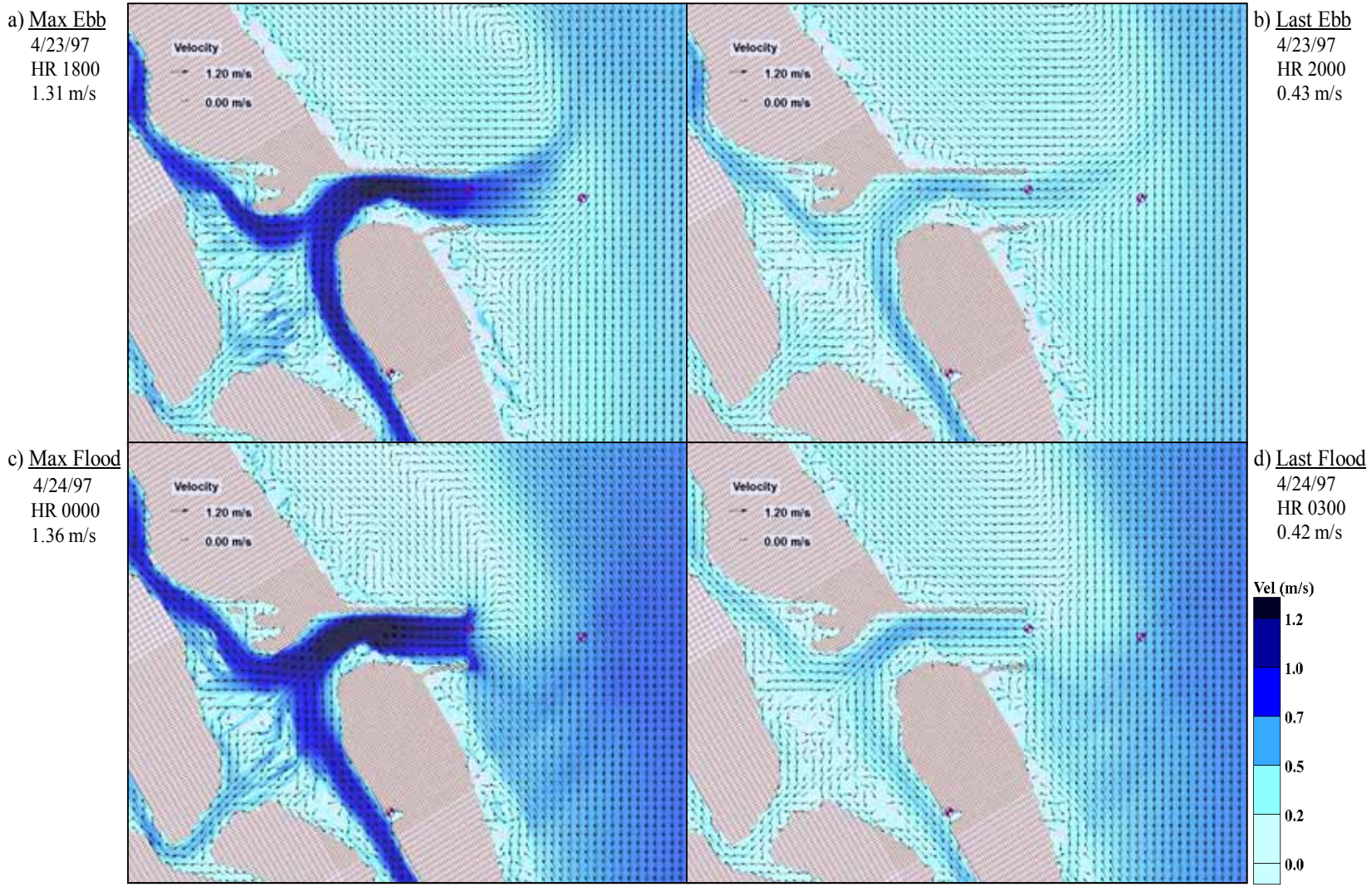

Figure 98. Flow velocities for South Jetty Extension during spring tide of 4/23/97. Maximum value from cell 26660 in channel.

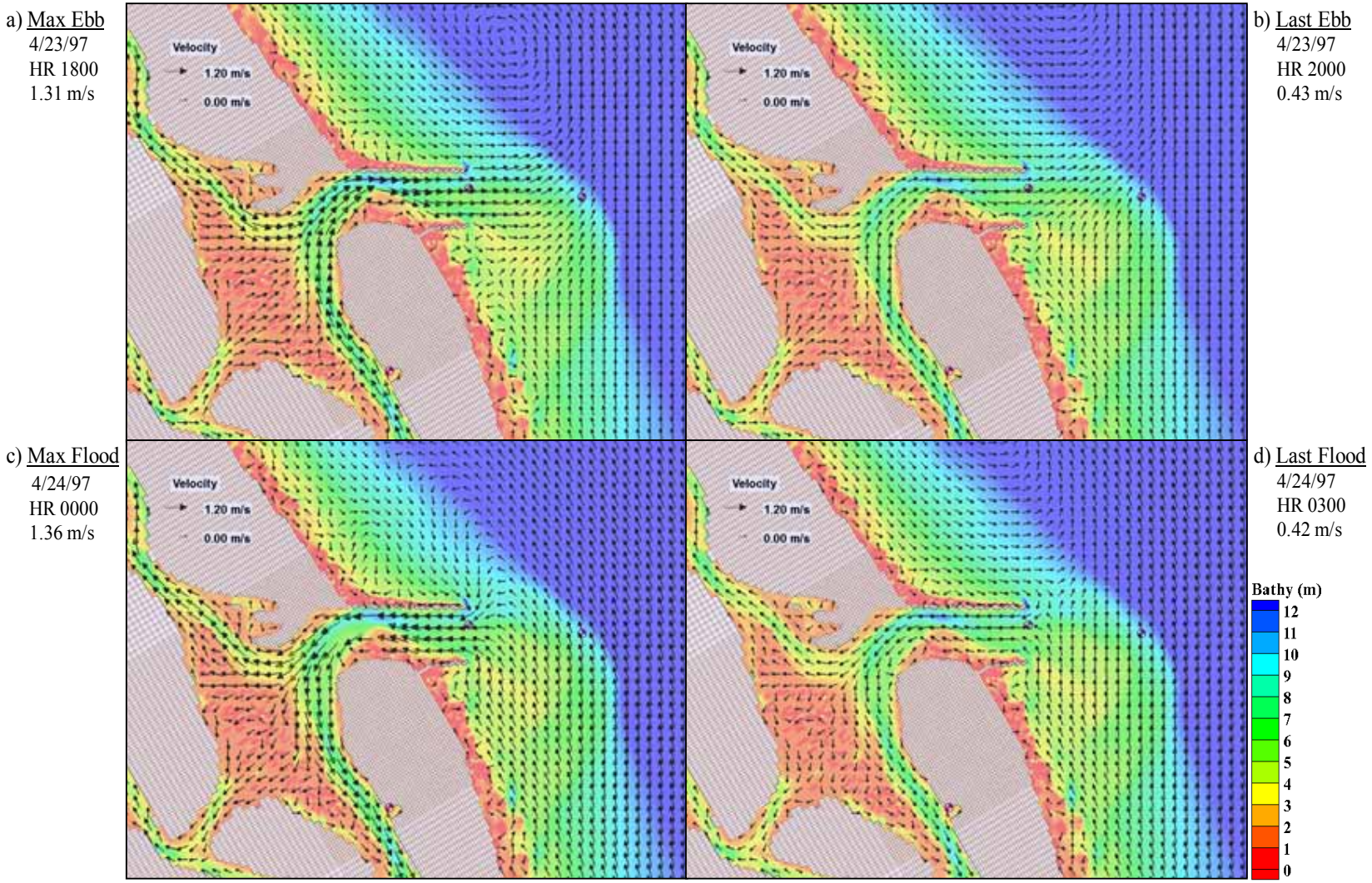

Figure 99. Morphology and flow velocities for South Jetty Extension during spring tide of 4/23/97. Maximum value from cell 26660 in channel.

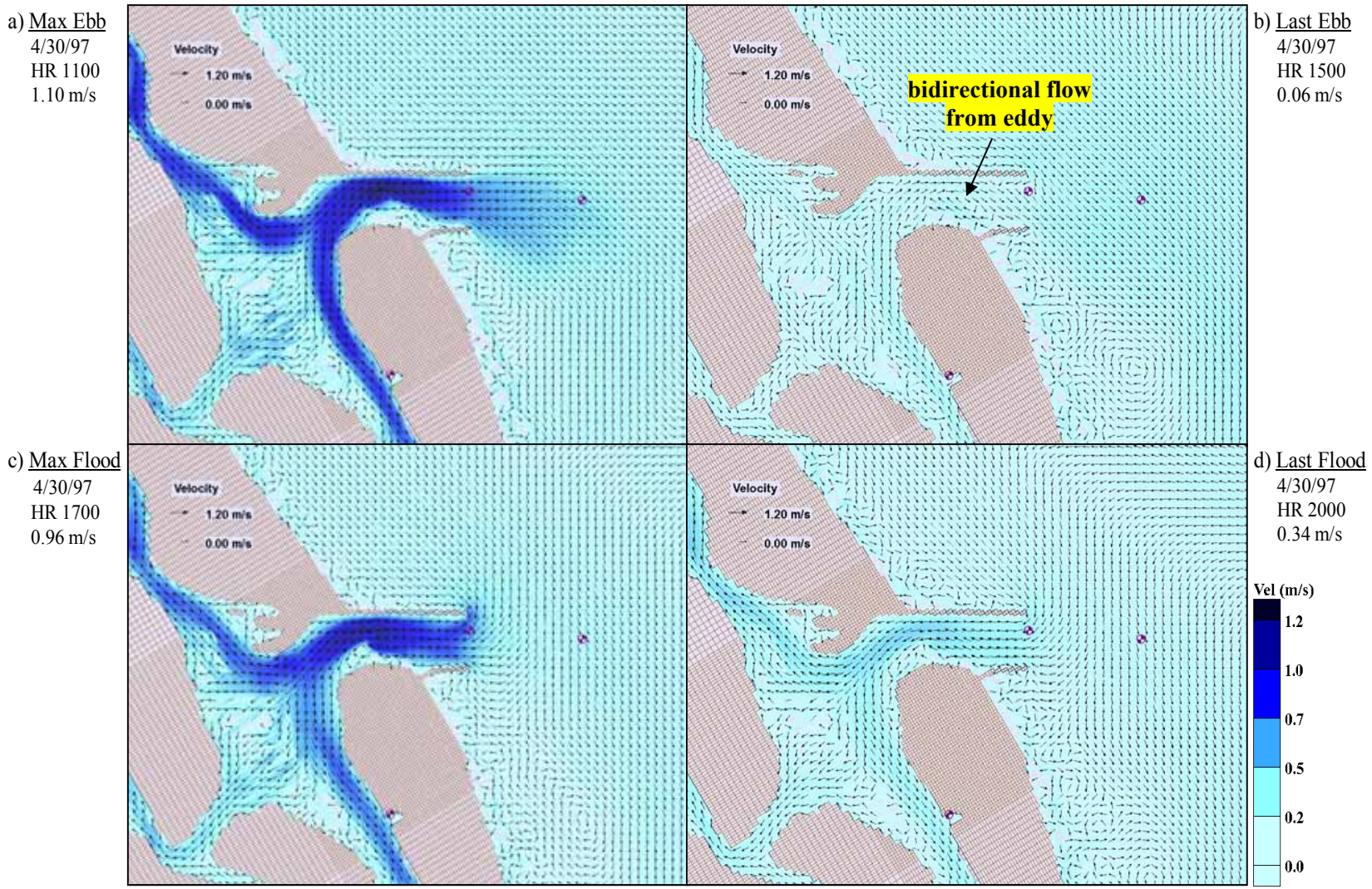

Figure 100. Flow velocities for South Jetty Extension during neap tide of 4/30/97. Maximum value from cell 26660 in channel.

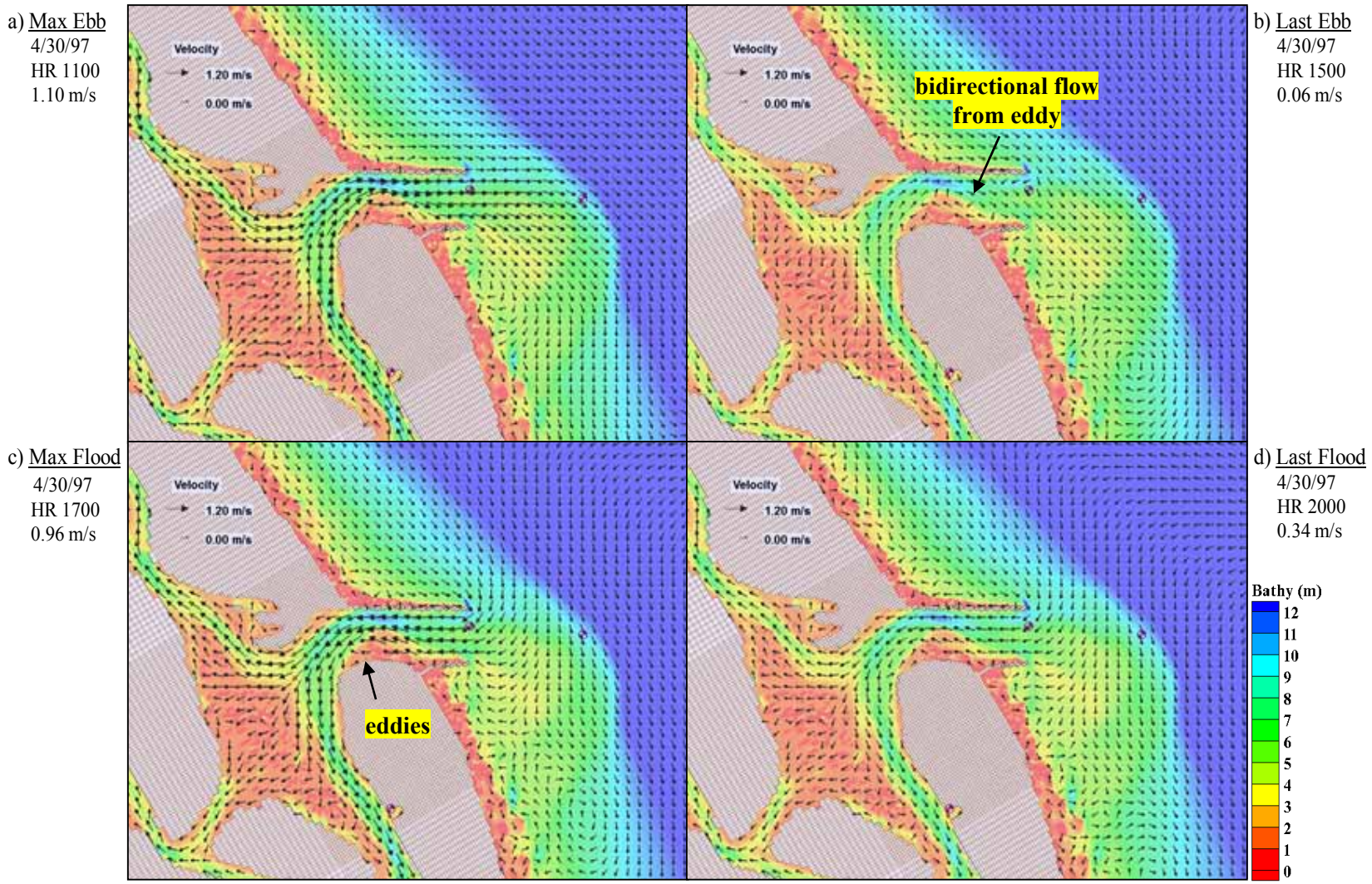

Figure 101. Morphology and flow velocities for South Jetty Extension during neap tide of 4/30/97. Maximum value from cell 26660 in channel.

5.3.3 South Jetty Extension with HB and Channel

Addition of the rubble mound hard bottom basin is identified in the starting morphology (Figure 102) by gold triangles and re-dredging of the centerline navigation channel is indicated by the z = 4.6 m contour. Final morphology (Figure 103) shows an increase in depth south of the HB (z ~ 9 m) and a larger scour area at the north jetty (z = 12 m). Although there is still shoaling for the South Spit, unlike in both previous designs, depths less than 4 m are confined to the southern half of the inlet and those less than 2 m confined to the shoreface. Downdrift bypassing follows the contours of the South Jetty Extension design, but the scour hole on the south beach is absent.

Net morphologic changes (Figure 104) show that intense scour (more than -3 m) stays within the Channel~4.6m mask as intended for the design. With little of the South Spit deposition reaching into this channel, the volume loss of -16% (Table 17) is the largest observed thus far. Volume gain for the South Spit is +15%. Volume gain for the Basin Channel (+6.1%) is the highest of the designs since little net change occurs in the Hard Bottom subset ($\Delta z \sim +0.5$ m, $\Delta vol = 0.05\%$). Scour near the south jetty tip actually occurs north of the tip, more in the entrance, and is less intense (lighter blue) than for the Extension Only option. Deposition along the downdrift bypass bar is also less ($\Delta z \sim +1$ m) producing a total volume change of -6.2% for the Ebb Complex. More erosion occurs in the nearshore of the South Jetty (-17%, the largest volume loss yet) than in the South Beach (-1.4%, the smallest volume loss yet). Despite shoaling along the Rockhouse Creek passage, the Flood Shoal lost -2.21% of its volume with this South Jetty Extension plus Hard Bottom and Channel option.

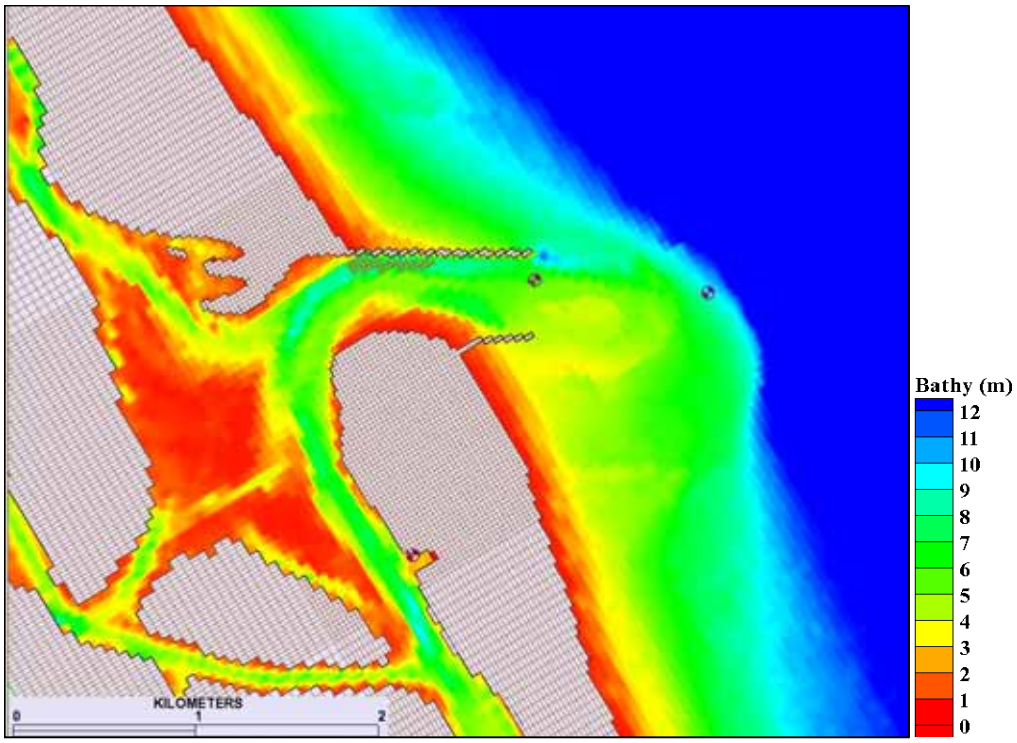

Figure 102. Morphology at 0 hr for South Jetty Extension with HB and C.

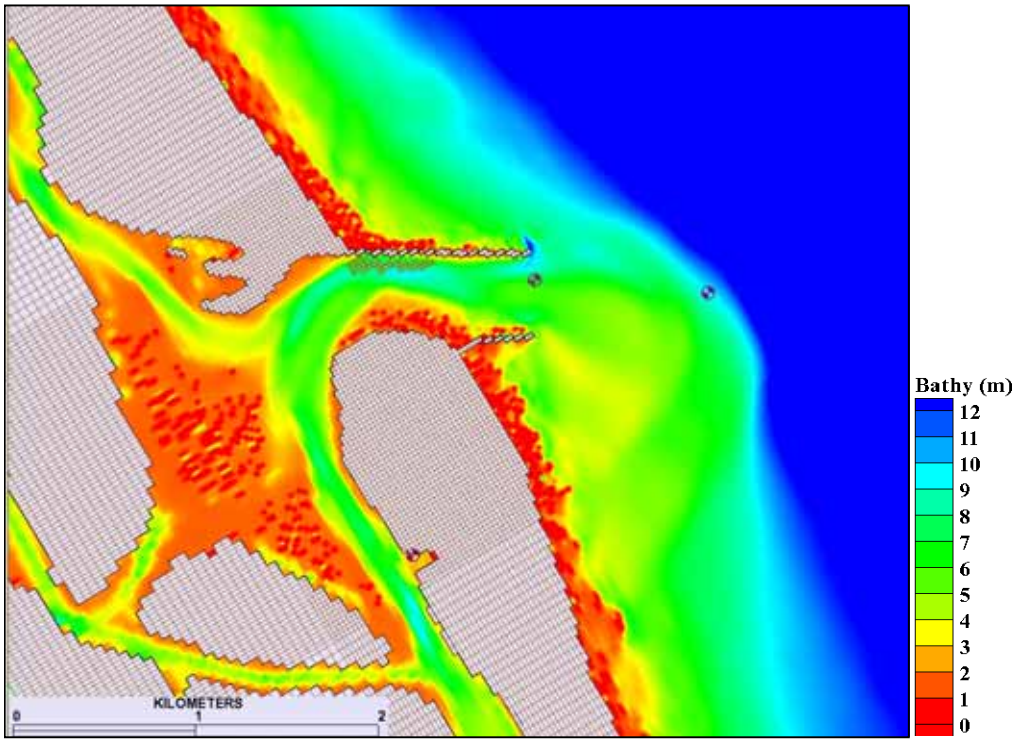

Figure 103. Morphology at 7284 hr (10 months) for South Jetty Extension with HB and C.

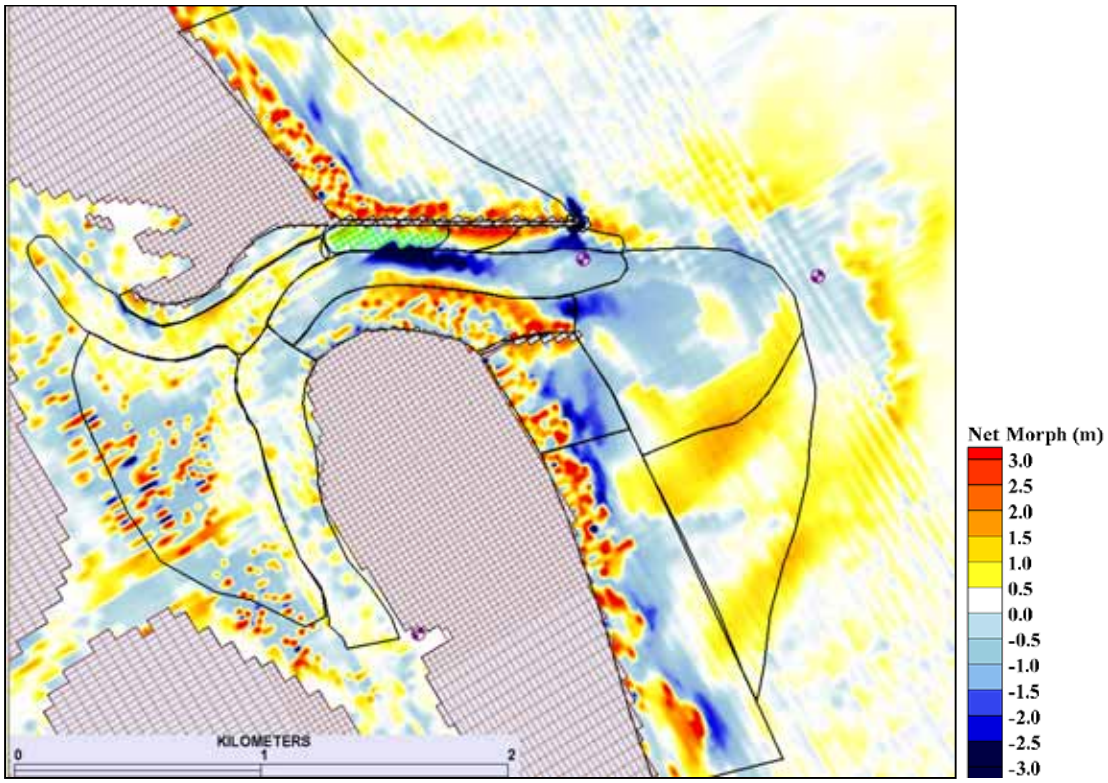

Figure 104. Net 10-month change in morphology for South Jetty Extension with HB and C.

Table 17. Volume Change (10 months) South Jetty Extension with HB and C: Normalized (%) and Net (Δvol).

Polygon Mask	%	Δvol (m^3)
Ebb complex	-6.19	-146203
South spit	14.65	73739
Channel ~4.6m	-16.48	-201144
Channel >7m	-6.07	-17312
Basin channel	6.13	32215
North channel	3.28	31577
South Jetty	-17.44	-64566
South channel	-1.23	-16382
South beach	-1.37	-23908
Outer bypass	7.57	174456
North tip	-57.14	-12469
North spit	0.30	391
North beach	3.60	74700
Hard bottom	0.05	162
Flood shoal	-2.17	-18774

Predicted flow velocities during the last spring tide and concurrent storm (April 23, 1997) reach 1.25 m/s for maximum ebb and 1.39 m/s for maximum flood (Figure 105 and Figure 106). Convergence of the flow within the throat is no longer observed, given that the south shoal does not reach as far north as for the previous 10-month run designs. As compared with only extending the south jetty, this design increases the turbulence north and south of the inlet adjacent to the jetties during maximum ebb and shifts the north beach anticyclonic eddy to flow along the north jetty during maximum flood. Flow over the flood shoal is concentrated through Rockhouse Creek during maximum flood and the well-defined, large cyclonic eddy over the western edge of the south spit is reduced during last flood, although more turbulence towards the east is also observed.

During the last neap tide of the 10-month run (April 30, 1997), flow velocities return to pre-storm conditions and are predicted to reach 1.06 m/s for maximum ebb and 0.98 m/s for maximum flood (Figure 107 and Figure 108). The large, well-defined anticyclonic eddy formed during maximum ebb just south of the south jetty tip moves offshore a bit to the south by the last hour of ebb. Magnitudes through the inlet are evenly distributed between the north jetty and the south spit for both peak ebb and flood. During the last hour of flood (Figure 107d), there is an organized trajectory of flow off the ebb shoal along the downdrift bypass bar approaching the south beach a bit farther south than for the Extension Only design. This circulation pattern helps to explain the difference in scour patterns observed in this region, given that the deep scour hole (z = 9 m) never forms in this design as it did for the extension only design.

a) Max Ebb
4/23/97
HR 1800
1.25 m/s

b) Last Ebb
4/23/97
HR 2000
0.38 m/s

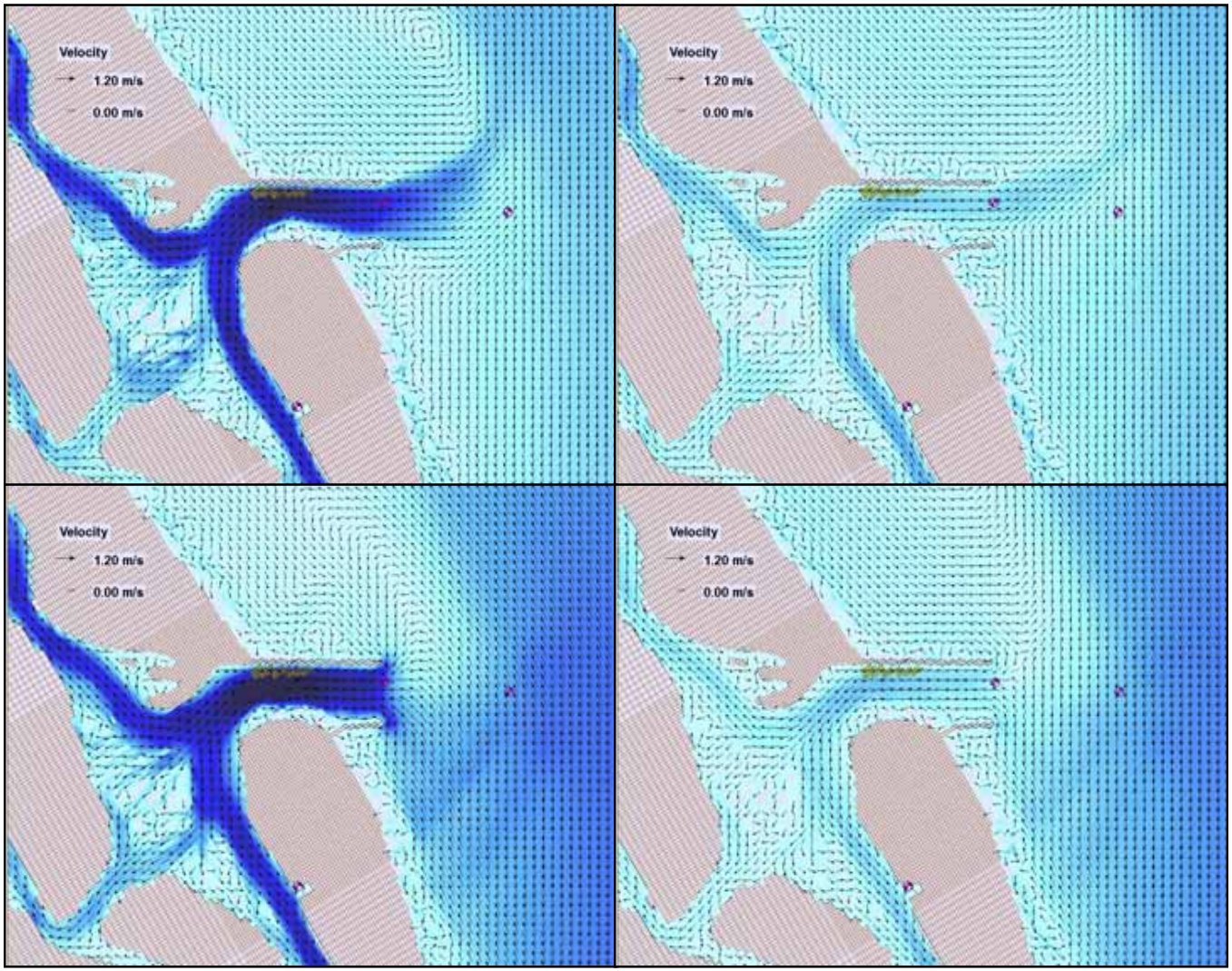

c) Max Flood
4/24/97
HR 0000
1.39 m/s

d) Last Flood
4/24/97
HR 0300
0.40 m/s

Figure 105. Flow velocities for South Jetty Extension with HB and C during spring tide of 4/23/97. Maximum value from cell 26450 in channel.

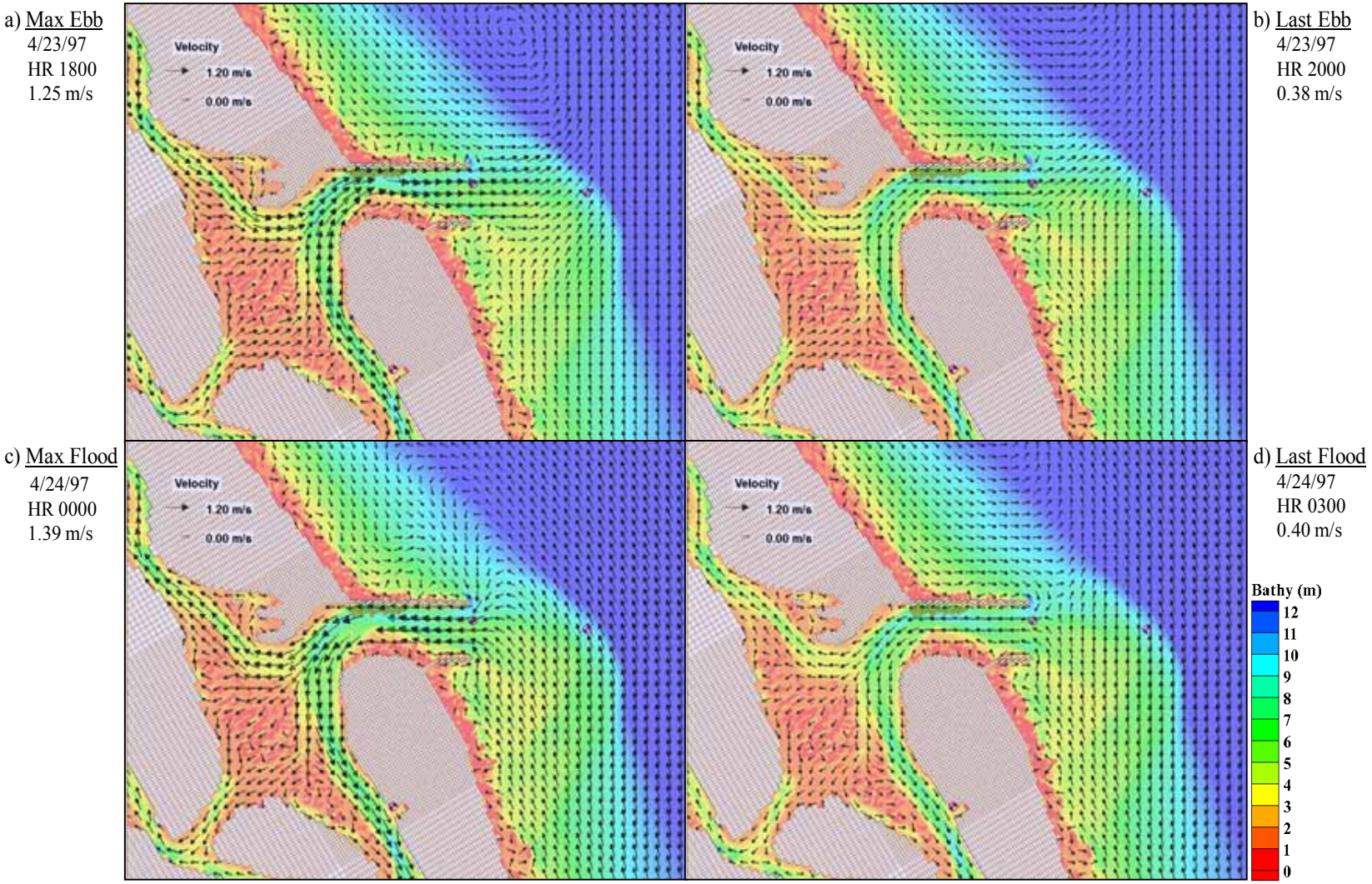

Figure 106. Morphology and flow velocities for South Jetty Extension with HB and C during spring tide of 4/23/97. Maximum value from cell 26450 in channel.

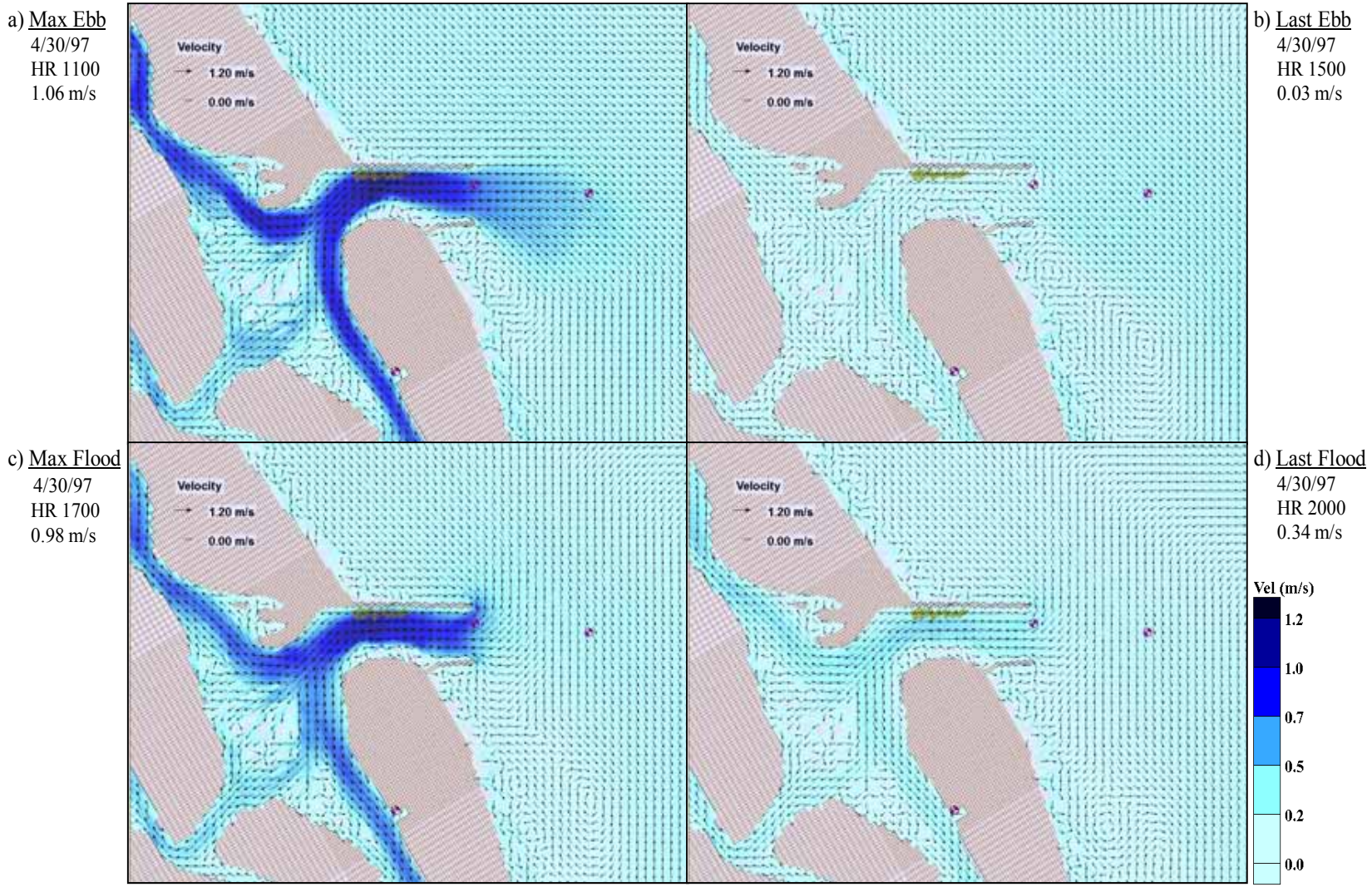

Figure 107. Flow velocities for South Jetty Extension with HB and C during neap tide of 4/30/97. Maximum value from cell 26450 in channel.

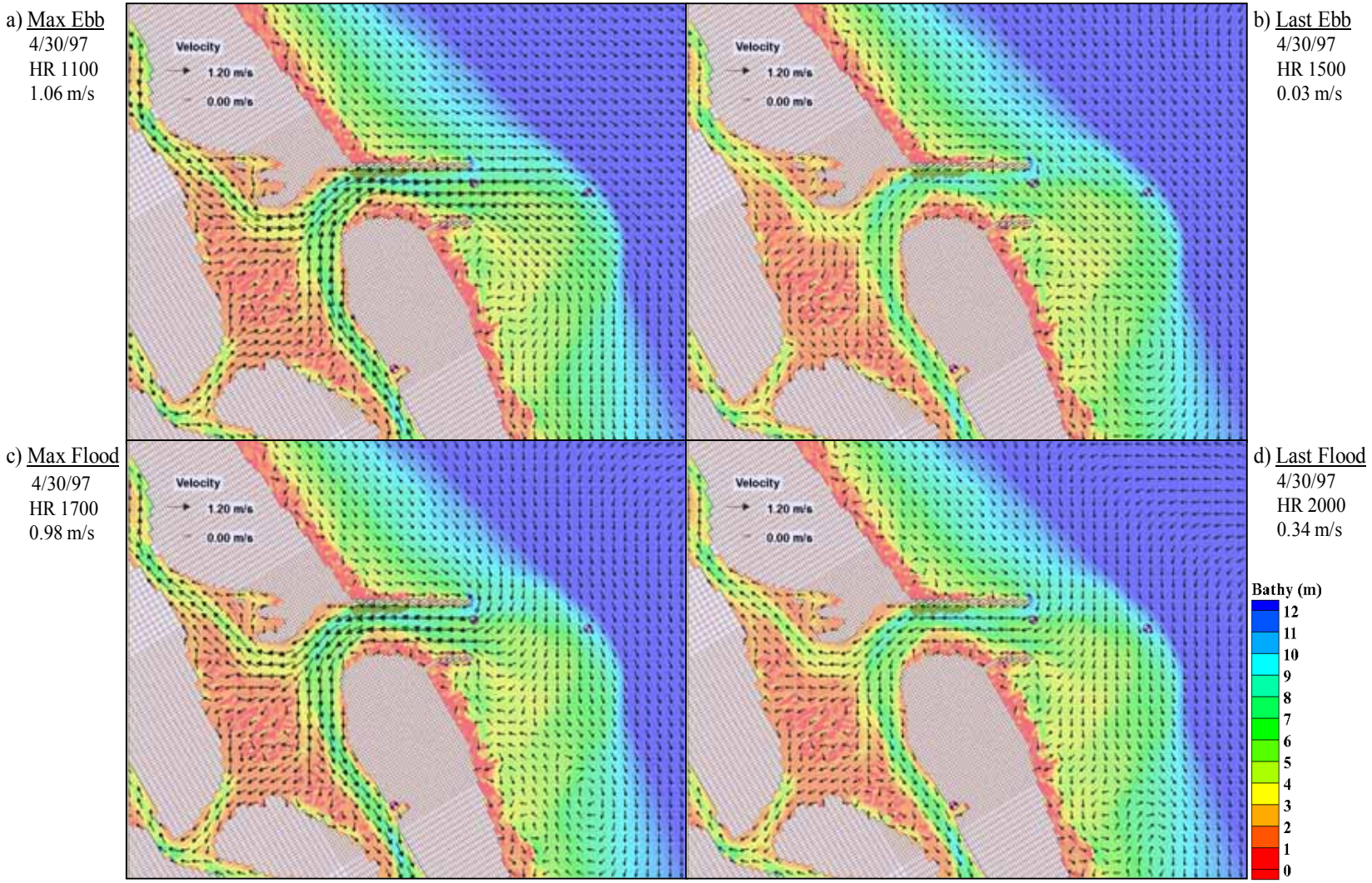

Figure 108. Morphology and flow velocities for South Jetty Extension with HB and C during neap tide of 4/30/97. Maximum value from cell 26450 in channel.

5.3.4 South Jetty Extension with Emergent Spur, HB, and Channel

Starting morphology (Figure 109) shows the attachment of 170 m of rubble mound forming an angled spur off the south jetty extension (ES) -2.24 m above 0 m NAVD88. Gold triangles inside the north jetty indicate the presence of the hard bottom basin and the re-dredged channel (C) has bathymetry less than 5 m. Final morphology after 10 months (Figure 110) shows that just south of the HB basin the navigation channel deepens (z ~ 10 m) and is now virtually adjacent to the south spit shoal that has extended north of the centerline. Although depths over most of the south shoal are less shallow than previously observed (z = 1.5 to 3 m), the presence of the spit so far north is a navigation hazard. Deposition along the emergent spur and behind the south jetty is evident with some cells now above the 0 m NAVD88 waterline. This configuration has not produced an observable scour hole anywhere near the south jetty tip, although inner cells of the jetty have deepened to 5 to 7 m. Passage through Rockhouse Creek to the Intercoastal Waterway will be difficult with depths less than 1.5 m.

Although morphology contours did not distinguish a scour hole near the south jetty tip, net topographic changes (Figure 111) show scour in the channel north of the tip (western part of the Ebb Complex) of more than - 3 m. This creates a loss of -3.7% for the Ebb Complex (Table 18). With increased erosion in the South Spit and the shoal shifted northward, this mask shows a loss of -9.5%. Expected volume losses for the Channel~4.6m are reduced due to the shoal migration (now only -7.9%). The North Beach lost -8.1% of its volume with the majority immediately updrift of the north jetty. The South Beach and South Jetty show volume gains of +3.8% and +9.3, respectively.

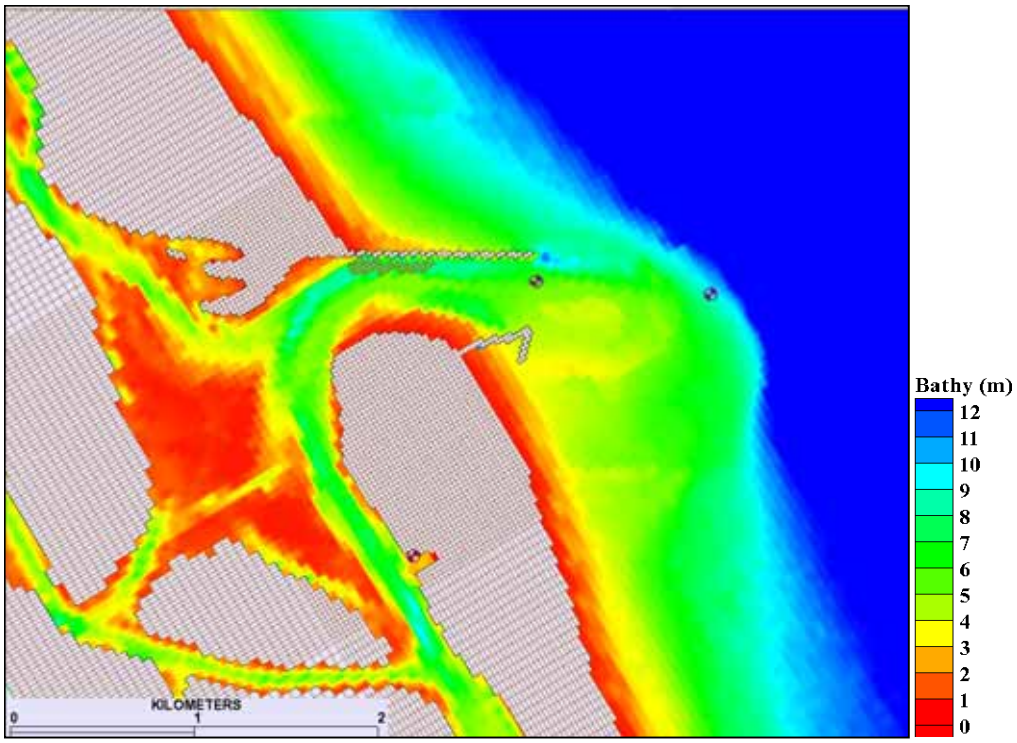

Figure 109. Morphology at 0 hr for South Jetty Extension with ES, HB, and C.

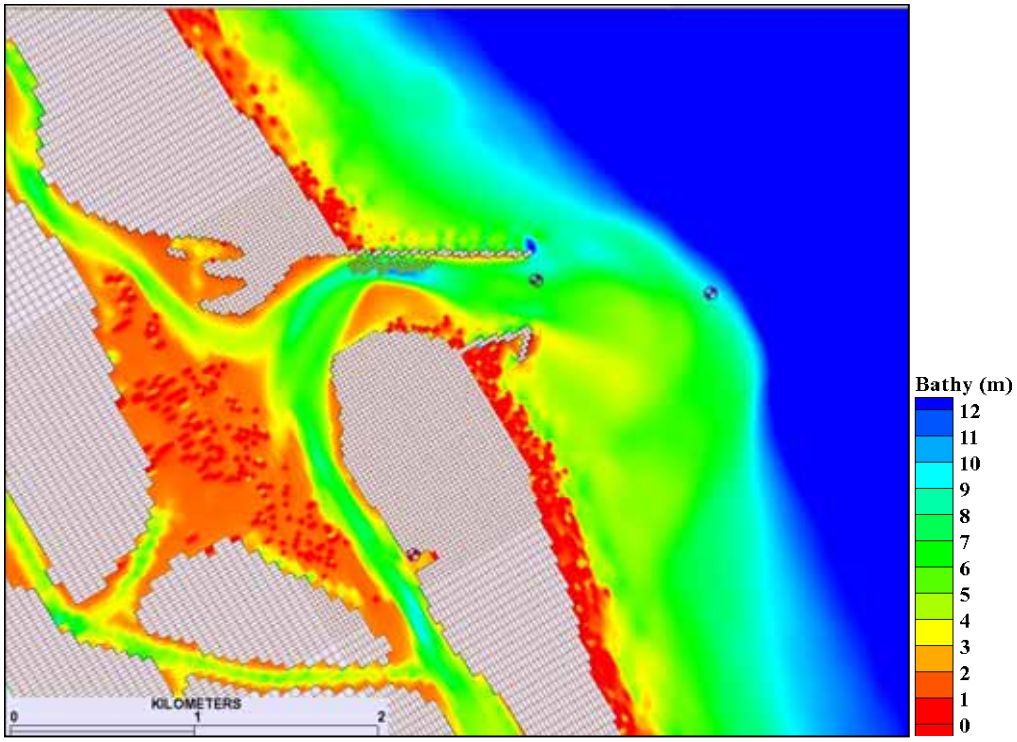

Figure 110. Morphology at 7284 hr (10 months) for South Jetty Extension with ES, HB, and C.

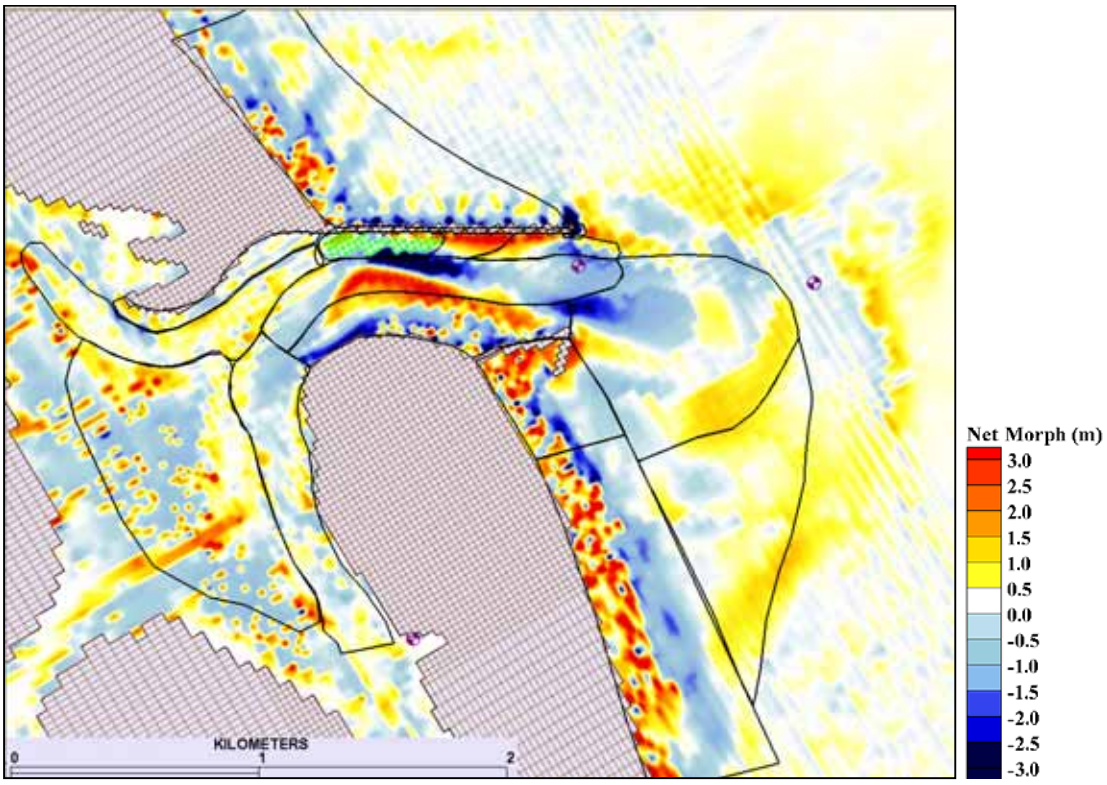

Figure 111. Net 10-month change in morphology for South Jetty Extension with ES, HB, and C.

Table 18. Volume Change (10 months) South Jetty Extension with ES, HB, and C: Normalized (%) and Net (Δvol).

Polygon Mask	%	Δvol (m^3)
Ebb complex	-3.69	-87147
South spit	-9.52	-46830
Channel ~4.6m	-7.82	-95415
Channel >7m	3.83	10932
Basin channel	4.28	22496
North channel	3.40	32782
South Jetty	9.20	32387
South channel	-2.09	-27911
South beach	3.76	65753
Outer bypass	4.58	105442
North tip	-45.39	-9905
North spit	1.49	1939
North beach	-8.06	-167413
Hard bottom	-3.28	-10878
Flood shoal	0.92	7928

Maximum flow velocities predicted for the last spring tide (April 23, 1997) again represent the effect of the storm on tidal currents with maximum flood (1.49 m/s) greater than maximum ebb (1.45 m/s) for cell 27069 in the navigation channel (Figure 112 and Figure 113). Despite the northward-encroaching shoal off the south spit, flow over this shoal is able to remain organized and to sustain relatively large magnitudes during the ebb phase (0.7 m/s for maximum ebb), although it is diverted NE. During the flood phase, flow moves the farthest south it has and is barely impacted by the shoal, reducing maximum flood to 0.5 m/s just as it bends west of the shoal. Because the bathymetry along the south beaches is quite shallow, little flow is observed in the upper shoreface even during the height of the storm (maximum flood). Magnitudes around the spur and south jetty tip are larger than without the spur on maximum flood (0.8 m/s) and circulation behind the spur is reduced due to deposition.

During maximum ebb (1.21 m/s) of the last neap tide (April 30, 1997), turbulence observed in the previous jetty extension designs is still present, though covering a larger area in the cross-shore direction (Figure 114 and Figure 115). During the last hour of ebb, the predicted bidirectional flow is still prevalent with more vectors showing NNW flow toward the Hard Bottom basin. The southeasterly offshore currents turn to the SSW over the ebb shoal and outer bypass bar during flood phase and contribute to the clockwise eddy formed along the south beaches. During maximum flood (1.09 m/s), nearshore currents get direct northward along the spur from the rotated flow off the ebb shoal so that only during the last hour of flood is flow from the ebb shoal observed to reach the south beach upper shoreface along the bypass bar (Figure 115c, d).

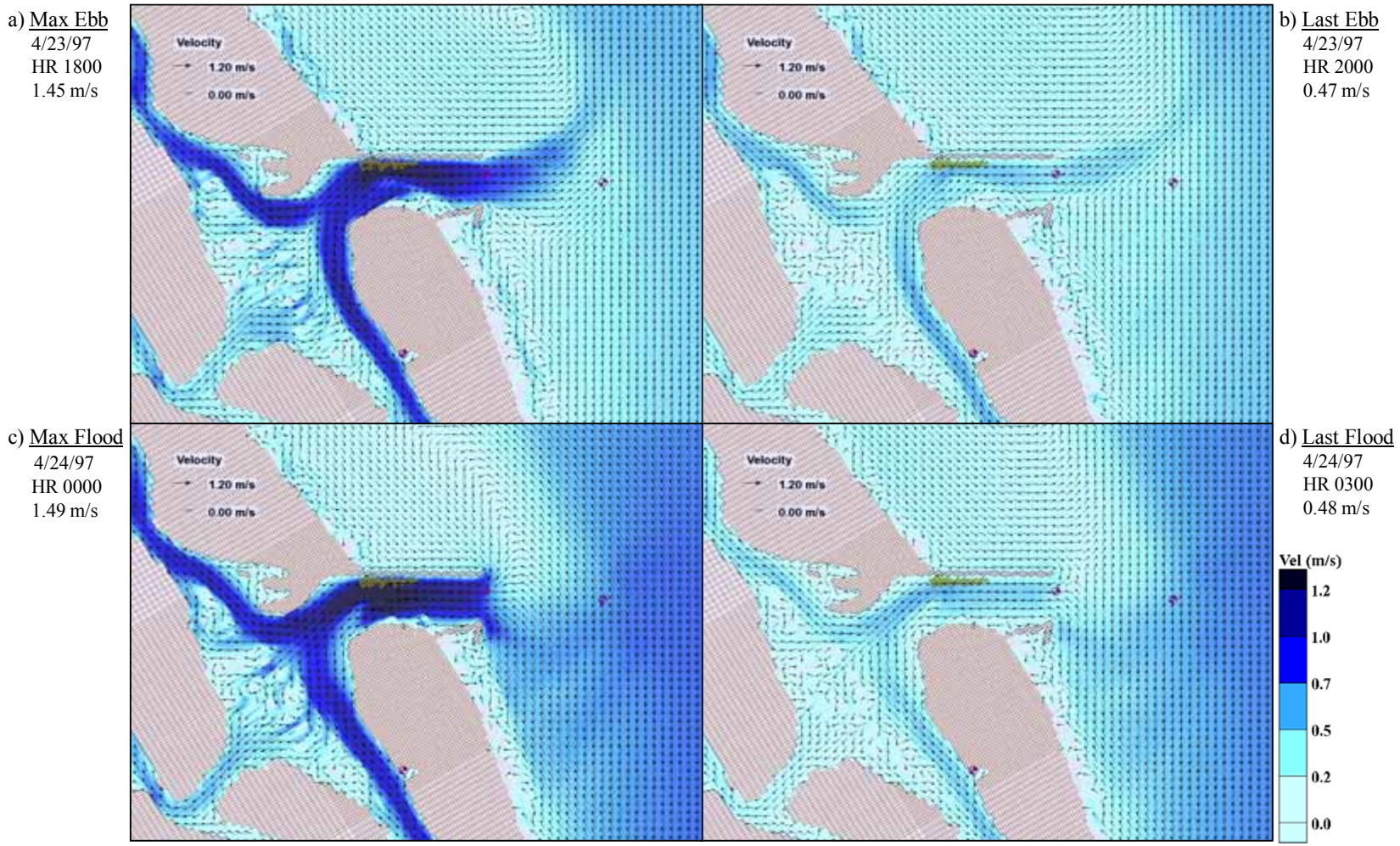

Figure 112. Flow velocities for South Jetty Extension with ES, HB, and C during spring tide of 4/23/97. Maximum value from cell 27069 in channel.

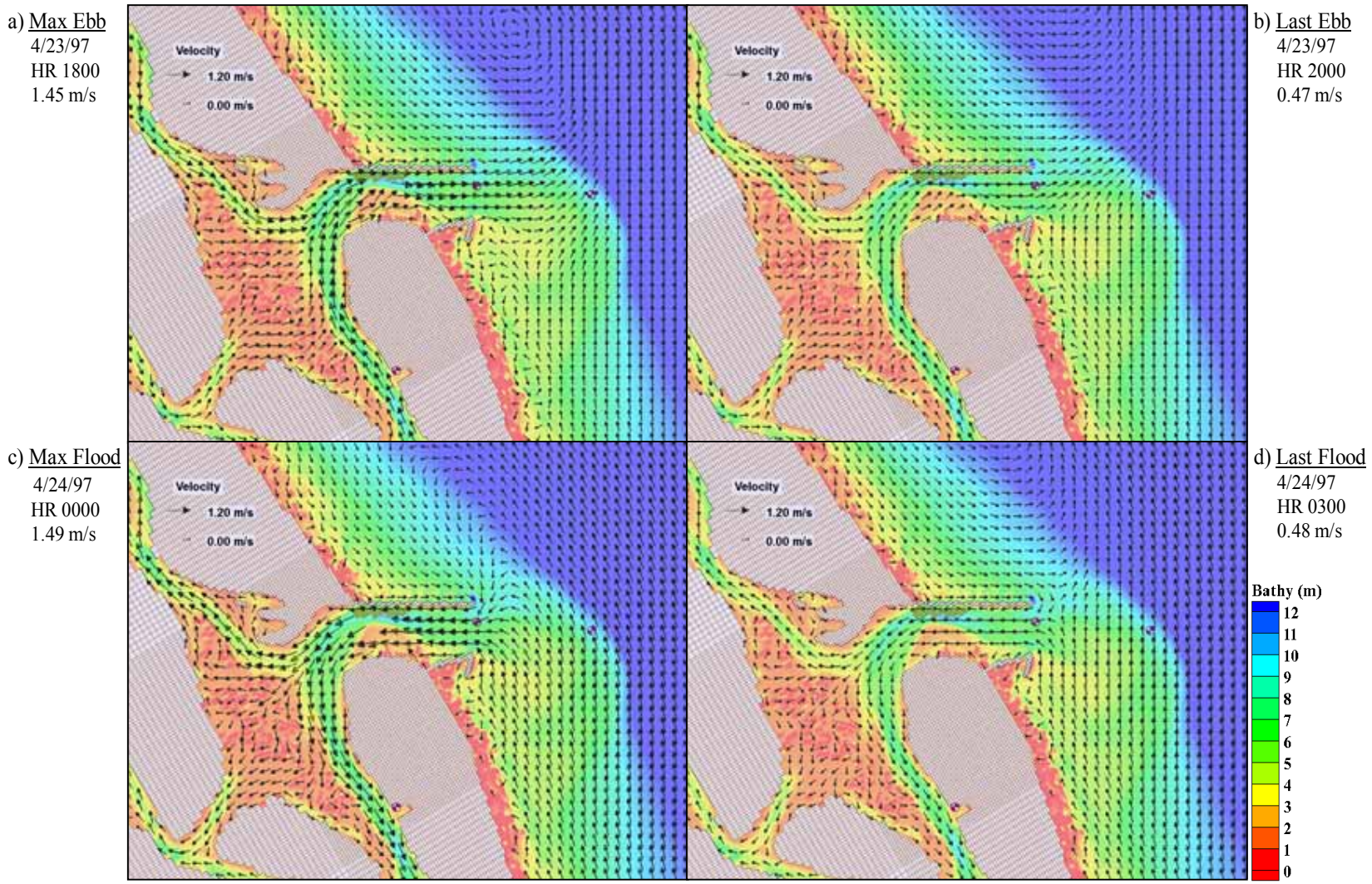

Figure 113. Morphology and flow velocities for South Jetty Extension with ES, HB, and C during spring tide of 4/23/97. Maximum value from cell 27069 in channel.

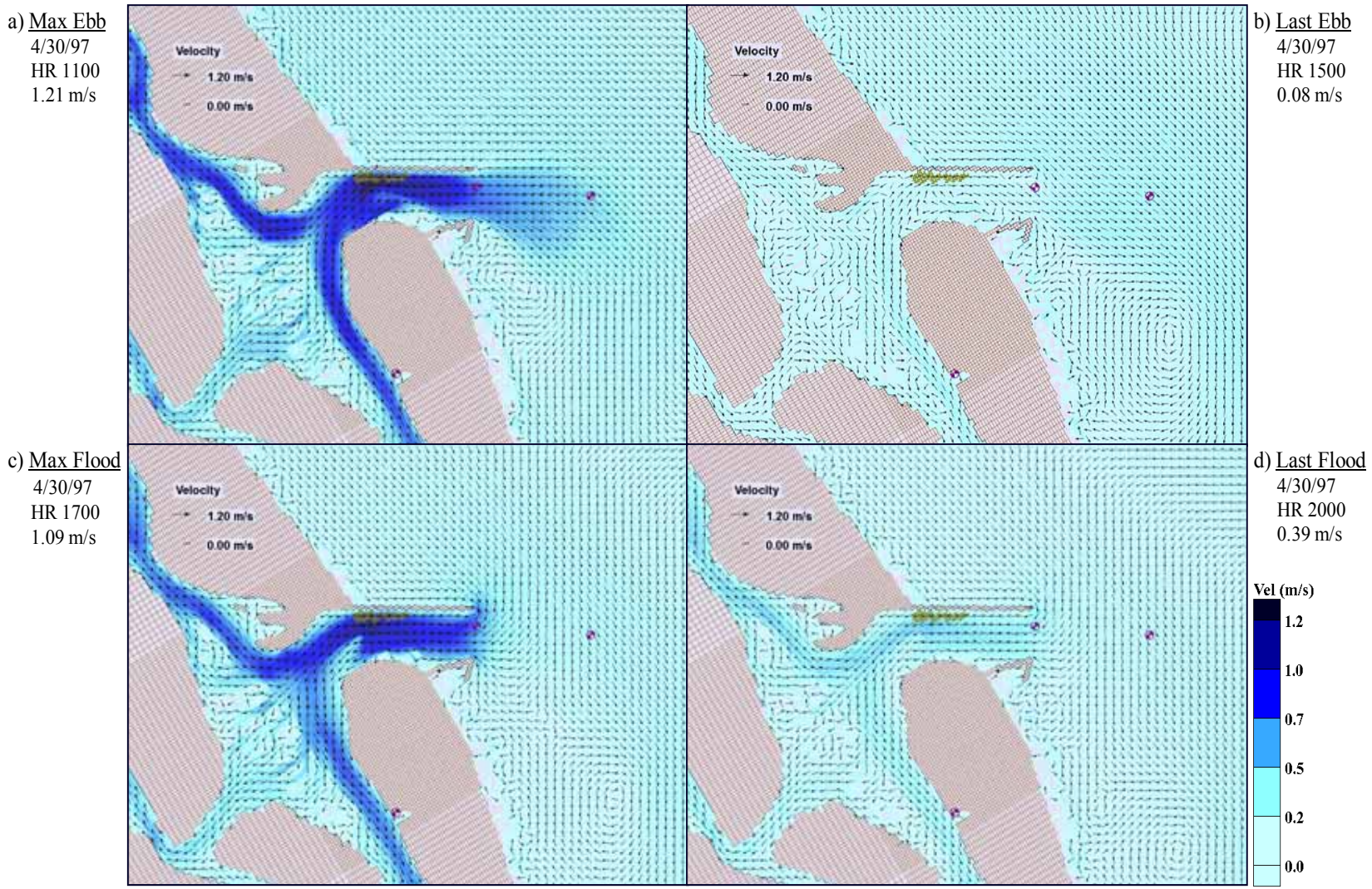

Figure 114. Flow velocities for South Jetty Extension with ES, HB, and C during neap tide of 4/30/97. Maximum value from cell 27069 in channel.

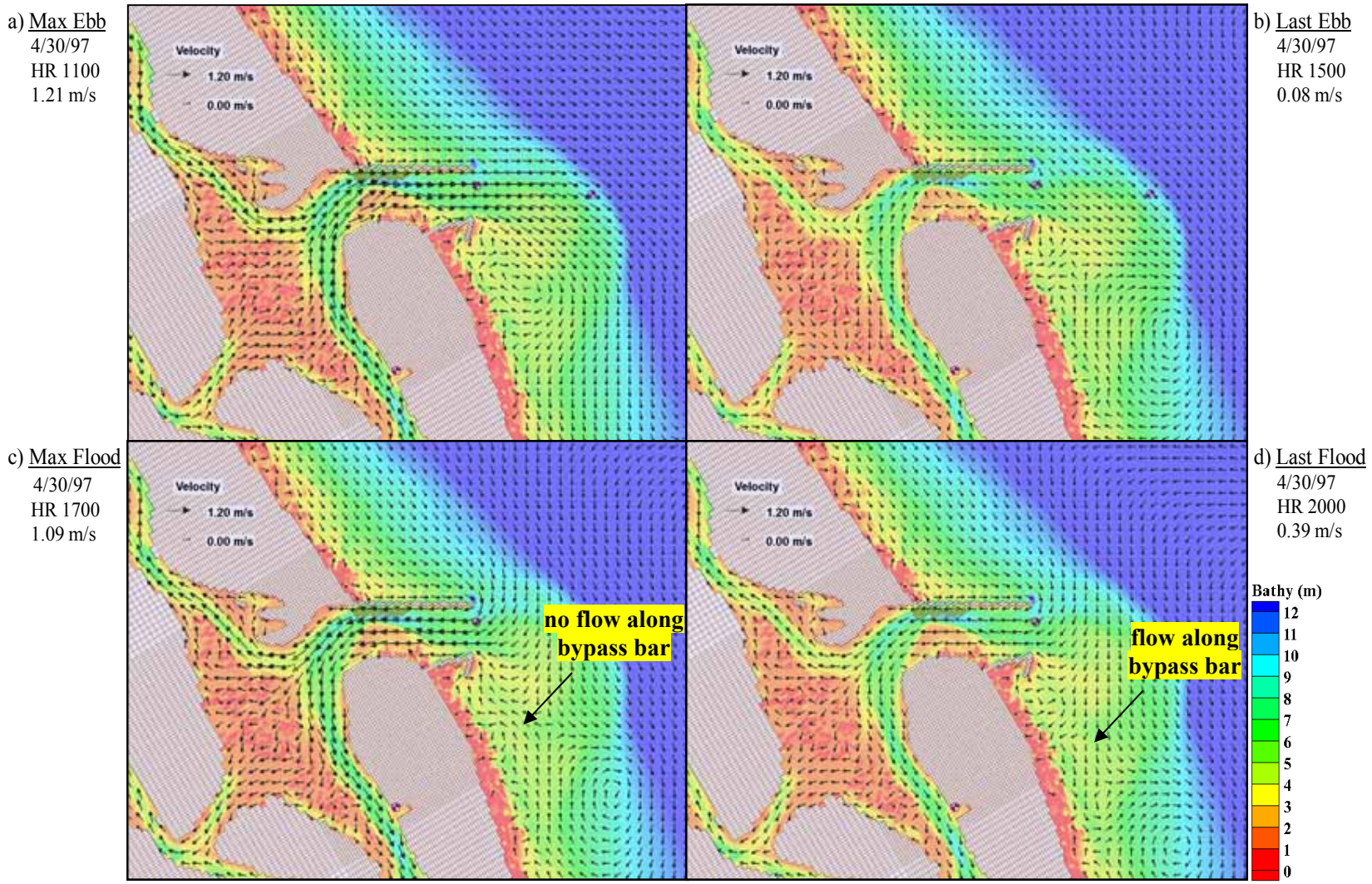

Figure 115. Morphology and flow velocities for South Jetty Extension with ES, HB, and C during neap tide of 4/30/97. Maximum value from cell 27069 in channel.

5.3.5 South Jetty Extension with Submergent Spur and Channel

Submersion of the spur is indicated using gold triangles (Figure 116) to represent the structure as non-erodible hard bottom (SS). Re-location of the navigation channel (C) through the centerline of the inlet is at least 4.6 m and all other starting morphology is the same as in the Present Design. Final morphology (Figure 117) shows reduced depths for the present location of the navigation channel ($z \sim 9.5$ m) having a slight southern migration. Shoaling on the south spit brought the entire area to less than 2 m but confined to south of the re-located navigation channel. A similar uniform pattern of accretion ($z < 2$ m) fully covering the nearshore is evident for the north beach and adjacent north jetty, both sides of the south jetty, and continues along the south beaches. Rockhouse Creek channel remains open to depths of approximately 3 m.

Net morphologic changes (Figure 118) indicate the extreme deposition for the North Beach ($\Delta z > +3$ m) lies landward of extreme erosion ($\Delta z < -3$ m) increasing the net volume by +0.7% (Table 19). Volume loss in Channel>7m (-7.1%) is attributed to scour at the adjacent north jetty tip, whereas scouring for Channel~4.6m ($\Delta z > -3$ m) occurs throughout the mask for a loss of -18%. A large scour area north of the south jetty tip ($\Delta z \sim -4$ m) contributes to both Ebb Complex and South Spit masks. For the Ebb Complex, this loss combines with erosion elsewhere for a volume loss of -3.5%, whereas intense deposition elsewhere in the South Spit favors +18% volume increase. Deposition on the upper shoreface south of the jetty lies adjacent to erosion on the lower for a South Beach volume loss of -1.5%, whereas the South Jetty shows an increase of +8.1%, benefiting from deposition behind the spur.

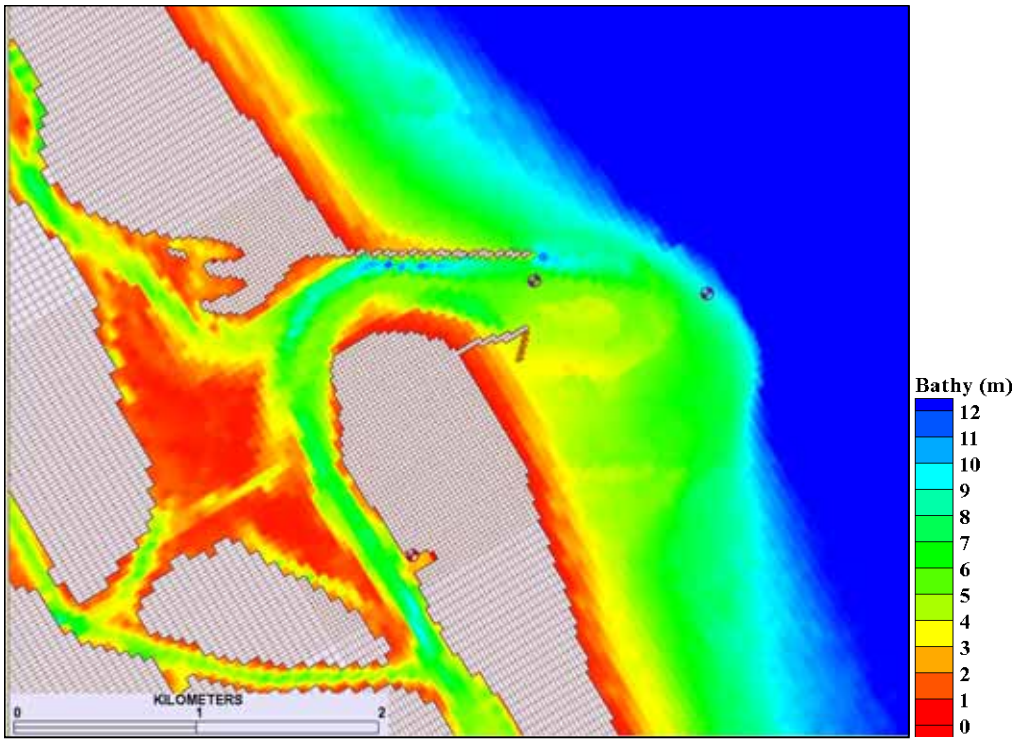

Figure 116. Morphology at 0 hr for South Jetty Extension with SS and C.

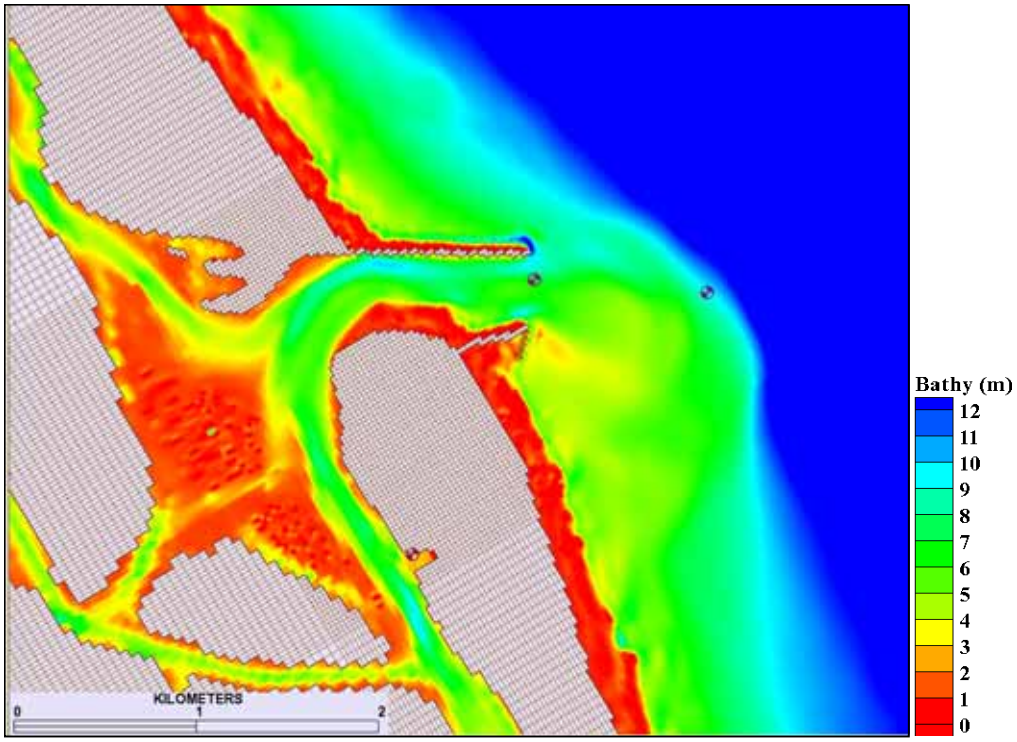

Figure 117. Morphology at 7284 hr (10 months) for South Jetty Extension with SS and C.

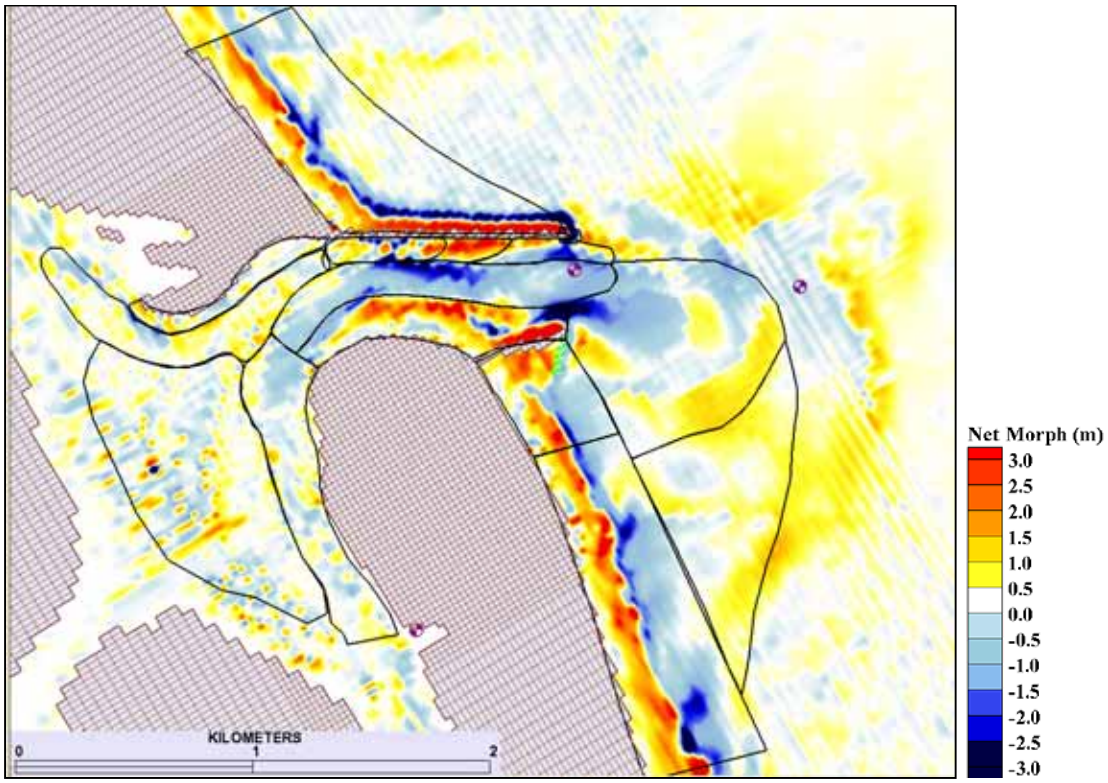

Figure 118. Net 10-month change in morphology for South Jetty Extension with SS and C.

Table 19. Volume Change (10 months) South Jetty Extension with SS and C: Normalized (%) and Net (Δvol).

Polygon Mask	%	Δvol (m^3)
Ebb complex	-3.48	-82086
South spit	18.42	90550
Channel ~4.6m	-17.77	-217052
Channel >7m	-7.11	-20321
Basin channel	5.61	32198
North channel	1.50	14425
South Jetty	8.10	28750
South channel	-1.63	-21727
South beach	-1.47	-25742
Outer bypass	4.09	94164
North tip	-62.34	-13603
North spit	1.93	2522
North beach	0.71	14747
Hard bottom	-2.01	-7214
Flood shoal	-0.74	-6417

Predicted velocities during the last spring tide (April 23, 1997) are 1.12 m/s for maximum ebb and 1.32 m/s for maximum flood (Figure 119 and Figure 120). Currents present along Rockhouse Creek reach 1.0 m/s for ebb, when very little flow moves over the exposed flood shoals, and reduce to 0.5 m/s for flood, when flow is distributed throughout the flood shoal at the height of the storm. Similar flow distribution patterns are evident between the ebb and flood for the North Beach, South Beach, and South Spit, where depths less than 1 m create numerous dry cells during ebb. During maximum ebb, northern currents approaching the inlet from the south diverge across the downdrift bypass bar, with the eastern branch joining the ebb flow and the western branch rotating toward the submerged spur to produce southern flow and an anticyclonic eddy (Figure 119a and Figure 120a). During flood, the increased water level, as indicated by the reduced number of dry cells, allows flow over the crest of the submerged spur, flushing the area behind the spur as northern currents flow east over the crest (Figure 119c, d).

During last neap tide (April 30, 1997), maximum ebb is 0.97 m/s and maximum flood 0.92 m/s, which is a smaller gap than previously observed for neap tides. Flow through Rockhouse Creek channel is still evident in both maximum tidal phases by the dark blue velocity magnitude contours of Figure 121a and c and the longer vectors of Figure 122a and c. Numerous small eddies (both clockwise and counterclockwise rotation) form south of and behind the spur in all phases. Bypassing from the ebb shoal to the downdrift attachment bar is evident immediately south of the spur for the last hour of flood, when the more southerly eddies have dissipated in the nearshore. Bidirectional flow within the inlet is present during last hour of ebb, but is confined along the east-west axis, having no northward component over the south spit shoal.

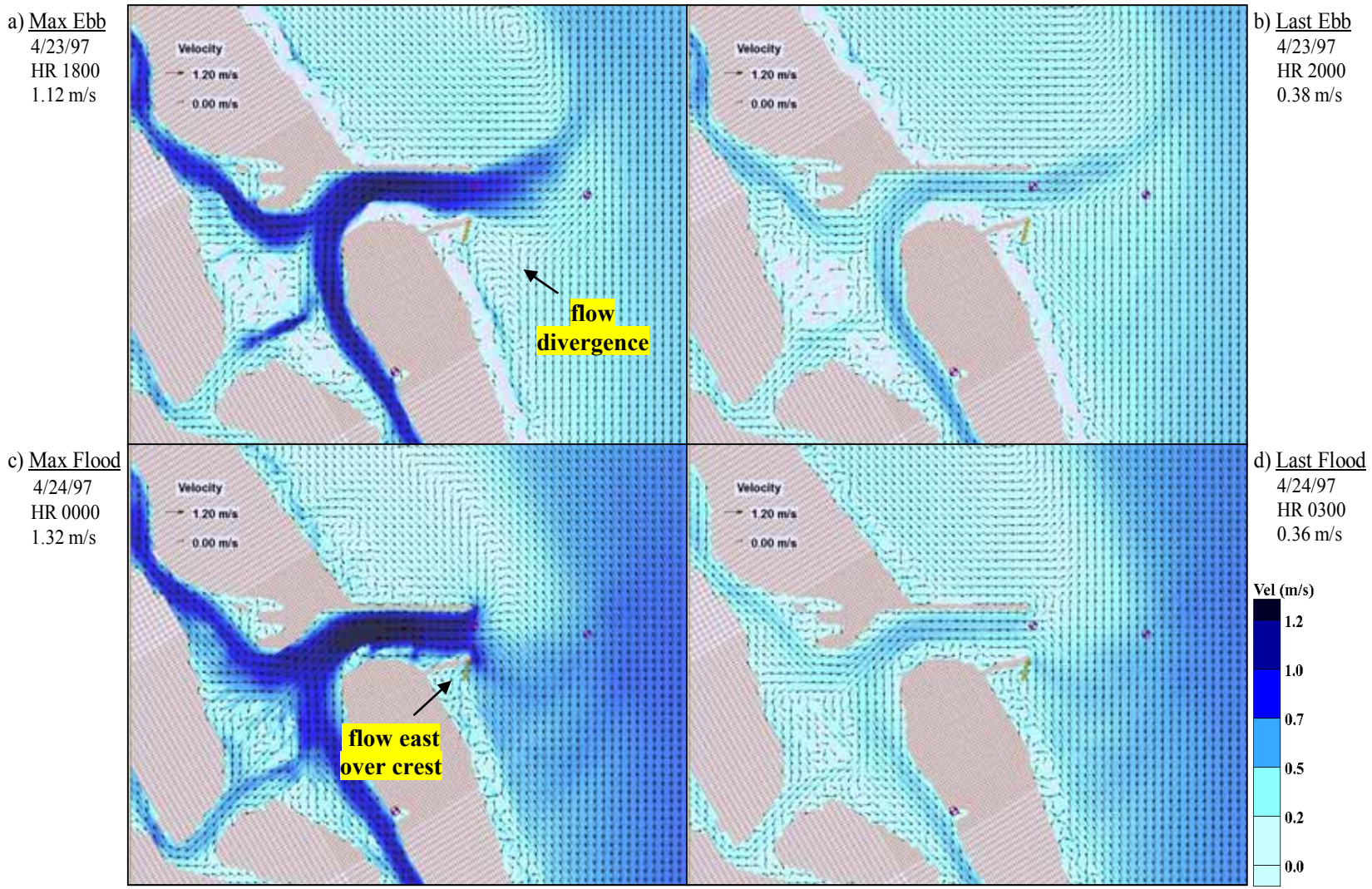

Figure 119. Flow velocities for South Jetty Extension with SS and C during spring tide of 4/23/97. Maximum value from cell 26447 in channel.

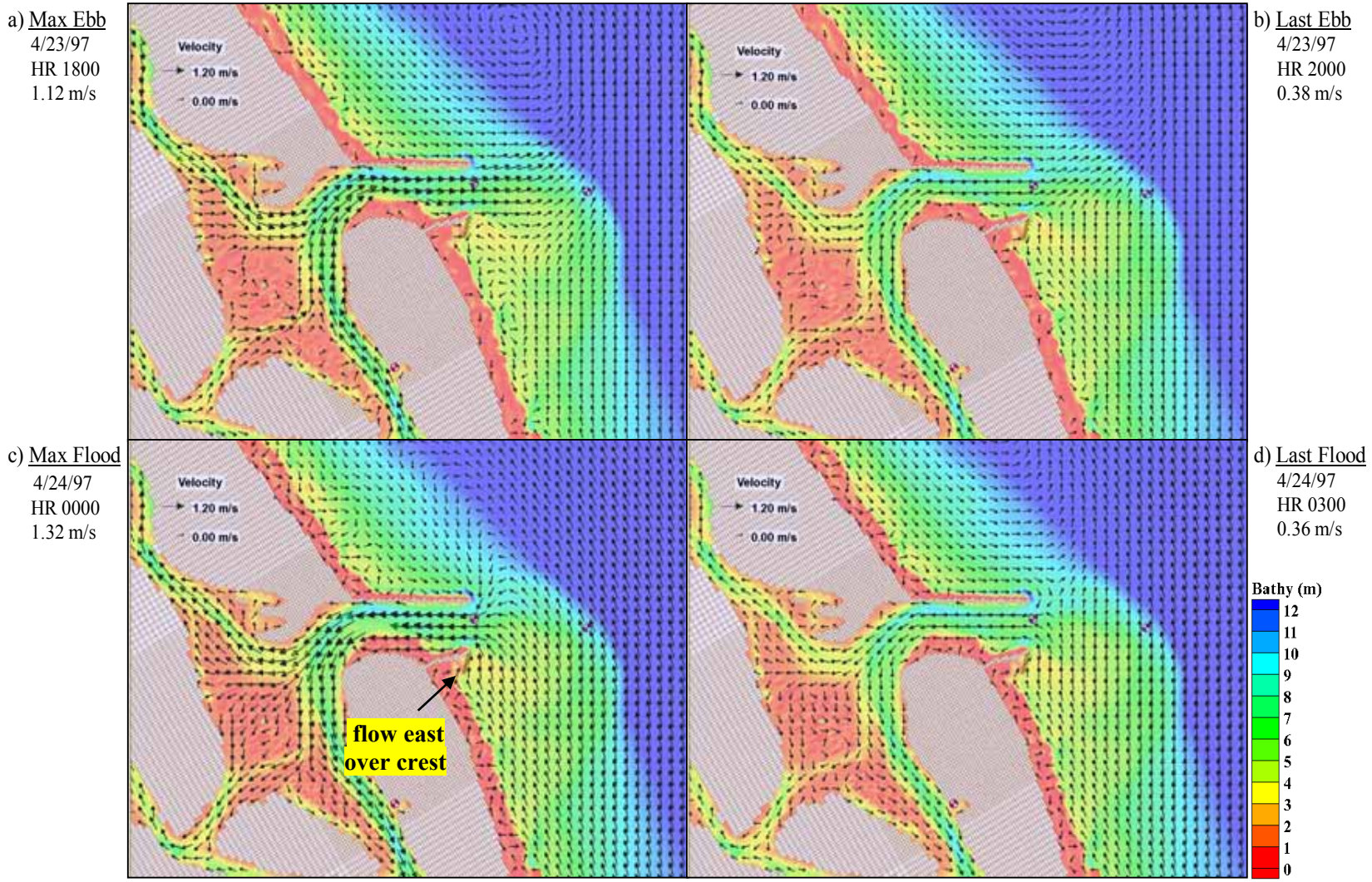

Figure 120. Morphology and flow velocities for South Jetty Extension with SS and C during spring tide of 4/23/97. Maximum value from cell 26447 in channel.

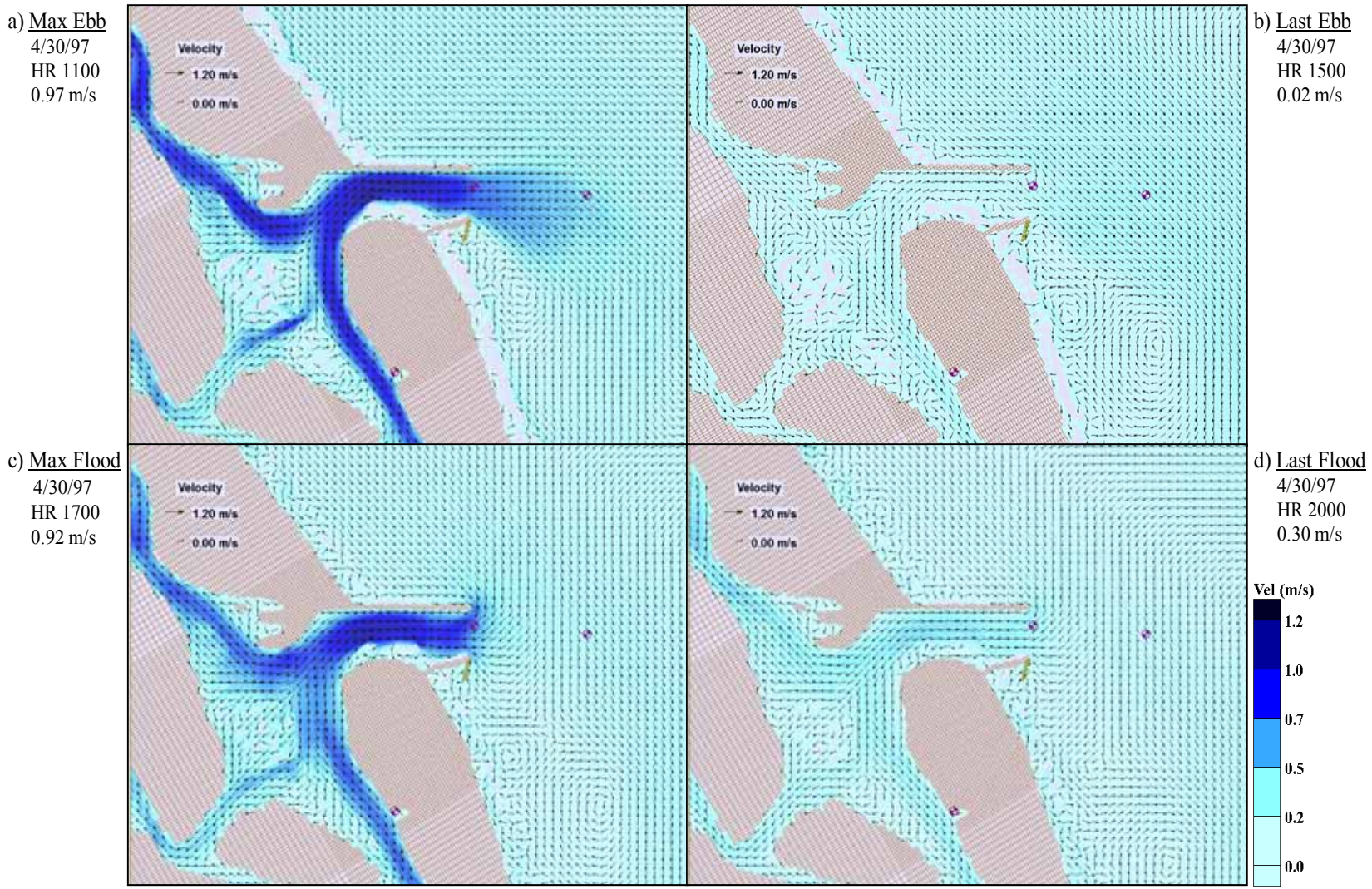

Figure 121. Flow velocities for South Jetty Extension with SS and C during neap tide of 4/30/97. Maximum value from cell 26447 in channel.

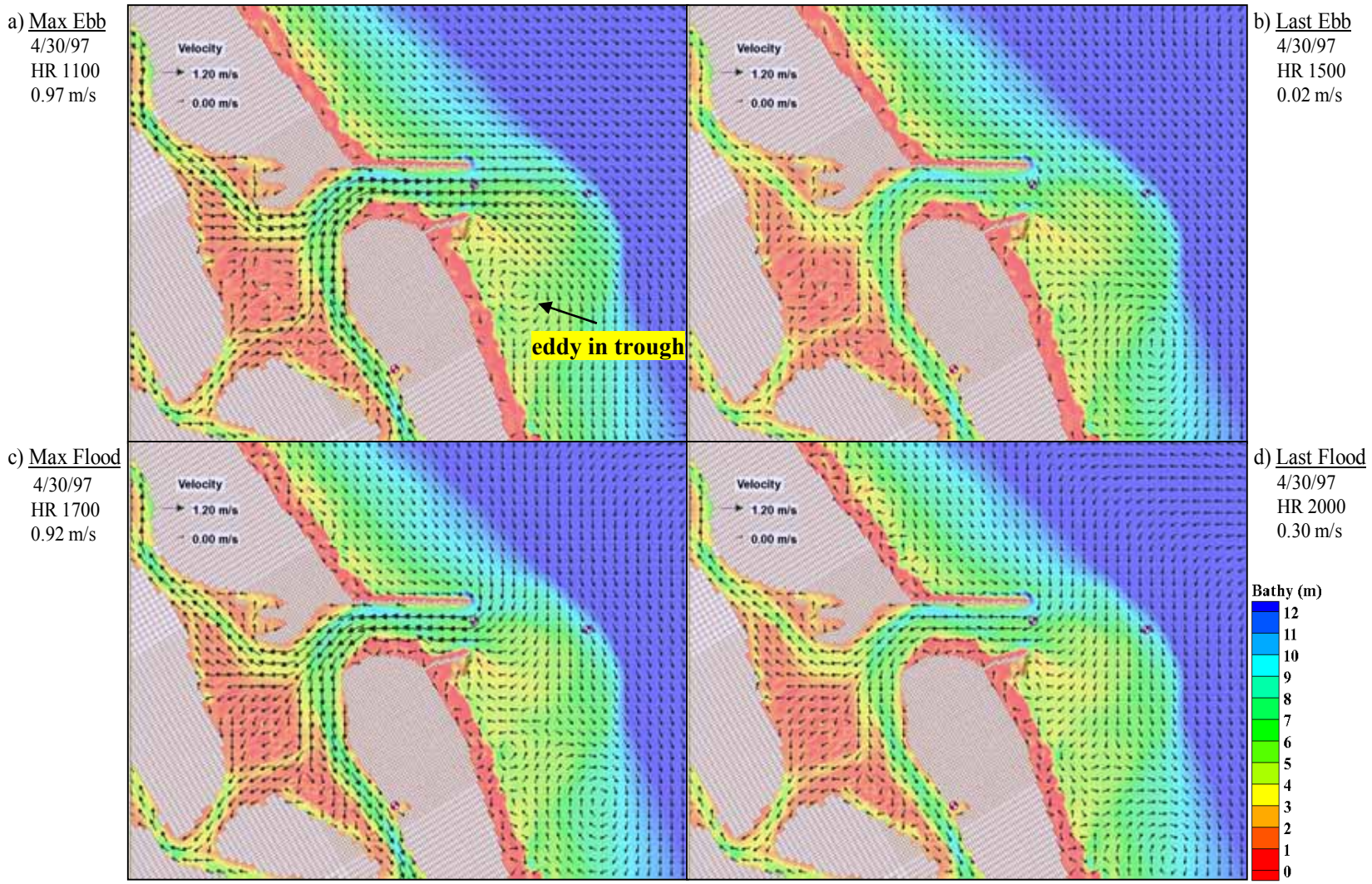

Figure 122. Morphology and flow velocities for South Jetty Extension with SS and C during neap tide of 4/30/97. Maximum value from cell 26447 in channel.

5.3.6 South Jetty Extension with Submergent Spur, HB, and Channel

Starting morphology (Figure 123) indicates the addition of the artificial hard bottom (HB) basin by the gold triangles in the north of the inlet for this Submergent Spur (SS) design. For the 10-month morphology (Figure 124), the relocated channel (C) reduces in depth as the south spit shoals into this designed navigation channel. This shoaling falls somewhere between the other Hard Bottom and Channel long-term designs, being less obtrusive on the channel than the Emergent Spur, but shallower ($z <$ 2 m) than the South Jetty Extension ($z < 3$m). South of the Hard Bottom basin, channel depth is increased and the south jetty tip has a 10.5 m scour hole. Deposition on the north beach and adjacent north jetty, both sides of the south jetty, and south beaches is equal to that for the previous Submerged Spur design without the hard bottom. Depths decreased ($z \sim 3$ m) all along the downdrift bypass bar as sediment shifted south of the ebb shoal. Rockhouse Creek is still somewhat definable ($z \sim 3$ m).

Net morphology contours (Figure 125) show more deposition in the Channel>7m mask reducing the volume loss to -2.0% (Table 20). With the scour area at the south jetty tip confined to the Ebb Complex and South Spit mask, the Channel~4.6m scouring produces a -18% decrease in volume. The Ebb Complex losses -6.8% and the South Spit gains +15% volume. The shifting of sand toward the attachment bar, as observed in the final morphology image (yellows south of the spur), contributed to the largest volume increase observed for the South Jetty (+13%). Despite the full coverage of positive net change over the upper shoreface for the South Beach ($\Delta z > +3$ m), a decrease in total volume of -0.9% occurred here.

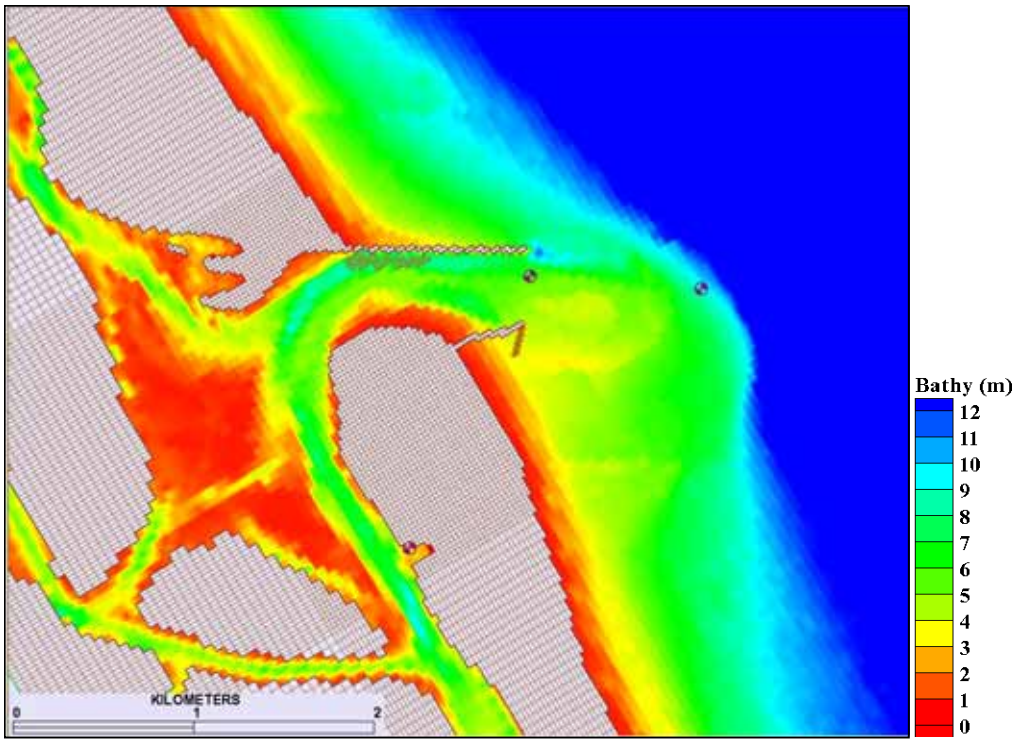

Figure 123. Morphology at 0 hr for South Jetty Extension with SS, HB, and C.

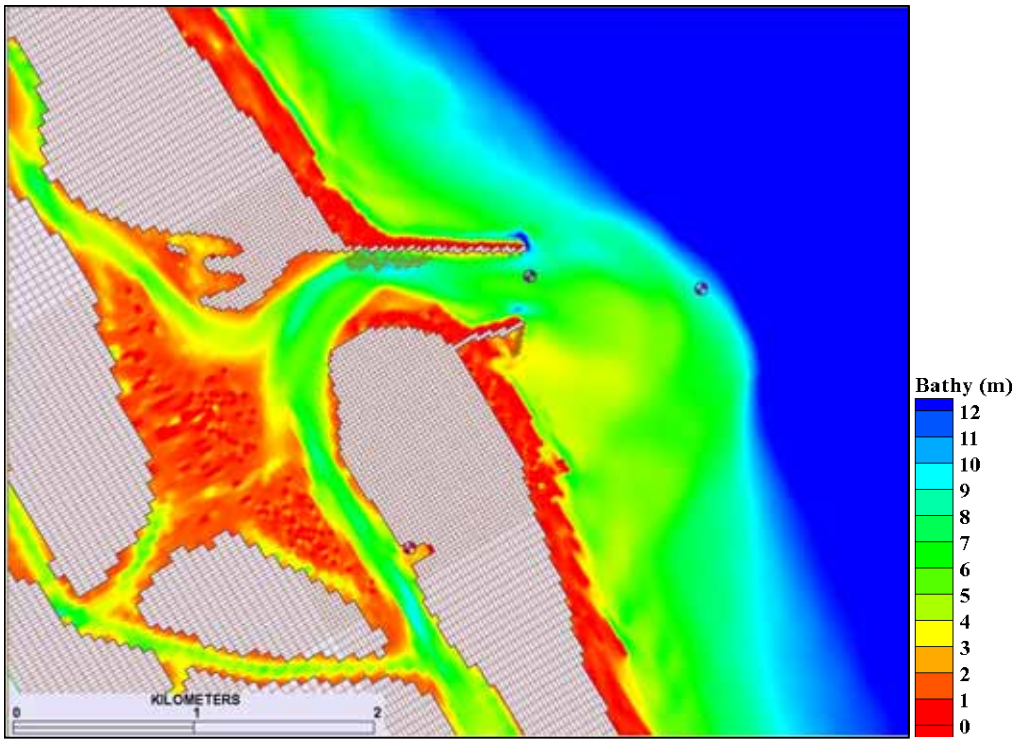

Figure 124. Morphology at 7284 hr (10 months) for South Jetty Extension with SS, HB, and C.

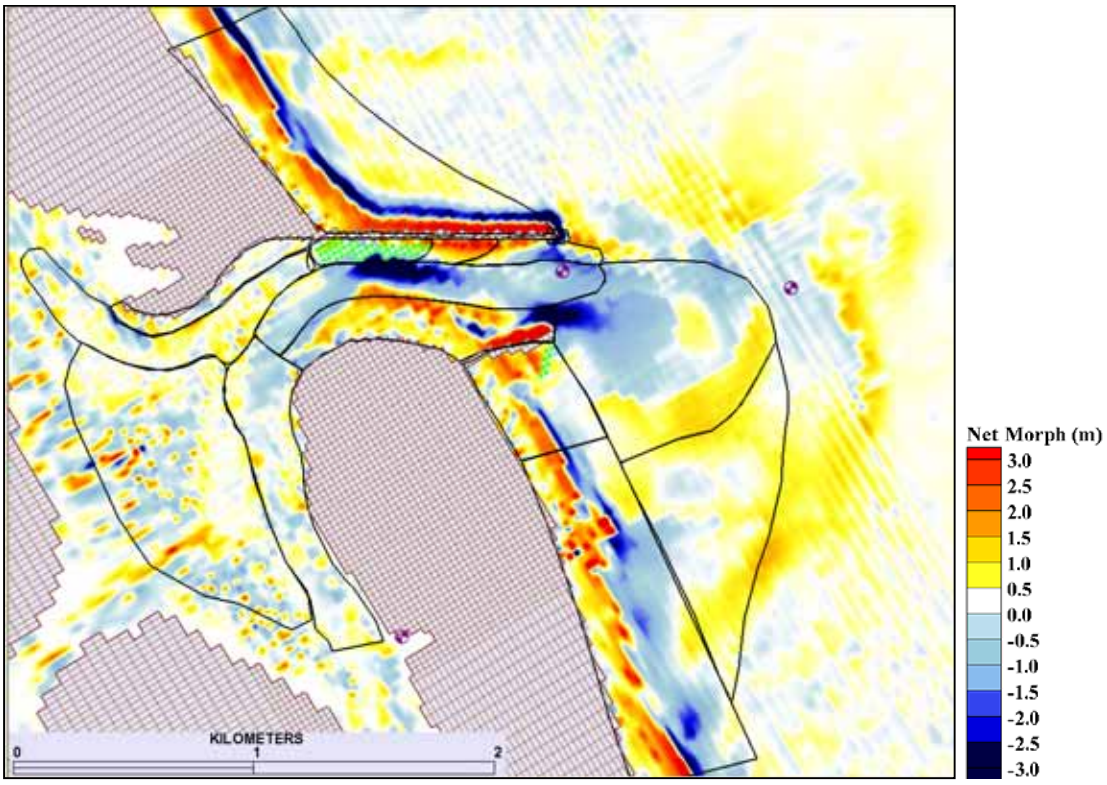

Figure 125. Net 10-month change in morphology for South Jetty Extension with SS, HB, and C.

Table 20. Volume Change (10 months) South Jetty Extension with SS, HB, and C: Normalized (%) and Net (Δvol).

Polygon Mask	%	Δvol (m^3)
Ebb complex	-6.76	-159584
South spit	14.88	73165
Channel ~4.6m	-17.88	-218263
Channel >7m	-2.04	-5814
Basin channel	4.33	22745
North channel	1.41	13577
South Jetty	12.86	45655
South channel	-1.19	-15848
South beach	-0.88	-15361
Outer bypass	4.11	94702
North tip	-60.22	-13141
North spit	2.07	2693
North beach	3.28	68149
Hard bottom	-2.68	-8883
Flood shoal	0.31	2672

Although predicted flow velocities within the inlet are of similar magnitude to the Submergent Spur with Channel design for the last spring tide (April 23, 1997), this HB version shows strong longshore currents in the nearshore (Figure 126), with increased magnitudes along the north beach (1.0 m/s) and adjacent jetty (0.7m/s). The long-term nearshore depths for this design were predicted to reduce by an order of magnitude (from 2 m to 0.2 m) by the time of this last spring tide (Figure 127). Maximum ebb of 1.20 m/s for cell 26449 in the center of the channel, just north of the south spit shoaling, is increased to 1.31 m/s during maximum flood associated with the passing storm. As compared with the non-HB option (Figure 119), more fully-developed eddies form throughout the spring tide, south of the submerged spur. However, during maximum flood, the larger magnitude currents around the south jetty, along the submerged spur, are reduced (Figure 126c), as compared with the non-HB.

During the last neap tide (April 30, 1997), traces of the longshore current are still evident, though at a reduced velocity (0.5 m/s). Flow velocities of 1.01 m/s for maximum ebb and 0.88 m/s for maximum flood have returned to a normal trend (Figure 128 and Figure 129). Flow through Rockhouse Creek is not as organized, as compared with that of the Submergent Spur with Channel (Figure 121), but is still discernible with magnitudes of 0.5 m/s. During maximum ebb, the eddy that had formed in the trough (z ~ 5 m) between the 4 m contours of the downdrift bypass/attachment bar for the non-HB option (Figure 122a), has shifted NW to become elongated and centered squarely over the more pronounced 3 m shoal/downdrift bypass bar along the south jetty spur (Figure 129a). Flow south of the jetty, along the south beaches (z = 4 m), shifts east toward deeper water north of the eddy that formed during flood phase (Figure 129c, d).

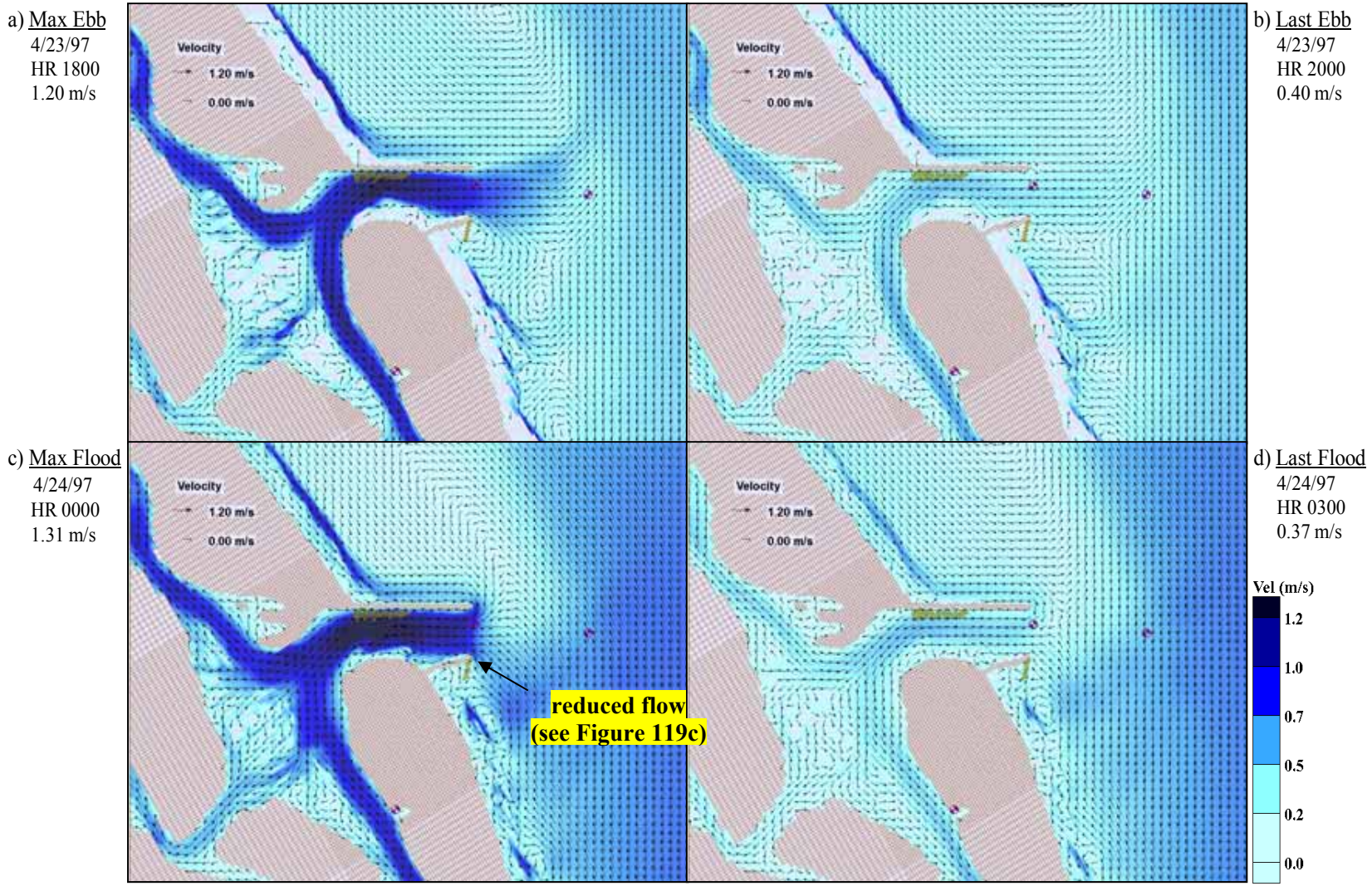

Figure 126. Flow velocities for South Jetty Extension with SS, HB, and C during spring tide of 4/23/97. Maximum value from cell 26449 in channel.

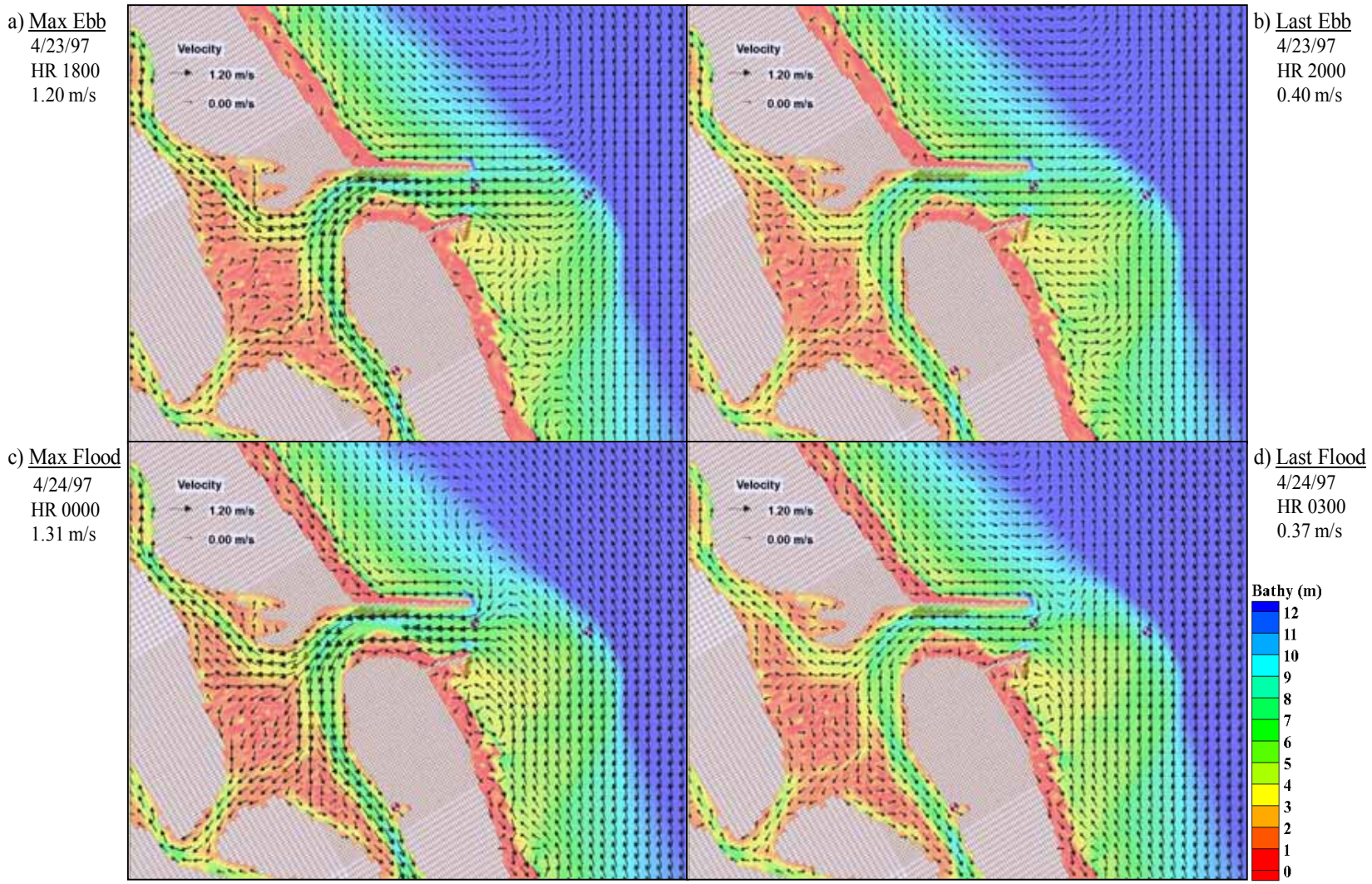

Figure 127. Morphology and flow velocities for South Jetty Extension with SS, HB, and C during spring tide of 4/23/97. Maximum value from cell 26449 in channel.

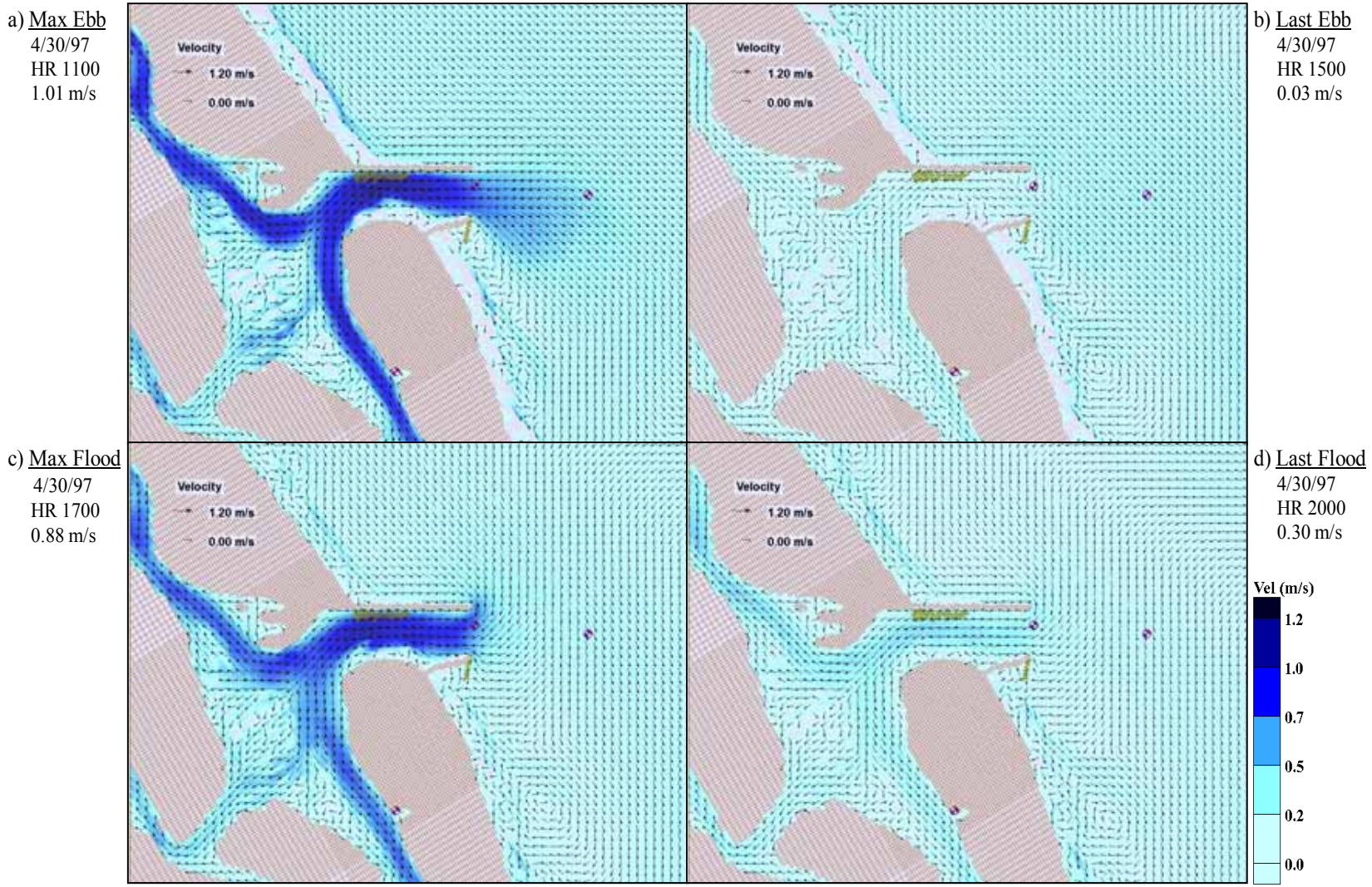

Figure 128. Flow velocities for South Jetty Extension with SS, HB, and C during neap tide of 4/30/97. Maximum value from cell 26449 in channel.

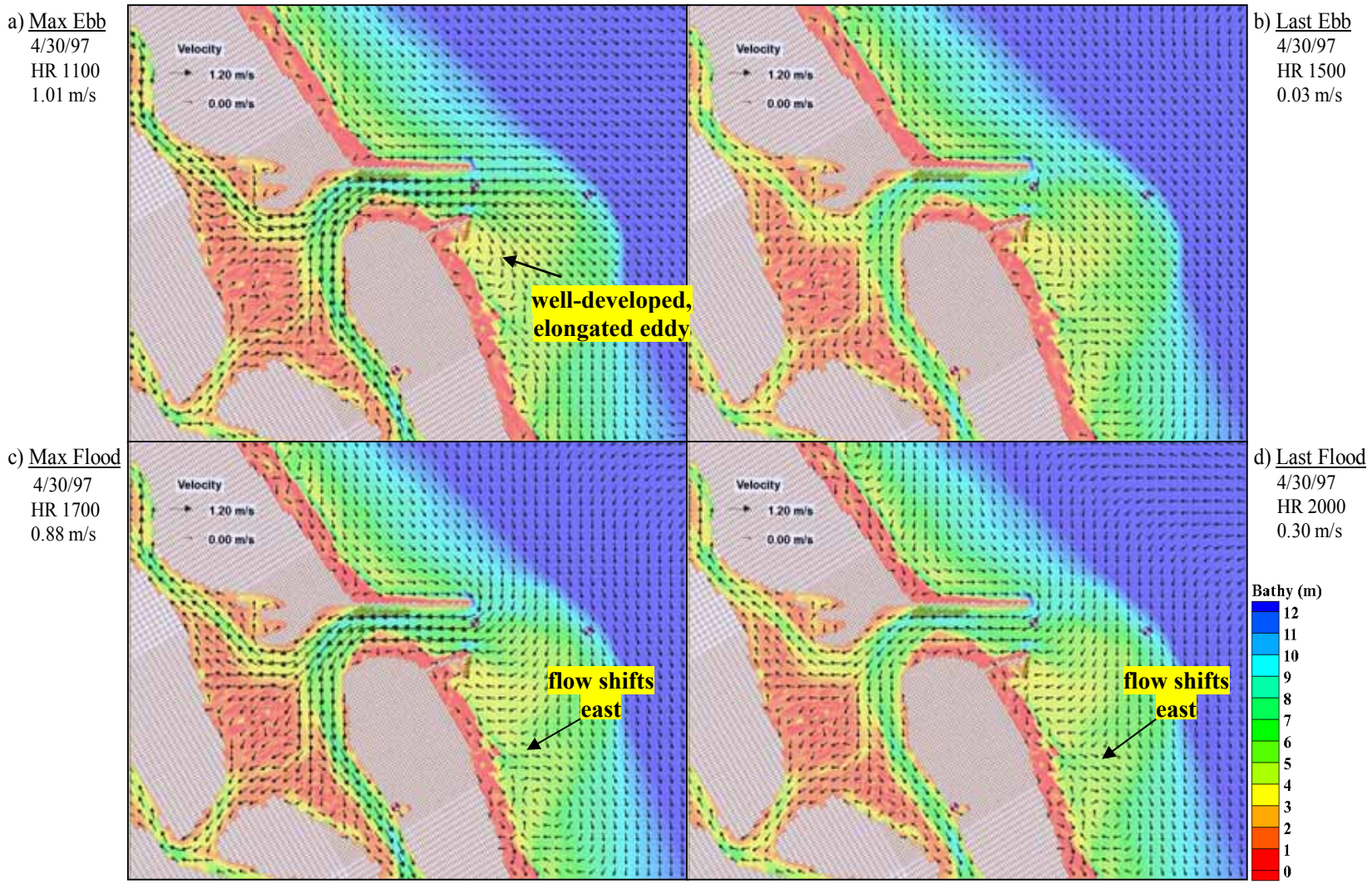

Figure 129. Morphology and flow velocities for South Jetty Extension with SS, HB, and C during neap tide of 4/30/97. Maximum value from cell 26449 in channel.

5.3.7 Comparison of Long-term Runs

This section provides a cumulative examination of the morphologic changes produced by each of the long-term designs with consideration for how the hydrodynamics impacts the observed morphologies. Detailed long-term analysis for each design is found in previous subheadings. Abbreviations for the design options, referenced in Table 3, are employed in this section to facilitate their comparison.

For the net morphology comparison contour plots presented below (Figure 130 and Figure 131), the Present Design net morphologic change plot is included in each figure for ease of comparison. However, the masks are no longer highlighted on the plots to get a better sense of the scope of the design changes. If necessary, the reader should refer to Figure 20 to review the mask/sub-domain locations.

Figure 130 compares the design alternatives that do not have the Hard Bottom basin. This figure includes results for the South Jetty with Emergent Spur and Channel design, which was not included in the long-term analysis. This run was shortened due to a re-start error for the steering module in the updated 10.1 beta version of SMS® that was unable to be corrected prior to the end of this study. As indicated on the plot, the net morphologic analysis only represents 4.5 months of long-term change. Recognizing that it is only 1.5 months beyond that of the 3-month run, it is obvious that only the beginning of the storm influences would be evident. However, this small amount of extended time does include a storm having winds ranging from 10.0 to 13.5 m/s from October 4-6, 1996 increasing to 10.5 to 16.6 m/s for October 7-8, 1996. There is also three other extended wind events before the model stops short on November 11. These

events included wind speeds near 12 m/s lasting for 8 to 12 hours. Therefore, it was deemed appropriate to include this shortened run for projected indicators as to Channel Only changes for the Spur designs.

One area of the major concerns for Ponce de Leon Inlet is shoaling of the South Spit. The 10-month volume changes (Table 21) show that all design options improve on the +22% increase observed in the Present Design. Although the SJ/ES/HB design actually shows a volume loss of -9.5%, this is due to shifting of the key deposition area northward into the navigation channel as observed in that net change plot (Figure 131). This shift was also observed for the SJ design, but produced a comparatively reduced volume gain of +13% since erosion in the lower section of the South Spit was quite less than for the Emergent Spur option.

Table 21. Comparison of Normalized Volume Changes (%) for Long-term Runs (10 months).

Polygon Mask	present Present	a1 SJ	a9 SJ/HB	a13 SJ/ES/HB	a14 SJ/SS/C	a15 SJ/SS/HB
Ebb complex	-8.62	-5.19	-6.19	-3.69	-3.48	-6.76
South spit	21.54	12.57	14.65	-9.52	18.42	14.88
Channel~4.6m	-13.29	-14.14	-16.48	-7.82	-17.77	-17.88
Channel>7m	-20.58	-10.51	-6.07	3.83	-7.11	-2.04
Basin channel	4.12	1.28	6.13	4.28	5.61	4.33
North channel	3.32	3.32	3.28	3.40	1.50	1.41
South Jetty	-6.70	-11.25	-17.44	9.20	8.10	12.86
South channel	-1.25	-1.09	-1.23	-2.09	-1.63	-1.19
South beach	-5.13	-3.31	-1.37	3.76	-1.47	-0.88
Outer bypass	7.76	5.77	7.57	4.58	4.09	4.11
North tip	-51.35	-62.38	-57.14	-45.39	-62.34	-60.22
North spit	0.26	-5.67	0.30	1.49	1.93	2.07
North beach	4.85	3.94	3.60	-8.06	0.71	3.28
Hard bottom	-2.47	-9.65	0.05	-3.28	-2.01	-2.68
Flood shoal	-0.19	0.04	-2.17	0.92	-0.74	0.31

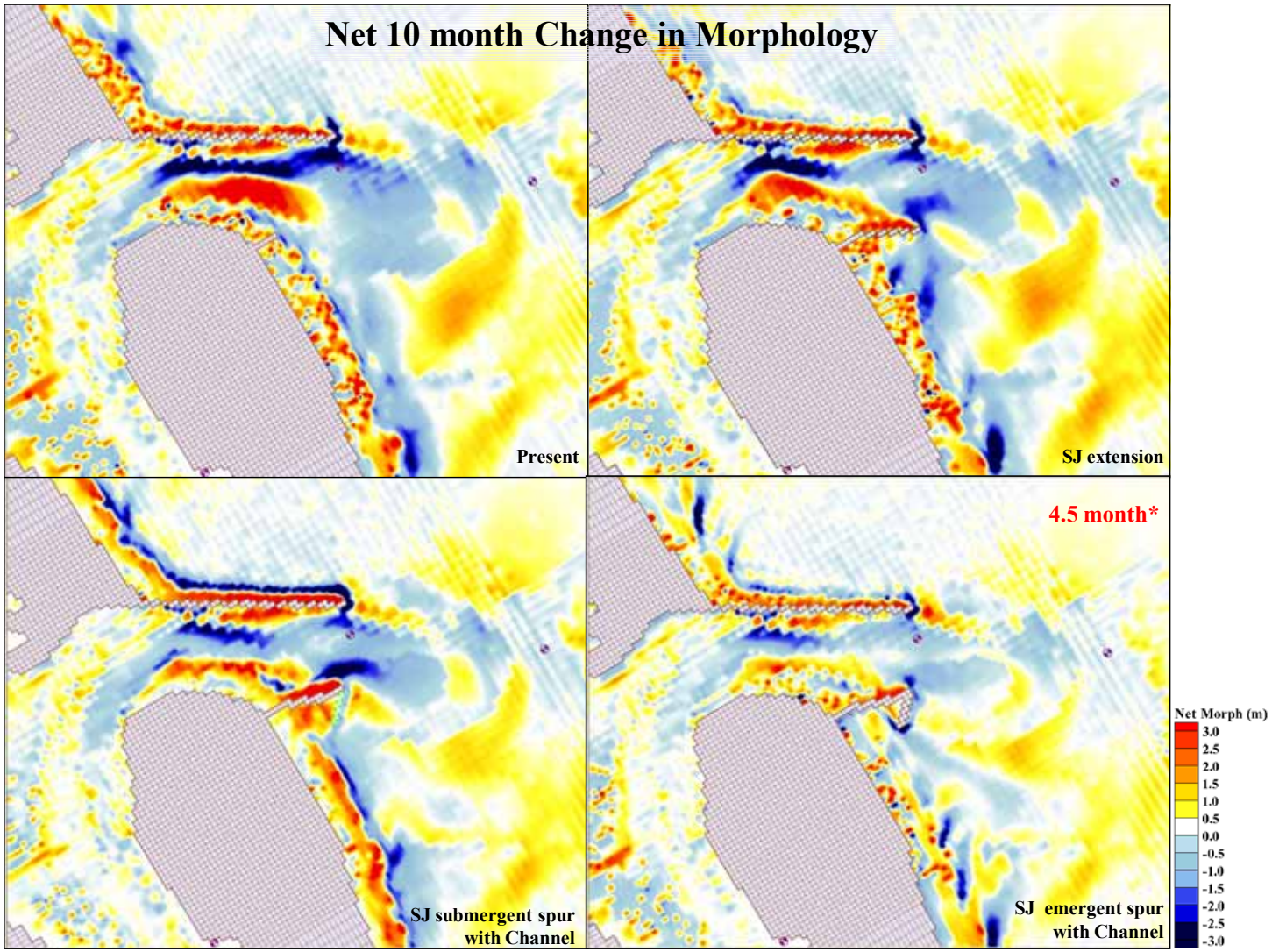

Figure 130. Comparison of net 10-month change in morphology for South Jetty Extensions with no HB.

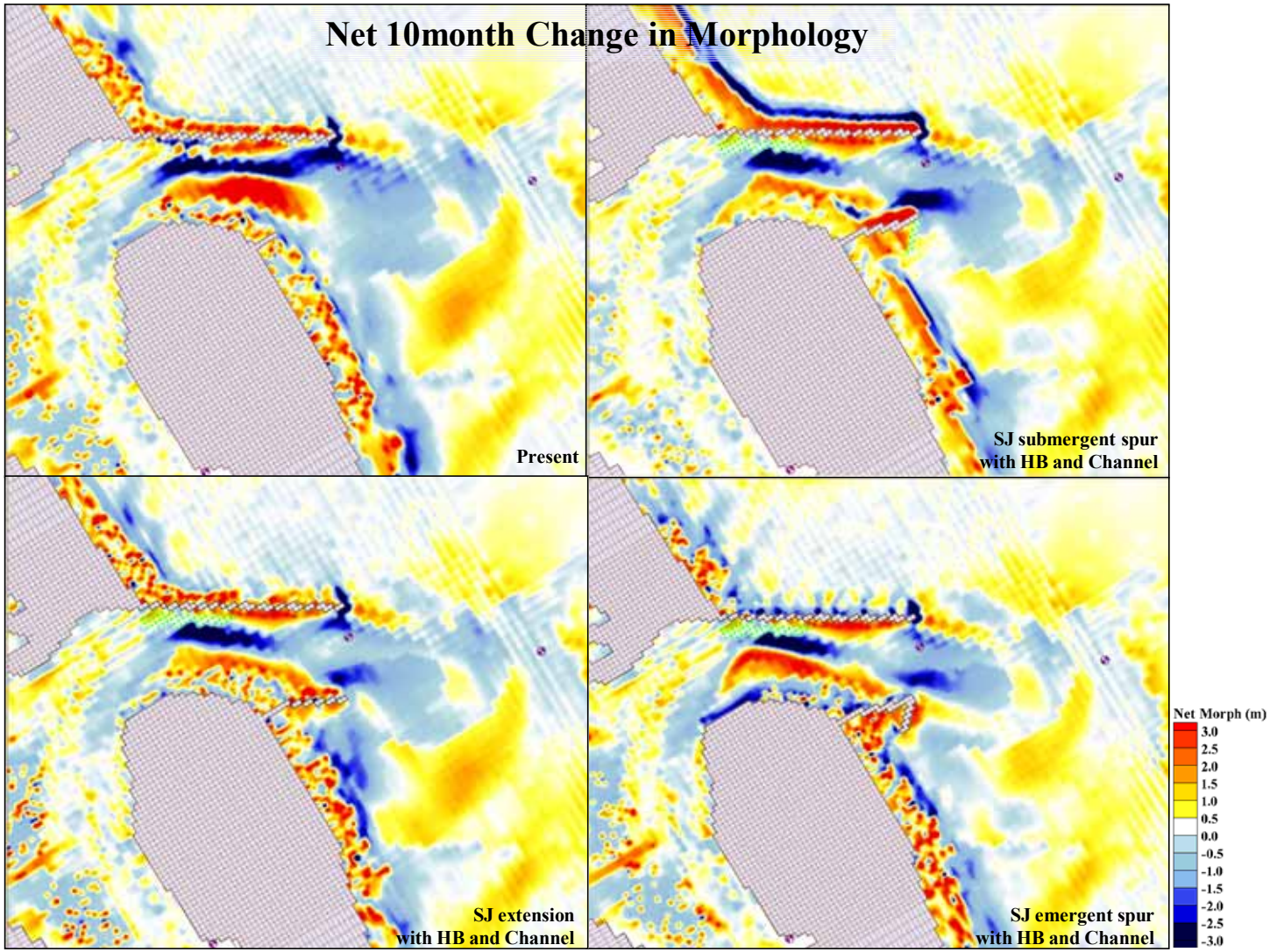

Figure 131. Comparison of net 10-month change in morphology for South Jetty Extensions with HB and Channel.

For the Channel~4.6m, the shifted South Spit shoal reduced the scouring effects in this mask for a volume loss of only -7.8% for the SJ/ES/HB design. Although all other designs improved on the intended volume loss over the -13% of the Present Design, only the losses in the SJ/SS/C design (-18%) cover the greatest width (y-axis) and length (x-axis) of erosion through the inlet, benefiting from the limited encroachment of the southern shoal (Figure 130).

Channel>7m is part of the shifted navigation channel running precariously close to the north jetty (upper left in Figure 130 and Figure 131). Ideally, this area would show reduced erosion and channel in-filling from the new design. The Present Design shows a net volume loss of -21%. The SJ/ES/HB performed the best in this mask with a volume increase of +3.8%, based on reduced scouring inside the inlet near the north jetty tip and increased deposition in this basin. The SJ/SS/HB also performed quite well with only a -2.0% decrease in volume.

The Basin Channel shows deposition in all the net topographic change contour plots. However, the SJ design only reaches a volume increase of +1.3%, as compared to that of the Present Design (+4.1%), having the majority of its erosion occurring in the Hard Bottom subset (-9.7% volume loss). The Present Design continues to erode in the Hard Bottom subset as well, for a net volume loss of -2.5%. This loss is of similar magnitude to the other designs, except for the SJ/HB that actually gains +0.05% volume in the Hard Bottom subset of the Basin Channel mask.

For the South Jetty, two trends emerge. Intense deposition downdrift of the spurs promotes volume gains of +8.1% for the SJ/SS/C design to +13% for the SJ/SS/HB design. Without the spur, this area is shown to loss volume from -6.7% for the Present

Design to -17% for the SJ/HB design. Concern for whether the large loss for the SJ/HB design is due to southern transport of the sediment is addressed by examining change in downdrift areas.

The South Beach shows a volume loss of -5.1% for the Present Design, making all the other options more beneficial to maintaining sand on these beaches. The SJ design still loses -3.3% after 10 months of volume change, whereas the SJ/ES/HB option actually nets a +3.8% increase. There is a reduction in erosion for the SJ/HB design in this area (-1.4% volume change), but gains in the adjacent Outer Bypass mask are equivalent to that of the Present Design and, therefore, do not appear to provide much relief for concern about erosion on the south beaches in that design. Other designs show volume gains in this area of approximately +4.5%.

Turning to the Ebb Complex to investigate the ability of each design to both temporarily store and eventually bypass sediment to the downdrift (south) areas, the observed loss of -8.6% volume for the Present Design should be considered in tandem with the net change in morphology plots. Given that this is the highest volume loss for any of the designs in this sub-domain and that there is no south jetty tip to account for the enhanced erosion to the Ebb Complex, it is fair to suggest that all other designs perform better with respect to bypassing than the present configuration.

Scouring at the tip of the north jetty (North Tip) is expected. The Present Design loses -51% volume and the other designs fall within ±10% of this loss. The North Beach is a different matter since the SJ/ES/HB design produces a large decrease in volume (-8.1%), whereas all other designs promote increases in sediment volume. The SJ/SS/C provides the lowest volume gain of +0.7% and the other designs, including the Present

Design show increases of approximately +4.0%. Despite the strong longshore currents observed in the nearshore of the SJ/SS/HB design during the spring tide of April 23, 1997, this design increased volume in the North Beach area by +3.3%.

Erosional concerns for the North Spit that prompted revetment in 2004 are continued if the SJ design is utilized. This design had not only the largest volume loss for the mask adjacent to the North Spit, the Hard Bottom mask, it is also the only design that removes sediment from the North Spit domain (-5.7%). Increased deposition in this area should be considered if design changes fall too close to the North Channel, especially at the western edge of the mask where the North Channel forms a dogleg around the lobes of the north spit.

Deposition is predicted to occur in the North Channel for all designs, with all but the Submergent Spur designs gaining approximately +3.3% in volume. The Submerged Spur options only gain approximately +1.4%. The South Channel mask shows erosion occurring for all designs of roughly the same magnitude (Δvol ~ -2%). The Flood Shoal shows a variety of net volume changes within the -2 to +0.9% range, but only the submergent spurs (SJ/SS/C and SJ/SS/HB) along with the SJ/HB design had organized and notable flow through Rockhouse Creek passage.

Taken in total, the best design from the long-term runs might well be the South Jetty Extension with Emergent Spur, Hard Bottom and Channel (a13 from Table 21) were it not for the intense shoaling that drastically encroaches the navigation channel. This concern is not easily identified in the net volume change comparisons. In fact, these look rather promising until one re-examines the net change in morphology to locate the gains and losses for the volume. Coupling this intense deposition with the

extreme erosion of the North Beach, this Hard Bottom design is not predicted to improve the areas of concern.

All Hard Bottom options remove the erosional pressure from the north jetty structure. The spur designs also show reduced scour of the Channel>7m next to the north jetty tip. The use of this artificial bottom is supported to minimize the scour along the north jetty. Unfortunately, the SJ/SS/HB comes with a fair amount of erosion north of the intense deposition immediately updrift of the north jetty, whereas the south shoaling is the issue for the SJ/ES/HB design. Shifting of the North Beach sands closer to the shoreline may not be undesirable over a longer period given the total volume change for this domain (+3.3%) is still on par with the Present Design (+4.9%).

Re-dredging the navigation channel to 4.6 m minimum depths seems to be a beneficial change as well. Shoaling of the south spit for the Spur designs is kept to the southern portion of the inlet in a more east-west orientation rather than angling toward the channel, as long as the HB basin is not present (Figure 130). The Emergent Spur with Channel 4.5-month run adds to this assertion, but should be further investigated.

The final results of the long-term runs indicate the South Jetty Extension with Submergent Spur, Hard Bottom and Channel may provide the best overall relief from the navigation and shoaling concerns presently affecting Ponce de Leon Inlet, FL. This design shows minimal shoaling for the North Channel and continued scouring of the all other navigation channels including Rockhouse Creek. Predicted volume losses to the South Beach are close to 0% and there is reduced deposition for the South Spit, despite the plethora of sand buildup just inside the inlet updrift of the south jetty. Encroachment of the south spit shoal is still a concern, but could be remedied with a smaller HB area.

6 Summary

The fully integrated 2D hydrodynamic and morphologic Coastal Modeling System (CMS) used in this study allowed for the comparison of several design alternatives to the configuration presently in place at Ponce de Leon Inlet, FL. The first step was a determination that the original design parameters for Ponce de Leon Inlet classify it as a stable inlet according to Escoffier Analysis, calculated using the Channel Equilibrium Area (CEA) analysis system from the Coastal Hydraulics Lab of the U.S. Army Corps of Engineers. From here, alternative designs that were modeled maintained at least the major original design parameters as well as incorporating other parameters designed to improve the three major areas of concern: severe shoaling of the south spit, mechanical stress on the north jetty structure caused by the shifted navigation channel, and hazardous passage along the navigation channel during high wave and wind events. Previous work by Taylor et al. (1996a, b) and Srinivas and Taylor (1999) indicated that a parallel extension of the south jetty and revetment of the north spit landward of the present north jetty was the option most likely to address the problems at Ponce de Leon Inlet. The idea to re-establish the weir-opening in concert with the south jetty extension was considered inadvisable given that the reduced velocities through the inlet entrance, especially during flood, would produce negative impacts on the hydraulics and concomitant shoaling. However, this option was included in the design alternatives of this study, for a preliminary run, since the previous studies did not utilize a fully integrated modeling approach to the morphologic changes.

After preparing the bathymetric dataset from a number of sources including profile and acoustic surveys, as well as Scanning Hydrographic Airborne LIDAR Surveys (SHOALS), the grid was designed consisting of 50 m x 50 m cells refined to approximately 25 m x 25 m within the vicinity of the inlet. A larger domain wave grid with larger cells (100 m x 100 m) was prepared using wave parameters gathered from the WIS hindcast model's gauge 429 and the wind speed and direction from the NOAA buoy 41009 for the calibration period (July to September, 1996) and validation period (October, 1996 to April 1997) periods. Spectrally-derived wave forcing at the offshore boundary allowed the waves to propagate into the smaller domain (7.5 km across shore and 13.5 km along shore with an azimuth of 31^{o}). The output from this larger wave domain was extracted and used as the wave forcing for the smaller CMS-Wave model. CMS-Wave is then integrated every 3 hours with the hydrodynamic and morphologic calculations of the CMS-Flow model through the steering module within the Surface Water Modeling System® (SMS) interface. Boundary conditions for the CMS-Flow model were derived from the Trident Pier tide gauge for the offshore, the Mosquito Lagoon tide gauge (now removed) for the south lagoon boundary, and a synthesized north lagoon boundary. The latter was constructed from the tidal signal at St. Augustine, reduced in amplitude for the lagoon and combined with the low-pass signal of the Mosquito Lagoon time series to simulate water levels with periods longer than 31 hours.

Lack of access to the velocity measurements from the long-term monitoring project, by the Coastal Inlets Research Program (King et al, 1999), limited calibration techniques to statistical analysis of phasing and amplitudes of water surface elevation and M2 tides between measured and modeled data at four gauges. This was not deemed

a concern given that the CMS model is a fully integrated system and the generated velocities are calculated based on finite-volume calculations. Therefore, if the continually updated morphology produced a time series of water levels that was statistically accurate for both the 3-month and the 7-month time periods, then confidence was sufficient to suggest calibration and validation were achieved. The statistical analysis presented in this study supported the accuracy of this model with normalized RMSD of between 3 and 11 "cm" (percent is here described as a length unit given the tidal range of 1 m), with the ebb shoal expectedly generating the most variability. Linear Regression analysis returned R^2 coefficients of 0.96 for the ebb shoal gauge and 0.98 for the Coast Guard gauge (increasing to 0.99 during validation for this gauge). Phasing for the water levels and for the M2 tides obtained from harmonic analysis of the water level time series also supported the calibration and validation of the model setup.

After calibration and validation, the alternate inlet designs were incorporated into the grid and 15 different preliminary runs were made for a 3-month time period using the prepared boundary conditions of the calibration time period. Post-processing of these runs contributed to the decision of which should be tested for long-term changes using the prepared boundary conditions of both the calibration and validation time period (10 months in total). The long-term allowed for inclusion of tropical depressions in fall and nor'easters in winter. Although preliminary analysis indicated that rebuilding the south jetty a bit closer and straighter for a parallel configuration might prove the most beneficial, this design was not chosen for the long-term run given the increased engineering costs. Based on the results of the previous research by Taylor

and Associates discussed above, modeling of the weir re-opening, and all its versions, did not proceed beyond the 3-month period, despite positive results for morphology changes in some of the polygon masks used to compare the designs. The 3-month runs indicated an extension of the south jetty in its present position as the most likely alternative to alleviate the concerns which have prompted this inlet redesign study.

Analysis of the long-term models indicates that all designs improve on the present configuration of Ponce de Leon Inlet. Dredging the centerline of the inlet to re-establish the location and depth of the original navigation channel has a positive effect on the self-scouring of this area. Coupling this Channel with a South Jetty Extension and Spur reduces the south spit shoaling and spatially limits it to the southern half of the inlet. Unfortunately, only the Submergent Spur version of the Channel Only designs was able to run to completion given the, as yet unresolved, restart error in the steering module of the newest beta version of SMS® 10.1, the interface for CMS. The creation of an artificial hard bottom, by adding rubble-mound into the deep and shifted present location of the navigation channel, is also beneficial for the structural integrity of the north jetty by impeding the self-scouring of this area. However, the combination of the HB and Channel, as modeled in this study, produced extension of the south shoal northward in the inlet following the flow observed during many of the last ebb phases of spring tides. Consideration is made, therefore, to design for a smaller artificial hard bottom basin limited to the deepest parts of the shifted navigation channel that run closest to the north jetty. Taken in total with the three areas of concern in mind, the South Jetty Extension with Submergent Spur, Hard Bottom, and Channel is considered the optimal candidate modeled in this study.

7 Conclusions

The conclusions reached in this study serve to set the framework for redesigning Ponce de Leon Inlet, FL to improve three major areas of concern: severe shoaling of the south spit, mechanical stress on the north jetty structure caused by the shifted navigation channel, and hazardous passage along the navigation channel during high wave and wind events. Hydrodynamic and morphologic changes between the short- and long-term runs, brought on by the more comprehensive modeling that incorporated storm and wind events, reversed the most likely candidate based on the 3-month run (the South Jetty only extension) to be the least likely candidate indicated by the results of the 10-month run. Therefore, the inclusion of long-term impacts is required for modeling alternative designs of inlets. The only limit on the length of a run is driven by the boundary condition files when using this PC-based CMS modeling suite. However, generation of these files for missing boundaries can be time-consuming.

Limited access to the archived data from the long-term field measurements at Ponce de Leon Inlet required calibration and validation be addressed by comparison of water level and tidal constituent amplitudes and phasing. Four gauges of varying record length were available from the King et al. (1999) dataset allowing statistical analysis using average eta, normalized root mean square deviation (RMSD), and linear regression. Results for the ebb shoal gauge provided the least best-fit (R^2 of 0.96, 11 cm deviation, 4^o phasing difference for M2 tide) and the Coast Guard gauge provided the best-fit (R^2 0.98, 3 cm deviation, 2^o phasing difference for M2 tide) with both

supporting calibration of the model. Although the extended validation period of 7 months produced a slightly larger normalized RMSD for the Coast Guard gauge (8 cm), this was an acceptable value and, when combined with the linear regression analysis having an R^2 of 0.99, indicated validation of the model setup.

Hindsight on this project reveals that the decision to remove the cost-prohibitive South Jetty Rebuild from the long-term run may not have been beneficial to improving our understanding of the impacts that such design considerations may have. The same may true of the weir options. Given that numerical modeling of weirs is limited in research applications, much is still to be learned. It is likely that successful application of weir designs may be site specific (Seabergh et al., 2008), requiring the use of fully integrated numerical models, like CMS, for such designs. The preliminary results in this study indicated that re-opening the weir reduced the self-scouring of the shifted channel, filled the deposition basin, and reduced the south spit shoaling. However, the long-term cost for mechanical bypassing and the impacts on the surf break just north of the inlet must be considered as well before any further action is taken for this design. Nevertheless, given the robust performance of the CMS models through the steering module of SMS®, it was perhaps a missed opportunity for contribution to long-term weir research to remove this design option and will be a consideration for further research at Ponce de Leon Inlet.

Advancements to the SMS® interfacing software are ongoing and the newest beta version 10.1 was utilized during this study. This allowed for the opportunity to create duplicate grids for the CMS-Wave and CMS-Flow models, as well as the assignment of rubble-mound structures to include porosity, waves breaking upon the

structure, and submergence. Unfortunately, an error in the developers code not yet resolved, limited the length of a valuable Channel Redesign alternative to 4.5 months. Its relevance was identified during comparison of the South Jetty Extension with Channel and Emergent vs. Submergent Spur options. The extension/channel/spur combinations showed that dredging the centerline of the inlet to re-establish the location and depth of the original navigation channel had a positive effect on the self-scouring of that area and reduced the south spit shoaling keeping it limited to the southern half of the inlet. However, since the Emergent Spur option ran for only 4.5 months, it may be premature to believe that this design would continue these effects as it did for the Submergent counterpart. Concern for the loss of this data did not alter the final results of the study, though, since scouring at the extended south jetty increased with the Emergent Spur. Addition of the artificial hard bottom basin worked well to maintain a shifted channel away from the north jetty, but it was offered that future designs use a smaller area limited to the deepest parts of the shifted navigation channel that run closest to the north jetty. Taken in total with the three areas of concern in mind, the South Jetty Extension with Submergent Spur, Hard Bottom, and Channel alternative was determined to be the optimal candidate modeled in this study.

Having established a protocol for the integrated hydrodynamic and morphologic modeling of Ponce de Leon Inlet, it is still fair to say that a few more model alternatives and for an even longer period of, perhaps, two years will be required before the stalemate on engineering activities is lifted at this well-established inlet that needs modification for effective management.

References

Barwis, J.H., 1975. Catalog of tidal inlet aerial photography. *GITI Report 75-2,* U.S. Army Engineer Waterways Experiment Station, Vicksburg, MS, and U.S. Army Engineer Research and Development Center, Fort Belvoir, VA.

Brown, E.I., 1928. Inlets on sandy coasts. *Proceedings of the American Society of Civil Engineers*, Volume LIV, pp. 505-553.

Bruun, P. and Gerritsen, F., 1960. *Stability of Coastal Inlets*. North-Holland Publishing Company, Amsterdam, 140p.

Buttolph. A.M.; Reed, C.W.; Kraus, N.C.; Ono, N.; Larson, M.; Camenen, B.; Hanson, H.; Wamsley, T., and Zundel, A.K., 2006. Two-dimensional depth-averaged circulation model CMS-M2D: Version 3, Report 2, Sediment transport and morphology change. *ERDC/CHL TR-06-09*, U.S. Army Engineer Research and Development Center, Vicksburg, MS.

Demirbilek, Z.; Lin, L., and Zundel, A., 2007. WABED Model in the SMS: Part 2. Graphical Interface. *Coastal and Hydraulics Engineering Technical Note ERDC/CHL CHETN-I-74* , U.S. Army Engineer Research and Development Center, Vicksburg, MS.

DiLorenzo, J.L., 1986. *The Overtides and Filtering Response of Inlet-Bay Systems*. Ph.D. Dissertation, State University of New York, Stony Brook, NY.

Goda, Y., 1970. A synthesis of breaker indices. *Transactions of the Japan Society of Civil Engineers*, 13, 227-230 (in Japanese).

Harkins, G.S.; Puckette, P., and Dorrell, C., 1997. Physical model studies of Ponce de Leon Inlet, Florida. *Technical Report CHL-97-23*, U.S. Army Engineer Research and Development Center, Vicksburg, MS.

Howell, G.L., 1996. A comprehensive field investigation of tidal inlet processes at Ponce de Leon Inlet, Florida. *Proceedings, 25th International Conference on Coastal Engineering. Chapter 257*, Venice, Italy: ASCE, pp. 295-307.

Hughes, S.A. and Krauss, N.C., 2006. Frequently-asked Questions (FAQs) about Coastal Inlets and the U.S. Army Corps of Engineers' Coastal Inlets Research Program (CIRP). *ERDC/CHL CHETN-IV-67*, U.S. Army Engineer Research and Development Center, Vicksburg, MS.

Irish, J.L.; Parsons, L.E., and Lillycrop, W.J., 1995. Detailed bathymetry of four Florida Inlets. *Proceedings, 8th National Conference on Beach Preservation Technology*. Tallahassee, FL: Florida Shore and Beach Preservation Association, pp. 243-58.

Jarrett, T., 1976. Tidal prism – inlet area relationships. *GITI Report 3*, U.S. Army Engineer Waterways Experiment Station, Vicksburg, MS.

Keulegan, G.H., 1967. Tidal flow in entrances water-level fluctuations of basins in communication with seas. *Technical Report No.14, Committee on Tidal Hydraulics*, U.S. Army Engineer Waterways Experiment Station, Vicksburg, MS.

King, D.B.; Smith, J.M.; Militello, A.; Stauble, D.K., and Waller, T.N., 1999. Ponce de Leon Inlet, Florida, Site Investigation. Report 1, Selected Portions of Long-Term Measurements, 1995-1997. *Technical Report CHL-99-1*, U.S. Army Engineer Waterways Experiment Station, Coastal Hydraulics Laboratory, Vicksburg, MS.

LeConte, L. J., 1905. Discussion on river and harbor outlets, 'Notes on the improvement of river and harbor outlets in the United States.' Paper No. 1009, by D. A. Watts, *ASCE Transactions* 55, 306-308.

Lillycrop, W.J.; Parsons, L.E., and Irish, J.L., 1996. Development and operation of the SHOALS airborne lidar hydrographic survey system, laser remote sensing of natural waters: From theory to practice. *Proceedings, the International Society of Optical Engineering*, V.I. Feigels and Y.I. Kopilevich (eds.), Volume 2964, 26-37, SPIE, Bellingham, WA.

Lin, L,; Demirbilek, Z.; Hajime, M.; Zheng, J., and Yamada, F., 2008. CMS-Wave: A nearshore spectral wave processes model for coastal inlets and navigation projects. *ERDC/CHL TR-08-13*, U.S. Army Engineer Research and Development Center, Vicksburg, MS.

Luettich, R.A.; Westerink, J.J., and Scheffner, N.W., 1992. ADCIRC: An advanced three-dimensional circulation model for shelves, coasts, and estuaries, Report 1, Theory and methodology of ADCIRC-2DDI and ADCIRC-3DL. *Technical Report DRP-92-6*, U.S. Army Engineer Waterways Experiment Station, Vicksburg, MS.

Militello, A., 1998. Hydrodynamics of Wind-Dominated, Shallow Embayments. Ph.D. Dissertation, Department of Marine and Environmental Systems, Florida Institute of Technology, Melbourne, FL, 232p.

Militello, A. and Zarillo, G.A., 2000. Tidal motion in a complex inlet and bay system, Ponce de Leon Inlet, Florida. *Journal of Coastal Research*, 16(3), 840-852.

Militello, A. and Zundel, A.K., 2002. Coupling of regional and local circulation models ADCIRC and M2D. *Coastal and Hydraulics Engineering Technical Note CHETN-IV-42*, U.S. Army Engineer Research and Development Center, Vicksburg, MS.

Militello, A. and Zundel, A.K., 2003. SMS Steering Module for coupling waves and currents, 2. M2D and STWAVE. *Coastal and Hydraulics Engineering Technical Note ERDC/CHL CHETN-IV-60*, U.S. Army Engineer Research and Development Center, Vicksburg, MS.

Militello, A.; Reed, C.W.; Zundel, A.K., and Kraus, N.C., 2004. Two-dimensional depth-averaged circulation model M2D: Version 2.0, Report 1: Documentation and user's guide. *ERDC/CHL TR-04-02*, U.S. Army Engineer Research and Development Center, Vicksburg, MS.

Nayak, I.V., 1971. Tidal prism-area relationship in a model inlet. *Technical Report HEL 24-1*, Hydraulic Engineering Laboratory, University of California at Berkeley, Berkeley, CA.

Nielsen, P., 1992. *Coastal Bottom Boundary Layers and Sediment Transport*. New Jersey: World Scientific, 324p.

O'Brien, M. P., 1931. Equilibrium flow areas of inlets on sandy coasts. *Journal of the Waterways and Harbors Division* 95(WW1), ASCE, 43-52.

Ochi, M.K., 1998. *Ocean Waves: The Stochastic Approach*. Ocean Technology Series 6, Cambridge, U.K.: Cambridge University Press, 319p.

Pawlowicz, R.; Beardsley, B., and Lentz, S., 2002. Classical tidal harmonic analysis including error estimates in MATLAB using T_TIDE. *Computers and Geosciences*, 28, 929-937.

Rosario-Llantín, J., 2000. Tidal Currents in Mona Passage. M.S. Thesis, Department of Marine Sciences, University of Puerto Rico, Mayagüez, Puerto Rico, 82p.

Sakai, S.; Kobayashi, N., and Koike, K., 1989. Wave breaking criterion with opposing current on sloping bottom: an extension of Goda's breaker index. *Annual Journal of Coastal Engineering*, 36, 56-59, JSCE (in Japanese).

Sargent, F.E., 1988. Case Histories of Corps Breakwater and Jetty Structures. Report 2: South Atlantic Division. *Technical Report REMR-CO-3*. U.S. Army Engineer Waterways Experiment Station, Coastal Hydraulics Laboratory, Vicksburg, MS.

Seabergh, W.C.; Demirbilek, Z., and Lin, L., 2008. Guidelines based on physical and numerical modeling studies for jetty spur design at coastal inlets. *International Journal Of Ecology and Development*, 11, 4-19.

Smith, S.J. and Smith, J.M., 2001. Numerical modeling of waves at Ponce de Leon Inlet, Florida. *Journal of Waterway, Port, Coastal and Ocean Engineering*, 127(3), 176-184.

Smith, J.M.; Militello, A., and Smith, S.J., 1998. Modeling waves at Ponce de Leon Inlet, Florida. *Proceedings, 5th International Workshop on Wave Hindcasting and Forecasting*, Environment Canada, pp. 201-214.

Srinivas, R. and Taylor, R.B., 1999. Impacts of proposed improvements to Ponce de Leon Inlet, Florida. *Proceedings, Coastal Sediments '99*, Volume 3, 2265-2279, ASCE, Long Island , NY.

Stauble, D.K., 1998. Evaluation of pre- and post-jetty inlet shoal evolution. *Proceedings, 11th National Conference on Beach Preservation Technology*. Tallahassee, FL: Florida Shore and Beach Preservation Association.

Taylor, R.B.; Hull, T.J.; Srinivas, R., and Dompe, P.E., 1996a. Ponce de Leon Inlet Feasibility Study, Numerical Modeling and Shoaling Analysis, Volume I. Taylor Engineering, Inc., Jacksonville, FL.

Taylor, R.B.; Hull, T.J.; Srinivas, R., and Dompe, P.E., 1996b. Ponce de Leon Inlet Feasibility Study, Numerical Modeling and Shoaling Analysis, Volume II. Taylor Engineering, Inc., Jacksonville, FL.

U.S. Army Corps of Engineers, 2006. Maintenance dredging: Intracoastal waterway-Vicinity of Ponce de Leon Inlet, Volusia County, Florida. *Revised Draft of the Environmental Assessment Report*, U.S. Army Corps of Engineers, Jacksonville District.

U.S. Army Corps of Engineers, 2002. Coastal Engineering Manual. *Engineer Manual 1110-2-1100*, U.S. Army Corps of Engineers, Washington, D.C. (in 6 volumes).

Volusia County Waterways Assistance Projects, 2007. Retrieved online: November 2007 from: http://www.aicw.org/wap/volusia.htm.

Zarillo, G.A. and Brehin, F.G.A., 2007. Hydrodynamic and morphologic modeling at Sebastian Inlet, FL. *Proceedings, Coastal Sediments '07*, Volume 1, 1297-1311, ASCE, New Orleans, LA.

Zarillo, G.A. and Militello, A., 1999. Ponce de Leon Inlet, Florida, Site Investigation. Report 2, Inlet Hydrodynamics: Monitoring and Interpretation of Physical Processes. *Technical Report CHL-99-1*, U.S. Army Engineer Waterways Experiment Station, Coastal Hydraulics Laboratory, Vicksburg, MS

Zarillo, G.A., 2003. Session 1 and 2: Engineering Analysis at tidal Inlets. *4th Annual Tech-transfer Workshop (PowerPoint)*. Retrieved online through Blackboard Course.

Zarillo, G.A.; Rosario-Llantin, J.; Christian, P.J.; Brehin, F.A., and Bishop, J.E., 2007. *State of Sebastian Inlet Report: An Assessment of Inlet Morphologic Processes, Historical Shoreline Changes, and Regional and Local Sediment Budget*. Report for Sebastian Inlet Tax District, Coastal Processes Research Group, Department of Marine and Environmental Systems, Florida Institute of Technology, Melbourne, FL.

Appendix A

This appendix proves an overview of the basic governing equations for the Coastal Modeling System. Many considerations are made for the complexities involved in accurately simulating the geophysical changes associated with coastal inlets. For the full description of these considerations, the reader is referred to the technical reports associated with the models: CMS-Flow (Buttolph et al., 2006) and CMS-Wave (Lin et al., 2008). These documents are readily available in the publications section of the Coastal Inlets Research Program website (http://cirp.wes.army.mil/index.html).

CMS-Flow Hydrodynamics

The vertically-integrated equations of motion and continuity are calculated using a flux-based, finite-difference approach. The equations are:

$$\frac{\partial q_x}{\partial t} + u\frac{\partial q_x}{\partial x} + v\frac{\partial q_x}{\partial y} + \frac{1}{2}g\frac{\partial (h+\eta)^2}{\partial x} = \frac{\partial}{\partial x}D_x\frac{\partial q_x}{\partial x} + \frac{\partial}{\partial y}D_y\frac{\partial q_x}{\partial y} + fq_y - \tau_{bx} + \tau_{wx} + \tau_{Sx} \qquad \text{(A.1)}$$

$$\frac{\partial q_y}{\partial t} + u\frac{\partial q_y}{\partial x} + v\frac{\partial q_y}{\partial y} + \frac{1}{2}g\frac{\partial (h+\eta)^2}{\partial y} = \frac{\partial}{\partial x}D_x\frac{\partial q_y}{\partial x} + \frac{\partial}{\partial y}D_y\frac{\partial q_y}{\partial y} - fq_y - \tau_{by} + \tau_{wy} + \tau_{Sy} \qquad \text{(A.2)}$$

$$\frac{\partial (h+\eta)}{\partial t} + \frac{\partial q_x}{\partial x} + \frac{\partial q_y}{\partial y} = 0 \qquad \text{(A.3)}$$

where

h	=	still water depth relative to a specific vertical datum
η	=	deviation of the water-surface elevation from the still-water level
t	=	time
q_x	=	flow per unit width parallel to the x-axis
q_y	=	flow per unit width parallel to the y-axis
u	=	depth-averaged current velocity parallel to the x-axis
v	=	depth-averaged current velocity parallel to the y-axis
g	=	acceleration due to gravity
D_x	=	diffusion coefficient for the x-direction
D_y	=	diffusion coefficient for the y-direction
f	=	Coriolis parameter
τ_{bx}	=	bottom stress parallel to the x-axis
τ_{by}	=	bottom stress parallel to the y-axis
τ_{wx}	=	surface stress parallel to the x-axis
τ_{wy}	=	surface stress parallel to the y-axis
τ_{Sx}	=	wave stress parallel to the x-axis
τ_{Sy}	=	wave stress parallel to the y-axis

The component velocities are related to the flow rate per unit width by the following:

$$u = \frac{q_x}{h + \eta} \tag{A.4}$$

$$v = \frac{q_y}{h + \eta} \tag{A.5}$$

The technical report provides details on the remaining terms in the governing equations.

CMS-Flow Sediment Transport

Three formulas are available in CMS-Flow for calculating sediment transport. The Lund-CIRP formula was used in this study. It calculates total load transport by combining bed load and suspended load, each of which is based on shear stress. Basic governing equations for the bed load transport under combined waves and current are:

$$\frac{q_{bw}}{\sqrt{(s-1)gd_{50}^3}} = a_w \sqrt{\theta_{net}}\,\theta_{cw,m} \exp\left(-b\frac{\theta_{cr}}{\theta_{cw}}\right) \tag{A.6}$$

$$\frac{q_{bn}}{\sqrt{(s-1)gd_{50}^3}} = a_n \sqrt{\theta_{cn}}\,\theta_{cw,m} \exp\left(-b\frac{\theta_{cr}}{\theta_{cw}}\right) \tag{A.7}$$

where

q_{bw} = bed load transport in the wave direction
q_{bn} = bed load transport in the direction normal to the waves
s = specific density
g = acceleration due to gravity
d_{50} = median grain diameter
a_w = transport rate coefficient in the wave direction
a_n = transport rate coefficient normal to the wave direction
θ_{net} = net contribution of the shear stress in the wave direction
θ_{cn} = net contribution of the shear stress normal to the wave direction
$\theta_{cw,m}$ = mean Shields parameter
θ_{cw} = maximum Shields parameter
b = coefficient for initiation of motion
θ_{cr} = critical Shields parameter

The basic governing equation for the suspended load transport (q_s) is:

$$q_s = U_c c_R \frac{\varepsilon}{w_s}\left(1-\exp\left(-\frac{w_f d}{\varepsilon}\right)\right) \tag{A.8}$$

where

U_c = magnitude of constant velocity

c_R = reference concentration

ε = sediment diffusivity (or mixing coefficient)

w_f = sediment fall velocity

d = water depth

Bed level change is calculated from the sediment continuity equation given by:

$$\frac{\partial h}{\partial t} = \frac{1}{1-p}\left(\frac{\partial q_x}{\partial x} + \frac{\partial q_y}{\partial y} + P - D\right) \tag{A.9}$$

where

h = still water depth relative to a specific vertical datum

t = time

p = porosity

q_x = flow per unit width parallel to the x-axis

q_y = flow per unit width parallel to the y-axis

P = pick-up rate

D = deposition rate

The technical report provides details on the remaining terms in the governing equations.

CMS-Wave

CMS-Wave is based on the WABED (Wave-Action Balance Equation with Diffraction), which takes into account effects of a horizontal current. Incident wave parameters were used to generate a wave density spectrum (.eng). The spectral wave density represents the wave energy per unit water-surface area per frequency interval. This study used a TMA (Shallow Water) spectrum, which incorporates finite depth effects for fetch-limited waves into a modified Pierson-Moskowitz spectrum (Ochi, 1998).

The basic governing equation for CMS-Wave is:

$$\frac{\partial(C_x N)}{\partial x}+\frac{\partial(C_y N)}{\partial y}+\frac{\partial(C_\theta N)}{\partial x}=\frac{\kappa}{2\sigma}\left[\left(CC_g\cos^2\theta N_y\right)_y-\frac{1}{2}\left(CC_g\cos^2\theta N_{yy}\right)\right]-\varepsilon_b N-S \quad \text{(A.10)}$$

with

$$N=\frac{E(\sigma,\theta)}{\sigma} \quad \text{(A.11)}$$

where

N = wave-action density to be solved; function of frequency and direction

σ = wave frequency

θ = wave direction

C_x = characteristic velocity with respect to x

C_y = characteristic velocity with respect to y

C_θ = characteristic velocity with respect to direction

C = wave celerity

C_g = group velocity

κ = empirical parameter representing the intensity of the diffraction effect

ε_b = parameterization of wave breaking energy dissipation

S = sources and sinks and non-linear wave-wave interaction

x = normal to offshore boundary

y = parallel to offshore boundary

The technical report provides details on the remaining terms in the governing equations.

According to the technical report on the formulation of CMS-Wave (Lin et al., 2008), the Extended Goda formula option, which was chosen for the wave breaking energy dissipation output in this study, is a modified version of Goda's original formula (Goda, 1970). That formulation simulated energy dissipation due to waves breaking using a Rayleigh distribution of wave heights truncated by breaker criterion based on bottom slope and wave steepness in deep water. The Extended Goda formula, modified by Sakai et al. (1989), includes opposing currents by applying a coefficient for the combined effects of currents, depth, deepwater wavelength, and bottom slope angle.

Appendix B

Table 22. Water level and meteorology data from tidal stations for Ponce de Leon Inlet.

STATION	NAME	FIRST	LAST	PARAMETER	LAT	LON	COMMENT
8721164	New Smyrna Beach	4/1/1999	6/30/1999	verified hourly WSE	29° 1.4 N	81° 55.1 W	removed 7/99
8721147	Ponce de Leon Inlet South	3/17/2006	10/31/2007	verified hourly WSE	29° 3.8 N	81° 54.9 W	established 12/78
		1/1/1978	10/31/2007	verified mo. mean WSE			reinstalled 2/06
8720587	St. Augustine Beach	7/26/1978	7/15/2002	verified hourly WSE	29° 51.4 N	81° 15.8 W	established 5/92
		2/14/1996	4/20/2003	wind			removed 8/04
		2/14/1996	4/20/2003	air temp			
		5/27/1992	10/2/2002	water temp			
		5/12/2000	4/20/2003	barometric pressure			
8721604	Trident Pier	10/21/1994	9/30/2007	verified hourly WSE	28° 24.9 N	80° 35.6 W	established 10/94
		2/15/1997	10/30/2007	wind			
		8/26/1998	10/30/2007	air temp			
		2/15/1997	10/30/2007	water temp			
		3/16/2000	10/30/2007	barometric pressure			

Appendix C

Table 23. Buoy data available for Ponce de Leon Inlet.

STATION		NAME	FIRST	LAST	PARAMETER	LAT	LON
Buoys	**41012**	St. Augustine 40 NM ENE	2002	present	wind	30.04 N	80.55 W
					air temp		
					water temp		
					wave height		
					wave period		
			2002	Jul 2007	wave density		
			2006	Jun 2006	wave direction		
	41113	Cape Canaveral Nearshore	2006	present	wave height	28.40 N	80.53 W
					wave period		
					water temp		
	41010	Canaveral East 120 NM E	1988	present	wind	28.95 N	78.47 W
					air temp		
					barometer		
					water temp		
			1996	present	wave density		
			45 days	present	wave height		
					wave period		
	41009	Canaveral 20 NM E	1988	present	wind	28.50 N	80.17 W
					air temp		
					water temp		
					barometer		
					wave height		
					wave period		
			1996	present	wave density		
			1996		wave direction		